UNIVERSIDAD NACIONAL AUTÓNOMA DE MÉXICO

PROGRAMA DE MAESTRÍA Y DOCTORADO EN INGENIERÍA
INGENIERÍA QUÍMICA – POLÍMEROS

MODELADO DE FLUJOS CONFINADOS TRANSITORIOS DE FLUIDOS COMPLEJOS

TESIS
QUE PARA OPTAR POR EL GRADO DE:
DOCTOR EN INGENIERÍA

PRESENTA:
JOSÉ ESTEBAN LÓPEZ AGUILAR

TUTOR (ES) PRINCIPAL(ES)
DR. OCTAVIO MANERO BRITO
COMITÉ TUTOR
DR. JUAN PABLO AGUAYO VALLEJO
DR. ÁNGEL ENRIQUE CHÁVEZ CASTELLANOS

MÉXICO, D. F. SEPTIEMBRE 2014

JURADO ASIGNADO:

Presidente:	DR. FEDERICO MENDEZ LAVIELLE
Secretario:	DR. RENÉ OSVALDO VARGAS AGUILAR
Vocal:	DR. JUAN PABLO AGUAYO VALLEJO
1 er. Suplente:	DR. EDTSON EMILIO HERRERA VALENCIA
2 d o. Suplente:	DR. OCTAVIO MANERO BRITO

Lugar o lugares donde se realizó la tesis: FACULTAD DE QUÍMICA, UNIVERSIDAD NACIONAL AUTÓNOMA DE MÉXICO

TUTOR DE TESIS:

DR. OCTAVIO MANERO BRITO

_____

FIRMA

(Seg u n d a ho j a)

AGRADECIMIENTOS

Agradezco el apoyo del Consejo Nacional de Ciencia y Tecnología (CONACYT) por el soporte monetario brindado mediante una beca nacional para la realización de mis estudios de Doctorado en Ingeniería (convocatoria 290604), bajo el Programa de Maestría y Doctorado en Ingeniería de la Universidad Nacional Autónoma de México, con sede en la Facultad de Química, Ciudad Universitaria, de Agosto de 2010 a Julio de 2014 y asignada bajo el número de CVU 229713. Además, agradezco al CONACYT me haya otorgado una beca mixta (convocatoria 290618) para una estancia de investigación (de Julio de 2011 a Junio de 2012) en el Instituto de Mecánica de Fluidos No-Newtonianos, en la Universidad de Swansea, Reino Unido, bajo la supervisión del Prof. Michael F. Webster, donde parte del trabajo en esta tesis fue realizado.

DEDICATORIA

Dedico este trabajo a mis padres Guadalupe Aguilar Ferrer y Esteban López Álvarez, que me han impulsado y apoyado durante toda mi vida. Con este trabajo quiero retribuirles y reconocer al menos un poco del gran trabajo que han hecho a lo largo de todos estos años. ¡Gracias, mami y papi!

Además, dedico este trabajo a mis hermanos y sobrinos en las familias Martínez López: Guadalupe, Manuel, Paulina, Alejandro; Sierra López: Diana, José Luis, Angélica, José Luis; y Gómez López: Ana Karen, Arturo, Valeria. Todos son y han sido gran inspiración durante todos estos años de trabajo. Especial mención merecen los señores Manuel Martínez Marquina y Teresa Pérez Castro, quienes me han demostrado gran cariño y apoyo desde siempre.

Dedico este trabajo a la memoria de mis abuelos Miguel Aguilar, Luz Ferrer, Apolinar López e Isabel Álvarez y de mi tía Cecilia Aguilar. “El tiempo vive en la memoria” - Maldita Vecindad y los Hijos del Quinto Patio.

Hay muchas personas que desde siempre me han apoyado, tantas que una lista de ellas sería interminable. En especial agradezco los consejos y grandes pláticas con mi hermano José Antonio Marín, a mi tía María de la Luz Aguilar y a Daniela Bucio. El apoyo y la amistad incondicional y constante de Violeta Rodríguez. El apoyo remoto y cariñoso a Judith Oliveros. Por tener fe en mí, a la Familia Arredondo Gutiérrez: Isabel, Ismael, Montserrat e Ismael. A mis hermanos y sobrinos de la Familia Guerrero Aguilar: Miguel, Bertha, Ximena, Ricardo, Daniel, Verónica, Andrea, Rebeca, Valeria, por los buenos momentos y la fe. A Constanza Sánchez, por el apoyo y el tiempo compartido en "Mordor".

A mis amigos y colegas Marcos Turcio, Francisco López-Serrano, Andrés Velasco, Irazema Alcántar, Rogelio y Cynthia Ortigosa, Pedro José Martínez, Juanma Salguero, Reem Bjrd, Marco Ellero, Yvonne Solomon, Cliff Rees, Ceren Gürkan, Monica Zakhari, Daniel de Bortoli, Antonios Valsamidis, Marco Ávila, Mireille Bravo, Alicia Cortés, Patsy Ramírez, Itzel Vallejo, Karla Salas, Jaime Jordán, Brenda Pérez, Carmen Dorado, Ángel Sánchez.

Agradezco la supervisión y revisión de este trabajo a los doctores Octavio Manero Brito, Mike Webster, Juan Pablo Aguayo Vallejo, Ángel Enrique Chávez Castellanos, Federico Méndez Lavielle, René Vargas Aguilar y Edtson Herrera Valencia, cuyas guía y sugerencias lo enriquecieron.

A nuestra Casa de Estudios la Universidad Nacional Autónoma de México, por darme la oportunidad de culminar este proyecto personal y profesional. “Por mi raza hablará el espíritu”.

Resumen

Esta tesis doctoral trata el *modelado numérico* de *fluidos complejos* en *flujos complejos (geometrías complejas)*. Este tipo de modelado requiere la solución de *sistemas de ecuaciones diferenciales parciales acopladas* y altamente *no lineales*, que representan a los principios de *conservación de masa* y *cantidad de movimiento* para *fluidos incompresibles* en condiciones *isotérmicas*. Además, la naturaleza compleja de los fluidos se especifica mediante una *ecuación constitutiva diferencial generalizada*, en la cual muchos *fluidos viscoelásticos* y *viscoelastoplásticos* conocidos tienen cabida. En la parte numérica, este tipo de problemas se resuelven usando un *esquema de discretizacion hibrido* que considera *elementos finitos* y *volúmenes finitos*. Aquí, se ha adoptado un método de *Taylor-Galerkin* con *corrección de presión* para las ecuaciones de *cantidad de movimiento* (*parabólica*) y *continuidad* (*elíptica*), mientras que una implementación de volúmenes finitos se usa para la *ecuación constitutiva* (*hiperbólica*).

Este trabajo se centra particularmente en el *problema típico* de *contracción-expansión redondeada* con relación de contracción *4:1:4* y la simulación numérica del flujo de *soluciones micelares tipo gusano*, bajo el esquema del modelo *Bautista-Manero*. Esta familia de *fluidos dependientes del tiempo* puede manifestar *pseudoplasticidad, engrosamiento y adelgazamiento por extensión, tixotropía, flujo bandeado* y *esfuerzo de cedencia* en ciertas condiciones de flujo. Así, con base en el modelo *Bautista-Manero modificado (MBM)*, se proponen algunas correcciones a este esquema constitutivo. La primera de ellas se basa en *observaciones fenomenológicas* en las soluciones numéricas para el modelo MBM, para las cuales la caída de presión en exceso (*epd*) resulta subestimada en el límite Stokesiano. La corrección de esta inconsistencia se propone mediante la *inclusión de la viscoelasticidad (mediante el Numero de Weissenberg, We) en la dinámica de construcción-destrucción de la estructura* del material. La segunda corrección considera el valor *absoluto de la función de disipación* como el factor que promueve la destrucción de la estructura del fluido. Esto *(i)* corrige las predicciones de *fluidez adimensional negativa* (y por lo tanto *viscosidad negativa*) en flujos complejos: y *(ii)* aumenta significativamente el nivel de viscoelasticidad para el cual las *soluciones numéricas* en flujos complejos son *estables*. Además, esta corrección es *aplicable en general*, y es examinada aquí para la familia de fluidos independientes del tiempo de Phan-Thien-Tanner, ampliamente conocidos.

La aplicación de estas correcciones se ve reflejada en la simulación numérica de *fluidos viscoelastoplásticos*, para los cuales se requieren soluciones estables a altos grados de no-linealidad debido a las *bajas fracciones de solvente* observadas para fluidos con *propiedades plásticas*. Estos fluidos son caracterizados reológicamente con *modelos híbridos* que involucran los modelos micelares estudiados en este trabajo, y el modelo de Papanastasiou (*modelos micelares-Papanastasiou*). En más aplicaciones, se realizó un *estudio experimental-numerico comparativo* de flujos en contracción expansión de *fluidos de Boger*, caracterizados con el *modelo FENE-CR*. Finalmente, se ha desarrollado una *herramienta predictiva* para un *reómetro extensional* aplicado a dos *fluidos biológicos*, que se representan mediante el modelo SXPP. Aquí, se consideran los flujos de *contracción 4:1* para representar *bilis* en los conductos biliares, y de *estiramiento de filamentos* para *fluidos en las vías respiratorias*. Se usaron dos variantes de flujos extensional, *FiSER* para la *estimación de la viscosidad extensional* y *CaBER* para el *tiempo característico*.

Abstract

This thesis is concerned with the *numerical modelling* of *complex fluids* in *complex flows (complex geometries)*. This type of modelling requires the solution of coupled systems of highly *non-linear partial differential equations* that represent the principles of *mass* and *momentum* for *incompressible* fluids in *isothermal* conditions. In addition, the complex nature of the fluids is specified in a *generalised differential constitutive equation* in which several well-known *viscoelastic* and *viscoelastoplastic* fluid representations may be accommodated. Numerically, these complex problems are resolved using *a hybrid finite element/finite volume* discretisation scheme. In this context, a Taylor-Galerkin/pressure-correction finite element method has been adopted for the *parabolic-elliptic momentum-continuity* equations, whilst a finite volume implementation is utilised for the *hyperbolic* subsystem comprising of the *constitutive equation*.

Particular attention has been devoted to the *benchmark 4:1:4 rounded contraction-expansion flow problem* and numerical simulation for the flow or *wormlike micellar systems* under the umbrella of the *Bautista-Manero approach*. Such a *time-dependent* family of complex fluids can display *shear-thinning, strain-softening, thixotropy, shear-banding and yield-stress* features. Then, starting from the modified Bautista-Manero (MBM) model, a number of corrections to this constitutive approach are proposed. The *first correction* is based on phenomenological observation with respect to numerical results using the MBM model, for which excess pressure drop is underestimated at the Stokesian limit. This inconsistency is dealt with by the *inclusion of the viscoelasticity* (via the Weissenberg number) into the *structure destruction-construction dynamics*. The *second correction* considers the *absolute value of dissipation function* as the driving influence for structure destruction. This *(i)* fixes the unphysical predictions on *negative dimensionless fluidity* and hence *viscosity* in complex flow; and *(ii)* significantly increases the elastic-level for which numerical solutions in complex flow are stable. Moreover, this last correction is found to have general applicability, and has been tested on the conventional *time-independent* PTT family of fluids.

Application of such corrections is considered through 4:1:4 contraction-expansion flow of *viscoelastoplastic fluids*, for which stable highly-nonlinear numerical solutions at *low solvent fraction* are required. These fluids are characterised by *a hybrid micellar-Papanastasiou model*. Further application is obtained through an *experimental-to-numerical contraction-expansion* study of *Boger* fluids, characterised by a *FENE-CR model*. Finally, a *predictive toolset* has been developed for an *extensional rheometer* and *two biofluid systems*, represented via the *SXPP model*. Here, *4:1 contraction* flow for *bile* in *biliary ducts* provides insight on flow structure and evolution; whilst, under *filament stretching* flows for *sputum* in the *lung airways* calibration of such a device is permitted (through FiSER-extensional viscosity estimation and CaBER-characteristic time estimation).

CONTENTS

CHAPTER 1

Introduction

Rheology and non-Newtonian fluid mechanics Rheology is the science and study of the deformation and flow of matter. This subject comprised of two main branches: (i) rheometry, and (ii) viscoelastic fluid mechanics. Category (i) deals with constitutive modelling and material function estimation, whilst category (ii) is concerned with the study of material response in complex flows. Controlled flows appear under category (i), in which the kinematics is imposed in an ideal linear framework. Meanwhile, for category (ii) and complex flows, the continuity and momentum equations must be solved together with a constitutive equation for stress, where kinematics are unspecified a priori (Denn 1990). The governing principles and state equations, expressed as non-linear partial differential equations, constitute initial and boundary-value problems. Solution to such problems necessitates robust numerical methods in their resolution (Walters and Webster 2003). The resulting numerical and computational analysis constitutes the science of Computational Rheology (Crochet and Walters 1993). As stated by Keunings (2000), "*the challenge to a computational rheologist is to develop numerical schemes to obtain accurate numerical solutions to governing equations at values of the Weissenberg number of practical interest, using a physically-realistic mathematical model.*" Accordingly, a number of benchmark problems have been established as a basis of comparison in computational rheology. Amongst these, flow of viscoelastic fluids through contractions or contraction-expansions, and flow past objects, are two of the most widely studied benchmark problems (Crochet & Walters 1993; Owens and Phillips 2002; Keunings 1990, 2000, 2001). These problems have been extensively studied over some years (Walters and Webster 2003; Crochet & Walters 1993), and multidisciplinary attempts have been made to answer the many fundamental

physical and scientific questions they provoke (Walter and Tanner 1992; Denn 2005, 2009; Bird 2004). Nevertheless, despite such effort, there are still several issues that lie unanswered, such as: (i) the disparity between experimental enhanced excess pressure drop and the contradictory numerical predictions in contraction-expansion flows for constant shear-viscosity Boger fluids (Walters et al. 2008, 2009), and the complex vortex-dynamics observed in these flows; and (ii) computation of accurate numerical solutions at high Weissenberg number levels, where the non-linearity of the systems prevails (Keunings 2000). Moreover, the advent of new technologies, with engineering and biomedical applications, requires the use of new materials, such as wormlike micellar solutions, polymers and biofluids (Dreiss 2007; Yang 2002; Verdier 2003).

Wormlike micellar solution systems Viscoelastic wormlike micellar solutions are one of the most widely used types of fluid in modern industry, given their complex rheological behaviour. Over the last two decades, these materials have been enthusiastically embraced from several points of view, ranging between - experimental probes for shear banding (Olmsted 2008; Radulescu et al. 1999; Bautista et al. 2000, 2007, 2012), constitutive modeling (Bautista et al. 1999; Manero et al. 2002; Boek et al. 2005; López-Aguilar et al. 2014; de Souza 2009, 2011, 2012; Vazquez et al. 2007) and numerical simulations in complex flow (Tamaddon-Jahromi et al. 2011; López-Aguilar et al. 2014). The presented thesis is principally concerned with the final category: that of numerical simulations in complex flow (chapters 5-7). This versatile family of fluids is constituted by mixtures of surfactants and salts in water; with typical surfactants - cetyltrimethylamonium bromide (CTAB) or cetylpyridinium chloride (CPyCl); and typical salts – sodium salicylate (NaSal) (Yang 2002; López-Aguilar et al. 2014). These components interact physically, depending on the concentration, temperature and pressure, to form elongated micelles that entangle and provoke interactions of viscosity, elasticity, and breakdown and formation of internal structure (López-Aguilar et al. 2014). This complex constitution spurns highly complex rheological phenomena, and manifests features associated with thixotropy (Bautista et al. 1999), pseudo plasticity (Bautista et al. 1999; Manero et al. 2002; Boek et al. 2005; López-Aguilar et al. 2014; de Souza 2009, 2011, 2012; Vazquez et al. 2007), shear banding (Olmsted 2008; Radulescu et al. 1999; Bautista et al. 2000, 2007, 2012) and yields stress (Calderas et al 2013). These features render them as ideal candidates for varied processing and present-day applications. For example, in use as drilling fluids in enhanced oil-reservoir recovery (EOR) (López-Aguilar et al. 2014), and as additives in many everyday products -

paints, house-hold products, cosmetics, health-care products, drag reducing agents (Yang 2002; López-Aguilar et al. 2014).

Micellar constitutive models – Many approaches have been pursued to model wormlike micelle flow behaviour. The original Bautista-Manero-Puig (BMP) model (Bautista et al. 1999; Manero et al. 2002) consisted of the upper-convected Maxwell constitutive equation coupled to a kinetic equation. The Maxwell model described stress evolution, whilst the kinetic equation accounted for flow-induced structural change. Such kinetic considerations were based on the rate of energy dissipation. Subsequently, Boek et al. (2005) corrected the BMP model for its unbounded extensional viscosity response in simple uniaxial extension – thus producing the base-form MBM model employed in the present analysis. This model has been calibrated in complex flow scenarios such as benchmark problems of 4:1 contraction flow (Tamaddon-Jahromi et al. 2011) and 4:1:4 contraction-expansion flow (López-Aguilar et al. 2014). There, it has been proven inconsistent in excess pressure drop (EPD) estimation towards the Stokesian limit. This anomaly has been resolved more recently through a corrected model approach (López-Aguilar et al. 2014), that introduces viscoelasticity into the structure construction/destruction mechanics. Accordingly, two such model variants have arisen, with energy dissipation given by: (i) the polymer contribution exclusively (NM_τ_p model), and (ii) polymer and solvent contributions (NM_T model). These considerations introduce new physics into the representation, by coupling explicitly the thixotropic and elastic nature of these fluids, alongside new key rheological characteristics, such as declining first normal stress difference in simple shear flow (López-Aguilar et al. 2014). For completeness, one may cite other alternative model approaches that have appeared in the literature, though these have largely focused on simple flows and the shear-banding phenomena. The VCM model, based on a discrete version of the 'living polymer theory' of Cates, has been tested on simple flows, where rheological homogeneity prevails (Vazquez et al. 2007), and under conditions of shear-banding. Another approach consists of using the Johnson–Segalman model, modified with a diffusion term for the extra/polymeric stress (so-called d-JS model) (Olmsted et al. 2000). The Giesekus model has also been used in the representation of wormlike micelles under simple shear flow scenarios, whilst using the non-linear anisotropy coupling parameter to introduce shear-banding conditions (Gurnon and Wagner 2012).

CFD modelling The mathematical tools required for the solution of real flow situations of complex fluids are robust computational techniques, based traditionally on finite-difference,

finite-volume and finite-element methods (Walters and Webster 2003). The advent of powerful computers, the need to understand the nature of and to develop technology for such flow situations with complex fluids, has triggered the creation of ever more advanced numerical techniques (Walters and Webster 2003). The present *in-house* CFD predictive modelling capability accommodates transient, mixed extensional-shear flows within complex geometrical settings, as well as highly-elastic, large-extensional deformation. Important computational issues dealt with in such dynamic extensional flows involve the accurate capture of temporal rheological adjustment. This necessitates consistent, accurate and stable treatment of specific (flux/source/time) term combinations in the underlying partial differential equation systems, variable selection and location, and discrete functional space representations. Furthermore, of specific relevance and in general terms, there is provision within this CFD modelling for adaptive highly-accurate, dynamic remeshing, stable and hybrid spatial discretisations (finite element and finite volume). In this study, a semi-implicit time-stepping incremental pressure-correction version of the scheme is employed, that involves a hybrid parent-subcell finite element/finite volume *fe*/*fv*(sc) numerical algorithm (Wapperom and Webster 1998, 1999; Aboubacar et al. 2001, 2002, 2005, Webster et al. 2004, 2005; Aguayo et al. 2006, 2008; Belblidia et al. 2006; Walters et al. 2008, 2009; Sujatha et al. 2008; Belblidia et al. 2007, 2008, 2011; Tamaddon-Jahromi et al. 2008, 2010, 2011; Nyström et al. 2013; Echendu et al. 2013; Al-Muslimawi 2013; López-Aguilar et al. 2014). This *in-house* scheme, is based on Taylor-series temporal expansions and Taylor–Galerkin/pressure-correction fractional-staged methodology, coupled with subcell cell-vertex finite-volume schemes. It has been extensively documented and tested for various viscoelastic flow configurations and is well-suited to the present solution process in-hand. Specifically, on flows through abrupt contraction/expansion (focusing attention on excess pressure drop and vortex activity) and flow past objects. Here, several constitutive equations have been used for incompressible/compressible polymer solutions and melts (Oldroyd-B for constant-viscosity, XPP, PTT for shear-thinning fluids). As such, pressure and flow-controlled, steady-state and transient flows, have been individually analysed and successfully solved.

The contraction–expansion flow problem offered in the current study is now a standard benchmark in experimental and computational rheology (Walters and Webster 2003). Some of the most outstanding features of this problem relate to its vortex dynamics (re-entrant/salient), stress fields, flow kinematics and pressure drop measurement (Aguayo et al. 2008; López-Aguilar et al. 2014). Here, diverse manifestations of the nature of the fluid can

be outlined, relating to vortex-size and evolution (extensional viscosity, N_2-effects), structure formation and numerical tractability (sharp/rounded corners) (Aboubacar et al. 2002). One notes that the pressure drop, which reflects the energy expended in the flow, is often studied through an EPD measure (Binding et al. 2006; Aguayo et al. 2008), which itself offers a significant challenge in accurate resolution through computational prediction (Binding 1991; Binding et al. 2006; Aguayo et al. 2008).

Biofluids systems From the bioengineering point of view and with the development of rheology, much attention has been paid to the relationship between the rheological properties of biofluid systems and their biological function, in the challenge to meet industrial, biological and medical needs (Verdier 2003). This emerging research field, termed biorheology, deals with flow-deformation and rheological properties of substances within living organisms. For example, one may cite flow properties of biofluids: blood, lymph, synovial fluid, sputum, saliva, cervical mucus, cerebrospinal and intra-ocular fluid; and deformation of soft tissues, such as: blood vessels and capillaries, heart, muscles, bladder, eye lens and cartilage; and solution of proteins, nucleic acid and polysaccharides. Today, there is a substantial body of biorheological work related to blood flow and blood vessels (haemorheology) at the macro, micro and nano-scale (Verdier 2003). The present research combines the study of bile rheological properties from both, the experimental and theoretical points of view for confined flows in complex geometries, such as those occurring in flows past objects, and contraction-expansion flows. Bile rheological properties may be associated with common bile duct disorders, conditions under which bile passage and transport is obstructed or prevented, stimulating gallstones or inflammatory narrowing. Moreover, the properties of bile are not only patient dependent, but also pathologically dependent. Also, the effects of the duct geometry (narrowing) flow dynamics and bile rheology on pressure drops (flow resistance) are highly significant. In addition, bile flows can reveal exotic deformation and extensional behaviour at the micro-scale, where shear-thinning, tension-hardening and pressure-drops are all relevant.

Therefore, the main motivation of this research work is the analysis of flow of complex fluids in complex flow situations, taking advantage of the predictive capability of the numerical tools produced in the computational rheology framework. Special attention is paid to the flow of time-dependent thixotropic wormlike micellar fluids through Bautista-Manero models, along with applications on viscoelastoplastic flow. In addition, further practical directions of study cover: an experimental-versus-numerical comparative analysis, performed

on contraction-expansion flow; and the development of numerical predictive tools for the extensional properties of biofluids, on filament-stretching. This thesis is structured in the following manner:

In Chapter 2 – Basic equations & rheology, the outline of the relevant conservation principles and governing equations is provided. Here, these equations are specified for the flow of viscoelastoplastic fluids in isothermal conditions. In addition, a general differential constitutive model is described. This model accommodates the conventional PTT and FENE models, along with the proposals of modifications to the micellar thixotropic Bautista-Manero models. Finally, the pom-pom model is described, which is used in this research to mimic the rheological characteristics of two biofluid systems, i.e. bile in biliary ducts and sputum in the lung-airways.

Material function response is provided in *Chapter 3.* Here, parametric variation is performed to illustrate their effect on shear and extensional viscosity and first normal stress differences data against deformation rate. This permits the acknowledgement of the physics introduced (by the parameters in each model) in ideal theoretical flow context, of simple shear and uniaxial extensional flows; and, more importantly, this provides a reference framework to compare and contrast against numerical solutions from complex flow situations.

Chapter 4 describes the *Numerical Scheme and Discretisation* utilised in this work for the simulation for benchmark problems of 4:1:4 contraction-expansion and filament stretching (FiSER and CaBER). This method is outlined as that based on a hybrid finite element/finite volume algorithm, centred around an incremental pressure-correction time-stepping scheme. In this section, a brief description of and background to the finite element and finite volume methods is given, in application to the Bautista-Manero framework.

The first section of results is given in *Chapter 5,* in which *A new constitutive model for worm-like micellar systems* is proposed through results for the *Numerical simulation of confined contraction-expansion flows* of the MBM model. This correction is based on phenomenological observations of underprediction of the conventional MBM-model for the excess pressure drop (*epd*) estimation in the Stokesian limit. In addition, these time-dependent thixotropic models are contrasted with the more conventional time-independent EPTT model. This produced interesting and contrasting trends in *epd*, vortex-dynamics and stress-fields data as the elasticity levels were risen. Finally, a relationship between the nature

of the steady state f_τ-functional (explicitly related to the structure of the fluid and its viscosity) and the limiting We_{lim} was obtained.

In *Chapter 6 High-Weissenberg predictions for micellar fluids in contraction-expansion flows*, a second correction to the Bautista-Manero family of models is proposed. The constitutive equation correction proposed takes into account the absolute value of the dissipation function in the structure destruction mechanism; $f_\tau \geq 1$ are predicted and, consistently, positive viscosity results are obtained. In addition, the positive nature of the corrected provides larger We_{crit} values, which are increased in one order of magnitude with respect to the natural-signed versions. This correction is found generally applicable, and proved successful under the EPTT framework. New findings surround strong control of flow-centreline deformation rates. Finally, the constitutive equation has been recasted in a conformation-tensor context, for which the positive-definiteness is enhanced, and then, We_{crit} increased with respect to the stress-tensor versions. Using the second eigenvalue of this conformation tensor, the stability of the numerical results is evaluated. Furthermore, a relationship between the eigenvalues and the first normal stress difference N_1 is derived theoretically, which indicate departure from the linear viscoelastic regime predictions.

The large We_{crit} attained in Chapter 6 imply that the levels of non-linearity attainable by the correction proposed are higher. Recently, Calderas et al. (2013) have provided evidence on the yield-stress predictive capability of the Bautista-Manero model in simple shear flow at low solvent fraction levels (meaning highly polymer-concentrated systems). Hence, in *Chapter 7 Numerical modeling of thixotropic and viscoelastoplastic materials in complex flows*, the applications of those results have leaded to the simulation of viscoelastoplastic flow in the 4:1:4 contraction-expansion complex flow setting using a hybrid NM_τ_p_ABS-Papanastasiou model at low solvent fraction levels (which represents an alternative way of increasing the non-linearity of the problem). Plastic characteristics are incorporated in both solvent and polymeric contributions. A Bingham-Papanastasiou model is introduced into the solvent part, whilst the polymer part is described through the micellar thixotropic NM_τ_p_ABS model. Here, results on vortex dynamics, *epd*, stress fields and yields fronts are all analysed.

A further section to this thesis on applications is in *Chapter 8 - Pressure-drop and kinematics of viscoelastic flow through an axisymmetric contraction-expansion geometry with various contraction-ratios.* This constitutes collaborative work between MEng M. Pérez-

Camacho (experimental data, contributes to Pérez-Camacho's DEng thesis) and MEng J. E. López-Aguilar (simulation data, under Prof. M. F. Webster supervision, performed at Institute of Non-Newtonian Fluid Mechanics, Swansea University UK). Both Pérez-Camacho and López-Aguilar are supervised by Dr. O. Manero Brito on UNAM DEng degrees at our Facultad de Química. The research lies in comparison of experimental and numerical data for flow of viscoelastic Boger and pseudoplastic fluids through axisymmetric contraction-expansion flows. Here, the contribution of López-Aguilar lies in the material functional data fitting for the Boger fluids and simulation solutions for the rounded 4:1:4 contraction expansion, using the FENE-CR model. In this work, there is a striking match between experimental and numerical predictions. This demands still further work, with matching between geometrical configuration (sharp corners and varying the contraction ratio), to fully capture the lip-to-corner-vortex transitions.

A predictive extensional viscosity and characteristic time toolset for biofluids is proposed in *Chapter 9 A Computational Extensional-Rheology Study of Two Biofluid Systems*. Here, complex flow through a 4:1 contraction and filament-stretching FiSER (Filament Stretching Extensional Rheometer) and CaBER (Capilary Break-up Extensional Rheometer) are analysed, with a view to describing flow structure in contraction-bile biliary ducts flows, and extracting reliable rheometric data for sputum in the lung airways from filament-stretching. The behaviour of these biofluids is emulated using the SXPP model, which is capable of reproducing shear-thinning strain-hardening response, through branching, entanglements and anisotropy physical characteristics.

Finally, in *Chapter 10*, the *Concluding remarks and future directions* are outlined.

CHAPTER 2

Conservation Principles & Rheology

The basic equations of fluid mechanics are presented that allow the description of fluid motion and conservation of mass. In addition, rheological models relevant to the present study are considered, which relate surrounding forces with the internal response from the material. These models are centred on the Bautista-Manero type models, which describe complex fluid systems capable to exhibit complex non-linear characteristics, such as thixotropy, shear banding and yield stress. Here, a number of corrections to these micellar models are described. These corrections are based on phenomenological and physical factors, such as, *epd* estimation and viscosity representation. Finally, a description of conventional PTT, pom-pom and FENE type models is also provided.

2.1 Background

Rheology is the science of deformation and flow. As such, the subject matter of rheology surrounds the *flow of complex fluids*, observing the change in fluid properties depending on the flow deformation and its time-scale, at fixed temperature. The scope of rheology spans between two classical linear laws of nature for the deformation of matter and flow: *(a)* that given by the Newton's law of viscosity for ideal fluids, and *(b)* that of Hooke's law for the deformation of ideal elastic solids. These two classical extremes are characterised by constant viscosity and modulus, for Newtonian liquids and Hookean solids, respectively. Correspondingly, water is the most representative example of a simple *Newtonian fluid*; and a metal spring stands for a *Hookean solid*

under small deformation. The variety of materials departing from these two extremes is wide: ranging from fluids used in industry (plastics, paints, oil in wells and out of them, surfactant solutions), biomaterials (sputum, blood, saliva, tissues), and foods - to name some examples. These ideal linear extremes provide the span that defines a viscoelastic material: which enjoys characteristics of a viscous liquid (in its dissipative nature); and an elastic solid, which stores energy and 'has memory' of its past state, to which it tends to return. The contributions of these fluid-like and solid-like features are reflected in what is termed a 'characteristic time' of a fluid. In general, the larger the characteristic time, the stronger its viscoelastic features. For example, water is a classified as a Newtonian liquid and has a characteristic time of 10^{-12}s; whilst a polymer melt under processing conditions may display a characteristic time of just a few seconds (Barnes et al. 1989). As such, the distinction between solids and liquids is often faint, yet still, a concise redefinition of the terms *solid* and *liquid* material can be stated. A *solid* can be defined as a *material* that *does not continually deform under a given stress*; whilst, a *liquid* is a *material* that *continually deforms when subjected to a given stress*, irrespective of *how small the stress* may be (Barnes et al. 1989).

Rheology can be studied on alternative levels of scale: either through a *continuum approach* level, or on the *molecular scale* (Barnes et al. 1989). The first, in which this thesis has been developed, is based on the assumption that the material is viewed as a continuous bulk body, often termed 'fluid element'. Within the *continuum approach*, the individual contribution of the molecules are ignored, given the fact that the largest molecular length-scale is still considerably smaller than the smallest characteristic length-scale in such an idealised macroscopic framework. In contrast, the *molecular scale* considers the interactions between molecules in a framework where the characteristic length-scale is comparable to the characteristic length-scale of a molecule. Whichever the framework chosen, such considerations need be incorporated within a constitutive equation that accounts for the relationship between the stress on an element (or molecule) of fluid and the deformation caused. Then, classical conservation principles of mass, energy and linear momentum should be satisfied. In particular, constitutive equations, governing rheological equations of state for stress, are then introduced, which contribute additional forces into the linear momentum conservation equation to account for the flow of a particular class of fluids, in space and time.

2.2 Viscometric flows

These theoretical ideal flows are reference deformation states within which a complex fluid is analysed to qualify and quantify its response characteristics. This procedure trials the physics supporting a particular constitutive equation that is intended to mimic a realistic fluid under such experimental deformation flow states. Viscometric flows are characterised by a controlled flow, in which the kinematics are fixed (determined from the solution of the momentum and mass balance equations), and are then introduced into the constitutive equation to derived closed-form expressions for the fluid material functions (i.e. shear and extensional viscosities, and normal stress coefficients). In addition, these ideal flows and material functions provide a common reference-basis, for comparison and interpretation against approximate numerical solutions. Such numerical solutions (to the full underlying system of equations) can be quite general and apply for both ideal (theoretical) and non-ideal (complex) flow states, as in combined shear and extensional flows. The most common types of viscometric flows are s*imple shear* and *simple extension*.

2.2.1 Simple shear flow

The most straightforward manner in which this ideal flow is often described is that of flow between parallel plates, as illustrated in Fig. 2.1. Here, the material is confined between two extremely-large parallel plates, separated by a gap h, with the upper-plate moving at constant velocity $u(h)=\dot{\gamma}h$, and a constant velocity gradient (shear-rate $\dot{\gamma}$), so that the shear stress is:

$$\sigma=\eta_{Shear}(\dot{\gamma})\dot{\gamma}\,. \tag{2.1}$$

In particular, a Newtonian fluid is characterised by a constant coefficient of proportionality η_{Shear} (known as shear viscosity, which symbolises the *resistance to flow*) and a linear relationship between the shear stress and shear-rate.

The kinematics imposed in this case is $\boldsymbol{u}=(u_1,u_2,u_3)=(\dot{\gamma}x_2,0,0)$. Hence, the rate-of-deformation tensor $\boldsymbol{D}$ under simple shear deformation is as follows:

$$\boldsymbol{D} = \frac{1}{2}\left[\nabla \boldsymbol{u} + \left(\nabla \boldsymbol{u}\right)^{T}\right] = \frac{1}{2}\begin{bmatrix} 0 & \dot{\gamma} & 0 \\ \dot{\gamma} & 0 & 0 \\ 0 & 0 & 0 \end{bmatrix}. \tag{2.2}$$

Here, (u_1, u_2, u_3) represent the vectorial components of fluid velocity in the three spatial reference directions of (x_1, x_2, x_3) In a planar configuration, as in Fig. 1, these spatial directions equate to (x_1, x_2, x_3)=(x, y, z).

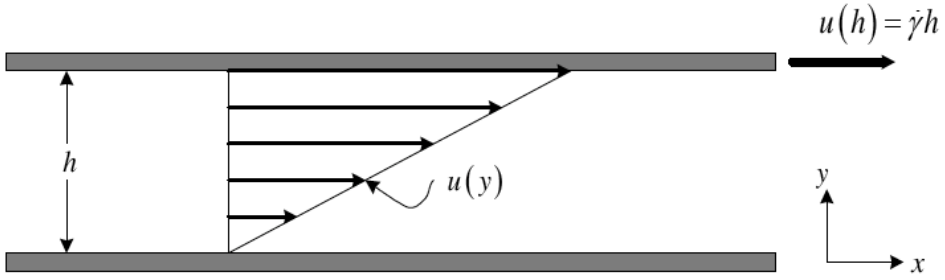

Figure 2.1 Schematic representation of simple shear flow

Normal stress differences The display of normal stress differences in non-Newtonian fluids is one of the key manifestations of their non-linear nature. These normal stresses are responsible for complex and attractive phenomena such as die-swell, rod-climbing (the so-called Weissenberg effect), tubeless syphon, the so-called Kaye effect (Boger and Walters 1993). Usually, the first and second normal stress difference, N_1 and N_2, respectively, are analysed. Their magnitudes are zero for Newtonian fluids, whilst for non-Newtonian fluids, their definitions are:

$$N_1\left(\dot{\gamma}\right) = \sigma_{11} - \sigma_{22} = \psi_1\left(\dot{\gamma}\right)\dot{\gamma}^2, \tag{2.3}$$

$$N_2\left(\dot{\gamma}\right) = \sigma_{22} - \sigma_{33} = \psi_2\left(\dot{\gamma}\right)\dot{\gamma}^2, \tag{2.4}$$

where $\psi_1\left(\dot{\gamma}\right)$ and $\psi_2\left(\dot{\gamma}\right)$, represent the first and second coefficients of normal stresses. Experimentally, it has been observed that (Barnes et al. 1989),

$$N_1 > 0 \qquad \text{and} \qquad N_1 >> \left|N_2\right|. \tag{2.5}$$

2.2.2 Extensional flows

A generalised extensional velocity field may be given as $\boldsymbol{u} = \left(\dot{\varepsilon} x_1, m\dot{\varepsilon} x_2, -(1+m)\dot{\varepsilon} x_3\right)$ (Macosko 1994). From here, the rate-of-deformation $\boldsymbol{D}$ may be written as follows:

$$\boldsymbol{D} = \begin{bmatrix} \dot{\varepsilon} & 0 & 0 \\ 0 & m\dot{\varepsilon} & 0 \\ 0 & 0 & -(m+1)\dot{\varepsilon} \end{bmatrix}, \tag{2.6}$$

where $\dot{\varepsilon}$ represents the constant extension rate in this simple and ideal extensional flow setting. Note that this generalised extensional flow field is designed to fulfill incompressibility ($\boldsymbol{trD = 0}$) $\forall m$. This parameter m may be at m={-1/2,1,0} to represent {uniaxial, biaxial, planar} extension, respectively. Under such states, there is no shear deformation, the fluid volume maintains essentially the same internal angles, but with modified lengths.

Simple uniaxial extension

In particular, for uniaxial extension (m=-1/2), the material is *stretched* in one particular direction *(1:flow direction)*, and due to incompressibility, compression occurs in the other two directions *(2 and 3)*, preserving the volume (incompressibility satisfied).

Then, the velocity field is $\boldsymbol{u} = \left(\dot{\varepsilon} x_1, -\frac{1}{2}\dot{\varepsilon} x_2, -\frac{1}{2}\dot{\varepsilon} x_3\right)$, and rate-of-deformation tensor becomes:

$$\boldsymbol{D} = \begin{bmatrix} \dot{\varepsilon} & 0 & 0 \\ 0 & -\frac{1}{2}\dot{\varepsilon} & 0 \\ 0 & 0 & -\frac{1}{2}\dot{\varepsilon} \end{bmatrix}, \tag{2.7}$$

The extensional viscosity is then expressed as follows,

$$\sigma_{11} - \sigma_{22} = \eta_{Ext}\left(\dot{\varepsilon}\right)\dot{\varepsilon}\,. \tag{2.8}$$

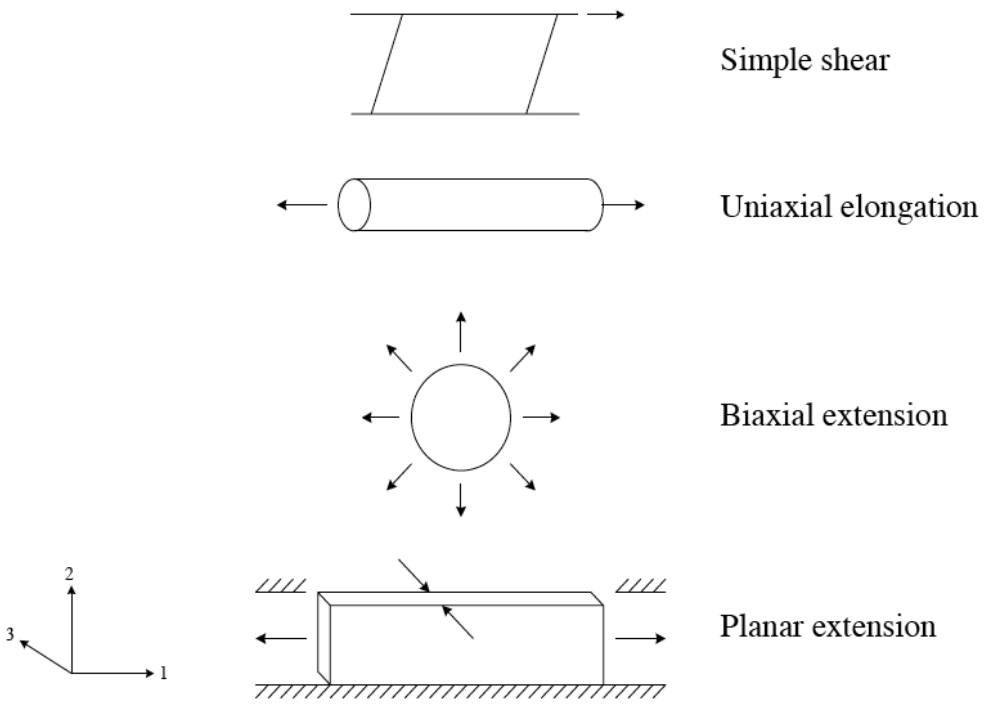

Figure 2.2 Schematic representation of extensional flows

Once more, the Newtonian fluid embodies the reference, for which the extensional viscosity η_{Ext} is constant $\forall\dot{\varepsilon}$. Here, the relationship of $\frac{\eta_{Ext}}{\eta_{Shear}}=3$ is observed, which defines the lower-rate limit for the Trouton ratio (see definition below). This zero-extension-rate limit is universal, including those with viscoelastic properties at low deformation-rates, $\frac{\eta_{Ext}\left(\dot{\varepsilon}\to 0\right)}{\eta_{Shear}\left(\dot{\gamma}\to 0\right)}\to 3$.

The *Trouton ratio* (Tr) is defined as the quotient of extensional and shear viscosities at equivalent deformation rates (Barnes et al. 1989):

$$Tr=\frac{\eta_{Ext}\left(\dot{\varepsilon}\right)}{\eta_{Shear}\left(\dot{\gamma}=\sqrt{3}\dot{\varepsilon}\right)}. \qquad (2.9)$$

Consistently with the Newtonian limit stated above, Tr =3 $\forall$ inelastic liquids. In contrast, for viscoelastic materials, this ratio is anticipated to satisfy $Tr\left(\dot{\varepsilon}\to 0\right)\to 3$. Beyond this range, common response for viscoelastic materials is that of initial early growth to values Tr >3 with $\dot{\varepsilon}$; rising subsequently to a peak in the relatively moderate

rate of deformation range (strain-hardening limit); to ultimately $Tr(\dot{\varepsilon} \to \infty) \to 3$ in the high deformation-rate regime (strain-softening).

Planar extension

This planar variant of simple extension is characterised with m=0, and illustrated in Fig. 2.2. Here, the material is extended in one direction (1), and compressed in another direction (3); whilst there is no deformation in the remaining direction. Consistently, the velocity field is $\boldsymbol{u} = (\dot{\varepsilon} x_1, 0, -\dot{\varepsilon} x_3)$ and the rate-of-deformation tensor becomes:

$$\boldsymbol{D} = \begin{bmatrix} \dot{\varepsilon} & 0 & 0 \\ 0 & 0 & 0 \\ 0 & 0 & -\dot{\varepsilon} \end{bmatrix}, \tag{2.10}$$

and, by analogous calculations, then, for a Newtonian fluid $\frac{\eta_{Ext}}{\eta_{Shear}} = 4$. In contrast, the Trouton ratio for a viscoelastic liquid is defined as $Tr = \frac{\eta_{Ext}(\dot{\varepsilon})}{\eta_{Shear}(\dot{\gamma} = 2\dot{\varepsilon})}$, with limiting value of $Tr(\dot{\varepsilon} \to 0) = \frac{\eta_{Ext}(\dot{\varepsilon} \to 0)}{\eta_{Shear}(\dot{\gamma} \to 0)} \to 4$, at vanishing deformation rates.

Interestingly, in contraction flows, pure extension takes place along the centreline, whilst a pure shear state applies along the wall; a mixture of both applies throughout the general flow-field domain. In particular, under axisymmetric configurations, this centreline elongation is that of *uniaxial extension* (m=-1/2); whilst in 2D planar flows, such deformation is that of *planar extension* (m=-0).

2.3 Conservation principles & Constitutive models

2.3.1 Conservation of mass

The principle of conservation of mass states that the net increase of mass in a volume control is equal to the net mass flow rate that passes through its boundaries. Equivalently, under steady-state conditions, the principle states that the accumulation of mass in any given system is determined by the mass entering minus the mass leaving

the system through its boundaries at any given time (Morrison 2001). This principle is expressed mathematically through the *continuity equation* (Aris 1962; Bird et al. 1960, 1977),

$$\frac{\partial \rho}{\partial t} + \nabla \cdot \left(\rho \boldsymbol{u} \right) = 0 . \tag{2.11}$$

Under transient, incompressible and isothermal flow conditions, the relevant mass conservation and momentum equations for viscoelastic flow, may be expressed in non-dimensional terms (see definitions below; omitting * notation for dimensionless variables) as:

$$\nabla \cdot \boldsymbol{u} = 0 , \tag{2.12}$$

where t represents time; the gradient and divergence operators apply over the spatial domain; field variable $\boldsymbol{u}$ represents fluid velocity.

The ***dimensionless variables*** utilised are defined as follows (see below for scales):

$$\boldsymbol{u}^* = \frac{\boldsymbol{u}}{U} \qquad t^* = \frac{U}{L} t \qquad \boldsymbol{\tau}_p^{\,*} = \frac{\boldsymbol{\tau}_p}{\left(\eta_{p0} + \eta_s \right) \frac{U}{L}} \qquad p^* = \frac{p}{\left(\eta_{p0} + \eta_s \right) \frac{U}{L}} \qquad \boldsymbol{D}^* = \frac{L}{U} \boldsymbol{D}$$

2.3.2 Conservation of linear momentum

The principle of conservation of linear momentum states that the rates of increase of momentum in a control volume are due to (i) the net flow of momentum into the system by convection (momentum of the stream of material entering and leaving from the volume control crossing its boundary); (ii) the diffusion of momentum due to internal forces in the material; and (iii) and the external body forces acting in the distance (such as gravity and electromagnetic forces, which are considered negligible in this work). This principle is Newton's second law of motion rephrased, which states that the change of linear momentum in a system is equal to the sum of the forces acting upon it. In dimensionless form, this principle can be written (Aris 1962; Bird et al. 1960, 1977; Morrison 2001):

$$Re \frac{\partial \boldsymbol{u}}{\partial t} = \nabla \cdot \boldsymbol{T} - Re \boldsymbol{u} \cdot \nabla \boldsymbol{u} - \nabla p \tag{2.13}$$

where field variables $\boldsymbol{u}$, p and $\boldsymbol{T}$ represent fluid velocity, hydrodynamic pressure and stress contributions, respectively; then, stress may be further split into *solvent (viscous-inelastic)* and *polymeric (viscoelastic)* contributions $\boldsymbol{T} = 2\eta_s \boldsymbol{D} + \boldsymbol{\tau}_p$. Body forces are neglected in the present analysis, since contributions from gravity are less significant than those from other forces (i.e. pressure and stress).

The non-dimensional group of the Reynolds number may be defined as $Re = \rho UL / \left(\eta_{p0} + \eta_s\right)$, with characteristic scales of U on fluid velocity (based on mean flow rate) and L on spatial dimension (based on minimum contraction dimension). Material density is ρ and reference viscosity is taken as the zero shear-rate viscosity, so that $\frac{\eta_{p0}}{\eta_{p0}+\eta_s} + \frac{\eta_s}{\eta_{p0}+\eta_s} = 1.0$. Here, η_{p0} is the zero rate polymeric viscosity and η_s is the solvent (zero shear-rate) viscosity, from which the solvent fraction can be defined as $\beta = \eta_s / \left(\eta_{p0} + \eta_s\right)$.

2.3.3 Constitutive equations

In general and for fluids of complex rheological behaviour, additional information is required to specify the state of stress and to complete the statement of the flow problem. This lies in the form of constitutive laws or state equations for stress, which relate the internal state of stress and the rate of deformation that a fluid experiences under flow. As such, the specification of the form of the extra-stress tensor $\boldsymbol{\tau}_p$ completes the minimum set of equations to describe the flow of a viscoelastic material. The description of the models used in this work starts with the basic principles constitutive equations must satisfy to represent general fluid flow behaviour. Subsequently, as a base reference, the Newtonian fluid (simplest viscous model) is described, followed by more complex constitutive models that account for viscoelastic and viscoelastoplastic behaviour.

Basic principles of continuum mechanics

Within a continuum mechanics framework and from a mathematical perspective, constitutive equations must satisfy the following basic criteria to adequately represent fluid response (Barnes et al. 1989; Astarita and Marucci 1974).

(i) Frame invariance The form of constitutive equations must be independent of the frame of reference used to describe the motion of the fluid it represents.

(ii) Invariance under superposed rigid body motion The constitutive equations must reflect independence of absolute motion in space; implying, any rigid body motion imposed on the whole fluid must not affect the response of the material.

(iii) Determination of stress and local action: The behaviour of a material element depends only on the previous history of that same material element and not on the state of neighbouring elements. Hence, the concept of 'fluid memory' must be associated with material elements and not with points in space.

Newtonian Fluids

The linear Newtonian-fluid constitutive equation is the traditional reference for comparison between inelastic and non-Newtonian fluids, given that non-Newtonian fluids at vanishingly small deformation rates tend to behave as Newtonian fluids. Newtonian fluids present a constant viscosity under isothermal and isobaric, shear and elongational flows. Moreover, they display an instantaneous response to deformation (interpreted through an extremely low characteristic time). The expression representing the relationship between stress and rate of deformation is linear for incompressible Newtonian fluids, i.e.:

$$\boldsymbol{T} = 2\mu \boldsymbol{D}, \tag{2.14}$$

where μ represents the constant viscosity characteristic of Newtonian fluids. Then, substitution of equation (2.14) into (2.13) produces the well-known Navier-Stokes equations.

Maxwell and Oldroyd-B models

The first differential viscoelastic model designed to describe viscoelastic fluid flow behaviour was introduced by Maxwell (Maxwell 1867). Based on total stress, the expression for this model is as follows,

$$\boldsymbol{T} + \frac{\eta_0}{G_0}\frac{\partial \boldsymbol{T}}{\partial t} = 2\eta_0 \boldsymbol{D}, \tag{2.21}$$

where G_0 and η_0 are the elastic modulus and the viscosity of the viscoelastic fluid, respectively. Then, the relaxation time for a Maxwell fluid is defined by $\lambda = \frac{\eta_0}{G_0}$. This is the first model to account for 'memory effects' (viscoelasticity) in non-Newtonian fluids. Nevertheless, eq.(2.21) does not fulfil the second principle of continuum mechanics, that of *invariance under superposed rigid body motion*.

Oldroyd (1950) proposed a correction to the Maxwell model, replacing the Eulerian time derivative with its convected alternative. Oldroyd introduced the upper- ($\overset{\triangledown}{\boldsymbol{\Omega}}$) and lower- ($\overset{\triangle}{\boldsymbol{\Omega}}$) convected derivatives of any tensor $\boldsymbol{\Omega}$, to fulfill the *basic principles of fluid mechanics* stated above. These convected derivatives are defined as follows:

$$\overset{\triangledown}{\boldsymbol{\Omega}} = \frac{\partial \boldsymbol{\Omega}}{\partial t} + \boldsymbol{u}\cdot\nabla\boldsymbol{\Omega} - \left(\nabla\boldsymbol{u}\right)^T\cdot\boldsymbol{\Omega} - \boldsymbol{\Omega}\cdot\nabla\boldsymbol{u} \tag{2.22}$$

$$\overset{\triangle}{\boldsymbol{\Omega}} = \frac{\partial \boldsymbol{\Omega}}{\partial t} + \boldsymbol{u}\cdot\nabla\boldsymbol{\Omega} + \left(\nabla\boldsymbol{u}\right)^T\cdot\boldsymbol{\Omega} + \boldsymbol{\Omega}\cdot\nabla\boldsymbol{u} \tag{2.23}$$

From eqs.(2.22)-(2.23), eq.(2.21) the upper-convected (UCM) and the lower-convected Maxwell (LCM) models are generated, respectively, as,

$$\boldsymbol{T} + \lambda\overset{\triangledown}{\boldsymbol{T}} = 2\eta_0\boldsymbol{D}\,, \tag{2.24}$$

$$\boldsymbol{T} + \lambda\overset{\triangle}{\boldsymbol{T}} = 2\eta_0\boldsymbol{D}\,. \tag{2.25}$$

Upon further consideration, and amongst more detailed model variants, Oldroyd (1950) proposed the inclusion of a solvent contribution in eq.(2.24). This introduced a retardation time, λ_J, as:

$$\boldsymbol{T} + \lambda\overset{\triangledown}{\boldsymbol{T}} = 2\eta_0\left(\boldsymbol{D} + \lambda_J\overset{\triangledown}{\boldsymbol{D}}\right). \tag{2.26}$$

Equation (2.26) is known as the Oldroyd-B model. Here, $\lambda_J = \frac{\mu_s}{\mu_s + \mu_p}\lambda$ is identified as a retardation time related to the presence of the solvent in the mixture. It is noteworthy that practical discretisation difficulties arise under numerical approximation when

dealing with the term $\overset{\nabla}{\boldsymbol{D}}$, and its counterpart higher order (second-order) spatial derivatives on velocity that themselves demand resolution. Nevertheless, this issue can be managed, with some additional steps in variable redefinition (see below).

Elastic-viscous stress splitting EVSS Considering variable redefinition, the Oldroyd-B model may be split into two different equations, one for the *polymeric contribution* and other for the that of *solvent*, to generate a general statement of the differential constitutive model that may be expressed in dimensionless form as (Barnes et al. 1989):

$$\boldsymbol{T} = 2(1-\beta)\boldsymbol{D} + \boldsymbol{\tau}_p \tag{2.27}$$

$$We\frac{\partial \boldsymbol{\tau}_p}{\partial t} = 2(1-\beta)\boldsymbol{D} - f_\tau \boldsymbol{\tau}_p - We\left(\boldsymbol{u}\cdot\nabla\boldsymbol{\tau}_p - \nabla\boldsymbol{u}^T\cdot\boldsymbol{\tau}_p - \boldsymbol{\tau}_p\cdot\nabla\boldsymbol{u}\right) \tag{2.28}$$

in which a second dimensionless group number is introduced governing elasticity, via a Weissenberg number ($We = \lambda_1 \frac{U}{L}$), which is a function of the characteristic material relaxation time, $\lambda_1 = \frac{\eta_{p0}}{G_0}$, and the characteristic velocity and length scales. By specifying the functional f_τ, the network nature and theoretical structure properties of any particular fluid may be imposed within this general framework. The Oldroyd-B model is the simplest such instance, and is represented by a fluid with $f_\tau = 1$.

In subsequent sections, the nature of the f_τ*-functional* is specified for a variety of models, covering the wormlike micelles-thixotropic Bautista-Manero models and the conventional approaches given by the PTT and pom-pom representations. Moreover, counterpart detail on FENE-CR, and viscoelastic and viscoelastoplastic hybrid models is also provided.

2.3.4 Bautista-Manero models

The original Bautista-Manero (BMP) and Modified Bautista-Manero (MBM) models

To represent the field of wormlike micellar systems and in the first instance, the modified Bautista-Manero (MBM) model (Boek et al. 2005) is adopted. This approach is based on the Bautista-Manero-Puig (Bautista et al. 1999; Manero et al. 2002), in which a non-linear differential structure equation for the fluidity ($\phi_p = \eta_p^{-1}$), dictates the

construction/destruction dynamics of the structure of the fluid; this also provides the polymeric viscosity η_p. Typically, this may begin from a fully structured state to be converted to a completely unstructured form, using the energy dissipated by the polymer under flow. This MBM model may be presented in stress-split form, in which the solvent contribution is of Newtonian-type and the polymeric contribution is given by the following expression:

$$\boldsymbol{\tau}_p + \frac{\eta_p}{G_0}\overset{\nabla}{\boldsymbol{\tau}}_p = 2\eta_p \boldsymbol{D}. \tag{2.29}$$

The structure equation is then:

$$\frac{\partial \eta_p^{-1}}{\partial t} = \frac{1}{\lambda_s}\left(\frac{1}{\eta_{p0}} - \frac{1}{\eta_p}\right) + \left(\frac{k}{\eta_\infty}\right)\boldsymbol{\tau}_p : \boldsymbol{D} \tag{2.30}$$

Defining $f_\tau = \left(\eta_{p0}/\eta_p\right)$ using the zero-rate viscosity η_{p0} as a scaling factor, Eq. (2.30) can be recast into that to determine f_τ, as follows:

$$\frac{\partial f_\tau}{\partial t} = \frac{1}{\lambda_s}\left(1 - f_\tau\right) + \left(\frac{k}{\eta_\infty}\right)\eta_{p0}\boldsymbol{\tau}_p : \boldsymbol{D}. \tag{2.31}$$

Applying non-dimensionalisation (again, omitting * for dimensionless variables), as above:

$$\frac{\partial f_\tau}{\partial t} = \frac{1}{\omega}\left(1 - f_\tau\right) + \xi_{\eta_{p0}}\boldsymbol{\tau}_p : \boldsymbol{D}. \tag{2.32}$$

The dimensionless parameters of this micellar model, which account for structural construction ($\omega = \lambda_s U/L$) and destruction ($\xi_{\eta_{p0}} = \left(k/\eta_\infty\right)\eta_{p0}\left(\eta_{p0} + \eta_s\right)U/L$), appear in the corresponding terms for these network mechanisms.

NM_τ_p and NM_T models - Inclusion of viscoelasticity into the structure construction-destruction mechanism (a correction to MBM)

In this work, a *key* modification has been proposed to Eq. (2.32) driven by phenomenological observation, which results in the *novel inclusion of viscoelasticity* within the destruction mechanics of the fluid structure, via $\eta_{p0} = G_0\lambda_1$. In the first

instance, the destruction term is further developed to accommodate only that energy involved in destroying the fluid structure from the polymeric dissipation (NM_τ_p model):

$$\frac{\partial f_\tau}{\partial t} = \frac{1}{\omega}\left(1 - f_\tau\right) + \xi_{G_0} We \boldsymbol{\tau}_p : \boldsymbol{D} \tag{2.33}$$

where $\xi_{G_0} = \left(k / \eta_\infty\right) G_0 \left(\eta_{p0} + \eta_s\right)$ is the new and replaced destruction dimensionless parameter[‡].

A second factor to consider is that there are energy contributions from both polymeric and solvent dissipation terms to the destruction of the fluid structure (NM_T model):

$$\frac{\partial f}{\partial t} = \frac{1}{\omega}\left(1 - f\right) + \xi_{G_0} We \boldsymbol{T} : \boldsymbol{D} . \tag{2.34}$$

When the dynamic differential eqs.(2.33)-(2.34) for structure evolution are recast into their steady-state form, then the equivalent algebraic form is recovered,

$$f_\tau = 1 + \omega \xi_{G_0} We \boldsymbol{\zeta} : \boldsymbol{D} . \tag{2.35}$$

Here, the two versions of eq.(2.35) arise to break the structure of the fluid, dependent on the choice of $\boldsymbol{\zeta}$-variable: one, considering the energy dissipated by the polymer constituent alone ($\boldsymbol{\zeta}=\boldsymbol{\tau}_p$, NM_$\tau_p$ model); and the other, involving both the polymer plus the solvent contributions ($\boldsymbol{\zeta}=\boldsymbol{T}$, NM_T model).

A correction for realistic material function estimation – NM_ τ_p_ABS model

Importantly, the dissipation function in eq.(2.30)-(2.36) is the driving influence in previous models for departure from Oldroyd behaviour (f_τ=1), which is modulated by the product of the construction and destruction parameters (thixotropy) (and with the Weissenberg number, where applicable). Here, this expression for the f_τ-functional links directly with the viscosity, which is a positive physical quantity that should remain finite and above unity in scaled form

[‡] The corresponding theory may be developed for constructive contributions also, to be addressed subsequently.

($\boldsymbol{\zeta} : \boldsymbol{D} \geq \boldsymbol{0}$),[1] during flow evolution (time) and throughout the spatial domain (in shear, extensional and mixed flow deformation). As such, negative values (and less than unity) of this f_τ-functional are inadmissible. As evidenced in our previous work (López-Aguilar et al. 2014), there are instances in complex 4:1:4 contraction/expansion flow, near numerical *We*-solution breakdown, in which the dissipation function becomes negative, thus predicting negative values of the f_τ-functional and unphysical thixotropic viscosities. To avoid this possibility arising, and consistent with the underlying ideal shear and extensional flow derivation theory, the following ABS-correction is proposed:

$$\frac{\partial f_\tau}{\partial t} = \frac{1}{\omega}\left(1 - f_\tau\right) + \xi_{G_0} We \left|\boldsymbol{\zeta} : \boldsymbol{D}\right|. \tag{2.36}$$

In eq.(2.36), the absolute value sign is applied to each component of the scalar dissipation function[2]. This ABS-correction becomes redundant in simple shear and extensional flows, since the domain of the variables in such viscometric flows is positive. As such, this correction provides correct physical and thermodynamical interpretation to this family of micellar models, in their departure from ideal flow.

2.3.5 Phan-Thien/Tanner models

This Phan-Thien/Tanner (PTT) model considers the creation and destruction of network junctions, as in a rubber network representation. Shear-thinning and extension-hardening/softening are predicted by this class of models, alongside finite extensibility (hence useful practically to represent polymer melt and solution response). The upper convected form of this model is expressed as:

$$f_\tau \boldsymbol{\tau}_p + \lambda \overset{\nabla}{\boldsymbol{\tau}}_p = 2\eta_{p0}\mathbf{D} \tag{2.37}$$

the additional network-structure function f_τ is,

$$f_\tau = \begin{cases} \mathrm{e}^{\left(\varepsilon \frac{\lambda_1}{\eta_{p0}} tr\left(\boldsymbol{\tau}_p\right)\right)} & \textit{exponential,} \\ 1 + \varepsilon \dfrac{\lambda_1}{\eta_{p0}} tr\left(\boldsymbol{\tau}_p\right) & \textit{linear.} \end{cases} \tag{2.38}$$

[1] Note, observations on trace($\boldsymbol{\tau}_p$)>0 of Hulsen (1990), to maintain positive stored elastic energy with viscoelastic PTT models.
[2] Alternatively, apply the absolute operation to the total dissipative sum

The model may be modified to incorporate combination of both upper and lower convected derivatives (Johnson-Segalman form). The linear form is extracted from truncation of a Taylor series expansion of the exponential form. Both forms predict shear-thinning behaviour and extension-hardening; strain-softening is anticipated for the exponential form; whilst the linear form displays sustained strain-hardening (limiting plateau behaviour); although, for some extreme values ($\varepsilon \to 1$) moderate softening is also observed with the linear variant.

2.3.6 PTT-ABS models

The same reasoning as with thixotropic models can be applied to PTT models, and the analysis returns towards classical Oldroyd-B behaviour in the limit of vanishing $tr\boldsymbol{\tau}_p$.[3] Consistently with the above f_τ-functional modifications expressed for thixotropic micellar models, the corresponding modification to PTT models becomes:

$$f_\tau = 1 + \frac{\varepsilon}{1-\beta} Wetr\left|\boldsymbol{\tau}_p\right| \text{ for LPTT,} \qquad \text{and} \qquad f_\tau = exp\left(\frac{\varepsilon}{1-\beta} Wetr\left|\boldsymbol{\tau}_p\right|\right) \text{ for EPTT.} \quad (2.39)$$

Note, in eq.(2.39), it is implied that the absolute value sign applies to every constituent component of the scalar $tr\boldsymbol{\tau}_p$. With non- thixotropic PTT models, the trace of the extra-stress is the function responsible for departure from Oldroyd-B form, as opposed to energy dissipation, $\boldsymbol{\zeta} : \boldsymbol{D}$, under the alternative thixotropic approximations.

2.3.7 Change of variable (translations $\boldsymbol{\tau}_p$ - $\boldsymbol{\Pi}$)

Following the developments on positive definiteness and loss of evolution by Dupret and Marchal (1986) and Hulsen (1988), a *dimensional* tensor $\boldsymbol{\Pi}=\boldsymbol{\tau}_p+(\eta_{p0}/\lambda_1)\boldsymbol{I}$ is adopted in this study, which is a translation identity between $\boldsymbol{\Pi}$ and $\boldsymbol{\tau}_p$ tensors. As such, the eigenvalues of the $\boldsymbol{\Pi}$ tensor may be taken as a form of guidance as to solution quality and, indeed, as an indicator towards violation in attaining converged steady-state numerical solutions at increasing *We*-increments (numerical divergence/breakdown). According to the non-dimensional variables above, the *dimensionless* form of this tensor is $\boldsymbol{\Pi}^*=[We/(1-\beta)]\boldsymbol{\tau}_p^*+\boldsymbol{I}$.

Application of the $\boldsymbol{\Pi}$–tensor definition leads to the following *dimensionless*

[3] Provided the model parameter set $\{\varepsilon, \beta, We\}>0$, as is necessary by definition

constitutive equation statement (eq.2.28):

$$We\overset{\nabla}{\boldsymbol{\Pi}} = -f_{\Pi}\left(\boldsymbol{\Pi}-\boldsymbol{I}\right). \tag{2.40}$$

For the time-dependent thixotropic micellar models, the functional f_{Π} is governed by the differential expression, where $\boldsymbol{\zeta}_{\Pi}$ represents the conformation-tensor form of $\boldsymbol{\zeta}$:

$$\frac{\partial f_{\Pi}}{\partial t} = \frac{1}{\omega}\left(1-f_{\Pi}\right)+\xi_{G_0}\left(1-\beta\right)\left|\boldsymbol{\zeta}_{\Pi} : \boldsymbol{D}\right|. \tag{2.41}$$

This reduces under steady-state conditions to the following expression:

$$f_{\Pi} = 1+\omega\xi_{G_0}\left(1-\beta\right)\left|\boldsymbol{\zeta}_{\Pi} : \boldsymbol{D}\right|. \tag{2.42}$$

For this family of fluids, it is noteworthy that the *We*-scaling on the non-dimensionalised dissipation function is omitted in the τ_p-to-Π translation.

Then, the corresponding f_{Π}-functional for the time-independent network-based PTT models (Hulsen 1990) are given by:

$$f_{\Pi} = 1+\varepsilon tr\left|\boldsymbol{\Pi}-3\right| \text{ for LPTT,} \qquad \text{and} \qquad f_{\Pi} = exp\left(\varepsilon tr\left|\boldsymbol{\Pi}-3\right|\right) \text{ for EPTT.} \tag{2.43}$$

One notes that eqs.(2.41)-(2.43) already include the ABS-correction, yet this assumption may be relaxed to consider natural-signed options.

2.3.8 Convoluted viscoelastic models

A hybrid modelling approach may also be pursued, by convoluting *f*-functionals of the EPTT and micellar models. Herein, a stronger, steady state *f-We* explicit relation is designed to attain highly elastic solutions for micellar fluids. For the steady-state case of the convolution of MBM and EPTT *f*-functionals (EPTT/MBM model):

$$f_{\tau} = \left(1+\omega\xi_{\eta_{p0}}\boldsymbol{\tau}_p : \boldsymbol{D}\right)exp\left(\frac{\varepsilon}{1-\beta}Wetr\boldsymbol{\tau}_p\right). \tag{2.44}$$

Now for the EPTT/NM_τ_p model,

$$f_{\tau} = \left(1+\omega\xi_{G_0}We\boldsymbol{\tau}_p : \boldsymbol{D}\right)exp\left(\frac{\varepsilon}{1-\beta}Wetr\boldsymbol{\tau}_p\right). \tag{2.45}$$

And finally for the EPTT/NM_T:

$$f_{\tau} = \left(1+\omega\xi_{G_0} We\boldsymbol{T} : \boldsymbol{D}\right) exp\left(\frac{\varepsilon}{1-\beta} Wetr\boldsymbol{\tau}_p\right). \quad (2.46)$$

2.3.9 Hybrid/convoluted viscoelastoplastic models

In this study, non-Newtonian viscoplastic properties are introduced via a regularization approach adopting the Bingham-Papanastasiou model (Papanastasiou 1989). The viscoelastoplastic contribution is given by the NM_τ_p_ABS model describe in previous sections. Hence, yield stress contributions are recognised as entering through the solvent viscosity functionality alone. Note, there are other alternative formulation choices to embrace plastic behaviour via Papanastasiou regularisation (Papanastasiou 1989), namely: *(a)* within polymeric viscosity functionality alone; and *(b)* via both solvent and polymeric viscosity contributions. Studies illustrating the consequences of applying these various options have already been conducted and reported upon elsewhere, with polymeric representations under Oldroyd-B (Belblidia et al. 2011) and EPTT (Al-Muslimawi et al. 2013) models.

The general differential statement of the ***viscoelastic model in eq.(2.27)-(2.28) is supplemented in the solvent contribution with the Bingham-Papanastasiou model***:

$$\boldsymbol{\tau}_s = 2\beta\varphi\left(II_D; m_p, \tau_0\right)\boldsymbol{D} \quad (2.47)$$

The Papanastasiou regularisation specifies an exponential functional-form in its solvent viscosity contribution, based on the second invariant, $II_D = \frac{1}{2} tr\boldsymbol{D}^2$, of the rate of deformation tensor, viz:

$$\varphi\left(II_D; m_p, \tau_0\right) = \eta_0 + \frac{\tau_0\left(1-e^{-m_p|II_D|^{1/2}}\right)}{2|II_D|^{1/2}}. \quad (2.48)$$

Here, parameters of $\{\tau_0, m_p\}$ represent: τ_0 the base cut-off yield stress factor, and m_p the regularisation stress growth exponent (with scale of time). The τ_0-parameter expresses the stress level below which plastic behaviour is observed and is equivalent to a Bingham Number, $Bn = \tau_0 = \tau_y L_{char}/\eta_0 U_{char}$.

2.3.10 FENE-CR model

The FENE-CR model was introduced by Chilcott and Rallison (1988). This model is appealed to under comparison against Boger fluids in the experimental versus numerical comparison chapter, considering vortex dynamics and pressure drop estimation for contraction-expansion flow. The attractive rheological properties sought under this comparison are those of its constant shear-viscosity and strain-hardening, reflecting those of Boger fluids. The model reads:

$$f_A \boldsymbol{A} + We \overset{\nabla}{\boldsymbol{A}} - f_A \boldsymbol{I} = 0, \tag{2.49}$$

where **A** is the conformation tensor, derived from Kramer's rule:

$$\boldsymbol{\tau}_p = \frac{1-\beta}{We} f_A (\boldsymbol{A} - \boldsymbol{I}), \tag{2.50}$$

and where the Warner spring-expression is:

$$f_A = \frac{1}{1 - \frac{tr\boldsymbol{A}}{L^2}}, \tag{2.51}$$

2.3.11 The Single-eXtended pom-pom (SXPP) model

In addition and by way of contrast, the kinetic-theory molecular-based pom-pom model is also considered when representing biofluid properties under some specific applications. This model may be represented in general form as:

$$De \frac{\partial \boldsymbol{\tau}}{\partial t} = -De\boldsymbol{u} \cdot \nabla \boldsymbol{\tau} - f_1 \boldsymbol{\tau} + 2(1-\beta)\boldsymbol{d} + De(\boldsymbol{\tau} \cdot \boldsymbol{L} + \boldsymbol{L}^{\dagger} \cdot \boldsymbol{\tau}) - De\,\xi(\boldsymbol{\tau} \cdot \boldsymbol{d} + \boldsymbol{d} \cdot \boldsymbol{\tau}) - \frac{\alpha De}{1-\beta} \boldsymbol{\tau} \cdot \boldsymbol{\tau} + \frac{1-\beta}{De}(f_2 - 1)\boldsymbol{I} \tag{2.52}$$

Here, for the Single Extended pom-pom (SXPP) model, one identifies the functionals (f_1, f_2) and four additional parameters (q, ε_{pom}, λ_{pom}, α_{pom}). These additional structure parameters govern the number of side-branch arms to the molecular-backbone chain-segment (q), system entanglement (ε_{pom}), the stretch of the back-bone segment (λ_{pom}), and the degree of system anisotropy (α_{pom}). Corresponding forms extracted from the physics for these functionals (f_1, f_2), in terms of the base network-description parameters (q, ε_{pom}, λ_{pom}, α_{pom}) and (β, De, $\boldsymbol{\tau}$) may be given by:

$$f_1 = f_2 = f(\lambda,\boldsymbol{\tau}) = \frac{2}{\varepsilon_{pom}}\left(1-\frac{1}{\lambda_{pom}}\right)\mathrm{e}^{\nu\left(\lambda_{pom}-1\right)} + \frac{1}{\lambda_{pom}^{2}}\left(1-\left\{\frac{D\,\mathrm{e}}{(1-\beta)}\right\}^{2}\frac{\alpha_{pom}}{3}\mathrm{tr}\left(\boldsymbol{\tau}\cdot\boldsymbol{\tau}\right)\right). \tag{2.53}$$

Here, the free parameter ν is estimated by data-fitting and found to be inversely proportional to the number of side-branch arms dangling from an end of a molecular chain-segment (ν = c/q, with c taken as 2), see Blackwell et al. (2000). The parameter ε_{pom} is the ratio of the backbone-stretch (λ_{0s}= λ) to the orientation (λ_{0b}) relaxation times (larger values indicate more highly-mobile system states, less degree of entanglement). Conveniently and with the single-equation (SXPP) approximation to the pom-pom model, representation of the back-bone stretch parameter λ_{pom}, collapses from its generalised differential evolutionary form to an instantaneous algebraic response, given through expression:

$$\lambda_{pom} = \sqrt{1+\frac{1}{3}\frac{D\,\mathrm{e}}{(1-\beta)}\left|\mathrm{tr}\left(\boldsymbol{\tau}\right)\right|},\ \varepsilon_{pom} = \frac{\lambda_{0s}}{\lambda_{0b}}. \tag{2.54}$$

This completes the statement of all models utilised within the present body of research.

CHAPTER 3

Material function response

3.1 Bautista-Manero and EPTT models

Material functions for the EPPT, MBM, NM_τ_p and NM_T models, along with the Oldroyd-B (f=1) reference, are plotted in Fig. 3.1. Solvent fraction variants considered in this work are β={1/9, 0.9} for highly-polymeric and solvent-dominated fluids, respectively (see Table 2.1 for details in parameter values). The EPTT model parameters are chosen to take values at benchmark settings of ε={0.25, 0.02}, characterising polymer melts and solutions [41], which are identified as applicable for moderate (MH, ε=0.25) and strong hardening (SH, ε=0.02) scenarios, respectively. The resulting micellar extensional viscosities are matched with those of corresponding EPTT forms at each {ε,β} combination. The micellar combinations adopt the structure-construction parameter values of ω=4.0 for MH, and ω=0.28 for SH fluids. The structure-destruction parameter assumes different values for each micellar model depending on the solvent fraction, hardening characteristics and their matching to EPTT. The corresponding sets of parameters are listed in Table 1 for β={1/9, 0.9}. Here, the distinction between parametric specification of NM_τ_p and NM_T models arises due to inclusion of the solvent contribution within the energy dissipation term, which introduces the further influence of the β-factor.

The material functions generated by the convoluted EPTT/MBM, EPTT/NM_τ_p and EPTT/NM_T models are plotted in Fig. 3.2 for β=1/9 and MH response (Table 3.1).

Here, in Fig. 3.2a, the extensional and shear viscosity curves lie closer to those for EPTT. After the peak in extensional viscosity, at *We*~0.7, the convoluted data provide larger extensional viscosity values than under MBM prediction, for which introduction of strain-softening is more abrupt. The EPTT/NM_T curve shows a steeper slope in the 20<*We*<400 range; yet, there is little difference observed outside this range with respect to the other convoluted cases. The MBM shear viscosity curve provides smaller values than the other curves for *We*>3 onwards. On N_1 in shear (Fig. 3.2b), the convoluted data follow the nature of their non-convoluted pairs: the EPTT/MBM and EPTT/NM_τ_p curves inherit the MBM-plateau, with larger magnitude. The EPTT/NM_T curve peaks at *We*~40 and declines thereafter with increasing *We*, as under NM_T prediction, which peaks at *We*~5 (Fig. 3.1).

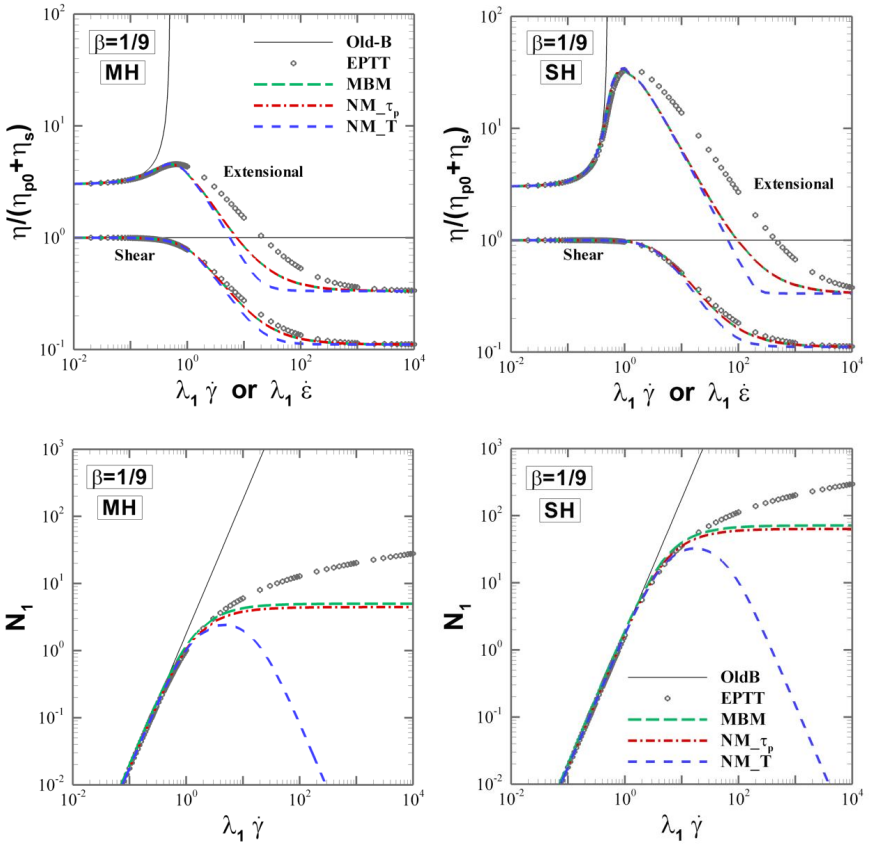

Figure 3.1 Material functions versus *We*: top-shear and extensional viscosity, bottom-shear N_1; EPTT, MBM, NM_τ_p and NM_T models; *left*-MH (EPTT ε=0.25; Micellar ω=4.0), *right*-SH (EPTT ε=0.02; Micellar ω=0.28) response; highly-polymeric (β=1/9) fluids

Table 3.1 Parameter sets; micellar and EPTT; highly-polymeric (β=1/9), solvent-dominated fluids (β=0.9)

	β=1/9		β=0.9	
Model - *f*-functional	MH	SH	MH	SH
EPTT $f = exp\left(\frac{\varepsilon}{1-\beta} Wetr\boldsymbol{\tau}_p\right)$	ε=0.25	ε=0.02	ε=0.25	ε=0.02
MBM $f = 1+\omega\xi_{\eta_{p0}}\boldsymbol{\tau}_p : \boldsymbol{D}$	ω=4.0 $\xi_{\eta p0}$=0. 1125	ω=0.28 $\xi_{\eta p0}$=0. 1125	ω=4.0 $\xi_{\eta p0}$=1.0	ω=0.28 $\xi_{\eta p0}$=1.0
NM_τ_p $f = 1+\omega\xi_{G_0} We\boldsymbol{\tau}_p : \boldsymbol{D}$	ω=4.0 ξ_{G0}=0.1125	ω=0.28 ξ_{G0}=0.1125	ω=4.0 ξ_{G0}=1.0	ω=0.28 ξ_{G0}=1.0
NM_T $f = 1+\omega\xi_{G_0} We\boldsymbol{T} : \boldsymbol{D}$	ω=4.0 ξ_{G0}=0.1030	ω=0.28 ξ_{G0}=0.1100	ω=4.0 ξ_{G0}=0.1500	ω=0.28 ξ_{G0}=0.5800
EPTT/MBM $f = \left(1+\omega\xi_{\eta_{p0}}\boldsymbol{\tau}_p : \boldsymbol{D}\right) exp\left(\frac{\varepsilon}{1-\beta} Wetr\boldsymbol{\tau}_p\right)$	ε=0.25 ω=4.0 $\xi_{\eta p0}$=0.0010	-	ε=0.25 ω=4.0 $\xi_{\eta p0}$=0.010	-
EPTT/NM_τ_p $f = \left(1+\omega\xi_{G_0} We\boldsymbol{\tau}_p : \boldsymbol{D}\right) exp\left(\frac{\varepsilon}{1-\beta} Wetr\boldsymbol{\tau}_p\right)$	ε=0.25 ω=4.0 ξ_{G0}=0.0010	-	ε=0.25 ω=4.0 ξ_{G0}=0.010	-
EPTT/NM_T $f = \left(1+\omega\xi_{G_0} We\boldsymbol{T} : \boldsymbol{D}\right) exp\left(\frac{\varepsilon}{1-\beta} Wetr\boldsymbol{\tau}_p\right)$	ε=0.25 ω=4.0 ξ_{G0}=0.0010	-	ε=0.25 ω=4.0 ξ_{G0}=0.010	-

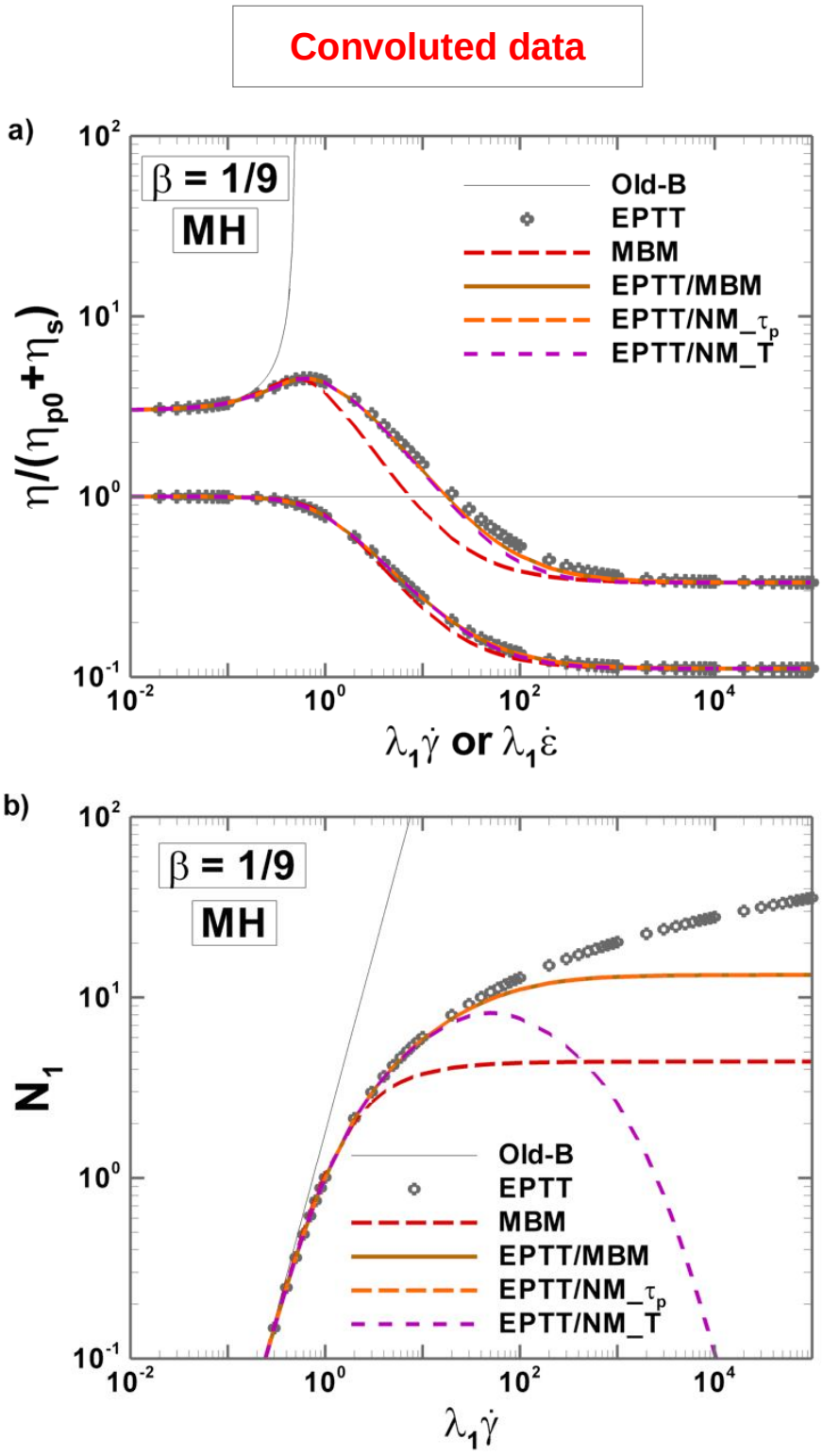

Figure 3.2. a) Shear and extensional viscosities, b) shear N_1 versus *We*; MBM, EPTT and convoluted models; MH (EPTT ε=0.25; Micellar ω=4.0) response, highly-polymeric (β=1/9) fluids

3.2 Hybrid NM_τ_p_ABS-Papanastasiou model

These material functions provide the vital background and model reference against which to interpret anticipated complex flow response. One notes the extremely low levels of β-solvent fraction attained practically, those of β={10^{-2},10^{-3}}; chosen to enhance the viscoelastoplastic characteristics inherent to these yield-stress polymeric micellar fluids, under NM_τ_p_ABS-Pap modelling. Moreover, the micellar construction and destruction parameters are ω=4.0 and ξ_{G0}={1,0.1125}. Here, at each solvent-fraction level, fluids with {ω,ξ_{G0}}={4,1} (relatively larger structure destruction parameter) display weaker strain-hardening characteristics (smaller peak in extensional viscosity) relative to those with {ω,ξ_{G0}}={4,0.1125} (relatively reduced structure destruction parameter) (see Fig. 3.1). Consideration of the solvent viscoplastic Papanastasiou features are evaluated through variation of yield stress parameter τ_0={0.01,0.1,0.5,1}, and the regularisation stress-growth exponent m_p={10,10^2,10^3,10^5,10^7}. Also, viscoelastoplastic behaviour is pursued through β-variation for NM_τ_p_ABS, with decreasing β={0.9,0.5,1/9,10^{-2},10^{-3},10^{-4},10^{-5}} (Calderas et al. 2013). The special cases for which either τ_0 or m_p attain null values, characterise absence of viscoplasticity, and thus collapse the fluid representation to that of the NM_τ_p_ABS model. In Fig. 3.3, 3.4 and 3.5, dimensionless plots are provided of the material function against deformation rates in simple shear and uniaxial extension deformations.

Yield-stress m_p-variation {10^s;s=1,2,…,7} Under {β,τ_0,ω,ξ_{G0}}={10^{-2},1,4,1}, the shear stress against shear-rate plot illustrates the influence of *m_p-variation,* and also the effect of this low solvent fraction regime on the apparent polymeric-plastic fluid characteristics (Fig. 3.3 top). Firstly, and as a consequence of the solvent viscoplastic characteristics at relatively low rates, the linear slope is gradually reduced as m_p is increased; shifts of ~one decade in rate for one decade increase in m_p, once $m_p \geq 10^2$. This shift leads to the appearance of a plateau (τ_{xy}=10^{-2}) at low rates, which is extended further into even lower-order rates as m_p is increased; to the point in which the linear low-rate slope is practically lost. This position corresponds to the theoretical Papanastasiou prediction, in which $m_p \to \infty$ leads to an ideal yield stress viscoplastic response. The shear and extensional viscosities behave as expected, with shear-thinning features, and strain-hardening-softening (only at ξ_{G0}=0.1125) features, as the deformation rate is increased. As m_p is increased, the η_0 plateau-value is incremented and thinning features onset at relatively low shear rates. Extensional viscosity curves reflect similar behaviour at low deformation rates, preserving the viscous factor of three units involved at each comparable m_p-level. Interestingly, the shear and extensional viscosity data curves $\forall\, m_p$ converge at deformation-rates of 10^{-1}, before encountering either onset of shear-thinning or strain-hardening-softening phenomena. Then, as the

deformation rate is increased, these data curves appear to overlap, irrespective of their corresponding m_p-level. The first normal stress difference in shear (N_1) reflects invariance with m_p-change. Here, the quadratic slope at low shear-rates is lost at unity deformation rate, evolving to a plateau of N_1~0.4.

As the thixotropic structure destruction parameter is decreased from ξ_{G0}=1 to 0.1125, the upper-limiting plateau becomes N_1~4 units; extensional strain-softening-hardening characteristics are exaggerated, with extensional viscosity peaks of ~6 units; both such effects apply irrespective of m_p-level. Moreover, as a consequence of this more structured fluid state at ξ_{G0}=0.1125, the second viscoelastic plateau in τ_{xy} is shifted to relatively larger shear-rates ($5<\lambda_1\dot{\gamma}<10^2$) and higher levels of shear-stress (~1 units).

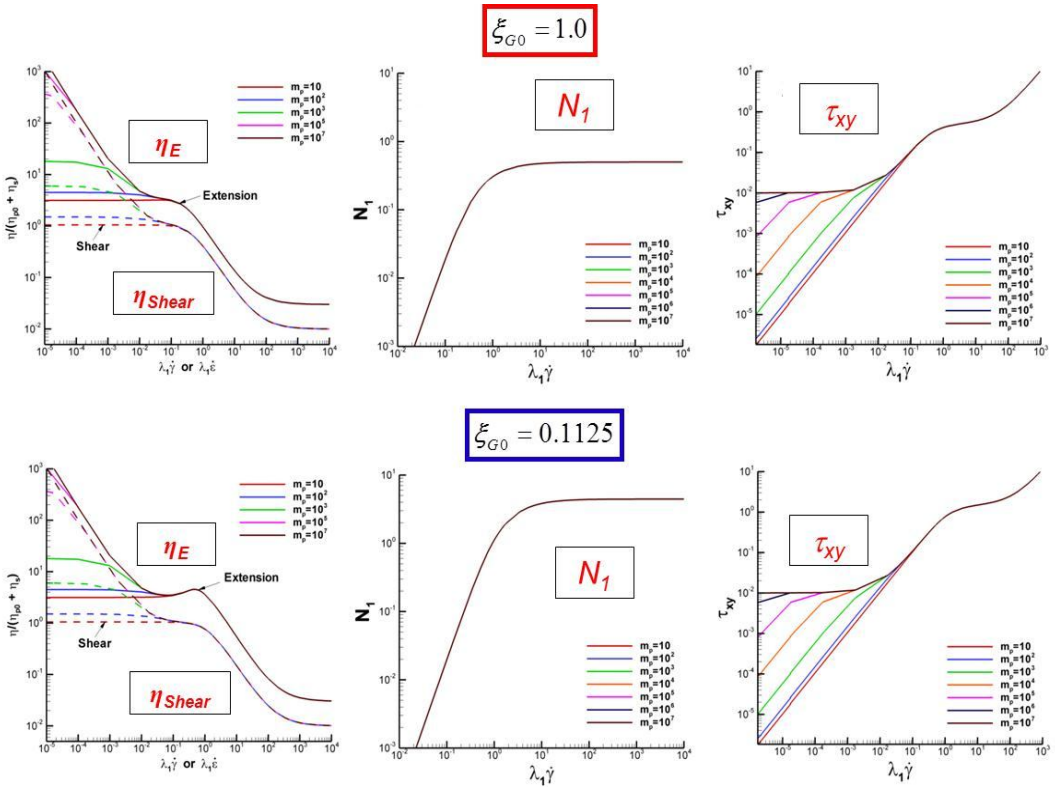

Figure 3.3 Material functions against dimensionless rate; shear (η_{Shear}) and extensional (η_{Ext}) viscosities, N_1, τ_{xy}; m_p-variation m_p={10^s;s=1,2,…,7}; {β,τ_0,ω}={10^{-2},1,4}; ξ_{G0}=1 (top), ξ_{G0}=0.1125 (bottom)

Yield-stress τ_0-variation {0.01,0.1,0.5,1} Alternatively, under {$\beta,m_p,\omega,\xi_{G0}$}={$10^{-2}$,$10^2$,4,1}, the shear stress against shear-rate plot (Fig. 3.4 top) illustrates the influence of yield stress *τ_0-variation.* In contrast to m_p-variation, the effects of varying τ_0 on the shear stress are relatively milder. In particular, as τ_0 is elevated and at relatively low shear-rate levels, the slope of linear dependency decreases. These data curves show united patterns at $\lambda_1\dot{\gamma}$ ~10^{-1} units. In this moderate-to-high shear rate range, τ_{xy}-data

curves follow the polymeric micellar-behaviour described above: a plateau is attributed to non-linear thixotropic-viscoelastoplasticity, that extends into $1<\lambda_1\dot{\gamma}<10^2$ range with further rise beyond $\lambda_1\dot{\gamma}>10^2$. Shear and extensional viscosity are affected in their corresponding zero-rate plateaux as τ_0 is increased, whilst preserving their 3:1 extensional-to-shear viscosity ratio. Here, for low-rate shear viscosity, η_0 levels elevate from ~1 units for τ_0=0.01, to ~1.5 units at τ_0=1. Accordingly, this increase is reflected in extensional viscosity curves, for which the zero-extension rate plateaux elevate from ~3 units for τ_0=0.01, to ~4.5 units at τ_0=1. As true for m_p-variation, the shear and extensional viscosity data curves $\forall\ \tau_0$ converge at deformation-rates of 10^{-1}, before either encountering - decline due to shear-thinning, or strain-hardening-softening phenomena.

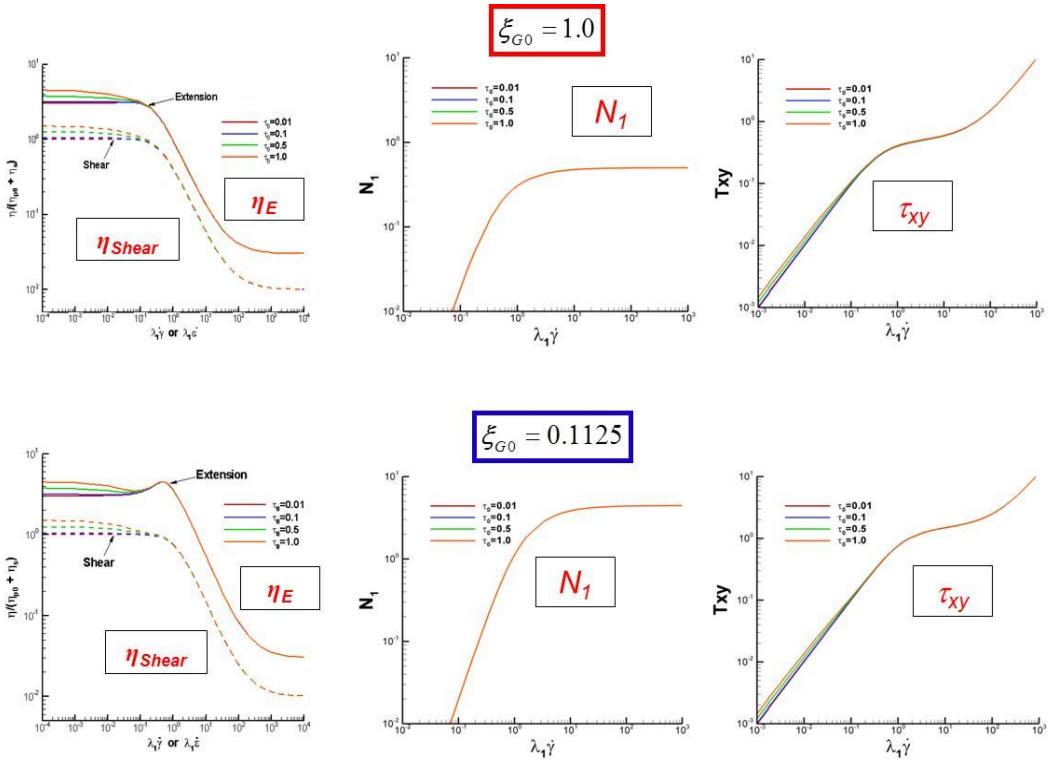

Figure 3.4 Material functions against dimensionless rate; shear (η_{Shear}) and extensional (η_{Ext}) viscosities, N_1, τ_{xy}; **τ_0-variation** τ_0={0.01,0.1,0.5,1}; {β,m_p,ω}={10^{-2},1,4}; ξ_{G0}=1 (top), ξ_{G0}=0.1125 (bottom)

Solvent-fraction β-variation {0.9,0.5,1/9,10^{-2},10^{-3},10^{-4},10^{-5}} Finally, under {τ_0,m_p,ω,ξ_{G0}}={0,0,4,1}, the solvent fraction β-variation is analysed in (Fig. 3.5 top), that accounts for variation in polymer concentration. Here, the shear stress data curves illustrate the thixotropic NM_τ_p_ABS property to generate a level τ_{xy}-plateau (value ~4.5) that applies over an ever wider shear-rate range as the β–factor declines (at β=10^{-5}, plateau over $3<\lambda_1\dot{\gamma}<10^4$). Signs of plateau-onset are observed at low solvent

fractions, $\beta \leq 10^{-2}$ at $\lambda_1\dot{\gamma}$ ~3 units. At larger rates and beyond the plateau period, the data curves return to a linear rise. One notes the appearance of this thixotropic τ_{xy}-plateau, located in the moderate-to-high shear-rate range, conforms to the current viscosity-scale chosen under non-dimensionalisation (η_{p0}). It is desirable to shift such a polymeric feature to still lower shear-rates, and henceforth, account for a realistic viscoelastoplastic plateau, as with the solvent viscoplastic Papanastasiou contribution. To achieve this, the characteristic viscosity-scale should be fixed at the second Newtonian plateau η_∞ instead. This adjustment rescales the f_τ-functional, and hence viscosity, to the range $\frac{\eta_\infty}{\eta_{p0}} \leq f_\tau \leq 1$. Computational analysis to bear this out is due to appear subsequently. Analysis on N_1 reflects, at low deformation-rates (in the linear elastic regime) that such β-variation provokes data-curve translation by one-half decade for β–change from 0.9 to 1/9. At $\lambda_1\dot{\gamma}$ ~6, these N_1-data curves unite, plateauing at N_1~0.4, independently of polymer concentration. The shear and extensional viscosity properties are also affected, with proportional decline in second Newtonian plateaux as β-decreases. The Newtonian ratio of 3 is upheld between limiting extensional (dashed lines) and shear (continuous lines) viscosity plateaux.

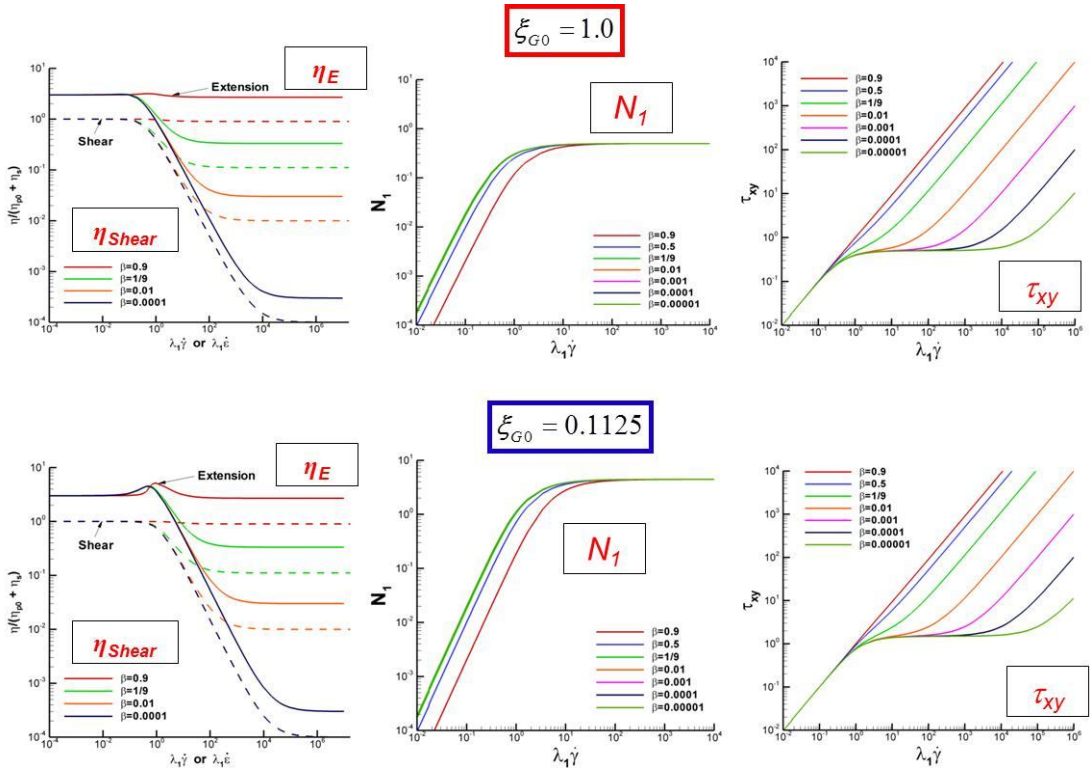

Figure 3.5 Material functions against dimensionless rate; shear (η_{Shear}) and extensional (η_{Ext}) viscosities, N_1, τ_{xy}; ***β*-variation** β={0.9,0.5,1/9,10^{-2},10^{-3},10^{-4},10^{-5}}; { τ_0,m_p,ω} ={0,0,4}; ξ_{G0}=1 (top), ξ_{G0}=0.1125 (bottom)

Thixotropic ξ_{G0}-variation As the micellar structure destruction parameter is decreased from ξ_{G0}=1 to 0.1125, again the strain hardening-softening property is exaggerated, with peak values reaching ~6 units (Fig. 3.3-3.5 bottom). Here, as the solvent fraction is decreased from β=0.9 to 10^{-4}, the appearance of an extensional viscosity peak is shifted to slightly lower deformation rates and reduces in size. Moreover, the plateaux in $\{\tau_{xy}, N_1\}$ at ξ_{G0}=0.1125 are shifted to larger levels of ~{1,4}, relative to the less structured ξ_{G0}=1 representation. These properties are unaffected by τ_0- or m_p-variation.

3.3 FENE-CR model

This constant shear-viscosity strain-hardening model has particularly been used in this work to match dimensional shear viscosity and N_1 from the experiments done with Boger fluids by MEng Mariano Perez-Camacho for his DrEng thesis at Facultad de Química, UNAM. With respect to the first normal stress difference in simple shear, N_1, as the extensibility parameter increases, its dependence on shear-rate is more quadratic in nature, approaching the behaviour of Oldroyd-B. N_1 is fitted to the extensibility parameters of L={3,6,8} at solvent fraction β=0.85 (Fig. 3.6). Note that increase in L, extensional viscosity plateaux attain higher levels and the quadratic nature of the N_1 data-curve is enhanced. Here, when $L \to \infty$, the Oldroyd-B quadratic N_1 behaviour is recovered. The shear viscosity is adjusted at a constant level of ~10 Pa s.

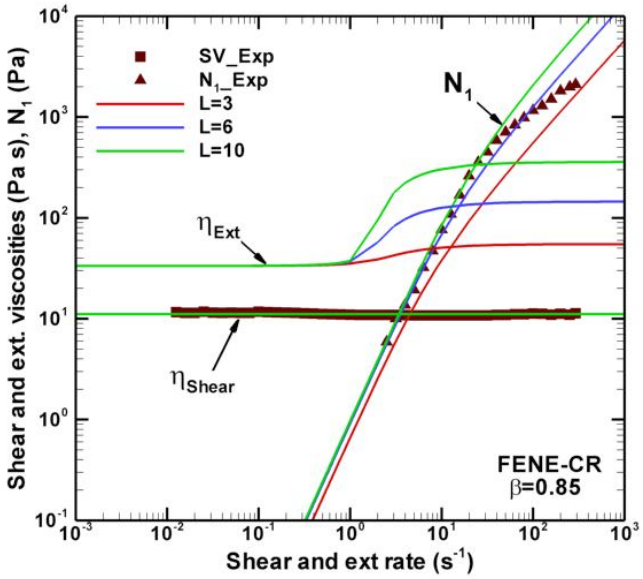

Figure 3.6 Dimensional material functions against deformation rate; shear (η_{Shear}) and extensional (η_{Ext}) viscosities, N_1; ***L*-variation** L={3,6,10}; $\{\beta,\lambda_1\}$={0.85,0.174}

3.4 SXPP model

In Fig. 3.7, the extensional viscosity of the SXPP model is plotted for two sets of parameters. These theoretical data curves display an initial rise to a peak (devoid of anisotropy, α_{pom}=0), or to a plateau (anisotropy $\alpha_{pom}\neq$0) with increasing extension-rate; and then, a decrease prior to reaching a limiting second plateau (controlled by β-parameter). The plots in the first row of Fig. 3.7 clearly demonstrate that there is significant growth in the peak-value of extensional viscosity with the *rise in the number of arms (q)*. Values of q={2, 5, 10} typically provide peak/plateaued-values of μ_e={5.4, 11.5, 16.3 units} at fixed entanglement state (ε_{pom}=0.666), solvent-fraction (β=1/9) and anisotropy level (α_{pom}=0.15). Moreover, *fall in the degree of entanglement* (ε_{pom}), with values of ε_{pom}={0.333, 0.666, 0.999} typically provokes peak/plateaued-values of μ_e={16.3, 18.1, 18.1 units} at fixed q=10 (pom-pom side-branch arms number), solvent-fraction (β=1/9) and anisotropy level (α_{pom}=0.15).

In contrast, at a fixed entanglement state (ε_{pom}=0.99), and solvent-fraction (β=0.262), with absence of anisotropy (α_{pom}=0), *rise in the number of arms (q)* provides peak-values of μ_e={5, 10, 30, 80 units} for values of q={2, 4, 8, 15}, respectively. Similar trends in elevation of peak extensional viscosity are also realised when the *degree of entanglement declines* (characterising more highly-mobile systems, rising ε_{pom}). Specifically, at q=8 with β=0.262 and α_{pom}=0, values of ε_{pom}={0.11, 0.2, 0.33, 0.99} provide peak-values of μ_e={4, 7, 10, 30 units}, respectively. With *change in the polymer concentration*, under q=8 and, ε_{pom}=0.99 conditions, extensional viscosity peak-values of highly-polymeric fluids (β=0.262) are larger and exhibit a lower second-plateau viscosity level (μ_∞) relative to the solvent-dominated fluids (β=0.915). Here, values of β={0.262, 0.915} provide extensional viscosity peak-values of μ_e={30, 6}, with second-plateau viscosity levels of μ_∞={0.8, 3}. Note, an important observation is that change in all three material parameters {q,ε_{pom},β}, provokes elevation in extensional viscosity to varying degrees, arising from different physics at the system level {molecular chain mobility, degree of entanglement, degree of polymer concentration}.

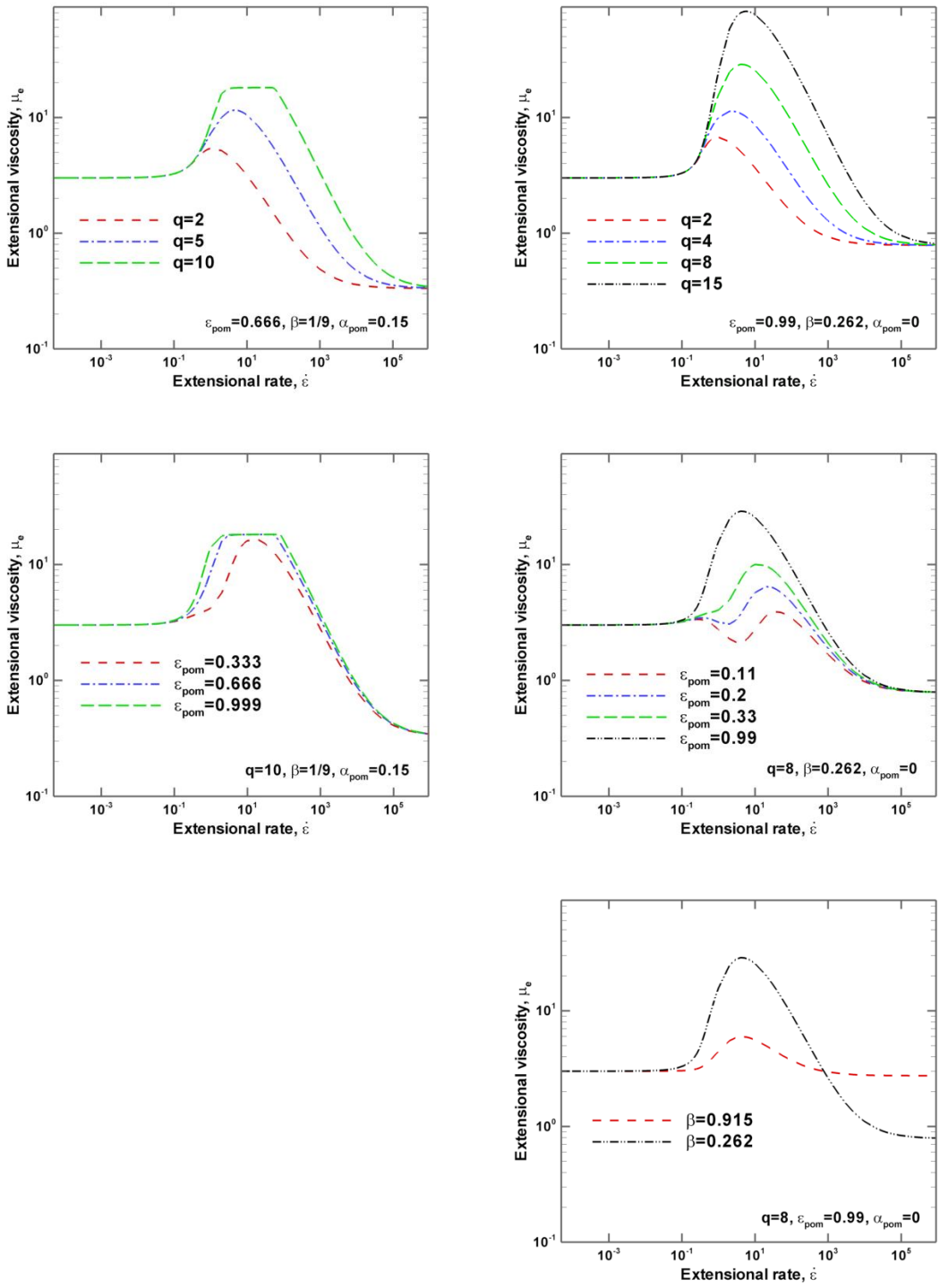

Figure 3.7 Extensional viscosity; SXPP model; variation of parameters

CHAPTER 4

Numerical scheme and discretisation

A hybrid method is used and modified in this work to accommodate the structure equation of the Bautista-Manero class models. The balance equations (momentum and continuity equations) are discretised using the *finite element method* (FEM); whilst the *finite volume method* (FVM) is used for the constitutive equation for stress. This hybrid implementation generates a stable fractional-staged high-order finite element/finite volume (*fe/fv*) scheme. Such a scheme has demonstrated success in solving complex flow problems of viscoelastic and viscoelastoplastic fluids (Wapperom and Webster 1998, 1999; Aboubacar et al. 2001, 2002, 2005, Webster et al. 2004, 2005; Aguayo et al. 2006, 2008; Belblidia et al. 2006; Walters et al. 2008, 2009; Sujatha et al. 2008; Belblidia et al. 2007, 2008, 2011; Tamaddon-Jahromi et al. 2008, 2010, 2011; Nyström et al. 2013; Echendu et al. 2013; Al-Muslimawi 2013; López-Aguilar et al. 2014).

Computational rheology has emerged and now become established as an independent science (Crochet and Walters 1993). In this, numerical modelling is employed to simulate the flow of complex fluids in complex geometries. Traditionally, in CFD modelling (Chung 2002), and subsequently in computational rheology (for viscoelastic flows refer to [Keunings 1989, 1990, 2000, 2001; Baaijens 1998; Owens and Phillips 2002; Webster and Walters 2003]), finite difference, finite element and finite volume schemes have been used to solve complex flow problems. In recent years with parallelisation facilities becoming available, other numerical approaches have been used to simulation the flow of non-Newtonian and viscoelastic fluids. Two examples are

- the highly parallelisable Lattice-Boltzmann method (Aidun and Clausen 2010), and the meshless smoothed particle hydrodynamics (SPH) method (Liu and Liu 2010).

4.1 Finite element/volume methods

In these methods, the problem domain is divided into a non-overlapping finite number of sub-domains. Here, the conservation and constitutive equations apply over each control finite element/volume, and solution unknowns ($\boldsymbol{u}, p, \boldsymbol{T}, f_\tau$) are approximated by 'shape' functions with their associated nodal values over these sub-domains. Practically, the equations describing the flow problem are multiplied by weighting functions and integrated over the flow domain, thus producing a system of algebraic equations whose solutions provide the nodal unknown values.

4.1.1 Galerkin finite element method

To illustrate the finite element method employed, a simple example is developed, that of the time independent Poisson equation,

$$\frac{\partial^2 u}{\partial x^2} = f(x). \tag{4.1}$$

Here, $u(x)$ and x represent the dependent and independent variables. The function $f(x)$ in the RHS of eq.(4.1) accounts for non-homogeneous source-terms. In this discretisation, the unknown solution variables are approximated by suitable trial (nodal) functions $\phi_i(x)$, usually polynomials of first or second order. The solution nodal values are given by u_i:

$$u(x) = \sum_i^N \phi_i(x) u_i. \tag{4.2}$$

Substitution of this trial solution into eq.(4.1) yields its corresponding residual, which is then weighted, being multiplied by the weighting (test) functions $w_i(x)$. This procedure is applied to all nodes *N* in each element. In the case of the Galerkin method, these test functions correspond to the trial functions, so that, $w_i(x) = \phi_i(x)$. Hence, applying this procedure to eq.(4.1) results in:

$$\int_{\Omega_e} \frac{\partial^2}{\partial x^2}\left[\phi_i(x)u_i\right]\phi_j(x)\,d\Omega_e = \int_{\Omega_e} f(x)\phi_j(x)\,d\Omega_e . \tag{4.3}$$

Reduction in differential operator order is then achieved through integration by parts of eq.(4.3), which generates boundary condition dependency. This is then the next step in the procedure,

$$\left.\frac{\partial\phi_i(x)}{\partial x}\phi_j(x)\right|_{\Gamma_e} - u_i\int_{\Omega_e}\frac{\partial\phi_i(x)}{\partial x}\frac{\partial\phi_j(x)}{\partial x}\,d\Omega_e = \int_{\Omega_e} f(x)\phi_j(x)\,d\Omega_e . \tag{4.4}$$

Eq.(4.4) represents the Poisson equation in a single elemental control volume. Addition of all such elemental contributions provided the full system of equations to solve. The first term on the LHS of eq.(4.4) is evaluated through the boundary conditions for each element. Consistently, this term is null for internal elements; otherwise, its value is determined by those conditions specified on the perimeter-boundary of the domain. For example, in this work, no-slip boundary conditions are adopted on solid-walls. This condition implies no movement ($\boldsymbol{u} = 0$) at the walls.

For conciseness and practicality, matrix notation is used to represent the whole system of algebraic equations given by consideration of each elemental contribution in eq.(4.4) on control volume (Ω_e):

$$\boldsymbol{K}\boldsymbol{u} = \boldsymbol{b}, \tag{4.5}$$

where $K_{ij} = \int_{\Omega_e}\frac{\partial\phi_i(x)}{\partial x}\frac{\partial\phi_j(x)}{\partial x}\,d\Omega_e$ and $b_j = \int_{\Omega_e} f(x)\phi_j(x)\,d\Omega_e$. The solutions for this system of algebraic equations provide the column-matrix $\mathbf{u}$ of nodal-solution values. Once this vector has been determined, the approximate solution to eq.(4.1) is found by eq.(4.2).

4.1.2 The finite volume method

To apply this method, the equation under consideration is conventionally written in conservative form, in order to apply the *Divergence Theorem*, i.e. $\int_{\Omega}\nabla\cdot\chi\,d\Omega = \int_{\Gamma}\boldsymbol{n}\cdot\chi\,d\Gamma$. This theorem translates the integral of a conservative quantity χ over the volume of the domain Ω, to integrals over its respective bounding surface Γ,

defined by its normal vector $\boldsymbol{n}$ (Versteeg and Malalasekera 1995). *The finite volume method* can be viewed as a subclass of the finite element procedure, with weighting functions chosen as unity, $w(x)=1$ (Puangkird 2007; Aguayo 2006). As such, and in general conservation law form:

$$\frac{\partial}{\partial t}\int_{\Omega}\chi d\Omega+\int_{\Gamma}\boldsymbol{n}\cdot\boldsymbol{f}d\Gamma=\int_{\Omega}\boldsymbol{q}d\Omega, \tag{4.6}$$

where $\boldsymbol{f}$ is the flux of χ, that can be separated into convective and diffusive parts, and $\boldsymbol{q}$ represents inhomogeneous source terms. Mean values in a *fv*-cell are defined as $\chi_i=\frac{1}{|\Omega_i|}\int_{\Omega_i}\chi d\Omega_i$.

Then, for a single finite volume, eq.(4.6) can be recast into,

$$\frac{\partial\chi_i}{\partial t}+\frac{1}{|\Omega_i|}\sum_k\int_{\Gamma_k}\boldsymbol{n}_k\cdot\boldsymbol{f}d\Gamma_k=q_i, \tag{4.7}$$

where k is the number of 'faces' of the *fv*-subcell and Γ_k is the area of those faces, defined by their normal vectors $\boldsymbol{n}_k$.

Moreover, the mean values can be approximated through numerical integration procedures,

$$\int_{\Omega_i}\chi d\Omega_i\approx\sum_{i=0}^{nn}\kappa_i\chi_i, \tag{4.8}$$

where $\kappa_i\geq 0$ are weights, and *nn* is the number of nodes of the integration procedure. Surface integrals, which represent the flow of the conservative property, are approximated as

$$\sum_k\int_{\Gamma_k}\boldsymbol{n}_k\cdot\boldsymbol{f}d\Gamma_k\approx F_k\int_{\Gamma_k}\mathbf{f}\cdot\mathbf{n}_k\mathrm{d}\Gamma_k\approx\sum_k F_k. \tag{4.9}$$

Similarly to the finite element method, implementation of this procedure for each finite volume throughout the whole domain, provides the system of equations representing the approximation to eq.(4.6).

4.2 Problem specification

As in chapter 2, under transient, incompressible and isothermal flow conditions, the relevant mass conservation and momentum equations for viscoelastic flow, may be expressed in non-dimensional terms (see definitions below; omitting * for dimensionless variables) as:

$$\nabla \cdot \boldsymbol{u} = 0\,, \tag{2.12}$$

$$Re\frac{\partial \boldsymbol{u}}{\partial t} = \nabla \cdot \boldsymbol{T} - Re\boldsymbol{u} \cdot \nabla \boldsymbol{u} - \nabla p\,. \tag{2.13}$$

An equation of state accounting for the response (the internal stresses) of viscoelastic fluids must be specified. Hence, in the general differential framework described in chapter 2:

$$\boldsymbol{T} = 2\left(1-\beta\right)\boldsymbol{D} + \boldsymbol{\tau}_p\,, \tag{2.27}$$

$$We\frac{\partial \boldsymbol{\tau}_p}{\partial t} = 2\left(1-\beta\right)\boldsymbol{D} - f_\tau \boldsymbol{\tau}_p - We\left(\boldsymbol{u} \cdot \nabla \boldsymbol{\tau}_p - \nabla \boldsymbol{u}^T \cdot \boldsymbol{\tau}_p - \boldsymbol{\tau}_p \cdot \nabla \boldsymbol{u}\right). \tag{2.28}$$

By specifying the functional f_τ, the network nature and theoretical properties of the fluid considered may be imposed into this general framework. The Oldroyd-B model is a simple case in this general framework. It is represented by a fluid with $f_\tau = 1$ (see chapter 2 for the variants used of this f_τ-functional, and hence fluids, considered).

The balance and constitutive equations of (2.12)-(2.13) and (2.27)-(2.28) should be supplemented with appropriate boundary and initial conditions to specify the physical conditions of the flow problem. In general, the boundary conditions may be of a mixed form,

$$\boldsymbol{u}_{\Gamma_1} = \boldsymbol{g}\left(\boldsymbol{x},t\right), \tag{4.10a}$$

$$\left(\boldsymbol{T} \cdot \boldsymbol{n}\right)_{\Gamma_2} = \boldsymbol{h}\left(\boldsymbol{x},t\right), \tag{4.10b}$$

$$\boldsymbol{T}_{\Gamma_3} = \boldsymbol{i}\left(\boldsymbol{x},t\right). \tag{4.10c}$$

These boundary conditions are defined at the boundary Γ that enclosed the flow domain Ω. The condition in (4.10a) treats the imposition of the velocity field $\boldsymbol{g}(\boldsymbol{x},t)$ in the subsection Γ_1 of the geometry-boundary. The expression in (4.10b) specifies the normal forces $\boldsymbol{h}(\boldsymbol{x},t)$ on the surface given at the boundary-subsection Γ_2. Finally, eq.(4.10c) specifies the stress state $\boldsymbol{i}(\boldsymbol{x},t)$ at the subsection Γ_3. Note that the subsections Γ_i do not overlap, so that the boundary conditions remain independent along the boundaries of the domain.

Specific to this analysis,

(i) 2D flows are considered,

(ii) no-slip conditions (vanishing velocity) are imposed at the boundary-wall,

(iii) for domain inlet and exit, velocity profiles for the Oldroyd-B model are imposed, providing sufficiently large inlet/exit channel sections are established for fully-developed flow to apply.

(iv) inlet stress conditions must be imposed.

Simulation procedure

(i) Simulation starts from some initial state in all variables (typically rest) and at low elasticity (or Weissenberg) levels (typically $We = 0.1$).

(ii) Then, once a calculation for a particular *We* has converged, continuation in *We* is employed to obtain subsequent larger elasticity levels, using the solution at the previous *We*-level as the initial condition for the next *We*-step. Consistency checks are also conducted, with We-backward stepping, for vanishing elasticity levels (such as $We=10^{-2}$-10^{-3}). This corroborates reduced Newtonian solutions.

(iii) Simulations are terminated (with non-convergence) when either *(a)* divergence is encountered, whereupon the errors in the dependent variables $\{\boldsymbol{u}, p, \boldsymbol{T}\}$ amplify and fail to reach the specified tolerance ($=10^{-6}$); or *(b)* when the errors in the dependent variables provide non-convergent oscillatory states during the time-stepping process.

4.3 The incremental Taylor-Galerkin/pressure-correction (iTGPC) scheme

The numerical algorithm employed in this work is based on a semi-implicit formulation on a Taylor-Galerkin/pressure correction scheme. Here, the time discretisation is based on a Taylor series expansion, which is enhanced in accuracy through a two-step Lax-Wendroff approach. The incompressibility condition is enforced through a fractional-staged incremental pressure-correction scheme, which leads to a time-stepping scheme of second-order accuracy.

4.3.1 Time semi-discretisation

The two-step Lax-Wendroff (predictor-corrector) procedure is based on a Taylor series expansion in time. This splits a time-step Δt into two halves, for which the first covers the $n \le t \le n+\frac{1}{2}$ range, whilst the second involves $n+\frac{1}{2} \le t \le n+1$. A second-order Taylor expansion for the scalar function $\Phi(\boldsymbol{x},t)$ is:

$$\Phi^{n+1} = \Phi^{n} + \Delta t\left(\frac{\partial \Phi}{\partial t}\right)^{n} + \frac{1}{2}\Delta t^{2}\left(\frac{\partial^{2}\Phi}{\partial t^{2}}\right)^{n}, \tag{4.11}$$

where Φ^{n+1} represents the function $\Phi(\boldsymbol{x},t)$ at time step t_{n+1}, and Φ^{n} represents the function $\Phi(\boldsymbol{x},t)$ at time step t_{n}, respectively. Now, for a differential equation of the form of

$$\frac{\partial \Phi}{\partial t} = F, \tag{4.12}$$

it follows that $\frac{\partial^{2}\Phi}{\partial t^{2}} = \frac{\partial F}{\partial t} = \frac{\partial F}{\partial \Phi}\frac{\partial \Phi}{\partial t} = \frac{\partial F}{\partial \Phi}F$, identifying the system Jacobian ($\frac{\partial F}{\partial \Phi}$), for which the Taylor series expansion becomes:

$$\Phi^{n+1} = \Phi^{n} + \Delta t F^{n} + \frac{1}{2}\Delta t^{2}\left(\frac{\partial F}{\partial \Phi}\right)^{n} F^{n}. \tag{4.13}$$

To obtain an $O(\Delta t^{2})$ accurate scheme, a two-step predictor-corrector approach is considered. The predictor step $\Phi^{n+\frac{1}{2}}$ is approximated to an error of $O(\Delta t^{2})$ with an

explicit Euler step; and the corrector step gives the approximation of Φ^{n+1} with an error of $O(\Delta t^3)$.

Step 1: $\Phi^{n+\frac{1}{2}} = \Phi^n + \frac{\Delta t}{2} F^n$, (4.14a)

Step 2: $\Phi^{n+1} = \Phi^n + \frac{\Delta t}{2} F^{n+\frac{1}{2}}$. (4.14b)

This approach can be directly applied to the stress equations in eq.(2.27)-(2.28). In contrast, the momentum equation must comply with the extra requirement of incompressibility. For this, pressure-correction is incorporated into the numerical scheme, as described below.

Thus, the time-step equations for the general constitutive law (including the f_τ-functional) can be written as,

Step 1a:

$$\frac{2We}{\Delta t}\left(\boldsymbol{\tau}_p^{\,n+\frac{1}{2}} - \boldsymbol{\tau}_p^{\,n}\right) = \left\{2(1-\beta)\boldsymbol{D} - f_\tau \boldsymbol{\tau}_p - We\left(\boldsymbol{u}\cdot\nabla\boldsymbol{\tau}_p - \nabla\boldsymbol{u}^T\cdot\boldsymbol{\tau}_p - \boldsymbol{\tau}_p\cdot\nabla\boldsymbol{u}\right)\right\}^n. \quad (4.15a)$$

Step 1b:

$$\frac{We}{\Delta t}\left(\boldsymbol{\tau}_p^{\,n+1} - \boldsymbol{\tau}_p^{\,n}\right) = \left\{2(1-\beta)\boldsymbol{D} - f_\tau \boldsymbol{\tau}_p - We\left(\boldsymbol{u}\cdot\nabla\boldsymbol{\tau}_p - \nabla\boldsymbol{u}^T\cdot\boldsymbol{\tau}_p - \boldsymbol{\tau}_p\cdot\nabla\boldsymbol{u}\right)\right\}^{n+\frac{1}{2}}. \quad (4.15b)$$

Pressure correction This method is a fraction step technique that decouples the velocity and pressure terms in the momentum equation, and implies the consideration of a Poisson equation for pressure (or its temporal increment) in each time-step. Applying such an approximation to eqs.(2.12)-(2.13) renders,

$$\left(\nabla\cdot\boldsymbol{u}\right)^{n+1} = 0. \quad (4.16)$$

$$\frac{Re}{\Delta t}\left(\boldsymbol{u}^{n+1} - \boldsymbol{u}^n\right) = \left(\nabla\cdot\boldsymbol{T} - Re\boldsymbol{u}\cdot\nabla\boldsymbol{u}\right)^n - \nabla p^{n+1}. \quad (4.17)$$

From the projection concept, an intermediate velocity field $\boldsymbol{u}^*$ can be determined, so that the momentum equation can be split as follows,

$$\frac{Re}{\Delta t}\left(\boldsymbol{u}^{*}-\boldsymbol{u}^{n}\right)=\left(\nabla\cdot\boldsymbol{T}-Re\boldsymbol{u}\cdot\nabla\boldsymbol{u}\right)^{n}. \tag{4.18}$$

$$\frac{Re}{\Delta t}\left(\boldsymbol{u}^{n+1}-\boldsymbol{u}^{*}\right)=-\nabla p^{n+1}. \tag{4.19}$$

Applying the divergence operator to eq.(4.19), and employing the approximated continuity equation, one gathers that

$$\frac{Re}{\Delta t}\nabla\cdot\boldsymbol{u}^{*}=\nabla^{2}p^{n+1}. \tag{4.20}$$

Then, the fractional steps for eq.(4.18) can be written as:

Step 1: $$\frac{Re}{\Delta t}\left(\boldsymbol{u}^{*}-\boldsymbol{u}^{n}\right)=\left(\nabla\cdot\boldsymbol{T}-Re\boldsymbol{u}\cdot\nabla\boldsymbol{u}\right)^{n}. \tag{4.21a}$$

Step 2: $$\nabla^{2}p^{n+1}=\frac{Re}{\Delta t}\nabla\cdot\boldsymbol{u}^{*}. \tag{4.21b}$$

Step 3: $$\frac{Re}{\Delta t}\left(\boldsymbol{u}^{n+1}-\boldsymbol{u}^{*}\right)=-\nabla p^{n+1}. \tag{4.21c}$$

The Lax-Wendroff predictor-corrector approximations for eq.(4.21a) are:

$$\frac{2Re}{\Delta t}\left(\boldsymbol{u}^{n+\frac{1}{2}}-\boldsymbol{u}^{n}\right)=\left(\nabla\cdot\boldsymbol{T}-Re\boldsymbol{u}\cdot\nabla\boldsymbol{u}\right)^{n}. \tag{4.22a}$$

$$\frac{Re}{\Delta t}\left(\boldsymbol{u}^{*}-\boldsymbol{u}^{n}\right)=\left(\nabla\cdot\boldsymbol{T}-Re\boldsymbol{u}\cdot\nabla\boldsymbol{u}\right)^{n+\frac{1}{2}}. \tag{4.22b}$$

The pressure term is treated implicitly, using a Crank-Nicolson treatment with $\theta=\frac{1}{2}$:

$$\nabla p^{n+1}\approx\theta\nabla p^{n+1}+\left(1-\theta\right)\nabla p^{n}, \tag{4.23}$$

or,

$$\nabla p^{n+1}\approx\nabla p^{n}+\theta\left(\nabla p^{n+1}-\nabla p^{n}\right). \tag{4.24}$$

Hence, and finally, replacing eq. (4.24) into (4.21)-(4.22) yields:

Step 1a:

$$\frac{2\,Re}{\Delta t}\left(\boldsymbol{u}^{n+\frac{1}{2}}-\boldsymbol{u}^{n}\right)=\left(\nabla\cdot\boldsymbol{\tau}_{p}-Re\,\boldsymbol{u}\cdot\nabla\boldsymbol{u}\right)^{n}-\nabla\left[\,p^{n}+\theta_{1}\left(p^{n}-p^{n-1}\right)\right]+\nabla\cdot\left(2\beta\,\frac{\boldsymbol{D}^{n+\frac{1}{2}}+\boldsymbol{D}^{n}}{2}\right).$$

(4.25a)

$$\frac{2We}{\Delta t}\left(\boldsymbol{\tau}_{p}{}^{n+1/2}-\boldsymbol{\tau}_{p}{}^{n}\right)=\left\{2\left(1-\beta\right)\boldsymbol{D}-f_{\tau}\boldsymbol{\tau}_{p}-We\left[\boldsymbol{u}\cdot\nabla\boldsymbol{\tau}_{p}-\boldsymbol{\tau}_{p}\cdot\nabla\boldsymbol{u}-\left(\boldsymbol{\tau}_{p}\cdot\nabla\boldsymbol{u}\right)^{T}\right]\right\}^{n}. \qquad (4.25b)$$

$$\frac{2}{\Delta t}\left(f_{\tau}{}^{n+1/2}-f_{\tau}{}^{n}\right)=\left[\frac{1}{\omega}\left(1-f_{\tau}\right)+\boldsymbol{\zeta}:\boldsymbol{D}\right]^{n}. \qquad (4.25c)$$

Step 1b:

$$\frac{Re}{\Delta t}\left(\boldsymbol{u}^{*}-\boldsymbol{u}^{n}\right)=\left(\nabla\cdot\boldsymbol{\tau}_{p}-Re\,\boldsymbol{u}\cdot\nabla\boldsymbol{u}\right)^{n+\frac{1}{2}}-\nabla\left[\,p^{n}+\theta_{1}\left(p^{n}-p^{n-1}\right)\right]+\nabla\cdot\left(2\beta\,\frac{\boldsymbol{D}^{*}+\boldsymbol{D}^{n}}{2}\right).$$

(4.25d)

$$\frac{We}{\Delta t}\left(\boldsymbol{\tau}_{p}{}^{n+1}-\boldsymbol{\tau}_{p}{}^{n}\right)=\left\{2\left(1-\beta\right)\boldsymbol{D}-f_{\tau}\boldsymbol{\tau}_{p}-We\left[\boldsymbol{u}\cdot\nabla\boldsymbol{\tau}_{p}-\boldsymbol{\tau}_{p}\cdot\nabla\boldsymbol{u}-\left(\boldsymbol{\tau}_{p}\cdot\nabla\boldsymbol{u}\right)^{T}\right]\right\}^{n+\frac{1}{2}}. \qquad (4.25e)$$

$$\frac{1}{\Delta t}\left(f_{\tau}{}^{n+1}-f_{\tau}{}^{n}\right)=\left[\frac{1}{\omega}\left(1-f_{\tau}\right)+\boldsymbol{\zeta}:\boldsymbol{D}\right]^{n+\frac{1}{2}}. \qquad (4.25f)$$

Step 2:

$$\nabla^{2}\left(p^{n+1}-p^{n}\right)=\frac{Re}{\theta_{2}\Delta t}\nabla\cdot\boldsymbol{u}^{*}. \qquad (4.25g)$$

Step 3:

$$\frac{2\,Re}{\Delta t}\left(\boldsymbol{u}^{n+1}-\boldsymbol{u}^{*}\right)=-\theta_{2}\nabla\left(p^{n+1}-p^{n}\right). \qquad (4.25h)$$

This three-stage structure must be solved over each time-step, $\left[t^n, t^{n+1}\right]$ until convergence to a limiting steady-state is secured. One notes that the f_τ-functional is simply treated as an additional stress variable component. Here, one may define (as elsewhere) a generalised stress variable, $\boldsymbol{\zeta}$, which can take either $\xi_{\eta_0}\boldsymbol{\tau}_p$, $\xi_{G_0}We\boldsymbol{\tau}_p$ or $\xi_{G_0}We\boldsymbol{T}$ values, to specify MBM, NM_τ_p or NM_T models, respectively. Dealing with models for which an algebraic f_τ applies, then the extra differential equation for f_τ is replaced by the relevant algebraic identity.

4.3.2 Spatial discretisation

As described above, here velocity and pressure field variables are spatially discretised through Galerkin approximation, whilst the stress equation is dealt with by a finite volume scheme.

4.3.2.1 Finite element scheme Under a finite element framework, scalar velocity components and pressure fields are approximated as,

$$\tilde{\boldsymbol{u}}(\boldsymbol{x},t) = \sum_i \boldsymbol{u}^i(t)\phi_i(\boldsymbol{x}), \tag{4.26a}$$

$$\tilde{p}(\boldsymbol{x},t) = \sum_i p^j(t)\psi_j(\boldsymbol{x}), \tag{4.26b}$$

where $\{\boldsymbol{u}^i(t), p^j(t)\}$ represent the vectors of nodal values for velocity and pressure drop, respectively. Similar forms apply to $\boldsymbol{u}^*$. Moreover, $\phi_i(\boldsymbol{x})$ are the piecewise-continuous quadratic shape functions for velocity, and $\psi_j(\boldsymbol{x})$ are the piecewise-continuous linear shape functions for pressure. The two-dimensional flow domain Ω is divided into triangular elements. Velocity components are evaluated at the vertex and mid-side nodes of this elements, and consistently, $i = 1...6$ (see Fig. 3.1 for complete domain reference). In contrast, pressure is evaluated only at vertex nodes and $j = 1...3$.

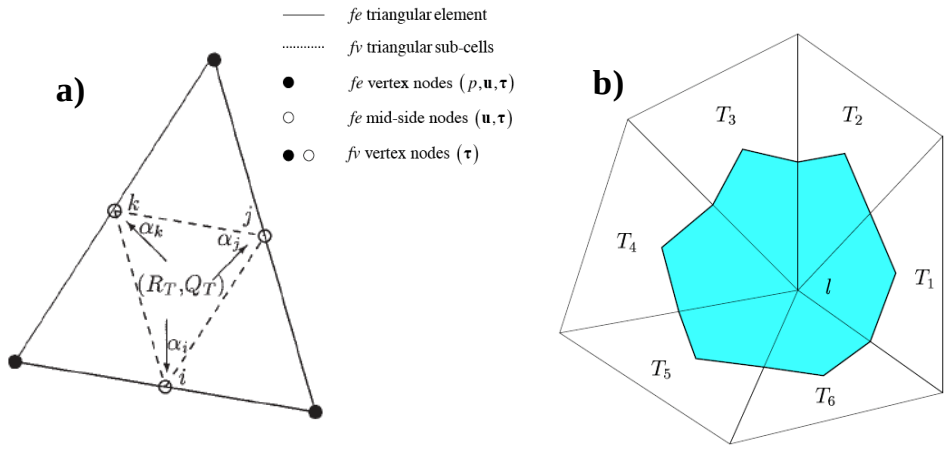

Figure 4.1 Spatial discretisation: a) *fe*-cell with four fv sub-cells and flux distribution (FD) per triangle T; b) *fv*-control volume per node *l*, with median-dual-cell configuration

For eqs.(4.25a,d,g,h), the Galerkin method of weighted residuals can be expressed as,

$$\int_{\Omega} \phi_i(\boldsymbol{x})\, \boldsymbol{R}_{u1,3}\big(\boldsymbol{u}(\boldsymbol{x},t)\big)\, d\Omega = 0\,, \tag{4.27a}$$

$$\int_{\Omega} \psi_j(\boldsymbol{x})\, \boldsymbol{R}_{p2}\big(\boldsymbol{u}(\boldsymbol{x},t)\big)\, d\Omega = 0\,. \tag{4.27b}$$

Here, $\{\boldsymbol{R}_{u1,3}, \boldsymbol{R}_{p2}\}$ are the residuals of velocity equations in steps 1a, 1b and 3; and the residuals of the pressure equation in step 2, respectively. Then, integration by parts of eqs.(4.25a,d,g,h) yields:

Step 1a:

$$\frac{2\,Re}{\Delta t}\Big[\boldsymbol{u}^{n+\frac{1}{2}} - \boldsymbol{u}^{n}, \phi_i(\boldsymbol{x})\Big] = -Re\Big[\boldsymbol{u}^{n}\cdot\nabla\boldsymbol{u}^{n}, \phi_i(\boldsymbol{x})\Big] + \nabla\Big[2p^{n} - p^{n-1}, \phi_i(\boldsymbol{x})\Big] - \nabla\cdot\left[\boldsymbol{\tau}_p{}^{n} + 2\beta\frac{\boldsymbol{D}^{n+\frac{1}{2}} + \boldsymbol{D}^{n}}{2}, \phi_i(\boldsymbol{x})\right] \tag{4.28a}$$

Step 1b:

$$\frac{Re}{\Delta t}\Big[\boldsymbol{u}^{*} - \boldsymbol{u}^{n}, \phi_i(\boldsymbol{x})\Big] = -Re\left[\boldsymbol{u}^{n+\frac{1}{2}}\cdot\nabla\boldsymbol{u}^{n+\frac{1}{2}}, \phi_i(\boldsymbol{x})\right] - \nabla\cdot\left[\boldsymbol{\tau}_p{}^{n+\frac{1}{2}} + 2\beta\frac{\boldsymbol{D}^{*} + \boldsymbol{D}^{n}}{2}, \phi_i(\boldsymbol{x})\right] + \nabla\Big[2p^{n} - p^{n-1}, \phi_i(\boldsymbol{x})\Big] \tag{4.28b}$$

Step 2:

$$\theta_2\left[\nabla\left(p^{n+1}-p^{n}\right),\psi_j\right]=\frac{Re}{\Delta t}\left[\nabla\cdot\boldsymbol{u}^{*},\psi_j\right]. \tag{4.28c}$$

Step 3:

$$\frac{2\,Re}{\Delta t}\left[\boldsymbol{u}^{n+1}-\boldsymbol{u}^{*},\phi_i\left(\boldsymbol{x}\right)\right]=\theta_2\nabla\left[2p^{n+1}-p^{n},\phi_i\left(\boldsymbol{x}\right)\right]. \tag{4.28d}$$

Here, the notation implies that (i) $\left[A\left(\boldsymbol{x},t\right),\vartheta\left(x\right)\right]=\int_{\Omega}\vartheta\left(x\right)A\left(\boldsymbol{x},t\right)d\Omega$, (ii) $\left[\boldsymbol{A}\left(\boldsymbol{x},t\right),\vartheta\left(x\right)\right]=\int_{\Omega}\vartheta\left(x\right)\boldsymbol{A}\left(\boldsymbol{x},t\right)d\Omega$ and (iii) $\left[\boldsymbol{A}\left(\boldsymbol{x},t\right),\boldsymbol{\vartheta}\left(x\right)\right]=\int_{\Omega}\boldsymbol{\vartheta}\left(x\right)\cdot\boldsymbol{A}\left(\boldsymbol{x},t\right)d\Omega$. Then, for eqs.(4.28), the problem statement in fully-discrete matrix form may be written as:

Step 1a:

$$\boldsymbol{A}_u^{a}\left(\boldsymbol{U}^{*}-\boldsymbol{U}^{n}\right)=\boldsymbol{b}_u^{a}\left(P^{n},P^{n-1},\boldsymbol{U}^{n},\boldsymbol{T}^{n},\boldsymbol{D}^{n}\right), \tag{4.29a}$$

Step 1b:

$$\boldsymbol{A}_u^{b}\left(\boldsymbol{U}^{*}-\boldsymbol{U}^{n}\right)=\boldsymbol{b}_u^{b}\left(P^{n},P^{n-1},\boldsymbol{U}^{n},\boldsymbol{U}^{n+\frac{1}{2}},\boldsymbol{T}^{n+\frac{1}{2}},\boldsymbol{D}^{n+\frac{1}{2}}\right), \tag{4.29b}$$

Step 2:

$$\boldsymbol{K}\left(P^{n+1}-P^{n}\right)=\boldsymbol{b}_2\left(\boldsymbol{U}^{*}\right), \tag{4.29c}$$

Step 3:

$$\boldsymbol{A}_3\left(\boldsymbol{U}^{n+1}-\boldsymbol{U}^{*}\right)=\boldsymbol{b}_3\left(P^{n},P^{n+1}\right). \tag{4.29d}$$

Here, the superscript ^{n} denotes the time level, Δt the time-step, and $\{\boldsymbol{U},\boldsymbol{U}^{*},P,\boldsymbol{T},\boldsymbol{D}\}$ represent the nodal values of velocity, non-solenoidal velocity, pressure, extra-stress and rate of deformation tensor (velocity gradient), respectively. Moreover,

$$\boldsymbol{A}_u^{a}=\frac{2\,Re}{\Delta t}\boldsymbol{M}+\frac{\beta}{2}\boldsymbol{S}, \tag{4.30a}$$

$$\boldsymbol{A}_u^b = \frac{Re}{\Delta t}\boldsymbol{M} + \frac{\beta}{2}\boldsymbol{S}\,, \tag{4.30b}$$

$$\boldsymbol{A}_3 = \frac{Re}{\Delta t}\boldsymbol{M}\,, \tag{4.30c}$$

where $\boldsymbol{M}$ and $\boldsymbol{S}$ are the consistent mass and diffusion matrices. For the extra-stress tensor equation, the corresponding mass matrix $\boldsymbol{A}_\tau$, under the finite element representation, equates to the identity matrix under finite volume approximation. In addition, the vector $\boldsymbol{b}_\tau$ is described in the following section, under finite volume approximation. The pressure matrix $\boldsymbol{A}_2 = \boldsymbol{K}$ is the standard stiffness matrix and $\boldsymbol{A}_3$ is identified with the mass matrix. The RHS of eq.(4.29) are defined as,

$$\boldsymbol{b}_u^a = \left\{-\left[\beta\boldsymbol{S} + Re\,\boldsymbol{N}\left(\boldsymbol{U}\right)\right]\boldsymbol{U} - \boldsymbol{B}\cdot\tau_p\right\}^n + \boldsymbol{L}^T\left\{P^n + \theta_1\left(P^n - P^{n-1}\right)\right\}, \tag{4.30d}$$

$$\boldsymbol{b}_u^b = \left\{-\left[\beta\boldsymbol{S} + Re\,\boldsymbol{N}\left(\boldsymbol{U}\right)\right]\boldsymbol{U} - \boldsymbol{B}\cdot\tau_p\right\}^{n+\frac{1}{2}} + \boldsymbol{L}^T\left\{P^n + \theta_1\left(P^n - P^{n-1}\right)\right\}, \tag{4.30e}$$

$0 \le \theta_1 \le 1$,

$$\boldsymbol{b}_2 = \frac{Re}{\theta_2\Delta t}\boldsymbol{L}\boldsymbol{U}^*, \tag{4.30f}$$

$$\boldsymbol{b}_3 = -\theta_2\boldsymbol{L}^T\left(p^{n+1} - p^n\right), \tag{4.30f}$$

where $\boldsymbol{N}\left(\boldsymbol{U}\right)$ and $\boldsymbol{L}$ represent the consistent advection and pressure gradient matrices, respectively. Using the summation convention with repeated indexes notation over the domain, the matrices are defined as $M_{ij} = \int_\Omega \phi_i\phi_j\,d\Omega$, $S_{ij} = \int_\Omega \nabla\phi_i\nabla\phi_j\,d\Omega$, $N\left(\boldsymbol{U}\right)_{ij} = \int_\Omega \phi_i\left(\phi_l\boldsymbol{U}_l\right)\nabla\phi_j\,d\Omega$, $K_{ij} = \int_\Omega \nabla\psi_i\nabla\psi_j\,d\Omega$, $B_{ij} = \int_\Omega \nabla\phi_i\phi_j\,d\Omega$, $L_{ij} = \int_\Omega \psi_i\nabla\cdot\phi_j\,d\Omega$.

4.3.2.2 Finite volume scheme This spatial discretisation scheme is adopted for its particular advantages when solving conservation-law type hyperbolic partial differential equations, with attractive retention of such properties as positivity and other conservation principles. In the fractional time steps described in eqs.(4.25) the stress equation is decoupled from the mass/momentum equation. This permits a

straightforward implementation of finite volume techniques (*fv*) for parent-child subcell stress equation discretisation. As observed in Fig. 4.1, the *fv* mesh is generated by connecting the mid-side nodes of each parent finite element triangle, thus obtaining four child triangular *fv*-sub-cells. Then, the general constitutive model considered in this work can be recast under the finite volume implementation in terms of flux and source terms as follows,

$$\frac{\partial \boldsymbol{\tau}_p}{\partial t} = \boldsymbol{R} + \boldsymbol{Q} \,. \tag{4.31}$$

Here, the flux term is represented by,

$$\boldsymbol{R} = \boldsymbol{u} \cdot \nabla \boldsymbol{\tau}_p \,, \tag{4.32a}$$

whilst the source term is given by,

$$\boldsymbol{Q} = \frac{2(1-\beta)}{We}\boldsymbol{D} - \frac{\boldsymbol{\tau}_p}{We} + \left[\left(\nabla \boldsymbol{u} \right)^T \cdot \boldsymbol{\tau}_p + \boldsymbol{\tau}_p \cdot \nabla \boldsymbol{u} \right]. \tag{4.32b}$$

Then eq.(4.31) may be integrated over suitable control volumes as,

$$\int_{\Omega_l} \frac{\partial \boldsymbol{\tau}_p}{\partial t} d\Omega = -\int_{\Omega_l} \boldsymbol{R} d\Omega + \int_{\Omega_l} \boldsymbol{Q} d\Omega \,. \tag{4.33}$$

These residuals are evaluated over each *fv* triangle Ω_l and are allocated proportionally by the selected cell-vertex distribution (upwinding) scheme to its three vertices. The nodal update is obtained by summing all contributions control volume Ω_l, composed of all *fv*-triangles surrounding the node l. In addition, these flux and source residuals may be evaluated over two separate control volumes associated with the node l within the *fv*-cell T (see Fig. 4.1b). These come from *(a)* an upwinded contribution that is governed over the *fv*-triangle *T*, ($\boldsymbol{R}_T$,$\boldsymbol{Q}_T$); and/or *(b)* an area-averaged contribution, subtended over the median dual cell (MDC) zone, $\left(\boldsymbol{R}^l_{MDC}, \boldsymbol{Q}^l_{MDC} \right)$. In this manner, a generalised fv-nodal update equation has been derived per stress component (Webster et al. 2005), by separate treatment of individual time derivative, flux and source terms, and integration over associated control volumes. Such steps yield,

$$\left[\sum_{\forall T_l}\delta_T\alpha_l^T\Omega_T+\sum_{\forall MDC_l}\left(1-\delta_T\right)\widehat{\Omega}_l^T\right]\frac{\Delta\boldsymbol{\tau}_l^{n+1}}{\Delta t}=\sum_{\forall T_l}\delta_T\alpha_l^T\boldsymbol{b}^T+\sum_{\forall MDC_l}\left(1-\delta_T\right)\boldsymbol{b}_l^{MDC},$$

where $\boldsymbol{b}^T=\left(-\boldsymbol{R}_T+\boldsymbol{Q}_T\right)$, $\boldsymbol{b}_l^{MDC}=\left(-\boldsymbol{R}_{MDC}+\boldsymbol{Q}_{MDC}\right)^l$, Ω_T is the area of the *fv*-triangle *T*, and $\widehat{\Omega}_l^T$ is the area of its median dual cell (MDC). The weighting parameter, $0\le\delta_T\le1$, ensures consistency and controls the balance taken between contributions from the median-dual-cell and the *fv*-triangle *T*.

Overall summary

The algorithm employed to solve the problem stated in eqs.(2.12)-(2.13), (2.27)-(2.28) and (4.10) is given in the general framework of the time-marching hybrid *fe/fv* scheme employed here involves two distinct aspects. First, velocity and pressure are computed via a semi-implicit incremental pressure-correction (*ipc)* procedure with *finite element* spatial discretisation. Secondly, a *finite volume* based fluctuation distribution scheme is adopted for the computation of the hyperbolic extra-stress equations. The algorithm consists of a two-step Lax-Wendroff time-stepping procedure, extracted via a semi-implicit Taylor series expansion in time. The incremental pressure-correction signature is apparent through the three time-level pressure-reference. This ensures that temporal error bounds are uniformly met, to an order one higher than under direct *pc*-implementation, hence of O(Δt^2) [43].

Here, first velocity and stress components are predicted to a half time-step (Step 1a), and then, corrected over the full time-step (Step 1b, Lax-Wendroff, split time-step, prediction-correction). To ensure the satisfaction of the incompressibility constraint, pressure at the forward time-step is derived from a Poisson equation for pressure-difference (Step 2). The solenoidal end-of-time-step velocity field is constructed at a final stage (Step 3). To attain second-order time accuracy, the free weighting parameter (θ), governing Step 2 and 3 across the time-step, is selected as the Crank-Nicolson option, ($\theta=0.5$). Defining initial time-step (t^n) solution components $(\boldsymbol{u}, p, \boldsymbol{\tau}_p)^n$, the semi-discrete three-stage algorithmic structure per time-step may be expressed as in eqs.(4.23)-(4.30).

CHAPTER 5

A new constitutive model for worm-like micellar systems - Numerical simulation of confined contraction-expansion flows

This chapter is concerned with the modelling of worm-like micellar systems, employing a new micellar thixotropic constitutive model with viscoelasticity within network-structure construction-destruction kinetics. The work focuses on steady-state solutions for axisymmetric, rounded-corner, 4:1:4 contraction-expansion flows. This has importance in industrial and healthcare applications such as in enhanced oil-reservoir recovery. Material functions for the micellar models (*time-dependent, thixotropic*) have been fitted to match two different extensional configurations of the exponential Phan-Thien/Tanner (PTT) model (rubber *network-based, non-thixotropic*). This covers mild and strong-hardening response, and re solvent fraction, highly-polymeric (β=1/9) and solvent-dominated (β=0.9) fluids. Solution results are described through normalised Excess Pressure Drop (EPD), vortex intensity and stream function, stress (N_1 & N_2), and *f*-functional data. EPD predictions with the new micellar models prove to be consistent (at low rates, some rising) with Newtonian results, contrary to the base-reference modified Bautista-Manero (MBM) results. Markedly different vortex intensity trends are found in comparing micellar and EPTT solutions, which correspond with N_2-N_1 and *f* data. In order to address the highly-elastic regime for thixotropic materials, a convoluted approach between EPTT and micellar models has been proposed. Here, numerically stable solutions are reported for impressively large *We* up to 300 and new vortex structures are revealed.

5.1. Introduction

This work is devoted to solve numerically the benchmark 4:1:4 rounded contraction/expansion flow of worm-like micellar systems using the Bautista-Manero constitutive approach (Bautista et al. 1999; Manero et al. 2002; García-Sandoval et al. 2012). Herein, a new approach is proposed that intimately introduces the viscoelasticity into the structure construction/destruction mechanism of worm-like micellar solutions. These non-Newtonian viscoelastic liquids present interactions of viscosity, elasticity, and breakdown and formation of internal structure. This spurns highly complex rheological phenomena, and manifests features associated with thixotropy, pseudo plasticity and shear-banding (Bautista et al. 1999; Olmsted 2008). The versatility and complex rheological behaviour of viscoelastic wormlike micellar solutions render them an ideal candidate for varied applications. In viscoelastic surfactant form, they have been termed 'Smart Fluids', due to their ability to self-select their rheological properties to appropriately fit to change in alternative deformation environments. Processing and modern-day applications of such material systems range amongst additives in house-hold products (hard surface cleaners and drain-opener liquid plumber), paints, cosmetics, health care products (nutrient-carriers in shampoo and body wash), and under specific application fluid design such as with drag reducing agents in heating and cooling systems and drilling fluids in enhanced oil-reservoir recovery (EOR) (Yang 2002).

Significantly in modern EOR processes, which consist of hydraulic stimulation of oil wells to increase productivity, these fluid systems have become highly important given their adaptability in rheological characteristics (Yang 2002). Fracturing fluids are required in this operation, with the capability of transforming their rheological properties according to the prevailing flow conditions encountered. This involves transitions from low viscosity Newtonian fluids, when pumped into the oil-wells to fracture the rock-pores; passing through to gel-like form, with highly viscoelastic characteristics, capable of transporting proppants to keep fractures open and enhance rock-pores permeability in the oil-well; to finally, reverting into low viscosity fluids which degrade easily and unblock the fractures as the prerequisite pressure levels are realised. Wormlike micellar solution systems fulfil these requirements, being constituted of mixtures of surfactants – typically cetyltrimethylamonium bromide (CTAB) or cetylpyridinium chloride (CPyCl) (Miller and Rothstein 2007) - and salts –sodium salicylate (NaSal) - in water. These mixtures arrange themselves into physically bonded units and change their network-

structure characteristics with temperature, surfactant and salt concentration (Moss and Rothstein 2010); but also with the forces and deformations they experience. The wormlike micelles are elongated surfactant groups that, under suitable conditions, can entangle and impart viscoelasticity to the fluid. Their behaviour is highly complex, although similar to that observed for polymer solutions and melts; hence their naming "living polymers" (Moss and Rothstein 2010). Unlike the covalently bonded polymer backbone, these micelles lie in thermodynamic equilibrium with the solvent and continuously break and reform under Brownian fluctuations. Therefore, additionally to reptation, wormlike micelles provide a mechanism for stress relief and entanglement elimination, creating and destroying temporary branch points, known as "ghost-like crossing" (Moss and Rothstein 2010).

Furthermore, wormlike micelles are particularly viable for industrial application, since a) fewer additives than for polymer-based fracturing fluids are required in their production, which render them a cheaper option (Yang 2002); b) in EOR, chemical-breakers are unnecessary, since after contact with crude oil, wormlike micelles systems rearrange into small spherical micelles (c. a. 10-50 nm). These are simpler and smaller physical arrangements, which finally form a low viscosity microemulsion. Additionally, c) wormlike micelles are more environmentally friendly and more easily biodegradable than polymer-based fracturing fluids (Yang 2002).

Many approaches have been pursued to model wormlike micelles flow behaviour. Bautista et al. (Bautista et al. 1999, 2000; Manero et al. 2002) proposed a rheological modelling approach for wormlike micelle solutions, the Bautista-Manero-Puig (BMP) model. This equation of state consists of the upper-convected Maxwell constitutive equation to describe stress evolution, coupled to a kinetic equation that takes into account structural changes induced by the flow, based on the rate of energy dissipation. This theory has demonstrated accuracy in the description of shear-banding (Bautista et al. 2000, 2007; García-Sandoval et al. 2012), pulsating flows of wormlike micelle solutions (Herrera et al. 2010), characterisation of associative polymers (Caram et al. 2006), and for evaluating the negative wake flow past a sphere (Mendoza-Fuentes et al. 2009) and drag correction (Mendoza-Fuentes et al. 2010). Some years later, Boek et al. (2005) corrected the BMP model, given its unbounded extensional viscosity in simple uniaxial extensional flow - thus producing the Modified Bautista-Manero (MBM) model. This has been utilised to model the transient flow of wormlike micellar solutions in planar 4:1 contraction flow setting (Tamaddon-Jahromi et al. 2011), being a forerunner in wormlike micellar simulations for

complex flows, along with others based on the principles of mesoscopic Brownian dynamics (Stukan et al. 2008). The VCM model, based on a discrete version of the 'living polymer theory' of Cates, has been tested in simple flows, where rheological homogeneity prevails (Vazquez et al. 2007; Cromer et al. 2011), and under conditions of shear-banding (Zhou et al. 2010). Another approach, consists of using the Johnson-Segalman model, modified with a diffusion term for the extra/polymeric stress (so-called d-JS model [Olmsted et al. 2000; Fielding and Olmsted 2003; Radulescu 1999]). This model has been tested against experimental data in simple shear flows and shear-banding conditions. The Giesekus model has also been used in the representation of wormlike micelles under simple shear scenarios, whilst using the nonlinear anisotropy coupling parameter to introduce shear-banding conditions (Libertatore et al. 2009; Gurnon et al. 2012; Thereja et al. 2011; Helgeson et al. 2009; Fisher et al. 1997). For this purpose, the appropriate Giesekus model parameters, for both banding and non-banding conditions, have been determined through Large Amplitude Oscillatory Shear (LAOS) (Gurnon et al. 2012) experiments in a coaxial-cylinder Couette geometry (Libertatore et al. 2009). In addition, whilst using parallel plate geometries, and adjusting temperature, salt concentration and shear rate, shear-banding and non-banding conditions have been studied by Rheo-small-angle 1ight scattering (Rheo-SALS) (Thereja et al. 2011), and flow-small angle neutron scattering (flow-SANS) (Helgeson et al. 2009). In this respect, findings reveal shear-induced separation into an isotropic low-shear band and another flow-aligned nematic high-shear band.

The surfactant:salt concentration of these fluid-systems dictates their nature and rheological response, providing a classification into three (or more) basic types. As such, the so-called 'salt curve' provides the dependency of the zero-shear viscosity η_{p0} on the surfactant:salt concentration. Studies on the composition of wormlike micellar solutions and their rheological implications (Rehage and Hoffmann 1991; Parker and Fieber 2013; Dreiss 2007), provide evidence that these solutions (i) have η_{p0} close to the Newtonian solvent *at low salt concentration*; this range is characterised by *spherical micelles*. (ii) When the salt concentration is increased to *moderate/semi-dilute levels*, the solution demonstrates a dramatic increase in its zero-shear viscosity, reaching η_{p0} peaks as large as six times the solvent zero-shear viscosity (Parker and Fieber 2013; Dreiss 2007); this range manifests the formation-growth *of wormlike structures* and beginnings of their *entanglement*, causing shear-thinning and normal stresses in shear (Dreiss 2007). (iii) *Further increase of the salt concentration* generates *longer wormlike*

micelles, which form an entangled network (Dreiss 2007). This is reflected in a steep decline in η_{p0} given by the proliferation of stress-relaxation points at the entanglement junctions (Parker and Fieber 2013). The work presented in this manuscript is based around the Bautista-Manero approach (Bautista et al. 1999, 2000; Manero et al. 2002; Boek et al 2005), and aims to represent wormlike micellar systems in the second-third type-stage, with significant pseudoplastic and elastic characteristics. This theory originated to represent semi-dilute concentrations of micellar solutions in water, composed of erucyl bis-(hydroxyehtyl)methylammonium chloride (EHAC) as surfactant, and sodium salicylate (NaSal) as counterion (Raghavan and Kaler 2001). In addition, such theory has proven effective more broadly to describe other micellar systems, such as cetylpyridinium chloride–sodium salicylate (CPCl) as surfactant, and brine as counterion; and cetyltrimethylammonium tosylate (CTAT), dodecyltrimethylammonium bromide (DTAB), Pluronics P103 as surfactants, with NaSal as counterion (Bautista et al. 2012).

Taking the experience gained in our prior work on modelling of wormlike micellar solutions (Tamaddon-Jahromi et al. 2011), we subsequently deploy a new micellar approach, driven by phenomenological observation (EPD attainment) in the axisymmetric rounded-corner 4:1:4 contraction/expansion domain, for which there is a dearth of comparable work available - micellar fluid solutions in complex flows. This study also sheds light on some other key related topics – that is limiting *We* (We_{lim}) and vortex dynamics – all absent in simple viscometric flows (Tamaddon-Jahromi et al. 2011; Stukan et al. 2008). We proceed to demonstrate that this new constitutive approach provides: (i) consistent EPD values at low *We* regimes - vital for oil-well rock-bed permeability estimation in EOR; (ii) larger We_{lim} in numerical solution reached through the explicit presence of the elasticity (*We*) in the structure equation; and (iii) attainment of rising EPD trends at high elasticity levels.

5.2. Governing equations, constitutive modelling and fluids considered

The governing equations and constitutive equations considered in this chapter have been detailed in chapter 2. The non-dimensional continuity and momentum conservation principles are expressed in eqs.(2.11)-(2.12), whilst the stress equations is given in (2.27)-(2.28). The specific time-dependent thixotropic micellar or time independent network-based nature is specified by the f_τ-functional. For the micellar framework eqs.{(2.33), (2.34), (2.35)} provide the {MBM, NM_τ_p, NM_T} representations. In contrast, the network-based Exponential PTT model is

represented in eq.(2.38). The hybrid approached proposed in this work, derived from the convolution of EPTT and {MBM, NM_τ_p, NM_T} is represented by eqs.{(2.44), (2.45), (2.46)}. Material function comparison for these models is provided in chapter 3, in Fig. 3.1-3.2.

5.3. Problem specification - The 4:1:4 rounded corner contraction/expansion flow

The schematic representation of the 4:1:4 axisymmetric, rounded-corner contraction/expansion flow problem with its corresponding zoomed mesh are shown in Fig. 5.1a and 5.1b, respectively. Mesh data are tabulated in Table 5.1. See Aguayo et al. (2008) for further detail on this problem, which provides a full mesh refinement analysis for some typical case studies.

Table 5.1 Mesh characteristics

Mesh characteristics	Elements	Nodes	Degrees of freedom ($\boldsymbol{u}$, p, $\boldsymbol{\tau}_p$)	R_{min}
Coarse	1080	2289	14339	0.0099
Medium	1672	3519	22038	0.0074
Refined	2112	4439	27798	0.0058

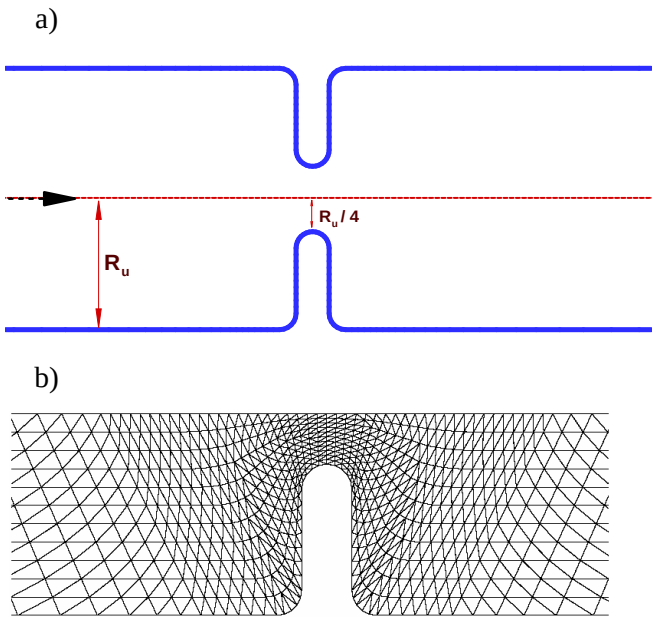

Figure 5.1 a) Schematic diagram, b) zoomed mesh sections 4:1:4 contraction/expansion

5.4. Results and discussion

Discussion around the rising *We*-results solutions is based on findings under EPD, limiting *We* (We_{lim}), vortex dynamics, stress fields contours, and *f*-functional fields, considered against variation in rising *We*.

5.4.1. Excess pressure drop

5.4.1.1. Low solvent fraction conditions (β=1/9)

The first point to highlight is the preservation of consistency in EPD in the Stokesian limit for the new versions of micellar models developed. In this limit of small deformation rates or vanishing elasticity, all fluids behave as the ideal universal fluid, for which non-linear characteristics vanish, and EPD (pressure drop measure relative to the equivalent Newtonian fluid) tends to the Stokes-Newtonian reference level of unity. Nevertheless, it is apparent from Fig. 5.2a that MBM EPD is inconsistent, providing *We*→0 limiting EPD values ~30% below the Stokes-Newtonian reference level. In contrast, EPTT models generate consistent EPD trends in the low elasticity asymptotic limit. With rising *We away from zero*, EPD-predictions generally tend to decrease and fall away from the Stokes-Newtonian reference EPD level (of unity); and this is upheld in MBM and EPTT solutions.

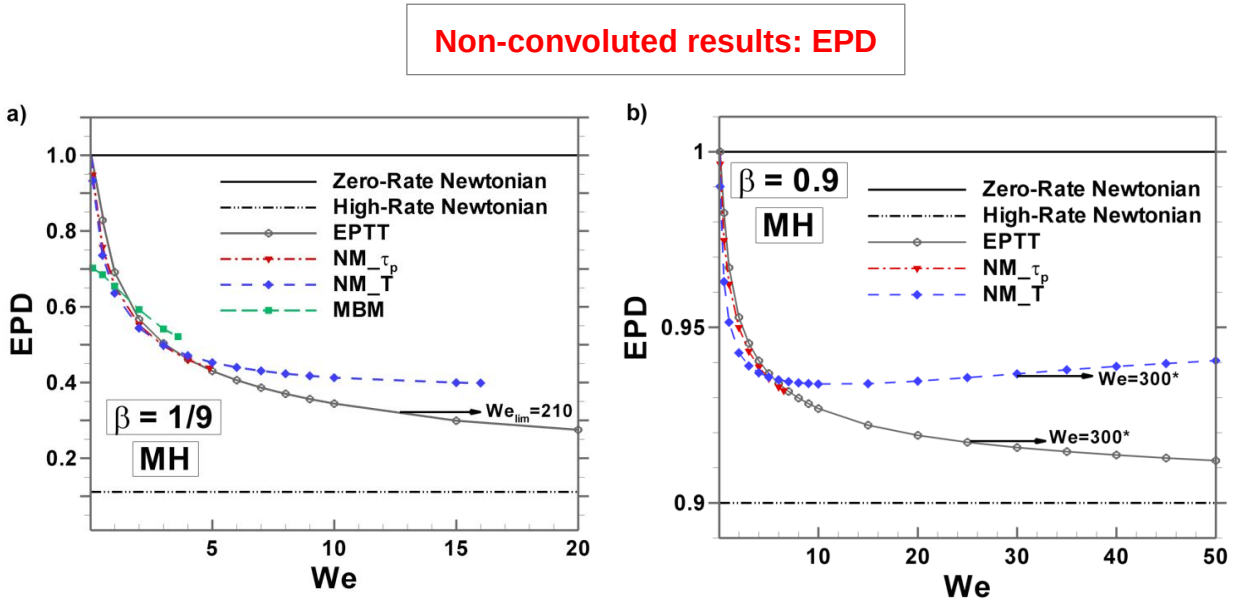

Figure 5.2 EPD versus *We*; MBM, EPTT, NM_τ_p and NM_T models; a) highly-polymeric (β=1/9) b) solvent-dominated (β=0.9) fluids; MH (EPTT ε=0.25; Micellar ω=4.0) response

As described in Chapter 2, here new versions of micellar models are developed to address the MBM-shortcoming in EPD when $We \rightarrow 0$, which incorporate the viscoelasticity in the structure-destruction term, with explicit dependency on the *We*-factor [see Eq. (2.33) and (2.34), Fig. 5.2a]. Conspicuously then, and in contrast to the MBM-results, both micellar approaches (NM_τ_p and NM_T) do not exhibit underprediction in EPD in the low *We*–range. NM_τ_p solutions provide EPD values tightly matching in trend to EPTT predictions. Subsequently, upon rise in *We* there is: (i) a slight deviation to lower EPD from EPTT data in the $0<We<3$ range; (ii) NM_τ_p data attains critical solutions to $We_{lim}=4.9$ (Table 5.2), where both NM_τ_p and EPTT curves intersect. In contrast when considering NM_T against EPTT solutions, some new EPD trends are gathered as *We* rises: (i) there is less degradation observed in EPD with NM_T than with EPTT, from the reference-line and in the low elasticity range ($0<We<3.5$); (ii) intersection between their respective EPD-curves occurs at a lower elasticity level ($We \sim 3.5$), taken relative to the NM_τ_p comparison. From $We \geq 3.5$ onwards, both NM_T and EPTT data-curves decline, but the loss of slope in EPD is more rapid with NM_T than EPTT as *We* rises; thus predicting ultimately larger EPD with NM_T for higher *We* up to $We_{lim}=16$. These differences in EPD and We_{lim} attainments with new micellar versions (_τ_p and _T) can be explained by appealing to their respective material functions (Fig. 3.1), and analysing the competing influences of extensional viscosity (strain-hardening) and normal stress difference on EPD (Walters et al. 2009). Whilst the NM_τ_p data-curve provides a plateau in N_1 for high *We* (Fig. 3.1), following the MBM results; the NM_T data-curve reveals a maximum in N_1 at moderate elasticity levels ($We \sim 5$), followed by a sharp decline over the extended range, $5<We<100$. This major disparity, firstly, generates lower stresses under NM_T compared with NM_τ_p solutions; consequently, yielding higher We_{lim} with NM_T than NM_τ_p. Secondly, as the competing roles between extensional viscosity (η_E) and N_1 in EPD predictions dictate (Walters et al. 2009) – rise in the former (strain-hardening) elevates EPD whilst it is weakening in N_1 (from quadratic form) that reinforces EPD. Therefore, the declining-N_1 of NM_T stimulates larger EPD than under EPTT-solutions, acknowledging that EPTT provides monotonically rising viscometric N_1 (itself with decay away from quadratic response). All comments apply equally under both strong and moderate-hardening settings, with exaggeration to higher η_E and N_1-maxima under the strong-setting.

In Fig. 5.3a, EPD predictions with convoluted models are reported, with restriction to MH-response and highly-polymeric ($\beta=1/9$) fluids, and compared to those for base-EPTT and NM_T

forms. Here, convoluted EPD data-curves principally inherit their parent-EPTT trends. Contrastingly, the NM_T solutions begin to show marginally larger EPD predictions, with respect to convoluted results, upon approaching the early We_{lim}=16 of NM_T. Notably, at high deformation rates, EPD predictions for the convoluted models are larger than the corresponding second-Newtonian EPD-plateau reference level indicated, and asymptote to a limiting plateau above that, accordingly.

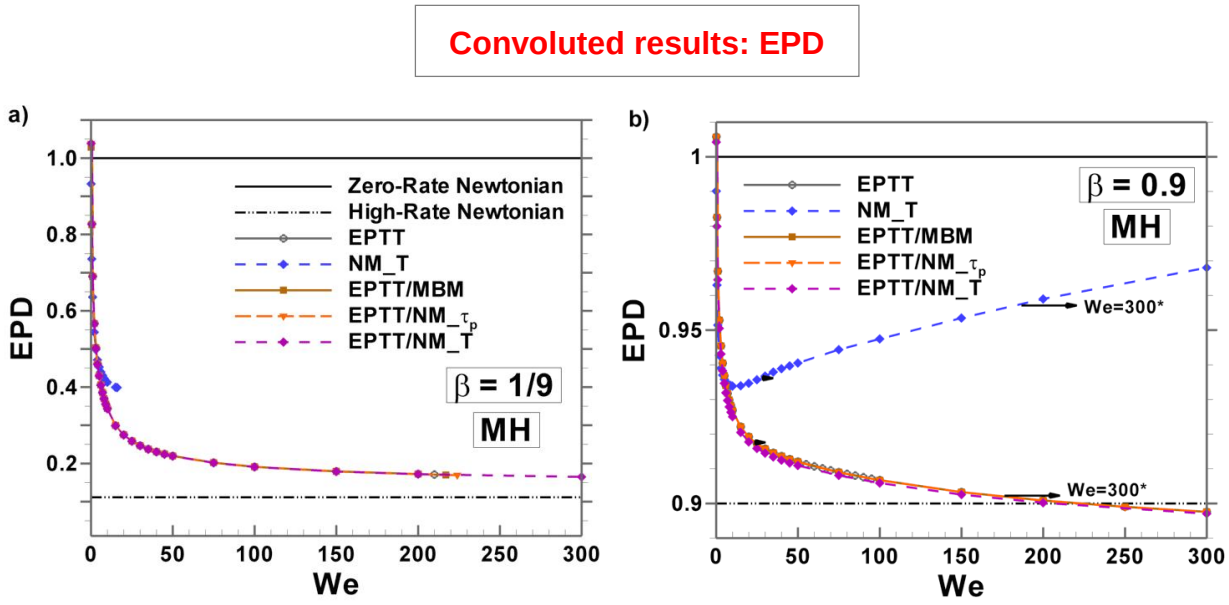

Figure 5.3 EPD versus *We*; EPTT, NM_T and convoluted models; a) highly-polymeric (β=1/9), b) solvent-dominated (β=0.9) fluids; MH (EPTT ε=0.25; Micellar ω=4.0) response

Table 5.2. Limiting *We*; highly-polymeric (β=1/9), solvent-dominated fluids (β=0.9)

	β=1/9		β=0.9	
Model	MH	SH	MH	SH
EPTT	210.0	3.6	300.0*	4.6
MBM	3.6	1.8	4.1	2.2
NM_τ_p	4.9	2.1	7.6	2.4
NM_T	16	2.2	300*	30.0
EPTT/MBM	217	-	300*	-
EPTT/NM_τ_p	224	-	300*	-
EPTT/NM_T	300*	-	300*	-

*Stable Solution

5.4.1.2. High-solvent fraction conditions (β=0.9)

In the high-solvent fraction scenario, with only mild strain-hardening properties and Newtonian-like response, NM_T solutions are observed to provide ultimately rising EPD trends with increasing elasticity (Fig. 5.2b). In contrast, NM_τ_p and EPTT solutions manifest only monotonic EPD-decline whilst traversing towards their We_{lim}. Similarly to the highly-polymeric scenario above, NM_τ_p solutions faithfully follow those of EPTT, locating their We_{lim} (=7.6) sooner than occurs with NM_T solutions, remaining numerically-stable at *We*=300+ (Table 5.2). The reason for this discrepancy in We_{lim}, again as argued above with β=1/9 fraction, lies in the base-N_1 material function response: recall, NM_T shows declining N_1 with rising *We*. This has the consequent effect of exhibiting a wider tractable window of numerical solution for NM_T, and favours the ultimate and opposite rising trend in EPD. This is the situation encountered beyond the local EPD-minima reached for NM_T at *We*=8.

Under this high-solvent fraction, the convoluted data-curves again all follow those of parent-EPTT, and actually intersect with the second-Newtonian EPD-plateau reference line at high *We* levels, *We*~220 (Fig. 5.3b). This latter observation contrasts with the distinctly different and remarkable NM_T model predictions (partially shown in Fig. 5.2b), which further pursue rising EPD trends with increasing elasticity levels (without encountering a limit).

5.4.2. Vortex dynamics

This section describes the various dynamic vortex structures developed in the flow, alongside their growth and decay patterns, through comparison across thixotropic and non-thixotropic models and their solutions at increasing levels of elasticity up to critical limits.

5.4.2.1. Vortex dynamics - low solvent fraction conditions (β=1/9)

Here, a comparison on vortex intensity, size and streamlines patterns is performed as *We* is increased. To facilitate direct comparison, both upstream and downstream vortex intensities are plotted in Fig. 5.4 as a function of *We*.

Non-convoluted solutions, vortex intensity. Upstream vortex activity: MBM, NM_τ_p and NM_T data for the upstream vortex follow each other closely in a rising vortex intensity pattern with increasing *We,* up to their We_{lim} (Fig. 5.4a). NM_T solutions attain the largest We_{lim} (=16)

amongst these micellar models, with indications of approach to an upper limiting plateau. Up to its first turning point at We=2 (local maximum), EPTT results exhibit a similar trend to that of the thixotropic micellar solutions. Beyond which for We>2, the EPTT data-curve indicates departure, initially through a decline to a second extremum at We=100 (local minimum), prior to upturn and ultimate rise towards its final We_{lim}=210 (Table 5.2) (Aboubacar et al. 2002).

Non-convoluted solutions, downstream vortex activity: Downstream vortex activity mirrors, in reverse form, the changes in upstream vortex activity (Fig. 5.4b), somewhat acting as an energy balance and release mechanism. So here, thixotropic MBM, NM_τ_p and NM_T data-curves also follow each other closely in a declining trend up to We=2. After this stage, NM_τ_p downstream vortex intensity declines suddenly and more rapidly than apparent with MBM or NM_T, noting that MBM is nearing its limit in this region at We_{lim}=3.6, followed by NM_τ_p with We_{lim}=4.9. The NM_T curve continues in its decline up to We=7, where it observes a local-minimum. Beyond We>7, NM_T downstream vortex intensity then rises up to its corresponding We_{lim}=16. Interestingly, the occurrence of this local minimum-extremum in the NM_T downstream vortex intensity response, roughly coincides in elasticity level (We=7) with extrema observed in viscometric-N_1 for this model (We~5) (Fig. 3.1). In contrast to micellar data, non-thixotropic EPTT results also exhibit a declining trend, but at slightly lower rate (hence, greater intensity), at relatively low elasticity levels (0.5<We<5). At We=5, the EPTT data-curve also locates a minimum, beyond which for 7<We<15, the curve rises to a local-maximum at We=15. After this second extremum, the trend is repeated of a subsequent decline, to find a third extremum (minimum) at 40<We<50. Finally and thereafter, the EPTT-curve rises up to its corresponding We_{lim}=210.

Significant difference is apparent in We_{lim} between EPTT and MBM-solutions under MH: with We_{lim}=O(10^2) for EPTT, and We_{lim}=O(10) for micellar data (Table 5.2). One may argue that this is due to the explicit presence of λ_1 (or We, in dimensionless terms) in the f-functional under the EPTT construction. This discrepancy is starkly evidenced in MH instances, and through the comparison between the We_{lim} for MBM and the new micellar model data, where the presence of λ_1 increases We_{lim} by one unit for NM_τ_p, and increases eight times under NM_T (Table 5.2). This observation is not so evident under the SH scenario, yet still present, since We_{lim} is relatively small for the high extensional viscosity levels these fluid models can display.

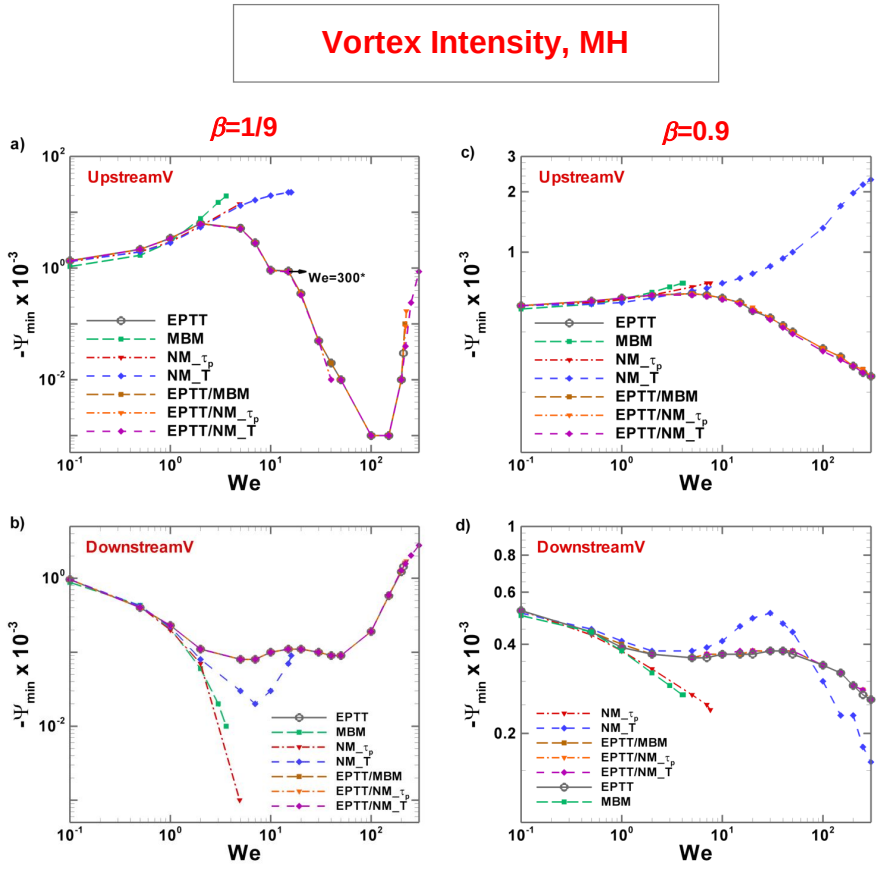

Figure 5.4 Vortex intensity profiles versus *We*: top-upstream, bottom-downstream; EPTT, MBM, NM_τ_p, NM_T and convoluted models; MH (EPTT ε=0.25; Micellar ω=4.0) response; highly-polymeric (β=1/9), solvent-dominated (β=0.9) fluids

Convoluted solutions, vortex intensity: The flow patterns displayed by the convoluted micellar solutions are markedly different to their non-convoluted counterparts; specifically, they inherit the behavioural response of the parent-EPTT non-thixotropic predictions. On ***upstream vortex*** intensity (Fig. 5.4a), it is worth highlighting that (i) the convoluted data-curves follow closely over 0.1<*We*<300 range; and (ii) after *We*=200 and for stable EPTT/NM_T solutions, the upstream vortex reappears and monotonically grows in strength up to the corresponding We_{lim}, or *We*=300+.

Convoluted solutions, downstream vortex intensity: In Fig. 5.4b, a more complex trend is extracted and relative to EPTT-solutions. Here, (i) the convoluted data-curves follow the trends for EPTT and lie between those the non-convoluted micellar data-curves; (ii) data-curves for convoluted solutions observe a local-minimum at *We*=7, beyond which for 7<*We*<15, they rise to a local-maximum at *We*=15. After this second extrema, the trend is one of subsequent

decline again to find a third extrema (minimum) at 40<*We*<50. Finally, for *We*>50, convoluted solutions show a monotonic rising trend up to their respective We_{lim}, with impressively high-*We* solutions generated for {EPTT/NM_τ_p, EPTT/MBM, EPTT/NM_T} with We_{lim}={217, 224, 300+} (Table 5.2). Comparatively, EPTT limitation is We_{lim}=210, and with MBM is We_{lim}=3.6, under the same solvent fraction (β=1/9) and MH conditions. This trend also holds for the other convoluted results.

Streamline patterns, non-convoluted: The streamline patterns of Fig. 5.5, provide the counterpart field-structure representation to Fig. 5.4 above, in which the columns relate to variation across models, whilst the rows refer to levels of elasticity (terminating in We_{lim}). Results for *non-convoluted* forms are shown in Fig. 5.5. At low *We*-levels, *We*~O(0.1), little difference is apparent in vortex size across models. Here, upstream and downstream vortex structures are symmetrical about the contraction. At *We*=1.0, for which the elastic and dissipative forces are balanced, asymmetry is observed in all solutions, with slight differences in vortex sizes noted. These are clearly exposed in the vortex intensity data of Fig. 5.4 with increasing elasticity: whilst the upstream vortex displays vortex enhancement, the downstream vortex displays vortex reduction. Reaching the stage *We*=2, where elastic effects are more dominant, this pattern of upstream growth/downstream shrinkage remains, and is reflected consistently in vortex size/shape across all solutions. MBM (We_{lim}=3.6) results are the first to exhibit numerical breakdown. For higher elasticity levels, NM_τ_p (at *We*=4.9) and NM_T (at *We*=5.0) streamlines reflect upstream vortex growth, whilst EPTT results show shrinkage – notwithstanding the relatively even larger shear and extensional viscosities with EPTT (see N_1 and N_2 below for justification; nb. in contrast [Aboubacar et al. 2002]). NM_τ_p results are the next in the sequence to show divergence (We_{lim}=4.9), with an almost vanishing downstream vortex at this stage. Increasing elasticity to *We*=10, the trends in vortex size evolution are well established. Consequently, NM_T (*We*=10) results provide an even larger upstream vortex with *We*<10, whilst comparably EPTT manifests vortex decay. The corresponding downstream vortex tends to disappear under NM_T, whilst that under EPTT prediction remains almost constant in size-shape as *We* rises. NM_T solutions locate their We_{lim}=16. Finally, EPTT solutions retain tractability up to We_{lim}=210; an impressively large level for stable numerical solutions.

Streamline patterns, convoluted: The streamlines in Fig. 5.6 for *convoluted* forms and data in Fig. 5.4 demonstrate that at *We*=200, convoluted solution-fields exhibit the formation of a

new upstream vortex (Fig. 5.6, inset). This grows and slightly shifts with *We*-rise, travelling towards the lip of the contraction wall. EPTT/NM_τ_p data at *We*=220 reveals this new upstream vortex growth, and a further vortex structure appears from the top wall; both these new features then subsequently tend to join up with further *We* rise. In EPTT/NM_T results at *We*=300, the upstream vortex appears completely formed, with comparable size to those at low elasticity levels (1<*We*<5), though now of one order of magnitude reduced in intensity. Meanwhile, as this complex upstream vortex activity is emerging, the downstream vortex shrinks over the 0.1<*We*<50 range, and afterwards with further *We* rise, consistently and continually grows and builds in intensity.

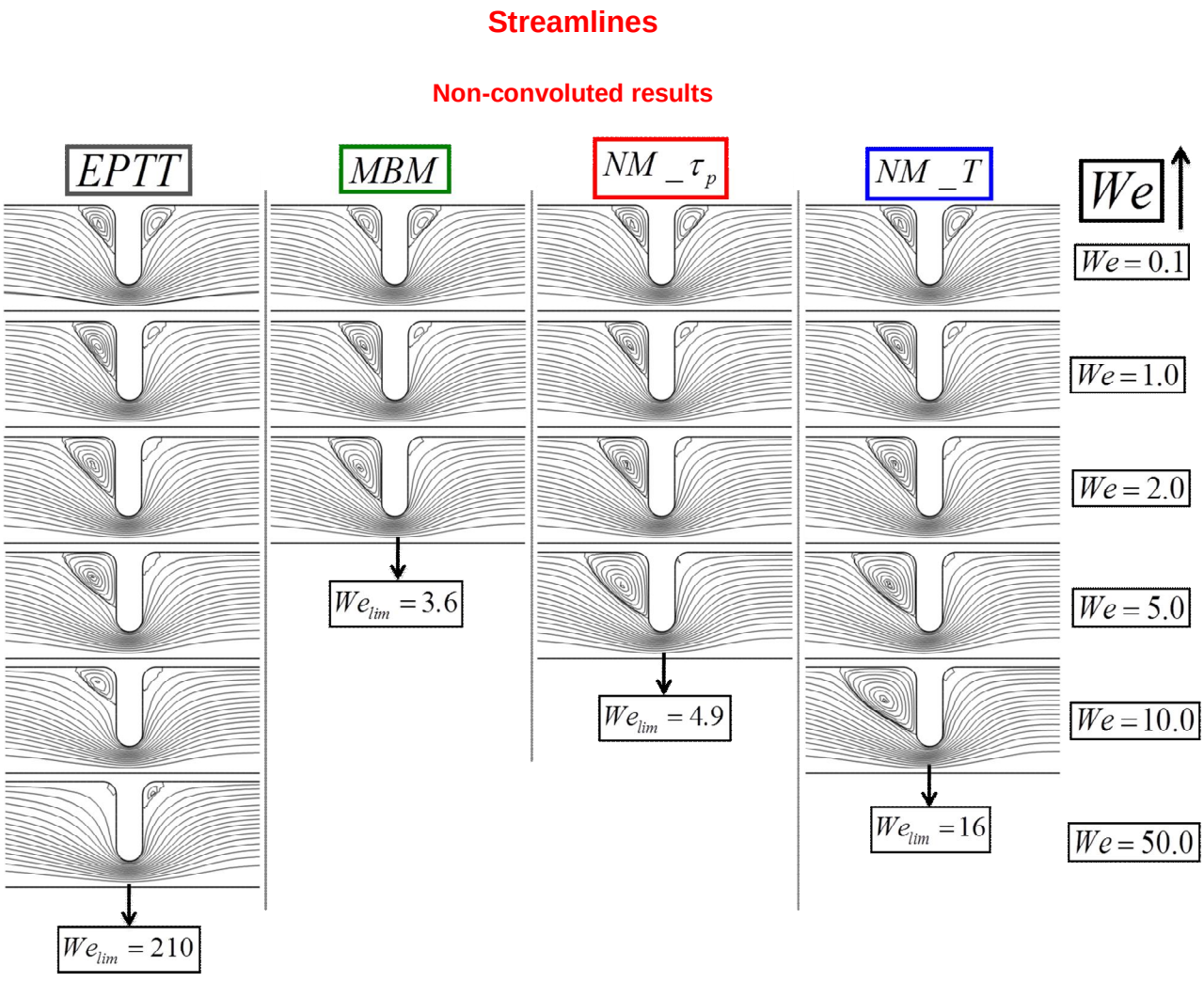

Figure 5.5 Streamlines versus *We*; EPTT, MBM, NM_τ_p, NM_T models; MH (EPTT ε=0.25; Micellar ω=4.0) response, highly-polymeric (β=1/9) fluids

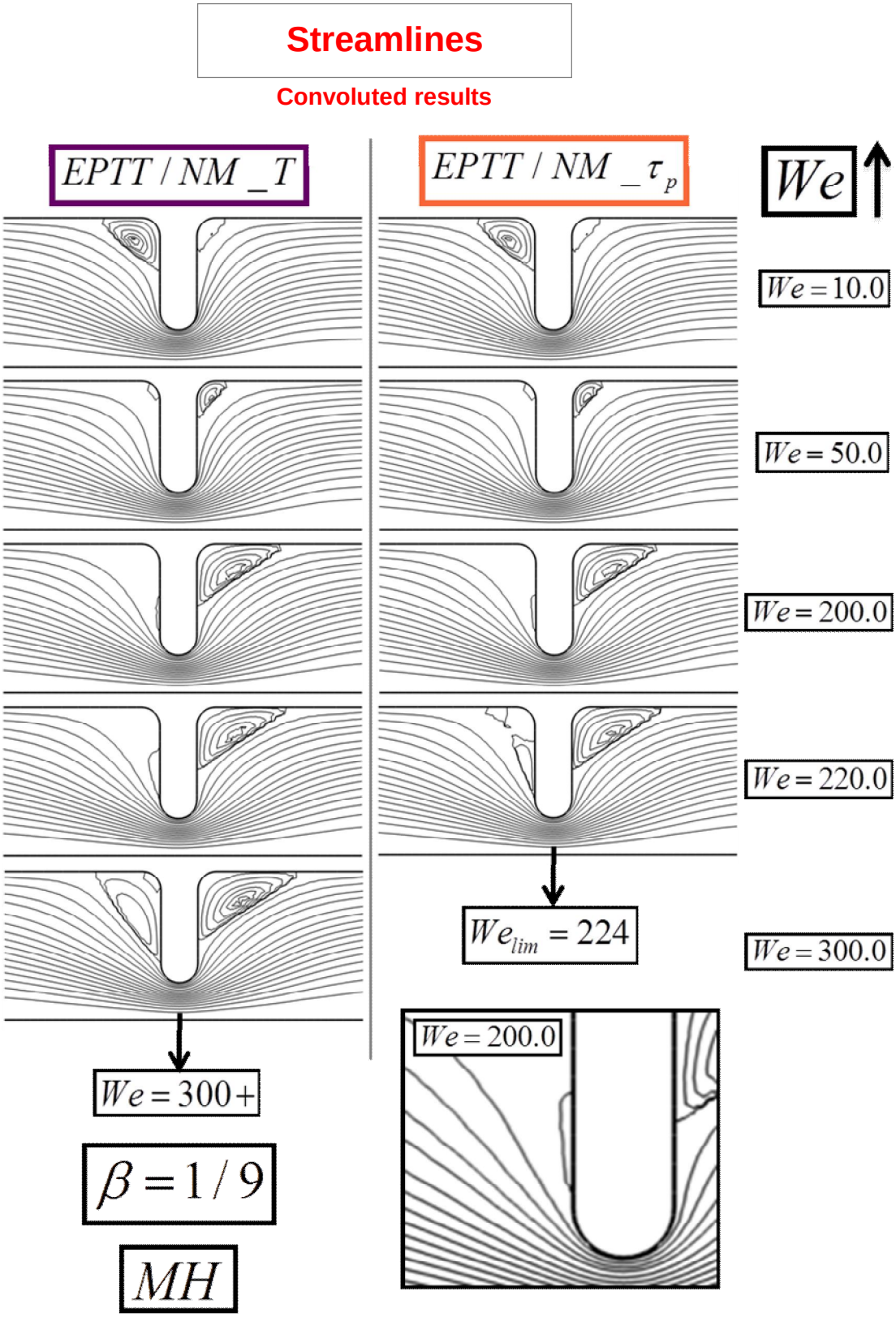

Figure 5.6 Streamlines versus *We*; EPTT/NM_τ_p, EPTT/NM_T models; MH (EPTT ε=0.25; Micellar ω=4.0) response, highly-polymeric (β=1/9) fluids

5.4.2.2. Vortex dynamics - high solvent fraction conditions (β=0.9); convoluted/non-convoluted results

***Vortex intensity, β=0.9*:** vortex intensity trends under solvent-dominated response (β=0.9) (Fig. 5.4c and d) are similar, but with smaller values, to the corresponding highly-polymeric data (β=1/9) (Fig. 5.4a and b). This applies in both *upstream and downstream* vortices.

The ***upstream vortex intensity*** results (Fig. 5.4c) exhibit smooth rise as *We* is increased at relatively low elasticity levels ($0.1<We<5$). Beyond $We>5$, EPTT and convoluted solutions depart in trend and decline as *We* increases, with stable solutions at {We=300+, We_{lim}=210} for {β=0.9, β=1/9}. In this zone, the convoluted curves decline smoothly, whilst EPTT data-curve once more encounters a minimum, but now at We=200. After this stage, EPTT suddenly rises up to We=250, where it locates another extremum (maximum), and declines sharply-rapidly thereafter. Contrastingly, again, the non-convoluted thixotropic data-curves illustrate a rising pattern with increasing We, up to their We_{lim}. Differently to β=1/9 results, the NM_T upstream data-curve now does not asymptote to a plateau. Here, at β=0.9, {MBM, NM_τ_p, NM_T} attain We_{lim}={4.1, 7.6, 300+}; in contrast at β=1/9, {MBM, NM_τ_p, NM_T} encounter We_{lim}={3.6, 4.9, 16}. Consistently, We_{lim} is notably extended under solvent-dominated predictions (β=0.9), specifically in contrast to the highly-polymeric (β=1/9) results above (Table 5.2 data). Recall, the non-linear polymeric part of the constitutive equation is present in smaller proportion, relative to the solvent contribution. Notably: (i) the NM_T extreme case predicts that We_{lim} is some nineteen times larger under β=0.9 than β=1/9; (ii) such major departure in We_{lim} is also apparent between EPTT and most non-convoluted micellar results; and (iii) the common trends observed behind these We_{lim} findings repeat consistently under SH response (Table 5.2).

On ***downstream vortex intensity*** Fig. 5.4d, a declining trend is observed at low elasticity levels ($0.1<We<2$). Beyond $We>2$, the following departure is observed: EPTT and convoluted results exhibit a local minimum at We=5, and rise to locate a plateau in $20<We<50$. Beyond $We>50$, an ultimate decline is apparent with the convoluted results, whereas EPTT evolves as with the upstream vortex data above. Notably, the thixotropic non-convoluted results generate some alternative trends: {MBM, NM_τ_p}-data-curves decline as elasticity is increased up to their We_{lim}={4.1, 7.6}. In contrast, the NM_T downstream vortex intensity pattern is more complex;

resembling the EPTT and convoluted solutions. The NM_T data-curve plateaus across 2<*We*<5 range; thereafter, this curve rises with increasing elasticity up to a peak of *We*=30. Subsequently after this local peak, for *We*>30, NM_T downstream vortex intensity ultimately declines, with stable solutions observed as far out as *We*=300+ and above.

5.4.3. *f*-functional and stress fields (N_1)

5.4.3.1. Low solvent fraction conditions (β=1/9)

In this section, results for *f*-functional and normal stress are considered. Firstly, correspondence between vortex activity (section 4.2) and normal stresses data (i. e. N_2) is outlined. Secondly, *f*-functional and N_1 results are described, in which close correlation is revealed through theoretical and numerical data. Markedly, an inverse relation between N_1 and *f* predictions is observed with the numerical solutions for contraction-expansion flow, similar to that obtained in simple viscometric shear. Fig. 5.7 provides ***shear viscometric f-functional data***, where all curves rise from the Oldroyd-B reference data as *We* is elevated. Consistently with their exponential nature, the response for EPTT and convoluted curves follow each other closely. Differently, (i) MBM-data yield smaller *f*-values in the $0.1<\dot{\gamma}<1.5$ range. For larger rates beyond $\dot{\gamma}>1.5$, MBM form provides larger *f*-values than arise for EPTT and its convoluted analogues. (ii) As *We* rises, only MBM response shows decline in the size of *f*-values at fixed shear-rate.

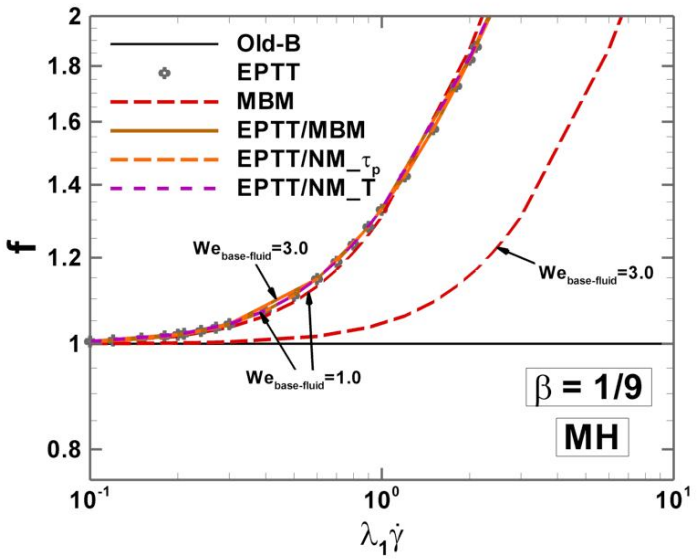

Figure 5.7 *f*-function profiles in simple shear versus *We*; MBM, EPTT and convoluted models; MH (EPTT ε=0.25; Micellar ω=4.0) response, highly-polymeric (β=1/9) fluids

N_2, N_1-vortex activity and relationship. Fig. 5.8 shows maximum N_1 and minimum N_2 in the *upstream vortex zone* across models as *We* is increased. Here, it is worth highlighting the correlation between N_2-minima and N_1-maxima observed in the upstream vortex region, alongside the location, size and intensity of the upstream vortices themselves. This provides concrete evidence as to the influence of elasticity in the flow kinematics. Solutions trends in N_1-maxima (Fig. 5.8a) and N_2-minima (Fig. 5.8b) correspond to those in Fig. 5.4a for maximum intensity in the upstream vortex. As above for vortex intensity, MBM, NM_τ_p and NM_T curves on N_1 and N_2 extrema in the upstream vortex, closely follow one another in a rising pattern with increasing *We* up to their We_{lim}. EPTT and convoluted results exhibit similar rising and further declining trends as *We* is elevated. Furthermore, N_2 results for convoluted versions (Fig. 5.8b) evidence larger values over $0.1<We<2$, and smaller values over $2<We<15$, in comparison to EPTT N_2-data. Beyond $We>15$, a sudden and steeper slope is noted in the convoluted solutions. The vortex-like structures in N_1 and N_2-fields, are absent for $We>20$ in the upstream zone, and disappear at low elastic levels in the downstream region. Hence, direct comparison with vortex patterns loses tractability beyond $We>20$. Fig. 5.9 contains the counterpart field-structure representation of Fig. 5.8, with the key results for EPTT and NM_T solutions. Particularly, N_2 plots render the most illustrative information (Tamaddon-Jahromi and Webster 2011), providing a signature for vortex development in the corner-region (Fig. 5.9b), whilst N_1 plots (Fig. 5.9a) only show its periphery through location and relative size.

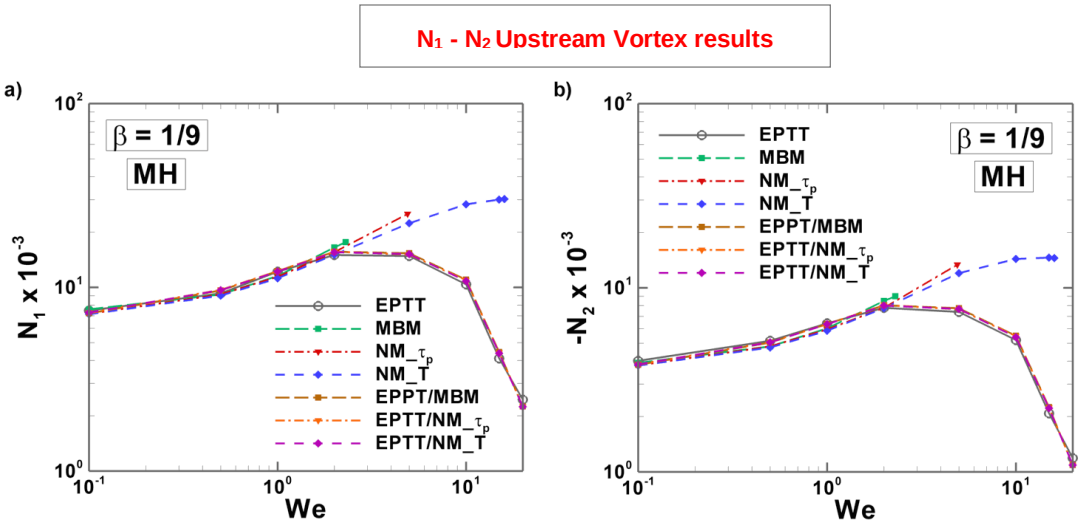

Figure 5.8 a) Maximum N_1 and b) minimum N_2 versus *We*; EPTT, MBM, NM_τ_p, NM_T and the convoluted models; MH (EPTT ε=0.25; Micellar ω=4.0) response, highly-polymeric (β=1/9) fluids

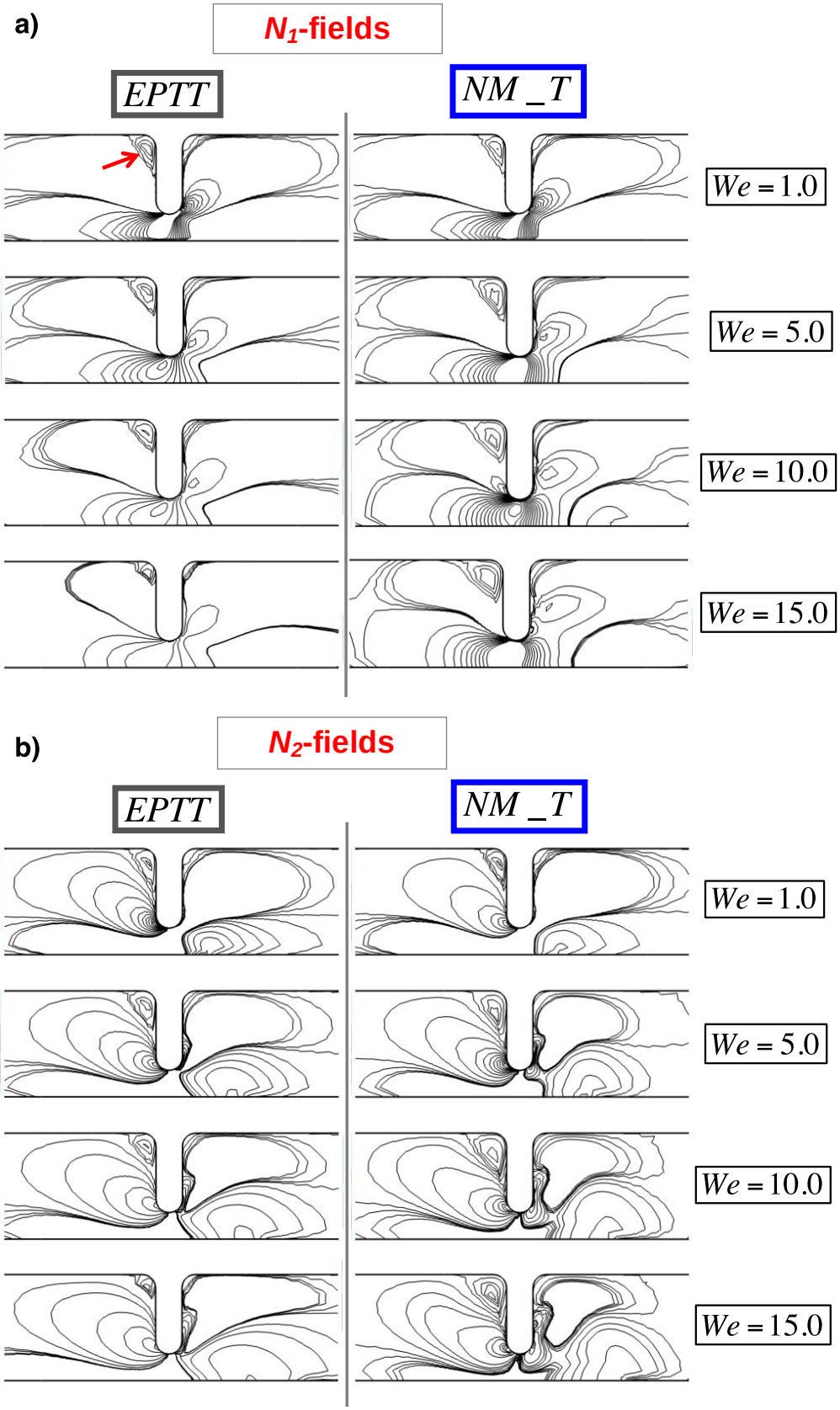

Figure 5.9 a) N_1 and b) N_2 contour fields versus *We* comparison for EPTT and the NM_T models for MH (EPTT ε=0.25; Micellar ω=4.0) response and highly-polymeric (β=1/9) fluids

***f*-functional expression, size of N_1 and impact on We_{lim}.** As specified in Section 2, Eq. (3) provides a general form for the equation of state for stress, where the only essential difference is given by the *f*-functional. This functional takes into account departure from Oldroyd-B-like behaviour. As argued above, the explicit presence of λ_1 (or *We*, in dimensionless terms) in *f* is most important for these new micellar models (NM_τ_p and NM_T), since it provides consistent EPD values at low *We* and produces relatively large We_{lim}. Hence, it is pertinent to discuss the nature and role played by this explicit *f*-*We* functionality on solutions. As listed in Table 1, the EPPT model contains an explicit, *exponential f*-*We* relation in its constitutive equation (with We_{lim}=210 under MH conditions, see Table 5.2). In comparison, an explicit, *linear f*-*We* functionality appears in the new micellar forms (NM_T with We_{lim}=16, and NM_τ_p with We_{lim}=4.9). The MBM model, which attains We_{lim}=3.6, does not possess an explicit relationship between *f* and *We*. These observations suggest a possible correlation between *f* and We_{lim}: the stronger the *f*-*We* functional relationship (expressed in powers or rate-rise), the larger the We_{lim}. *Size of f-functional and N_1 forms across these micellar models* are provided in Table 5.3 and 5.4. NM_τ_p solutions (with We_{lim}=4.9) generate larger N_1 (smaller *f*-) values than under NM_T (with We_{lim}=16.0) at comparable elasticity levels. Furthermore, MBM solutions yields larger N_1 (smaller *f*-) values (with We_{lim}=3.6) than under NM_τ_p prediction (with We_{lim}=4.9) for $1<We<2$.

N_1 and f-functional fields, non-convoluted: Fig. 5.10a provides a complete record for the (***N_1 fields non-convoluted)*** predictions. First, *EPTT-N_1 results* exhibit fields with vanishing negative zones and declining maximum values as *We* rises. This is consistent with (i) the inverse, quadratic relation between the *f*-functional and N_1 in simple shear flow (specifically $N_1 = 2\lambda_1\eta_{p0}\dot{\gamma}^2 / f^2$, based upon Eq. 2.27-2.28), where *f*-increases with rising-$\dot{\gamma}$ (see Fig. 5.7); and (ii) the EPTT *f*-results in complex flow, with relatively large *f*=O(360) and large We_{lim}=210 (cf. Table 5.3), and small N_1. In contrast, the *thixotropic MBM, NM_τ_p and NM_T results* produce relatively more intense and larger N_1 maxima zones (Fig. 5.10a), smaller *f* and We_{lim}. For example, at *We*=2, MBM-N_1 is twice as large as for EPTT and NM_τ_p (cf. Table 5.4). The non-convoluted *f*-maxima range is from {*f*=O(1), *We*=0.1} to {*f*=O(20), *We*=O(10)} (cf. Table 5.3). Consequently, critical elasticity levels are much smaller and lie around We_{lim}=O(10). In Fig. 5.11a (***f*-functional fields non-convoluted)**, notable differences in EPTT *f*-field results are apparent relative to the non-convoluted thixotropic solutions from low *We* levels (*We*=0.5).

EPTT data show a red-intense zone with relatively large, positive values about the contraction. As *We* is increased, the EPTT red zone grows in size and magnitude notably, from *f*=O(10) at *We*=0.1, to *f*=O(10^2) at *We*=100 (Table 5.3); until almost filling the region about the contraction. Moreover, localised small-*f* zones are apparent at the re-entrant and downstream corner for EPTT solutions at *We*=50 and onwards. Contrastingly, the micellar MBM, NM_τ_p and NM_T *f*-field results do not exhibit such growth in size and intensity as *We* is elevated. Indeed, these results exhibit a blue-light zone with relatively small, and even negative, values arising from the centreline. This is shifted downstream and lies within the red zone. Conspicuously and in contrast to EPTT *f*-fields, the micellar *f*-fields reveal that the blue patch at the contraction grows until it touches the wall, before encountering numerical solution breakdown.

***Convoluted vs. non-convoluted, f-maximum values at We_{lim}* (Table 5.4), *f*-fields.** In this comparison, significantly larger *f*-maxima are obtained for the EPTT and convoluted versions (*exponential f*), relative to their non-convoluted thixotropic analogues (*linear f*) at their respective We_{lim}: in fact, one order of magnitude larger. Specifically, EPTT/MBM results render *f*=O(390), whilst MBM predicts *f*=O(7), and EPTT originate *f*=O(360). Similarly, EPTT/NM_τ_p and NM_τ_p data result in *f*=O(400) and *f*=O(10), respectively. Moreover, EPTT/NM_T solutions evidence *f*=O(500) at *We*=300 and beyond, whilst NM_T results show *f*=O(20) at its We_{lim}. Accordingly, the convoluted N_1-values are smaller than for the non-convoluted counterparts (Table 5.4), and decline as *We* is elevated, thus rendering larger We_{lim}. In the *f*-fields displayed in Fig. 5.11b, the convoluted solutions exhibit micellar features at low elasticity levels (0.1<*We*<2.0): a blue relatively small zone that disappears as *We* is increased, when EPTT characteristics emerge, with the growing large-*f* red zone for *We*>5.0 onwards. Accordingly, the convoluted N_1-fields exhibit the inverse relationship with *f*-functional as *We* is elevated (Fig. 5.10b).

Table 5.3. Maximum and minimum *f*-function values versus *We*; MH (EPTT ε=0.25; Micellar ω=4.0) response, highly-polymeric fluids (β=1/9)

		f						
We		EPTT / NM_T	EPTT / NM_τ_p	EPTT / MBM	EPTT	MBM	NM_τ_p	NM_T
0.1	Max.	1.15	1.15	1.25	1.14	6.35	2.06	2.17
	Min.	0.98	0.98	0.99	1.00	0.99	1.00	1.00
0.5	Max.	2.50	2.49	2.53	2.46	5.82	4.11	5.00
	Min.	0.94	0.94	0.95	0.97	0.81	0.87	0.91
1.0	Max.	4.12	4.10	4.11	4.09	5.62	5.62	7.25
	Min.	0.91	0.91	0.91	0.96	0.60	0.59	0.69
2.0	Max.	6.86	6.80	6.76	6.81	5.62	7.40	9.77
	Min.	0.96	0.96	0.96	1.00	0.11	-0.34	0.05
5.0	Max.	13.55	13.43	13.39	13.24	D**	11.04***	13.74
	Min.	0.94	0.94	0.94	0.99		-4.92	-2.76
10.0	Max.	23.37	23.14	23.07	22.86		D	17.73
	Min.	0.92	0.92	0.92	0.95			-8.05
15.0	Max.	32.81	32.47	32.39	32.08			19.76
	Min.	0.95	0.95	0.95	0.94			-13.66
20.0	Max.	41.93	41.48	41.39	41.01			D
	Min.	0.96	0.96	0.96	0.94			
50.0	Max.	97.29	98.25	98.46	96.84			
	Min.	0.93	0.93	0.93	0.91			
100.0	Max.	192.22	196.08	196.53	179.78			
	Min.	0.86	0.86	0.86	0.86			
200.0	Max.	380.06	393.88	394.91	360.40			
	Min.	0.78	0.17	0.07	0.08			
220.0	Max.	417.08	433.75	D	D			
	Min.	0.76	0.005					
300.0	Max.	564.65	D*					
	Min.	0.09						

* Diverged

** Diverged at We_{lim}=3.6

*** Diverged at We_{lim}=4.9

Table 5.4. Maximum and minimum N_1 dimensionless values versus *We*; MH (EPTT ε=0.25; Micellar ω=4.0) response, highly-polymeric fluids (β=1/9)

		N_1						
We		EPTT / NM_T	EPTT / NM_τ_p	EPTT / MBM	EPTT	MBM	NM_τ_p	NM_T
0.1	Max.	8.24	8.25	7.89	8.30	2.41	5.48	5.20
	Min.	-5.08	-5.08	-4.98	-5.09	-2.18	-4.18	-4.05
0.5	Max.	7.84	7.87	7.79	7.98	3.09	4.83	3.59
	Min.	-3.08	-3.08	-3.07	-3.09	-2.15	-2.64	-2.50
1.0	Max.	5.71	5.75	5.76	5.84	4.46	4.46	2.95
	Min.	-2.22	-2.22	-2.22	-2.23	-2.19	-2.20	-2.04
2.0	Max.	3.70	3.75	3.78	3.80	7.44	4.17	2.72
	Min.	-1.46	-1.46	-1.46	-1.46	-2.98	-1.77	-1.61
5.0	Max.	1.93	1.98	2.00	2.00	D**	4.11***	2.94
	Min.	-0.93	-0.93	-0.94	-0.94		-3.53	-1.72
10.0	Max.	1.15	1.18	1.20	1.20		D	3.01
	Min.	-0.66	-0.66	-0.67	-0.67			-2.26
15.0	Max.	0.83	0.87	0.88	0.88			3.03
	Min.	-0.49	-0.49	-0.50	-0.49			-2.02
20.0	Max.	0.67	0.70	0.70	0.70			D
	Min.	-0.40	-0.40	-0.40	-0.40			
50.0	Max.	0.33	0.34	0.34	0.34			
	Min.	-0.19	-0.20	-0.20	-0.20			
100.0	Max.	0.19	0.19	0.19	0.19			
	Min.	-0.11	-0.11	-0.11	-0.11			
200.0	Max.	0.11	0.11	0.11	0.11			
	Min.	-0.06	-0.06	-0.06	-0.06			
220.0	Max.	0.10	0.10	D	D			
	Min.	-0.06	-0.05					
300.0	Max.	0.07	D*					
	Min.	-0.04						

* Diverged

** Diverged at We_{lim}=3.6

*** Diverged at We_{lim}=4.9

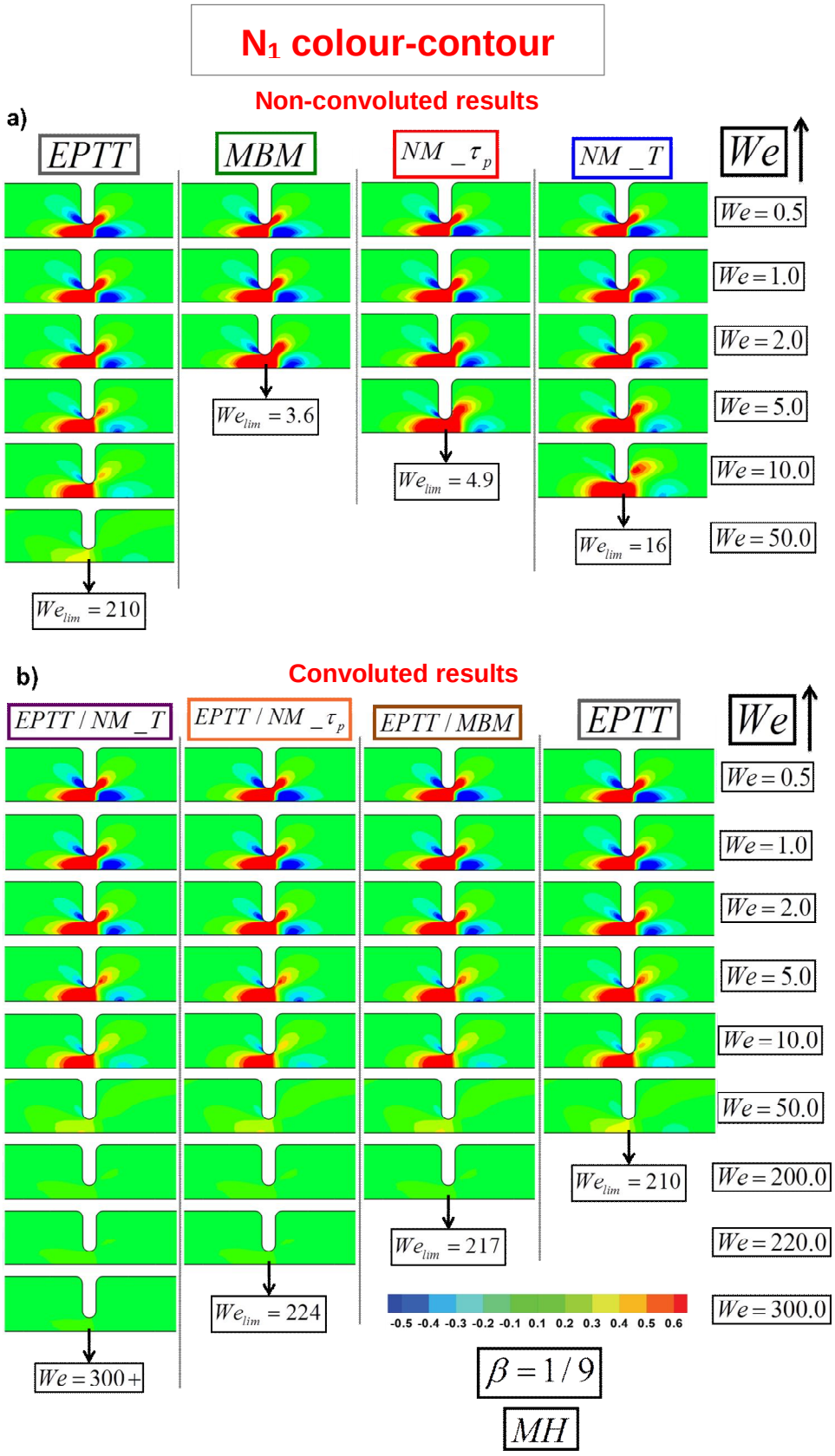

Figure 5.10 N_1 fields versus *We*: a) EPTT, MBM, NM_τ_p and NM_T models, b) EPTT, EPTT/MBM, EPTT/ NM_τ_p and EPTT/NM_T models; MH (EPTT ε=0.25; Micellar ω=4.0) response, highly-polymeric (β=1/9) fluids

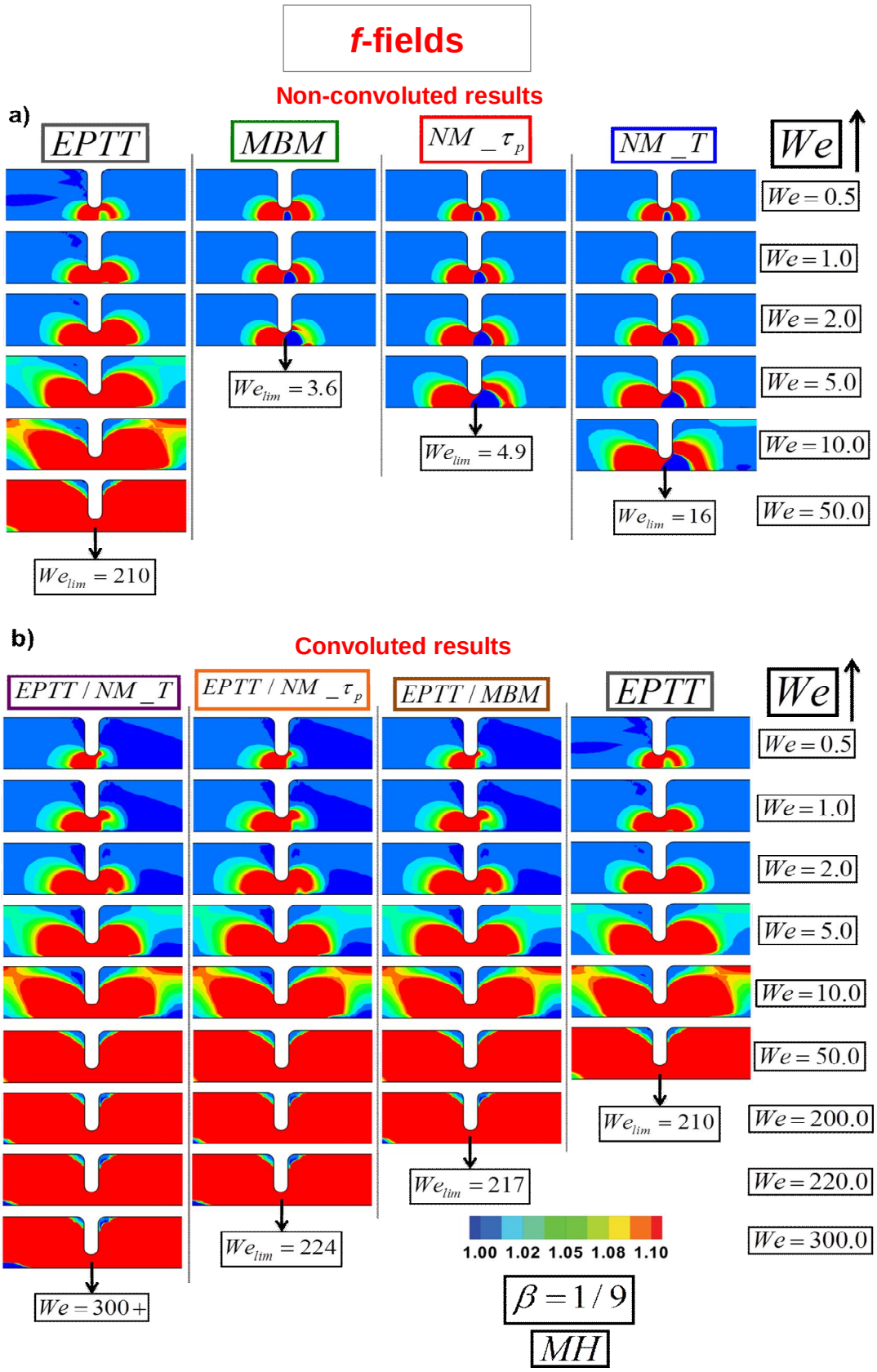

Figure 5.11 *f*-function fields versus *We*: a) EPTT, MBM, NM_τ_p and NM_T models, b) EPTT, EPTT/MBM, EPTT/ NM_τ_p and EPTT/NM_T models; MH (EPTT ε=0.25; Micellar ω=4.0) response, highly-polymeric (β=1/9) fluids

All above findings can be related to the corresponding materials functions (Fig. 3.1 and 3.2) and their impact on flow kinematics (Fig. 5.4a, 5.5a, 5.6 and 5.8 above). Both constitutive representations, the time-independent (meaning a model for which the *f*-functional is defined in terms of an algebraic equation; see 2.38) network-based EPTT, and the time-dependent (which in contrast have their *f*-functional given by a differential equation with time as the independent variable, and therefore capable of displaying thixotropy) micellar models, provide shear-thinning in steady simple shear and strain-hardening/softening effects in steady simple uniaxial extension (Fig. 3.1). Moreover, they exhibit an inverse, quadratic relation between N_1 and *f* in viscometric simple shear flow (Fig. 5.10). Nevertheless, EPTT results evidence a more complex kinematics than the micellar forms (Fig. 5.4a, 5.5a, 5.6 and 5.8 above). Major differences in *f*-results between the EPTT and non-convoluted micellar forms become apparent. Therefore, one may argue that the manifestation of the strain-hardening and softening characteristics (on vortex size/intensity, and N_1) is influenced by the magnitude of the *f*-functional predicted in complex flow, which seems to be largely dictated by the *f*-*We* functionality. Specifically, as noted for EPTT and convoluted models, and in contrast with the strain-hardening effects observed exclusively in the thixotropic non-convoluted micellar solutions. The exponential *f*-functional of EPTT and convoluted forms (Table 5.3) provide impressively larger *f*-results, which generate relatively smaller N_1 values, and consistently, larger We_{lim} in complex flow. Alternatively the linear *f*-expression, as in NM_τ_p and NM_T models, yields relatively smaller *f*-predictions, with larger N_1 and smaller We_{lim} than those of EPPT. These trends become even more noticeable for the MBM predictions, a model devoid of *f*-*We* explicit functionality.

5.5. Conclusions

A new set of constitutive models based on the MBM model (Boek et al. 2005) for wormlike micellar solutions has been presented, involving the viscoelasticity in the structure construction/destruction mechanics. Solutions are compared between time-dependent thixotropic MBM models and network-based time-independent EPTT models. Complex flows for a 4:1:4 rounded contraction/expansion are considered, under relatively moderate and strong strain-hardening response, and highly-polymeric and Newtonian like instances.

Analysis for the MBM model in the complex axisymmetric 4:1:4 contraction/expansion flow has provided information based on phenomenological observation (EPD attainment). Here, feedback between viscometric theory and complex flow analyses complement and improve the micellar constitutive approach, reflecting the new physics involved. In this study, this point is illustrated through the observation of the EPD underprediction at low elasticity levels, for which the MBM model provides inconsistent results, and upon which a correction is performed.

The new constitutive framework provides a) consistent EPD predictions at low elasticity levels, (contrary to the MBM model), b) larger limiting *We* to those obtained with the MBM model, by the explicit presence of *We* in the micellar *f*-functional, and c) rising EPD tendency at high-elasticity instances for Newtonian-like, moderate hardening fluids.

Moreover, impressively high-*We* results, of interest for industrial applications and microfluidics/nanotechnology (*We*~300+), have been obtained for the models characterising micellar solutions. This was achieved through the convolution of the *f*-functional of the micellar and EPPT models. The analysis of the *f*-functional across models evidences notable trends as to the level of attainable We_{lim}. Here, models with stronger explicit mathematical functionality between *f* and λ_1 (*We*) provide larger We_{lim}. Furthermore, the effects of these large-*f* results are reflected, firstly, on the N_1 magnitude predicted. These obey the inverse, quadratic functionality between N_1 and *f*, found in simple shear flow. Secondly, as demonstrated in this study and elsewhere (Tamaddon-Jahromi and Webster 2011), the vortex dynamics proves to be a function of the N_2–minima, as located in the vortices generated. Moreover, the relative size of *f*-predictions influences the manifestation of strain-softening/hardening characteristics through the vortex dynamics. Thus, outstandingly definite trends are established regarding the various constitutive models proposed. Significantly, the EPTT and its convoluted solutions evidence relatively complex kinematical behaviour with *We* rise, based on the relatively large *f*-values generated. Here, increasing vortex growth to a maximum is reported for the low-to-moderate elasticity range, with further decrease to a minimum over the moderate-to-high elasticity range, and ultimate rise in the high elasticity range. In particular, this rise in vortex intensity at high *We* is related to the formation and enhancement of a second upstream vortex, which is observed with the convoluted models. In contrast, solutions with non-convoluted micellar models and relatively smaller *f*-values, provide only vortex enhancement before their earlier numerical breakdown.

CHAPTER 6

High-Weissenberg predictions for micellar fluids in contraction-expansion flows

In this chapter the numerical modelling of thixotropic and non-thixotropic materials in contraction-expansion flows at high Weissenberg number (*We*) is analised. Thixotropy is represented via the new micellar time-dependent constitutive model for worm-like micellar systems proposed chapter 3, and contrasted against network-based time-independent PTT forms in complex flow in chapter 5. The work focuses on steady-state solutions in axisymmetric rounded-corner 4:1:4 contraction-expansion flows for the benchmark solvent-fraction of β=1/9 and moderate hardening characteristics (ε=0.25). In practice, this work has relevance to industrial and healthcare applications, such as enhanced oil-reservoir recovery and microfluidics. To obtain high-*We* solutions, both micellar and PTT constitutive equation *f*-functionals have been amended by (i) adopting their absolute values appealing to physical arguments (ABS-correction); (ii) through a change of stress variable, $\boldsymbol{\Pi}=\boldsymbol{\tau}_p+(\eta_{p0}/\lambda_1)\boldsymbol{I}$, that aims to prevent the loss of evolution in the underlying initial value problem; and finally, (iii) through an improved realisation of velocity gradient boundary conditions imposed at the centreline (VGR-correction). On the centreline, the eigenvalues of $\boldsymbol{\Pi}$ are identified with its $\boldsymbol{\Pi}$–stress-components, and discontinuities in $\boldsymbol{\Pi}$–components are located and associated with the *f*-functional-poles in simple uniaxial extension. Quality of solution is described through τ_{rz}, N_1 and N_2 (signature of vortex dynamics) stress fields, and $\boldsymbol{\Pi}$-eigenvalues. With {micellar, EPTT} fluids, the critical *We* (We_{crit}) is shifted from critical states of We_{crit}={4.9, 220} without correction, to We_{crit}={O(10^2), O(10^3)} with ABS-VGR-correction. Furthermore, such constitutive-equation correction has been found to have general applicability.

6.1 Introduction

This study addresses the topic of high Weissenberg (*We*) number solutions for worm-like micellar systems using the class of Bautista-Manero models (Bautista et al. 1999; Manero et al. 2002; Boek et al. 2005; López-Aguilar et al. 2014). The work concentrates on the rounded 4:1:4 contraction/expansion benchmark flow problem, and various alternative procedural and constitutive approaches are introduced. Herein, high-elasticity levels are accessible through two routes: (i) a correction to the constitutive model based on physical arguments, in which absolute values of the dissipation-function components are considered in complex flow; and (ii) the imposition of consistent boundary conditions at the axisymmetric geometry centre flow-line. There, in complex flow, the deformation is purely extensional (inhomogeneous) and shear-free flow prevails.

One of the principal challenges in the field of computation rheology has been to address the problem of seeking convergent numerical solutions to the underlying partial differential equation system for steady-state complex flows at high levels of Weissenberg number, referred to as the so-called 'High-Weissenberg Number Problem' (HWNM) (Binding et al. 2006; Aguayo et al. 2008). Strictly speaking this applies to the differential Maxwell/Oldroyd context, but in practice, often arises under strong-strain hardening alternatives, with shear-thinning (EPTT, LPTT, FENE-P; where *We*-definition may vary) or without shear-thinning (FENE-CR). Though many possible resolutions to this challenge have been proposed [see Walters & Webster (2003), Keunings (1986), Baaijens (1998)], still for many complex flows there are often limitations in Weissenberg number solutions met – due to issues such as sharp stress boundary layers and flow singularities (Keunings 2001). Relevant factors influencing the determination of a particular critical *We* solution state are: the numerical technique and discretisation for the independent variables (often stress, velocity, pressure, in space and time), the complex flow problem itself and the constitutive equation choice (Keunings 1986). Here, and largely motivated by findings with thixotropic constitutive model adjustments, this issue is revisited and further light is cast upon the problem.

Variable transformation and positivity: Dupret et al. (1985) and Dupret and Marchal (1986) state that, for theoretical flows (i.e. simple flows, from which we extract material functions), a well-posed initial-value problem in the context of a Maxwell fluid is one in which: (a) the tensor $\boldsymbol{\Pi}=\boldsymbol{\tau}_p+(\eta_{p0}/\lambda_1\boldsymbol{I})$ remains positive definite; (b) there is no solutions of a transient three-dimensional flow of a Maxwell fluid if the tensor $\boldsymbol{\Pi}$ does not remain positive-

definite; (c) in a steady-state scenario with well-defined boundary conditions (i.e. with Π positive definite at the boundary that crosses the streamlines), a solution cannot exist when Π is non positive-definite; and (d) the change of mixed-type of the underlying differential equation system, from {elliptic to hyperbolic, steady} or {hyperbolic-parabolic to hyperbolic-hyperbolic, unsteady}, which influences the stability of the numerical scheme in terms of loss of evolutionary character, and by implication, the requirements (completeness - necessity and sufficiency) on boundary conditions themselves.

Application of positive definiteness principles to viscoelastic complex flows: Dupret et al. (1985) applied the principles specified by Dupret and Marchal (1986) to the finite element solution of Maxwell and Oldroyd-B fluids, dealing with 2D complex flows such as 4:1 contraction flow with sharp borders in planar and axisymmetric geometries, and flow past a cylinder. These authors found that Oldroyd-B solutions proved more stable in comparison with those with the Maxwell model, due to the solvent presence inherent in the former choice, which provides its contribution through solvent diffusion to the momentum transport. The stability of their numerical scheme was evaluated through an S-parameter, defined in terms of the eigenvalues of Π as $S=2/(s_1/s_2-s_2/s_1)$. This parameter characterises three possible outcomes: (i) $S>0$, when both s_1, $s_2 > 0$; (ii) $S = 0$, when either s_1 or $s_2 = 0$ (not simultaneously); and (iii) $S<0$, when s_1, s_2 have opposite signs. This last instance was denoted as a precursor and sign of numerical convergence problems (numerical breakdown in stable steady-state extraction, subject to an imposed and consistent detection criterion). Later, Dupret and Marchal (1986) extended their studies on viscoelastic fluids for Johnson-Segalman and White Metzner equations, where '*evolutionary flow*s' are those for which the '*solutions at a present time t is a valid initial condition for determining the flow fields at subsequent moments*', otherwise '*non-evolutionary flows*' are obtained. This classification was based on (a) the positive definiteness of the appropriate extra-stress tensor; and (b) the existence of an extremum in the determinant of the same tensor.

Classification of differential models and conformation-tensor form: Van der Zanden and Hulsen (1988) and Hulsen (1988) proposed a classification of differential models to analyse computationally inclusion of a Newtonian solvent contribution. In their work, they studied the Leonov and Giesekus models, finding that the inclusion of such a solvent contribution resulted in a more well-posed scheme for numerical computation (as argued above). With this in mind, Hulsen (1990) generalised the work to define an alternative stress-like variable [as

proposed similarly under Dupret and Marchal (1986)], termed the configuration tensor, with its corresponding constitutive model statement, and with the objective of positive-definiteness retention under numerical solution. Here, the positive-definiteness of a differential constitutive equation system relies upon the property that the non-evolutionary terms therein remain positive and finite. Based upon such specification, corresponding expressions for equations of state were derived equivalent to commonly used models such as Giesekus and PTT.

6.2 Governing equations, constitutive modelling & theoretical framework

6.2.1 ABS and Π tensor approaches The governing equations and constitutive equations considered in this chapter have been detailed in chapter 2. The non-dimensional continuity and momentum conservation principles are expressed in eqs.(2.11)-(2.12), whilst the stress equations is given in (2.27)-(2.28). The specific time-dependent thixotropic micellar or time independent network-based nature is specified by the f_τ-functional. For the micellar framework, the natural-signed NM_τ_p is represented by eq.(2.34). In contrast, the network-based Exponential PTT model is represented in eq.(2.38). Material function comparison for these models is provided in chapter 3, in Fig. 3.1-3.2. The *dimensionless variables* utilised are defined in chapter 2. Here, an additional definition with respect to the conformation tensor should be emphasised, i.e. $\boldsymbol{\Pi}^* = \dfrac{\boldsymbol{\Pi}}{\dfrac{\eta_{p0}}{\lambda_1}}$.

In this chapter, a new correction to the time-dependent thixotropic micellar theory is proposed, as outlined in chapter 2, with the inclusion of the absolute value of the dissipation function in the structure construction-destruction eq.(2.36):

$$\frac{\partial f_\tau}{\partial t} = \frac{1}{\omega}\left(1 - f_\tau\right) + \xi_{G_0} We \left|\boldsymbol{\zeta} : \boldsymbol{D}\right|. \qquad (2.36)$$

Under network theory, the same reasoning as with thixotropic models can be applied to PTT models, and the analysis returns towards classical Oldroyd-B behaviour in the limit of vanishing $tr\boldsymbol{\tau}_p$.[1] Consistently, the corresponding modification to the PTT models becomes:

$$f_\tau = 1 + \frac{\varepsilon}{1-\beta} Wetr\left|\boldsymbol{\tau}_p\right| \text{ for LPTT, and } f_\tau = exp\left(\frac{\varepsilon}{1-\beta} Wetr\left|\boldsymbol{\tau}_p\right|\right) \text{ for EPTT.} \qquad (2.38)$$

[1] Provided the model parameter set $\{\varepsilon, \beta, We\}>0$, as is necessary by definition

Note, material functions for the models considered, along with the Oldroyd-B (f=1) reference, are reported in Fig 3.1, since the ABS-correction does not have any impact in simple ideal flow. For such theoretical flows, the domain of the stress and deformation rate variables is positive.

6.2.2 Change of variable (translations $\boldsymbol{\tau_p}$ - $\boldsymbol{\Pi}$) A change of variable between the conventional stress tensor and a conformation tensor has been derived in chapter 2, section 2.3.7. In this chapter, this change of variables in tested to generate stable high-We solutions. With this change of variable, the stress equation eq.(2.28) is transformed into eq.(2.40). The conformation-tensor versions for the constitutive equations are given in eqs.(2.41) and (2.43) for NM_τ_p and PTT models, respectively. One notes that eqs.(2.36)-(2.38) already include the ABS-correction, yet this assumption may be relaxed to consider natural-signed options.

6.2.3 $\boldsymbol{\Pi}$-eigenvalues in the field The eigenvalues of any tensor can be calculated via the solution of the characteristic equation obtained as follows (applied to $\boldsymbol{\Pi}$):

$$det\left(\boldsymbol{\Pi} - s\boldsymbol{I}\right) = 0\,, \tag{6.1}$$

where $\boldsymbol{s}$ denotes the vector of eigenvalues (s_i) of the tensor $\boldsymbol{\Pi}$. If we apply this principle to the symmetric $\boldsymbol{\Pi}$ tensor relevant to axisymmetric {z, r, θ}-flow, as pertinent to this study with vanishing shear components - $\Pi_{r\theta}$=$\Pi_{z\theta}$=0, given by:

$$det\begin{pmatrix} \Pi_{zz} - s & \Pi_{rz} & 0 \\ \Pi_{rz} & \Pi_{rr} - s & 0 \\ 0 & 0 & \Pi_{\theta\theta} - s \end{pmatrix} = 0\,, \tag{6.2}$$

and thus producing the cubic characteristic equation:

$$\left[\left(\Pi_{zz} - s\right)\left(\Pi_{rr} - s\right) - \Pi_{rz}{}^2\right]\left(\Pi_{\theta\theta} - s\right) = 0\,. \tag{6.3}$$

In this form, firstly note the decoupling of the $\theta\theta$-component from the remainder of the system, which provides the independence of the subsystem in r-z components (replicating that of planar flow). This is reflected in eigenvalue s_3=$\Pi_{\theta\theta}$, which is termed the third eigenvalue and identified unambiguously with $\Pi_{\theta\theta}$ over the whole field. Then, the remaining two eigenvalues can be determined from the quadratic equation for the r-z subsystem:

$$\left(\Pi_{zz}-s\right)\left(\Pi_{rr}-s\right)-\Pi_{rz}^{2}=0\,, \tag{6.4}$$

which can be recasted as:

$$s^{2}-\left(\Pi_{zz}+\Pi_{rr}\right)s+\left(\Pi_{zz}\Pi_{rr}-\Pi_{rz}^{2}\right)=0 \tag{6.5}$$

or more simply,

$$s^{2}-tr\boldsymbol{\Pi}^{sub}s+\det\boldsymbol{\Pi}^{sub}=0 \tag{6.6}$$

where use is made of trace and determinant operations, in $\mathrm{tr}\boldsymbol{\Pi}^{\mathrm{sub}}=\Pi_{zz}+\Pi_{rr}$ and $\det\boldsymbol{\Pi}^{\mathrm{sub}}=\Pi_{zz}*\Pi_{rr}-\Pi_{rz}^{2}$.

Thus, the two solutions of eq.(6.6) provide the first (s_1) and second (s_2) eigenvalues, respectively:

$$s_{1}=\frac{tr\boldsymbol{\Pi}^{sub}+\sqrt{\left(tr\boldsymbol{\Pi}^{sub}\right)^{2}-4\det\boldsymbol{\Pi}^{sub}}}{2}, \tag{6.7}$$

$$s_{2}=\frac{tr\boldsymbol{\Pi}^{sub}-\sqrt{\left(tr\boldsymbol{\Pi}^{sub}\right)^{2}-4\det\boldsymbol{\Pi}^{sub}}}{2} \tag{6.8}$$

Notably, the discriminant of the square-root represents a balance on sub-system components between the $(\mathrm{tr}\boldsymbol{\Pi}^{\mathrm{sub}})^2$ and $\det\boldsymbol{\Pi}^{\mathrm{sub}}$, and to conform to real eigenvalues should comply with the restriction that $[(\mathrm{tr}\boldsymbol{\Pi}^{\mathrm{sub}})^2-4\det\boldsymbol{\Pi}^{\mathrm{sub}}]\geq 0$.[2]

Corresponding and detailed analysis for the $\boldsymbol{\Pi}$-eigenvalues at the centreline (in shear-free flow) is given below, along with their relationship to the poles of the *f*-functional in simple uniaxial extension. This detail is called upon in the results sections below.

6.2.4 ***Π*-eigenvalues at the centreline (shear-free flow)** The eigenvalues of the $\boldsymbol{\Pi}$-tensor at the centreline reveal some interesting properties, worthy of further inspection. Shear-free flow applies along this flow-line ($\Pi_{rz}=0$), and hence, eqs.(6.4) and (6.6) reduce to:

$$\left(\Pi_{zz}-s\right)\left(\Pi_{rr}-s\right)=0\,, \tag{6.9}$$

[2] In practice, this condition has always been met for computable and stable steady-state *We*-solutions

$$s^2-\left(\Pi_{zz}+\Pi_{rr}\right)s+\left(\Pi_{zz}\Pi_{rr}\right)=0\,. \tag{6.10}$$

The discriminant associated with the solution of eq.(6.9) is:

$$\left(\Pi_{zz}+\Pi_{rr}\right)^2-4\Pi_{zz}\Pi_{rr}=\left(\Pi_{zz}^{\ 2}+2\Pi_{zz}\Pi_{rr}+\Pi_{rr}^{\ 2}\right)-4\Pi_{zz}\Pi_{rr}=\Pi_{zz}^{\ 2}-2\Pi_{zz}\Pi_{rr}+\Pi_{rr}^{\ 2},$$

viz,

$$\left(\Pi_{zz}+\Pi_{rr}\right)^2-4\Pi_{zz}\Pi_{rr}=\left(\Pi_{zz}-\Pi_{rr}\right)^2=N_1^2$$

From which the eigenvalues are then given by:

$$\left\{s_1,s_2\right\}=\frac{\Pi_{zz}+\Pi_{rr}\pm\left|N_1\right|}{2} \tag{6.11}$$

With dependence on the sign-switch of N_1 on the centreline, three instances can be identified from eq.(6.11):

a) when $N_1>0$ ➔ $N_1=\Pi_{zz}-\Pi_{rr}$, $s_1=\Pi_{zz}$, $s_2=\Pi_{rr}$;

b) $N_1=0$ ➔ $\Pi_{zz}=\Pi_{rr}$, $s_1=\Pi_{zz}=s_2=\Pi_{rr}=tr\boldsymbol{\Pi}^{sub}/2$;

c) when $N_1<0$ ➔ $N_1=\Pi_{rr}-\Pi_{zz}$, $s_1=\Pi_{rr}$, $s_2=\Pi_{zz}$.

Hence, theoretically on the centreline, a duality exists in the nature of the component identities between the $\{s_1, s_2\}$ eigenvalue pairs, and is dictated by the sign-switch in the first normal stress difference at this shear-free flow-line. What is clear is that each eigenvalue here picks up the identity of the local Π_{ii} component, and that this tensor component switches over its roll of eigenvalue dependency as the sign-switch in N_1 is traversed. Hence, both eigenvalues have an intimate roll to play in the analysis. Universal findings, to be discussed subsequently below, reveal that the corresponding centreline pattern of behaviour taken up by $\{s_1, s_2\}$ is such that s_1 remains positive $\forall z$, whilst s_2 has the potential to decline into minor negativity, subject to a number of constraints. Hence, it is s_2-response that is particularly instructive to focus attention on below.

6.2.5 ***Π-eigenvalue relationship with f-functional poles in simple uniaxial extension***

Consideration of simple uniaxial extension (or compression) within eq.(2.40) under deformation rate $\dot{\varepsilon}$, applicable to the linear viscoelastic regime, realises:

$$\overset{\nabla}{\boldsymbol{\Pi}}=-2\begin{bmatrix}\dot{\varepsilon}\Pi_{zz} & 0 & 0\\ 0 & \left(-\frac{\dot{\varepsilon}}{2}\right)\Pi_{rr} & 0\\ 0 & 0 & \left(-\frac{\dot{\varepsilon}}{2}\right)\Pi_{\theta\theta}\end{bmatrix}, \tag{6.12}$$

from which one extracts solutions of the form:

$$\boldsymbol{\Pi} = \begin{bmatrix} f_{\Pi}/\left(f_{\Pi} - 2We\dot{\varepsilon}\right) & 0 & 0 \\ 0 & f_{\Pi}/\left(f_{\Pi} + We\dot{\varepsilon}\right) & 0 \\ 0 & 0 & f_{\Pi}/\left(f_{\Pi} + We\dot{\varepsilon}\right) \end{bmatrix}. \qquad (6.13)$$

Hence and from the above analysis, the first and second eigenvalues on the centreline, in non-homogeneous uniaxial extension, may be approximated by $s_1 = \Pi_{zz} = f_{\Pi}/\left(f_{\Pi} - 2We\dot{\varepsilon}\right)$ and $s_2 = \Pi_{rr} = f_{\Pi}/\left(f_{\Pi} + We\dot{\varepsilon}\right)$. This equivalence holds exactly in the linear viscoelastic regime and for homogeneous extension conditions. Hence, one may identify departure in numerical solutions generated under inhomogeneous extensional conditions, and indeed the various windows of influence of departure from fully-developed flow.

6.2.6 Centreline shear-free boundary condition imposition – VGR-correction Consistent boundary conditions are required for any differential problem to be well-posed. In the contraction-expansion flow problem, the symmetry flow-line is the unique region in the flow-domain where uniaxial (inhomogeneous) extension exclusively occurs, as opposed to the contraction-wall where (inhomogeneous) shear flow prevails. Conventionally, the so-called stick-boundary condition is assumed along the contraction-wall, by which the fluid is treated as at rest on the wall ($\boldsymbol{u}$=0). At the shear-free centreline, flow symmetry boundary conditions apply. In this work, under VGR-correction and on the centreline, we propose imposing specific analytical restrictions on the deformation gradients (see section below). Here, the deformation gradients themselves are determined throughout the flow domain by a superconvergent local recovery technique and imposed on the stress equation [akin to well-known DEVSS-G methodology, but applied locally in quadratic form (Matallah et al. 1998)]. This enforces: (i) shear-free flow, to ensure 1D-extensional deformation (eq.(6.14a)); (ii) a pure uniaxial extension relationship between the normal deformation-gradients (eq.(6.14b)); and (iii) nodal-pointwise continuity imposed exactly, in discrete form (eq.(6.14c)). With computed knowledge of the normal deformation-gradients, the third of these conditions may be utilised throughout the domain, irrespective of 1D-centreline arguments. Assuming

specific notation for the extensional rate on the centreline in the axial direction, as $\hat{\dot{\varepsilon}} = \frac{\partial u_z}{\partial z}$,[3] then the following identities may be established and imposed on the numerical solution under VGR-correction:

$$\frac{\partial u_z}{\partial r} = \frac{\partial u_r}{\partial z} = 0\,, \tag{6.14a}$$

$$\frac{\partial u_r}{\partial r} = -\frac{1}{2}\frac{\partial u_z}{\partial z} = -\frac{1}{2}\hat{\dot{\varepsilon}}\,, \tag{6.14b}$$

$$\frac{u_r}{r} = -\left(\frac{\partial u_z}{\partial z} + \frac{\partial u_r}{\partial r}\right) = -\frac{1}{2}\hat{\dot{\varepsilon}}\,. \tag{6.14c}$$

Corresponding solutions results are discussed below, when this methodology is considered. As such, the VGR-correction is intended to eliminate noise proliferation, originating at the centreline, which may provoke numerically polluted solutions and earlier numerical solution breakdown.

6.3 Problem specification

The schematic representation of the 4:1:4 axisymmetric, rounded-corner contraction/expansion flow problem with its corresponding mesh data are reported in chapter 5. See Aguayo et al. (2008) for further detail on this problem, which provides a full mesh refinement analysis for some typical case studies.

Velocity-gradient approximation (VGR-correction) In Matallah et al. 1998; Hawken et al. 1991, both local (direct-recovery) and global (Galerkin) schemes for the treatment of velocity-gradients (VGR) were analysed and compared. There, a direct and nodal method was advocated, based on averaging velocity-gradient elemental-contributions to a triangular mesh-node. It is particularly significant that for midside nodes, this is the only scheme that enjoys superconvergent properties. In contrast, the global Galerkin approach fits an appropriate set of nodal gradient values that satisfy an associated weighted-residual formulation. Hawken et al. (1991) observed that the local recovery method offered improved performance, for solution gradients in complex flow problems, such as flow past a cylinder. Likewise, Matallah et al. (1998) conducted similar analysis on a 4:1 contraction problem and flow around a cylinder, observing that the local recovery technique was more stable than a local Galerkin equivalent; see summary in Walters and Webster (2003). Furthermore, in

[3] As a function of *z*-spatial variable, in uniaxial extension along the flow centreline

Belblidia et al. (2008) the above analysis was revisited under velocity-stress, parent/subcell approximation, as used here. This covered the various function-spaces and combination-options available for velocity-gradient representation (parent/subcell control-volume, quadratic/linear order), with special reference to stress-subcell approximation. In Belblidia et a. (2008), the localised-quadratic velocity-gradient (parent-cell) treatment was shown to achieve both stability and accuracy, applying robustly for both linear (subcell) and quadratic (parent) stress interpolations.

Entry flow kinematics is determined computationally for the equivalent entry-channel problem. These may be imposed through the time-stepping procedure, either as steady-state, or via a smooth transient build-up. Then, fully-developed outflow conditions are established ensuring no change in streamwise and vanishing cross-stream kinematics. Once fully-developed entry-flow kinematics is known, stress may be determined through the derived and corresponding initial-value-problem ODE system (consistent with internal domain solution discretisation).

6.4. Solutions with Micellar NM_τ_p model – natural-signed form

Negative f-values in complex flow In Fig. 6.1, zones of small and negative f_τ-value, appear at the centreline from low *We*-solution levels onwards (i.e. *We*=0.1, dark blue regions). These regions grow towards the contraction wall and are convected downstream as elasticity level increases, for all three micellar models (i.e. MBM, NM_τ_p, NM_T) (López-Aguilar et al. 2014), which vary in dissipation function.

The structure equation given in terms of the *f*-functional for the micellar models is represented in [1 + g($\boldsymbol{\zeta}$:$\boldsymbol{D}$)] form. The only way this expression can generate negative *f*-values in complex flow is if g($\boldsymbol{\zeta}$:$\boldsymbol{D}$)$<$-1. This occurrence is unphysical with respect to the second law of thermodynamics, since any viscous flow is dissipative; thus increasing the entropy of the system (Bird et al. 1960, 1977; Aris 1962). As outlined by Bird et al. (2007), for viscoelastic fluids, elasticity acts as a energy storage feature. As such, the global dissipation could be zero or negative when the elastic-storage is more important than the viscous-dissipative contribution. Complex flows, with their mixed shear-extensional nature caused by change of geommetry, display regions with localized positive and negative values in stress and velocity components, with the corresponding change of sign in their gradients (see Fig. 5.10 for positive and negative N_1 values, for example). This can originate regions with dissipation-

function negative values that in our particular case of micellar fluids, are used to change of structure of the material and ultimately estimate its viscosity across the field. Moreover, the *f*-functional for these thixotropic micellar models is explicitly related to viscosity-inverse (see Eq. 2.32-2.35 and recall $f=\left(\eta_{p0}/\eta_{p}\right)$). Thus, from Eq. 2.35, one may conclude that sufficiently large negative dissipation-function values may generate negative *f*-values, that represent negative viscosities in the field (again unphysical); and moreover, when g($\boldsymbol{\zeta}$:$\boldsymbol{D}$)=-1, *f*=0, an infinite viscosity would be predicted. As reported elsewhere (López-Aguilar et al. 2014), numerical breakdown for each micellar variant, characterised by the critical-*We* (denoted We_{crit}) solution, is observed when the small and negative *f*-function region reaches the contraction wall (see Fig. 6.1 and Table 6.1). In this study, for the sake of conciseness only, the NM_τ_p micellar version is studied in detail; nevertheless, all observations are quite general.

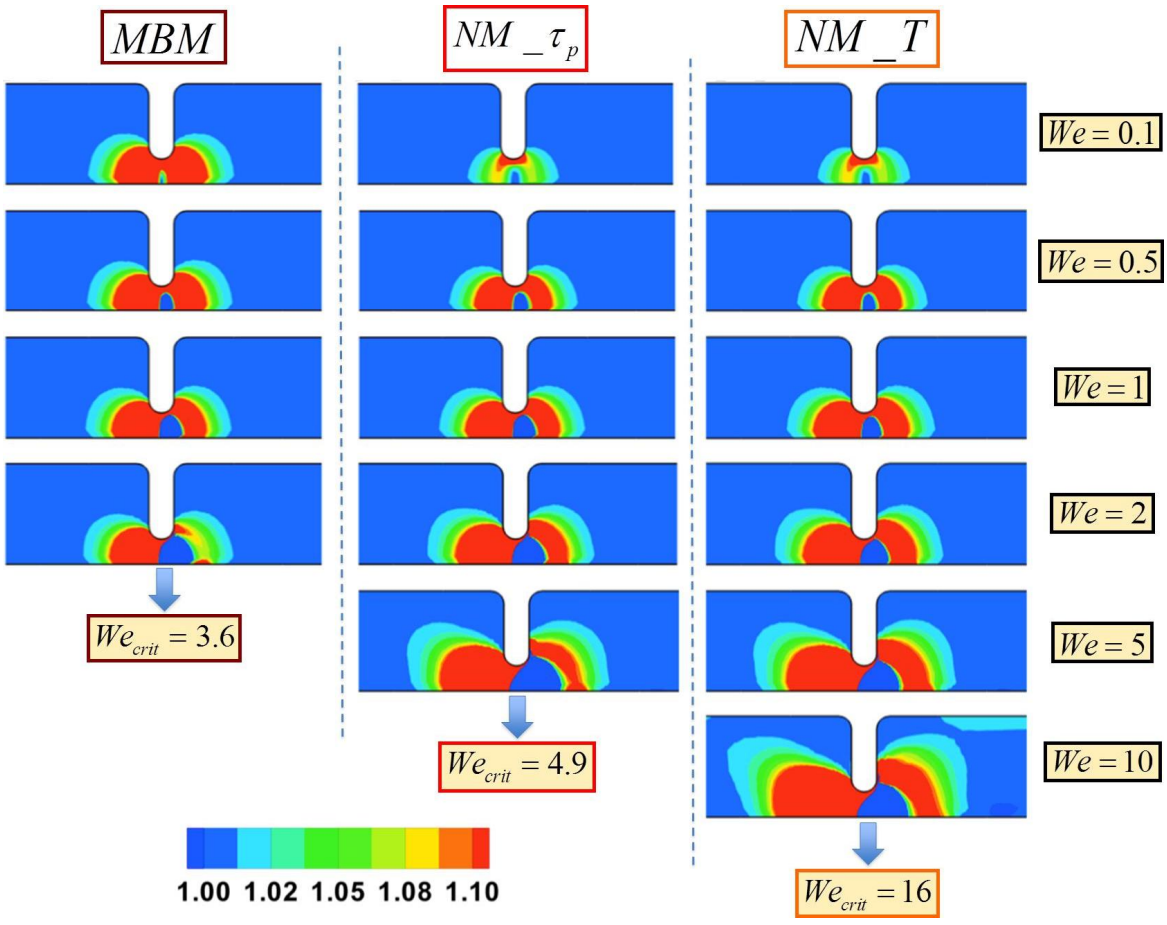

Figure 6.1. f_τ-functional 2D-fields versus *We*; MBM, NM_τ_p and NM_T

s_2-field trends and numerical breakdown In Fig. 6.2, the evolution of NM_τ_p s_2-fields through increasing elasticity to We_{crit} is depicted. This graduated change in solution state with elasticity level is evidence to the regional loss of positive-definiteness and the consequence this has on evolution in *We*-solution, which provokes numerical breakdown (Dupret and Marchal 1986). Firstly, at low elasticity levels (*We*=0.5) (Fig. 6.2a), s_2 remains positive throughout the field, with variations about the centreline given by the mixed nature of shear-extensional flow. The s_2-minimum value (s_{2min}=0.53; see Table 6.2) is located on the centreline, downstream with respect to the contraction. This first low s_2 peak (blue spot on centreline; see 2D field) is connected to the contraction wall by another light-blue positive contour level, originating at the centreline and reaching out across the flow to the contraction wall. The s_2-maximum value (red spot s_{2max}=1.03) is located off the centreline, but close to it; this is surrounded by a green contour-banded region of relatively low-s_2 levels, that connects locations on the centreline to those on the wall, both upstream and downstream of the contraction.

Interestingly, when elasticity level is increased further to *We*=2 (Fig. 6.2b), negative-blue s_2 values begin to penetrate into the field. The location of the minimum-negative value is observed through the first-peak at the centreline (s_{2min}=-0.23), which appears to be convected downstream. This negative region remains connected to that on the contraction wall by a similar green-positive fringe to that identified when *We*=0.5. In addition, this green fringe (disconnected downstream) partially surrounds the second-red positive-peak. This second-red peak appears to have grown in size and strength (s_{2max}=1.24), and is convected downstream in contrast to the *We*=0.5 solution. Moreover, a new feature has now arisen at this *We*-level: a third peak on the downstream contraction wall (see 3D field-plot). The value for this peak (s_2=0.27 units) remains positive. The fully-developed flow region upstream and downstream of the contraction is characterised by levels of $0.8 \leq s_2 \leq 1$ units.

Fig. 6.2c provides corresponding results at *We*=3. Here, strong features in s_2 are established which become more intense with rise in *We*. The first and second-peaks, are identified by s_{2min}=-0.29 and s_{2max}=1.35, respectively; these have been convected even more and become relatively more intense, with reference to lower *We*-level solutions. At *We*=3, the positive surrounding-level connecting the first-peak between the centreline and contraction wall, appears larger and fully-connected upstream. The third-peak at the downstream wall has become sharper and its local minimum value has just wandered into negativity (s_2=-0.05).

Table 6.1. f_τ, f_{Π} extrema versus *We*; micellar models

		f_τ			f_{Π}
We		Natural	ABS	VGR	Π
0.1	Max.	2.06	2.06	2.06	2.69
	Min.	0.998	1.00	1.00	1.00
0.5	Max.	4.11	4.18	4.18	5.82
	Min.	0.87	1.00	1.00	1.00
1	Max.	5.62	6.59	6.59	7.87
	Min.	0.59	1.00	1.00	1.00
2	Max.	7.4	10.94	10.94	12.14
	Min.	-0.34	1.00	1.00	1.00
3	Max.	8.72	13.35	13.35	15.07
	Min.	-1.82	1.00	1.00	1.00
4	Max.	9.98	15.39	15.39	17.58
	Min.	-3.44	1.00	1.00	1.00
5	Max.	11.04*	17.35	17.35	19.92
	Min.	-4.91	1.00	1.00	1.00
10	Max.		25.48	25.48	30.40
	Min.		1.00	1.00	1.00
15	Max.		32.20	32.20	41.72
	Min.		1.00	1.00	1.00
20	Max.		36.85	36.85	42.65
	Min.		1.00	1.00	1.00
30	Max.		41.29	41.29	53.19
	Min.		1.00	1.00	1.00
40	Max.		74.51**	85.54	115.87
	Min.		1.00	1.00	1.00
75	Max.			195.49	256.53
	Min.			1.00	1.00
100	Max.			279.89	321.52
	Min.			1.00	1.00
140	Max.			427.52	450.44
	Min.			1.00	1.00
175	Max.			534.31	562.73
	Min.			1.00	1.00
200	Max.			606.83	
	Min.			1.00	
250	Max.			748.47	
	Min.			1.00	
370	Max.			1037.10	
	Min.			1.00	

*We_{crit}=4.9; **We_{crit}=39

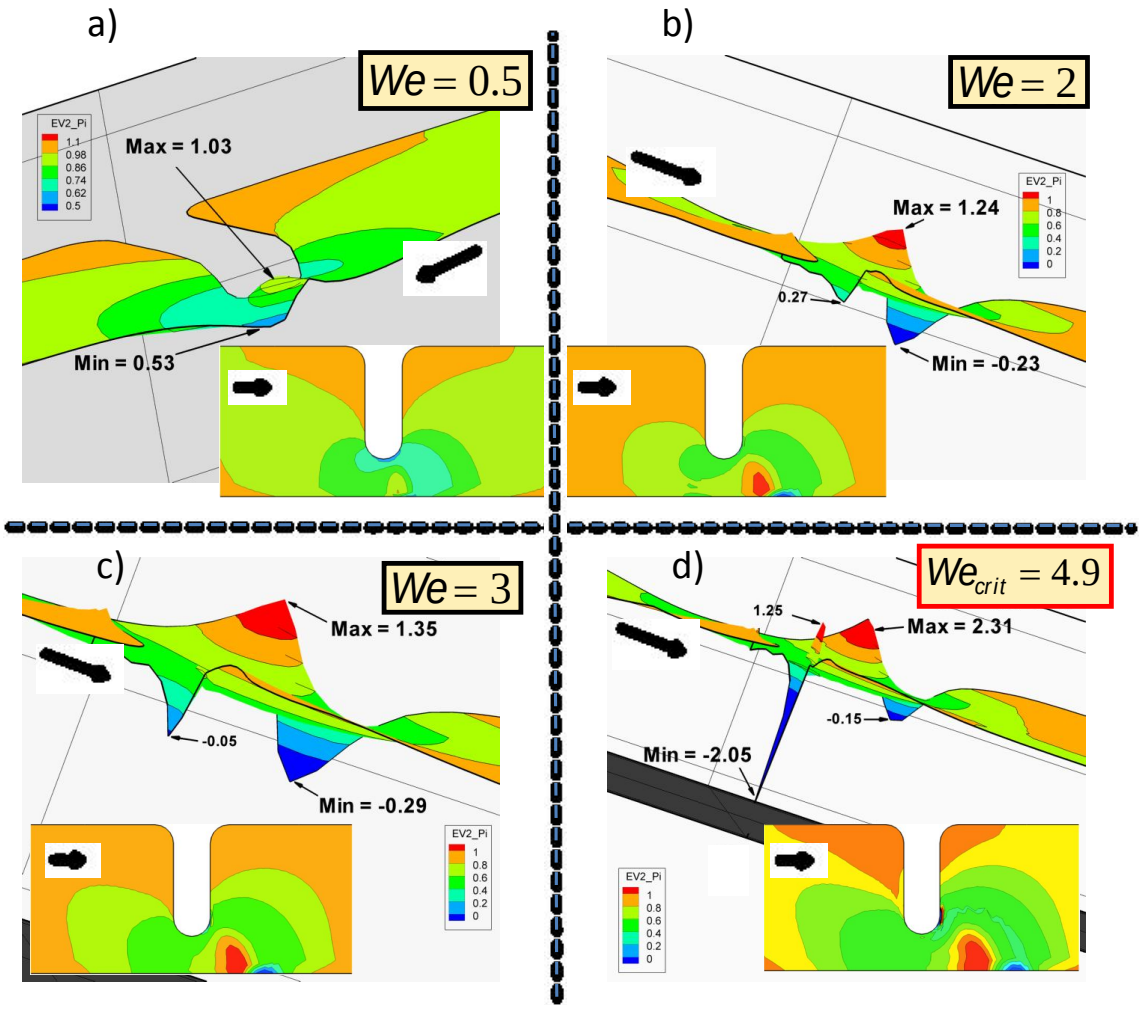

Figure 6.2. s_2 2D, 3D-fields versus *We*; NM_τ_p

Finally and most conspicuously for *We*=4.9, the stage is reached beyond which steady-state numerical breakdown is observed (Fig. 6.2d, We_{crit}=4.9, breakdown at *We*=5). Note, the important switch in location of the global s_{2min}=-2.05 in the NM_τ_p case at We_{crit}=4.9, from previous *We*–levels on centreline, to presently on the wall (backface-tip of contraction). In addition here, a fourth-red positive-peak also becomes apparent on the downstream wall, next to the third-peak, as fresh evidence to the appearance of solution overshoot-undershoot. Moreover, the first two peaks appear completely attached to the centreline and convected downstream. The first-peak has become less intense at this *We*-level (s_2=-0.15), whilst the second-peak has grown in size and intensity (s_{2max}=1.39). The first-peak at the centreline still remains connected to the wall by a slim-positive s_2-band (light-blue).

Table 6.2. s_2 extrema versus *We*; micellar models

		s_2			
We		Natural	ABS	VGR	Π
0.1	Max.	1.00	1.00	1.00	1.00
	Min.	0.74	0.74	0.74	0.74
0.5	Max.	1.03	1.03	1.03	1.01
	Min.	0.53	0.55	0.55	0.48
1	Max.	1.13	1.09	1.09	1.06
	Min.	0.10	0.17	0.17	0.24
2	Max.	1.24	1.22	1.22	1.22
	Min.	-0.23	-0.11	-0.11	0.03
3	Max.	1.35	1.31	1.31	1.31
	Min.	-0.29	-0.18	-0.18	-0.04
4	Max.	1.52	1.4	1.4	1.41
	Min.	-0.80	-0.19	-0.2	-0.05
5	Max.	2.31*	1.47	1.47	1.49
	Min.	-2.05	-0.22	-0.22	-0.08
10	Max.		1.75	1.74	1.83
	Min.		-0.28	-0.3	-0.13
15	Max.		1.98	1.97	2.11
	Min.		-0.96	-0.96	-0.69
20	Max.		2.17	2.17	2.3
	Min.		-2.00	-2.00	-95.75
30	Max.		2.57	2.57	2.91
	Min.		-109.98	-109.97	-105.67
40	Max.		2.82**	2.75	3.15
	Min.		-143.55	-154.13	-258.04
75	Max.			7.82	3.89
	Min.			-354.61	-490.08
100	Max.			10.73	3.88
	Min.			-474.41	-665.58
140	Max.			6.77	5.04
	Min.			-663.73	-932.55
175	Max.			9.33	6.05
	Min.			-791.01	-1166.40
200	Max.			10.34	
	Min.			-902.81	
250	Max.			11.81	
	Min.			-1124.60	
370	Max.			17.30	
	Min.			-1641.20	

*We_{crit}=4.9; **We_{crit}=39

s_1-s_2 vs. Π_{zz}-Π_{rr} @ centreline In Fig. 6.3, a plot for NM_τ_p data at We_{crit}=4.9 illustrates the theory of section 2.4 for the swapping-over character of the eigenvalues at centreline. As predicted by the theory, $s_1=\Pi_{zz}$ and $s_2=\Pi_{rr}$ when N_1 remains positive, whilst $s_1=\Pi_{rr}$ and $s_2=\Pi_{zz}$ when N_1 becomes negative. The switch-over point in N_1 lies at z=1.6 units (at We_{crit}=4.9). Interestingly, the switch-over point in N_1-sign is independent of counterpart conditions in rate of deformation. Along this flow-line, uniaxial extension is apparent upstream and uniaxial compression downstream. Moreover, given that a constant flow rate is maintained in these λ_1-increasing simulations, the localised inhomogeneous rate of deformation is barely changed throughout the *We*-continuation procedure.

Π_{zz}-Π_{rr} vs. f_{Π}-functional poles @ centreline As discussed above and applicable on the centreline, a correlation may be extracted between numerical Π-components and their corresponding simple uniaxial extensional predictions from viscometric/linear viscoelastic regime theory. Fig. 6.4 gathers this comparison together at low elasticity levels *We*={0.001, 0.01, 0.1}. As *We* tends to zero, the continuous reference line is that of unity. As elasticity is elevated, the inhomogeneous nonlinear solution is contrasted against its linearised inhomogeneous counterpart. To be precise, the latter is extracted functionally from viscometric theory along the centreline, yet by imposing the derived inhomogeneous state of stress and deformation from the numerical solution. The numerical data curves at *We*=0.001, for Π_{zz} (symbols) and its theoretical linear estimation (f-pole$_1$ related to $2\dot{\varepsilon}We$ – dashed lines) are practically superimposed over the reference line. For *We*=0.01, departure from viscometric data is now evident, yet not relatively significant, ranging around 2% for the largest departure. In contrast for *We*=0.1, this departure appears significantly large, with the largest difference ranging around 25% over the unity reference line. Comparison of Π_{rr} with its theoretical linear estimation (f_{Π}-functional -pole$_2$ related to $\dot{\varepsilon}We$ – dashed lines; see inset Fig. 6.4) provides similar trends as pole$_1$ analysis, with two main differences: (i) at *We*=0.1, the maximum departure of the linear estimation from unity reference line, is smaller (14%) than occurs with f_{Π}-functional-pole$_1$, and (ii) now, the maximum departure appears downstream. Note, the shape of Π_{rr} is the reflected-scaled image of Π_{zz} in the reference line; also, all curves intersect at z=0.

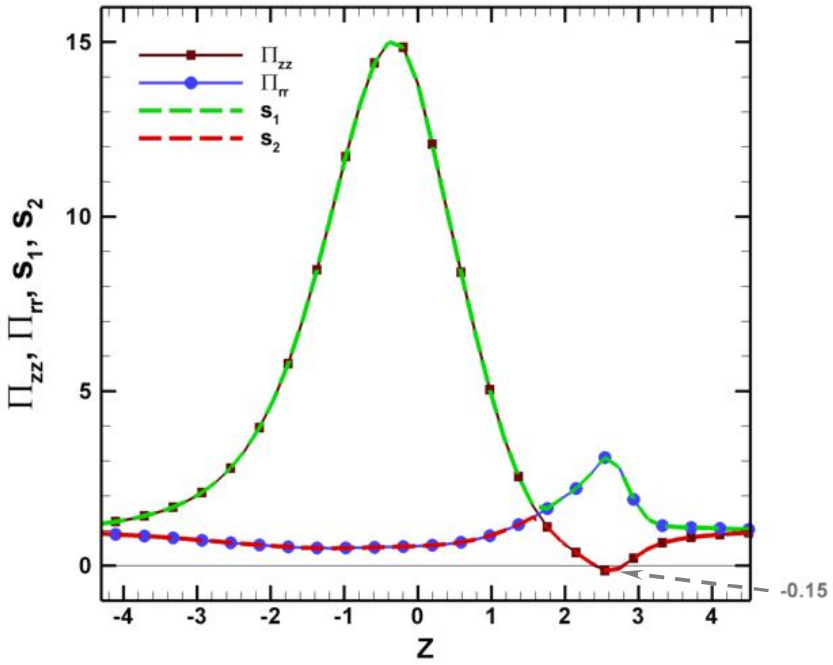

Figure 6.3. Π_{zz}, Π_{rr}, s_1, s_2 at centreline; We_{crit}=4.9; NM_τ_p

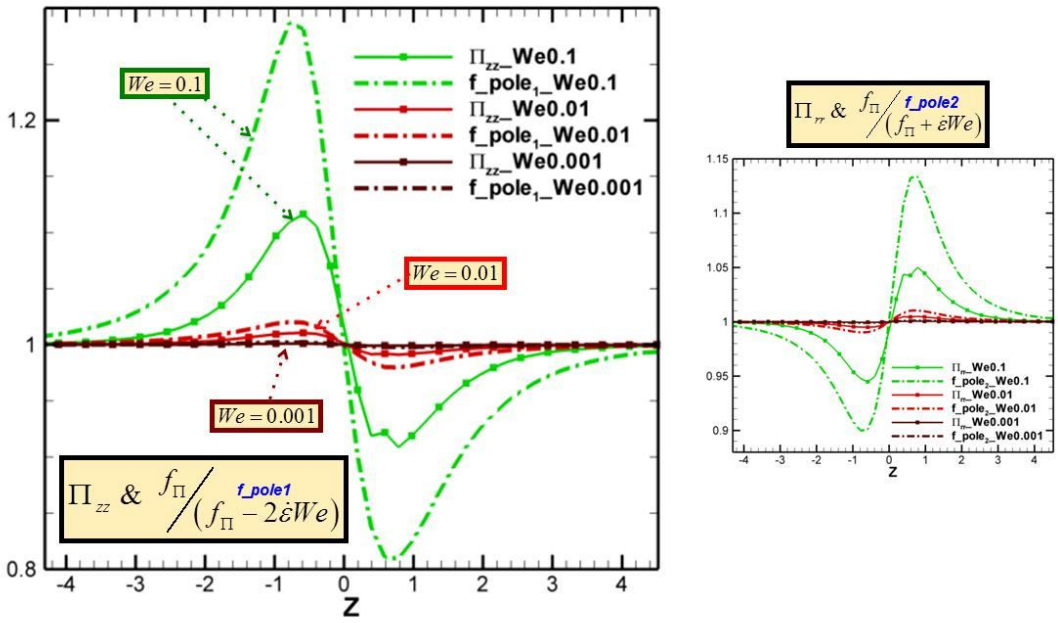

Figure 6.4. Π_{zz}, linear-pole$_1$ estimation (inset Π_{rr}, linear-pole$_2$ estimation) at centreline;

We={0.001, 0.01, 0.1}; NM_τ_p

Fig. 6.5 provides additional information at more elevated elasticity levels, including We_{crit}=4.9. At We=0.5, a singularity in Π_{zz} linear viscometric estimation is observed at z~-0.9. The reason for their appearance is illustrated in the plot below, in which a comparison between the Π_{zz} viscometric estimation (top-row) and the components of the pole$_1$ (bottom-row) are plotted as We rises and complex flow becomes more dominant. These singularities correspond in location to the centreline-zone at which the components of pole$_1$ (i.e. f_{Π} & $2\dot{\varepsilon}We$) balance one another (bottom-row). A similar situation arises with f_{II}-functional-pole$_2$ (i.e. f_{Π} & $-\dot{\varepsilon}We$), for which singularities are observed first at larger We=2 relative to f_{II} -functional-pole$_1$.

6.5 The ABS correction - Micellar NM_τ_p_ABS model and larger We_{crit}

Correction on negative f-values & consequence on positive definiteness To correct for the inconsistency in the f_τ-functional, and therefore in viscosity predictions described in section 6.4, these thixotropic models have been amended - adopting absolute components values in the dissipation function. Considering such ABS-correction provides the global f_{τ_min}=1 (extrema, Table 6.1), applicable spatially and through all We-levels for NM_τ_p_ABS. In contrast, NM_τ_p provides negative values (f_{τ_min}=-4.92) at We_{crit}=4.9. Moreover, global f_{τ_max} is observed to increase. For example, this extremum for We={2,3,4,4.9} goes from f_{τ_max}={7.40, 8.72, 9.98, 11.04} for NM_τ_p, to f_{τ_max}={10.94, 13.35, 15.39, 17.34} with We ={2,3,4,5} and NM_τ_p_ABS. Fig. 6.6 compares f_τ and s_2 in 2D and 3D-fields at We=4.9 (We_{crit} for NM_τ_p). Consistently, the blue-region containing negative NM_τ_p f_τ-functional values is lost in NM_τ_p _ABS 2D-fields, and replaced by a continuous red-region about the contraction. The 3D-f_τ-fields reveal further detailed features, with NM_τ_p providing (i) a pronounced negative-dip just downstream of the contraction and filling the gap across the flow; and (ii) a sharp negative-peak to this f_τ-dip at the downstream contraction-wall (f_τ=-3.37); which now coincides in location with the negative-peak observed in the second eigenvalue data (s_{2min}=-2.05). In contrast, NM_τ_p_ABS 3D-f_τ-field data provides a less-erratic field about the contraction, with two local maxima f_τ={4.51, 3.86}, and a minimum f_τ=1.35 at the centreline. Note under NM_τ_p_ABS, values of f_τ slightly larger than unity are located over the *fully-developed regions*, upstream and downstream of the contraction, where shear flow prevails. f_τ–values grow with increasing We and along the radial direction at any fixed z-

coordinate in these locations; from $f_{\tau min}$=1 at the centreline (since τ_{rz}=0, hence $\boldsymbol{\tau}_p : \boldsymbol{D} = \tau_{rz}\left(\frac{\partial u_z}{\partial r} + \frac{\partial u_r}{\partial z}\right) = 0$), to f_τ–values larger than unity at the wall (where $\boldsymbol{\tau}_p : \boldsymbol{D} \neq 0$). For instance, the NM_$\tau_p$_ABS solution at We_{crit}=39, provides f_τ-values that range between $f_{\tau min}$=1 at the centreline, and f_τ=1.06 at the wall.

2D and 3D field s_2-data Furthermore, the s_2-data counterpart to f_τ-data in Fig. 6.6 (see more at Fig. 6.8), clearly exhibits the strong influence of the ABS-correction: the sharp negative-peak on the wall observed in NM_τ_p results is practically lost under NM_τ_p_ABS. With NM_τ_p_ABS, this key contraction-wall feature appears positive (s_2=0.24) and relatively less prominent; whilst it is negative (s_{2min}=-2.05; Table 6.2) and sharp in the natural-signed NM_τ_p results. Moreover, overshoot-undershoot in s_2 is absent at this location for NM_τ_p_ABS, whilst this is evident in the NM_τ_p 3D-field data, through a prominent positive red-peak (s_2=1.25) next to the negative blue-peak (s_{2min}=-2.05). One notes, the severity of solution gradients at this location and degradation in the quality of their capture, which all hints at pending numerical solution breakdown. The global s_{2min} is smaller and on centreline (*cl*) for NM_τ_p_ABS compared with NM_τ_p, noting the final *We*=4.9 s_{2min} value switches location from -0.19_{cl} to -2.05_{wall}. At fixed *We*=4.9, contrasting *local s_{2min} on centreline* between NM_τ_p_ABS and NM_τ_p solutions and (Fig. 6.6), reveals an even more intense peak for NM_τ_p_ABS (global s_{2min}=-0.19) relative to NM_τ_p (*local* s_{2min}=-0.15). See Fig. 6.8 for additional data on stress fields.

We_{crit} levels Table 6.3 lists critical Weissenberg number (over models and methods) according to the final stable solution-state (We_{crit}), and that at which solution breakdown (failure) is first detected (We_{fail}). For these micellar models, the inclusion of the ABS-correction generates an increase of some eight times in We_{crit}, from {We_{crit}=5, NM_τ_p} to {We_{crit}=39, NM_τ_p_ABS} representation. Generally, increasing f_τ-magnitude elevates the levels of computable We_{crit}-solutions (López-Aguilar et al 2014) (down-scaling elasticity prominence). This is clearly the case when selecting the ABS-correction, and moreover, is exaggerated by selecting the absolute value of each individual component of the dissipation function (as opposed to the absolute value of the total dissipation function).

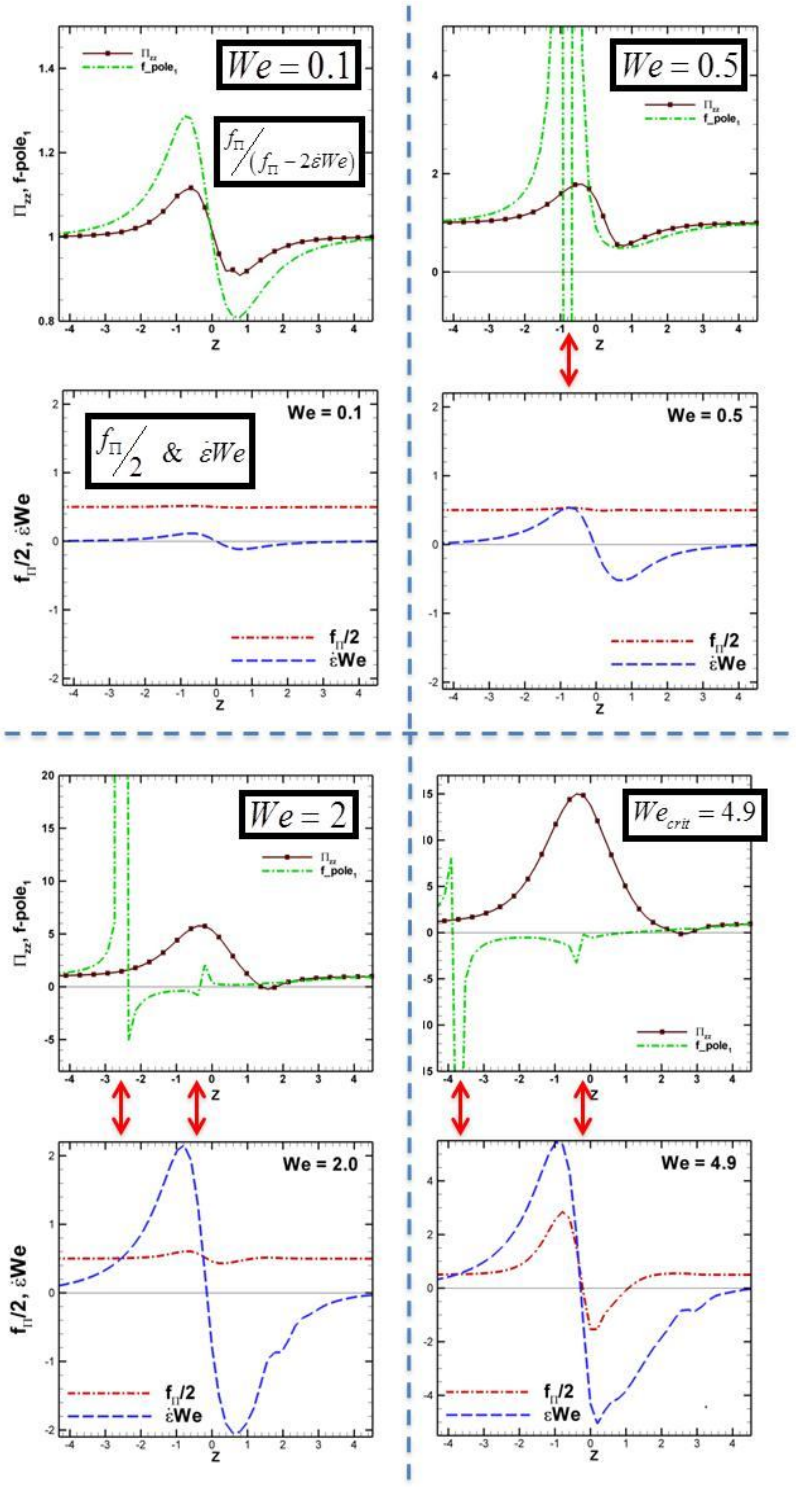

Figure. 6.5 Π_{zz}, linear-pole$_1$ estimation and pole$_1$-components at centreline; We={0.1, 0.5, 2, 4.9}; NM_τ_p

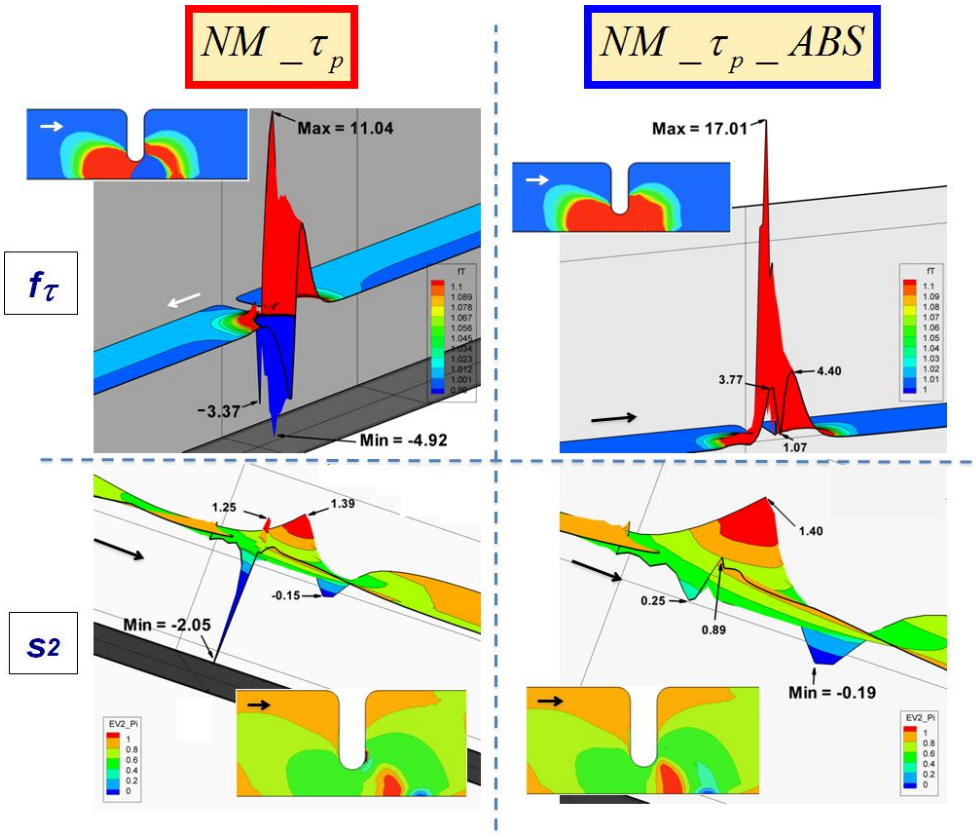

Figure 6.6. f_τ-functional and s_2 2D, 3D-fields at We=4.9; NM_τ_p

Table 6.3. {Critical, first-failure} Weissenberg numbers {We_{crit}, We_{fail}} across models

		We_{crit}, (We_{fail})			
Model	f_τ	Natural Sign	ABS	VGR	Π
NM_τ_p	$1+\omega\xi_{G_0} We\boldsymbol{\tau}_p : \boldsymbol{D}$	4.9, (5)	39, (40)	370, (380)	175, (180)
LPTT	$1+\frac{\varepsilon We}{1-\beta} tr\boldsymbol{\tau}_p$	11, (12)	210, (220)	-	-
EPTT	$exp\left(\frac{\varepsilon We}{1-\beta} tr\boldsymbol{\tau}_p\right)$	210, (220)	4000, (4250)	4250, (4500)	1000, (1250)

s2 vs. We history plot Fig. 6.7 provides the detailed graphical data across models on s_{2min} as a function of *We*,[4] following Table 6.2. From the zoomed figure-inset in $0.1 \leq We \leq 0.5$ range, the NM_τ_p and NM_τ_p_ABS curves drop from s_{2min}=0.74 at low elasticity levels (*We*=0.1) and closely match, upholding the same declining trend up to *We*=0.5. Subsequently for *We*>0.5, the curves begin to depart from each other, with the NM_τ_p curve adopting the strongest negative declining slope. This is reflected in the precise *We* at which each data-curve crosses the zero-reference line. The NM_τ_p curve provides an intercept at *We*~1.4, whilst the intercept for NM_τ_p_ABS curve is slightly retarded in this respect to *We*~1.6. From this situation and from $We \geq 2$ onwards, NM_τ_p and NM_τ_p_ABS s_{2min}-curves differ in solution gradient response, and markedly so for $We \geq 3$. The NM_τ_p curve gradually declines in slope in the interval $2 \leq We \leq 5$, locating drops with increasing magnitude at points *We*=3, 4. Thereafter, for *We*>4, the NM_τ_p curve declines most sharply, continuously and up to its We_{crit}=4.9 state, with s_{2min}=-2.05 now on the contraction-wall. In contrast and relative to NM_τ_p, the NM_τ_p_ABS s_{2min}-curve adopts a continuous and shallow decline in slope which appears to reach a plateau in $3 \leq We < 20$ range (see full-scale plot). Around and after this *We*=20 state, the NM_τ_p_ABS curve locates variation points at *We*={20, 25, 30}, first declining less rapidly at *We*=20, then more rapidly at *We*=25, returning to less rapidly at *We*=30, and continuing onwards towards We_{crit}=39. At this critical solution stage, the negativity in s_2 has reached levels of s_{2min}=-143.55. It is noteworthy that negativity in s_2 would appear to provide an over-strong indicator of primary solution quality, and indeed convergence to steady-state, as some degree of negativity in this factor is tolerated (under *We*-continuation, as opposed to IVP time-evolution, where the theory more strictly applies), whilst this does not hinder computation of smooth unpolluted solutions in all primary solution variables.

Stress fields – solution quality Fig. 6.8(i) gathers together comparatively a sample of stress data for the NM_τ_p_ABS model, via *first* (and *second*) *normal stress-difference* N_1 (and N_2), *shear stress* τ_{rz} and *second eigenvalue* s_2-data (2D-fields) at selected *We*={0.5, 2, 5, 39}. Notably, these N_1 and τ_{rz} 2D-fields display continuous change through *We* incrementation, without evidence of numerical pollution (see section 5.2.3 for identification of eigenvalues, positive-definiteness). More sporadic field patterns become apparent in s_2-data and *We*>40,

[4] We_{inc} – NM_τ_p: unity to *We*=4, in 0.1 to We_{crit}=4.9; NM_τ_p_ABS: unity to *We*=10, in 5 to *We*=30, unity to We_{crit}=39

useful to hold comparatively against the stress data. Particularly on N_1 (Fig. 6.8(i)a) at We=0.5, regions with positive (red) and negative (blue) values can be identified, with extrema indicated of $\{N_{1\max}=4.48,\ N_{1\min}=-2.49\}$. At We=2 and under greater influence of shear-thinning/extension-softening, these extrema have diminished in magnitude to $\{N_{1\max}=4.20,\ N_{1\min}=-1.47\}$. At We=5 stage (NM_τ_p We_{crit}=4.9), N_1-extrema continue to decrement, with $\{N_{1\max}=3.73,\ N_{1\min}=-1.92\}$. Importantly at We_{crit}=39, there is evidence of overshoots-undershoots in N_1 attached to the obstruction downstream backface-wall, as a new and third positive-region has emerged, located alongside the third blue-region (now larger and more conspicuous than before). Notably, this local behaviour correlates to s_{2min} negative-extremum. N_1-extrema at this critical stage are smallest reported, with $\{N_{1\max}=3.67,\ N_{1\min}=-1.76\}$. N_2-data with rising We is also included, to indicate trends in vortex region activity [see NM_τ_p in (López-Aguilar et al 2014) up to We_{crit}=4.9], where upstream growth is apparent (deep-blue zone) and sustained through increasing We; whilst only vortex decay is displayed downstream (absent by We=2). In Fig. 6.8(i)c, comparable τ_{rz}-field response is less dramatic than in N_1. In the τ_{rz}-field at We=0.5, τ_{rz}-extrema are largest reported at $\{\tau_{rz\max}=1.54,\ \tau_{rz\min}=-1.77\}$; diminishing by We=2 to $\{\tau_{rz\max}=1.28,\ \tau_{rz\min}=-1.10\}$, due to greater shear-thinning. Furthermore at We=5, even greater shear-thinning effects render reduced extrema of $\{\tau_{rz\max}=0.91,\ \tau_{rz\min}=-0.94\}$. Proceeding to We_{crit}=39; the most prominent feature to report is the splitting of the second-downstream red-positive region (already apparent at We=20), leaving a zone located above the obstruction backface-tip and a satellite zone that has drifted off downstream, periphery to the downstream-vortex region; τ_{rz}-extrema are now least in magnitude, being $\{\tau_{rz\max}=0.66,\ \tau_{rz\min}=-0.84\}$.

Shear deformation rate fields In Fig. 6.9 du_z/dr 3D and 2D-fields are contrasted for NM_τ_p_ABS versus NM_τ_p_ABS_VGR at rising We. Elimination of noise proliferation under VGR-correction is clearly observed in the undulating centreline patterns in the du_z/dr 3D-NM_τ_p_ABS solutions at every elasticity instance (shown for We=2). These centreline undulations (in $du_z/dr\neq0$) are convected downstream of the contraction as We is elevated, although there is evidence here for the continued persistence of these undulations in the contraction-gap itself on the centreline (permanent deformation) and via upstream field-penetration. In contrast, for NM_τ_p_ABS_VGR solutions, this flow-line remains unperturbed throughout the We-continuation process. Moreover for $We\geq2$, signals of pollution in

NM_τ_p_ABS solutions are evident off the centreline, upstream and downstream of the contraction; whilst NM_τ_p_ABS_VGR fields remain unpolluted up to *We*=8. Some solution gradient activity is becoming apparent on the backface obstruction-wall at *We*=5 (more prominent at *We*=9), for both NM_τ_p_ABS and NM_τ_p_ABS_VGR. This is manifest through *three locations*: one located at the centre of the obstruction-wall and the other two near its extremities, in the salient and corner-tip neighbourhoods. Through *We*-rise, the most influential of these three is that near the tip of the obstruction. This feature continues to grow downstream penetrating the field, and subsequently links up in a stalagmite-stalactite fashion to its counterpart downstream, just-off-centreline, positive growth-point, uniting at *We*=19. The growth pattern of this positive-point is: first appears at {*We*=5, NM_τ_p_ABS} and {*We*=9, NM_τ_p_ABS_VGR}; with a distinct gap to centreline under NM_τ_p_ABS.

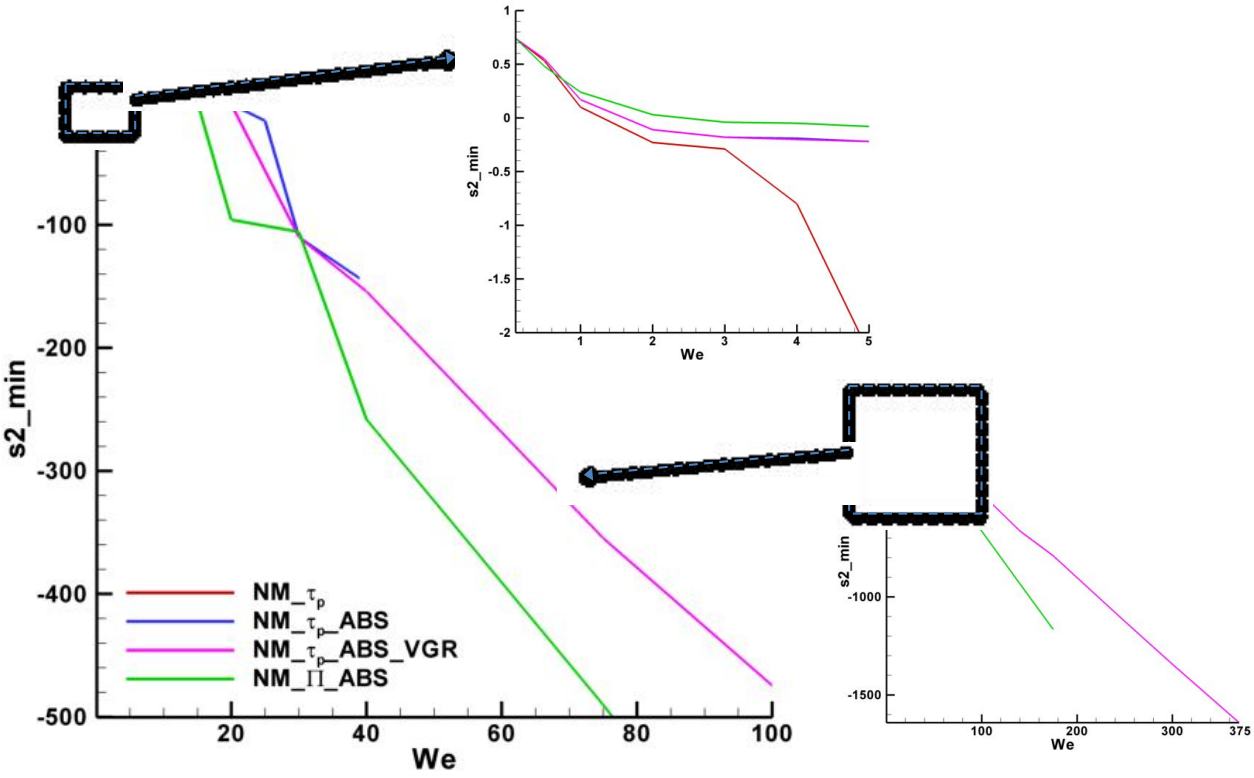

Figure 6.7. s_{2min} versus *We*; NM_τ_p, NM_τ_p_ABS, NM_τ_p_ABS_VGR and NM_Π_ABS

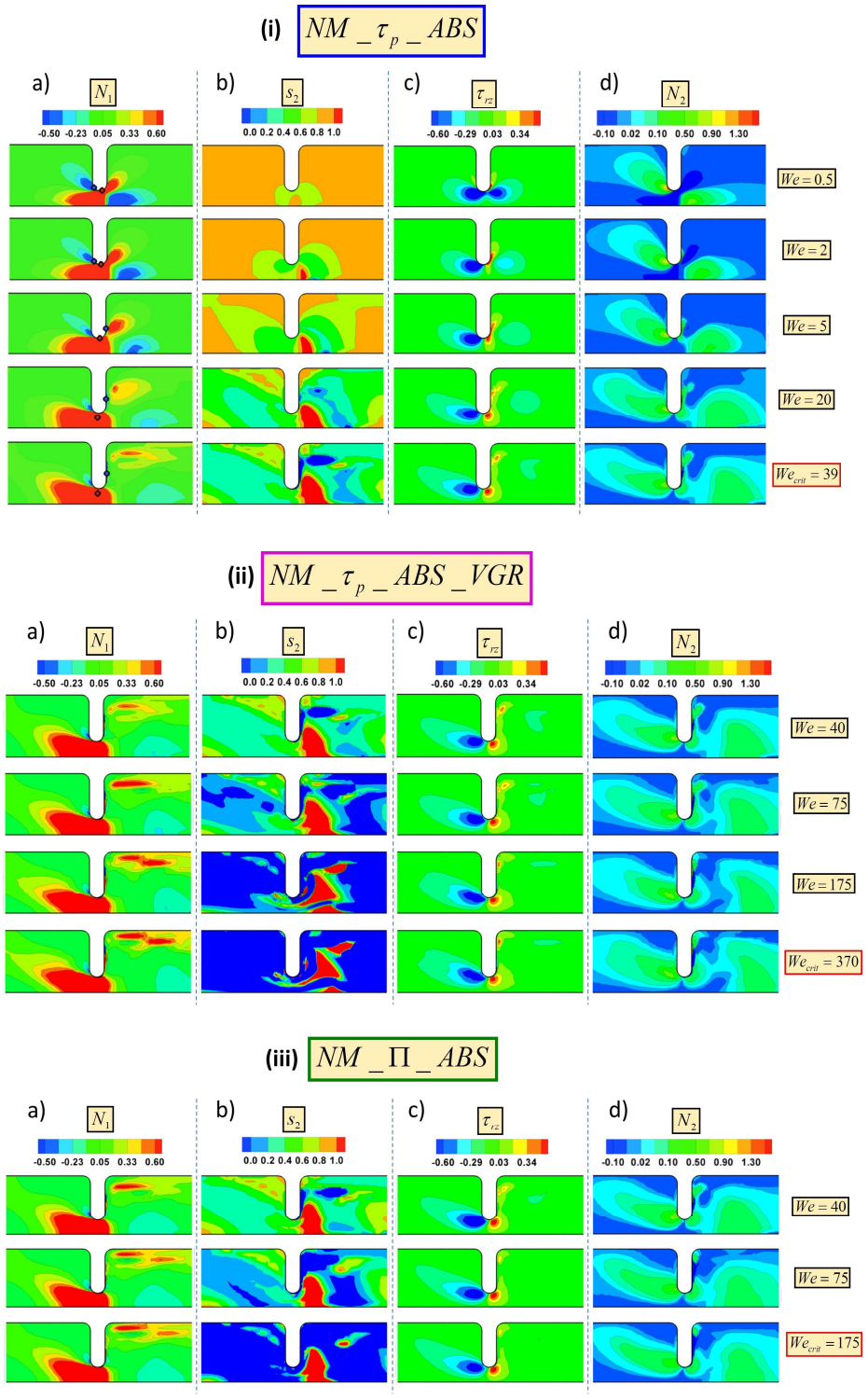

Figure 6.8. N_1, s_2, τ_{rz}, N_2 2D-fields versus *We*; (i) NM_τ_p_ABS, (ii) NM_τ_p_ABS_VGR and (iii) NM_Π_ABS

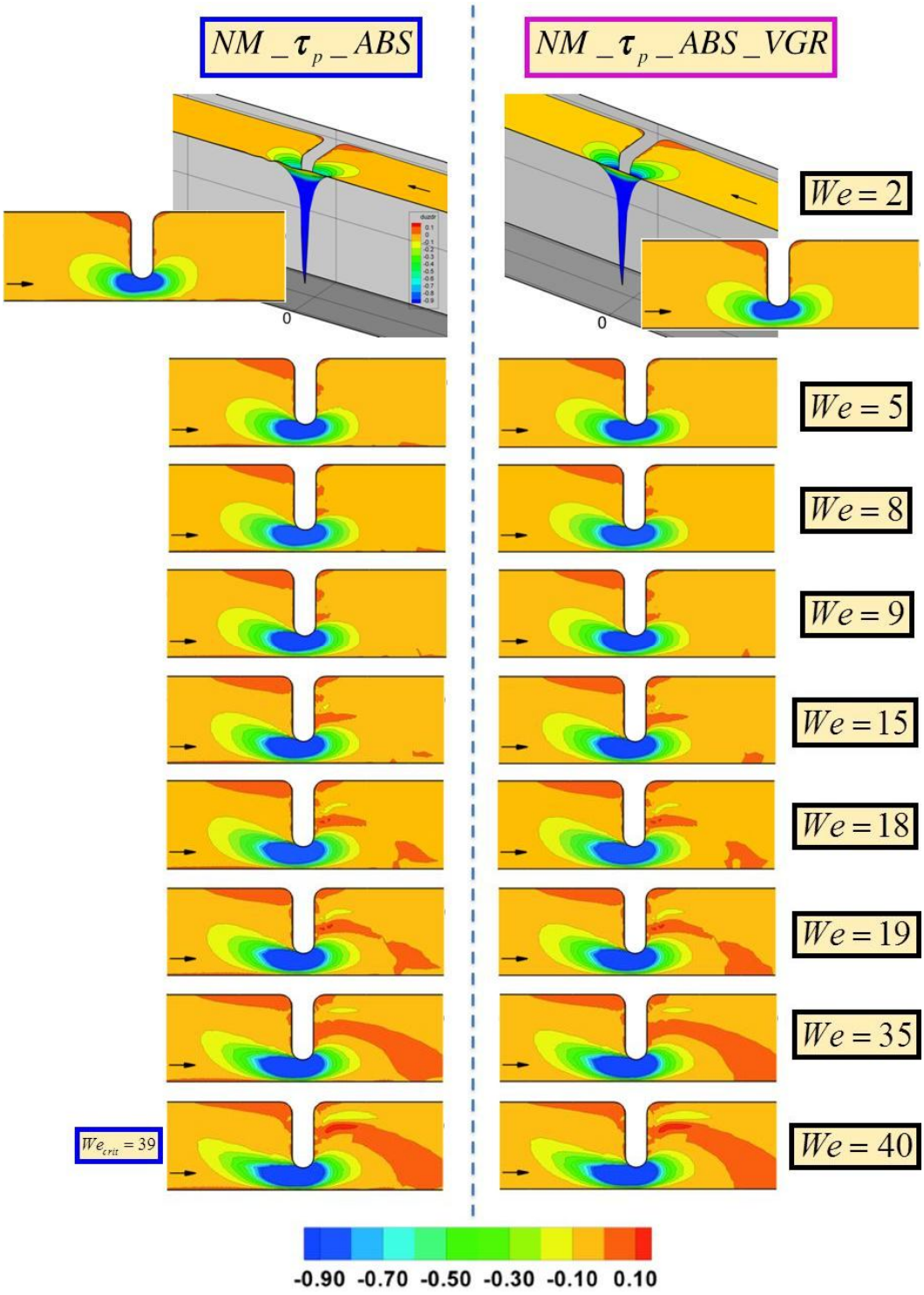

Figure 6.9. $du_z dr$ 2D, 3D-fields versus *We*; NM_τ_p_ABS and NM_τ_p_ABS_VGR

6.6. Highly elastic solutions

*6.6.1 The VGR-correction - Micellar NM_ τ_p_ABS*_VGR *model*

We_{crit} levels In addition to the ABS-correction and with the imposition of the enhanced centreline boundary conditions (NM_τ_p_ABS_VGR) as described in section 2.6, converged steady-state solutions now become attainable at considerably higher Weissenberg numbers[5]. With reference to Table 6.3, an increase in We_{crit} level of some ten times is observed under NM_τ_p_ABS_VGR, relative to NM_τ_p_ABS capability. Specifically, NM_τ_p_ABS numerical solution breakdown is observed at We_{crit}=39, whilst NM_τ_p_ABS_VGR attains the exaggerated response of We_{crit}=370. This position is interrogated further below, through exposure to solution perturbation on the centreline via the deformation-gradients themselves, and hence the consistency of the problem. One notes, there is practically ***no change in f_τ-functional extrema*** between NM_τ_p_ABS and NM_τ_p_ABS_VGR; and hence, elevation in We_{crit} with NM_τ_p_ABS_VGR is attributed solely to the VGR-correction.

s2 vs. We history plot Fig. 6.7 provides for comparison between NM_τ_p_ABS and NM_τ_p_ABS_VGR s_{2min}-solution response, and emphasizes the more gradual/smoother changes gathered in the NM_τ_p_ABS_VGR s_{2min}-curve up to and around We_{crit}=39 for NM_τ_p_ABS. This theme is continued up to We_{crit}=370, with essentially the same declining gradient trend after {NM_τ_p_ABS, We_{crit}=39}; the refined deformation-gradient centreline conditions clearly provide for the advance in high *We*-number attenuation. One notes with look ahead, that the data on NM_Π_ABS, is of similar form to that under NM_τ_p_ABS_VGR, displaying only slightly greater rate in s_{2min}-decline beyond *We*~30.

Deformation rates @ centreline See Fig. 6.9 for detail on corresponding field data. Fig. 6.10 graphs contrast NM_τ_p_ABS versus NM_τ_p_ABS_VGR data, for rising *We* and on the centreline, in shear du_z/dr and the extensional du_z/dz deformation gradient components. In Fig. 6.10a, there is conspicuous noise present in the *shear gradient* du_z/dr (NM_τ_p_ABS); absent under NM_τ_p_ABS_VGR, where the shear gradient vanishes. *Upstream* of the contraction, these NM_τ_p_ABS non-zero du_z/dr values tend to increase as *We* is elevated. Notably, at the axis *z*=0, a minimum is observed for every *We*-data-curve; yet, the magnitude

[5] We_{inc} – NM_τ_p_ABS_VGR: unity to *We*=10, in 5 to *We*=200, in 10 to We_{crit}=370

of this minimum is rising for $0.1 \leq We \leq 5$, whilst decreasing for $We \geq 10$. *Downstream* of the contraction, du_z/dr-data-curves reflect rather oscillatory behaviour, adopting a damped pattern with *We* rise, somewhat resembling the convected patches in N_1 and s_2-fields (Figs. 10a,b). In contrast, data-curves under NM_τ_p_ABS_VGR (Fig. 6.10b) display null du_z/dr at the centreline. In terms of normal gradient component representation, *extensional rate* du_z/dz data is imposed on the other two normal components, discretely conveyed through du_r/dr approximation (Fig. 6.10c, d). VGR-correction at $We=\{2,5\}$ is evident, through localised differences and their subsequent downstream convection; this may be gathered in the comparison between data-curves in NM_τ_p_ABS and NM_τ_p_ABS_VGR solutions downstream of the contraction. Relatively smoother trends in du_r/dr curves are observed under the (pink) NM_τ_p_ABS_VGR data-curve. Conspicuously, adjustments in the shear du_z/dr component prove to be an order of magnitude larger than those in the extensional du_r/dr component.

Stress fields – solution quality Fig. 6.8(ii) gathers VGR-correction data in N_1, s_2, τ_{rz} and N_2 2D-fields, with rising *We* and sampled at incremental stages. Between NM_τ_p_ABS (Fig. 6.8(i)) and NM_τ_p_ABS_VGR Fig. 6.8(ii) solutions up to $We \sim 40$, there are no noticeable solution differences in f_τ-fields or other variables. Of the $\boldsymbol{N_1}$**-field** in the $75<We<370$ range (Fig. 6.8(ii)a), the most significant feature lies in the red-positive downstream-zone that originated from the second bulbous-zone in Fig. 6.8(i)a and split off downstream around $We \sim 20$; this has now further elongated downstream and parallel to the channel-wall, passing incrementally in steps through $We=\{40,75,175,370\}$, with signs of splitting about its centre around $We \sim 175$. This has certainly occurred at the advanced stage of $We_{crit}=370$. Similarly in the same *We*-range and on $\boldsymbol{\tau_{rz}}$**-field** data, the downstream obstruction-backface detached-satellite red-positive zone (from $We \sim 20$, Fig. 6.8(ii)c) is continuously convected with rising *We* along the obstruction face towards the salient vortex region and becoming more intense. The $\boldsymbol{N_2}$**-field** data continues to convey the signature of vortex activity in the upstream salient corner of Fig. 6.8(i)d (López-Aguilar et al 2014), increasing upstream in Fig. 6.8(ii)d up to $We \sim 175$; strain-softening eventually provides some slight shrinkage of this structure, apparent at $175<We<370$. One notes ahead that the equivalent stress-data on micellar NM_Π_ABS (Fig. 6.8(iii)), largely replicates that of NM_τ_p_ABS_VGR; only noting clearer downstream splitting of the N_1 red-zone earlier around $We \sim 75$, and less intense structures on

the downstream obstruction-backface.

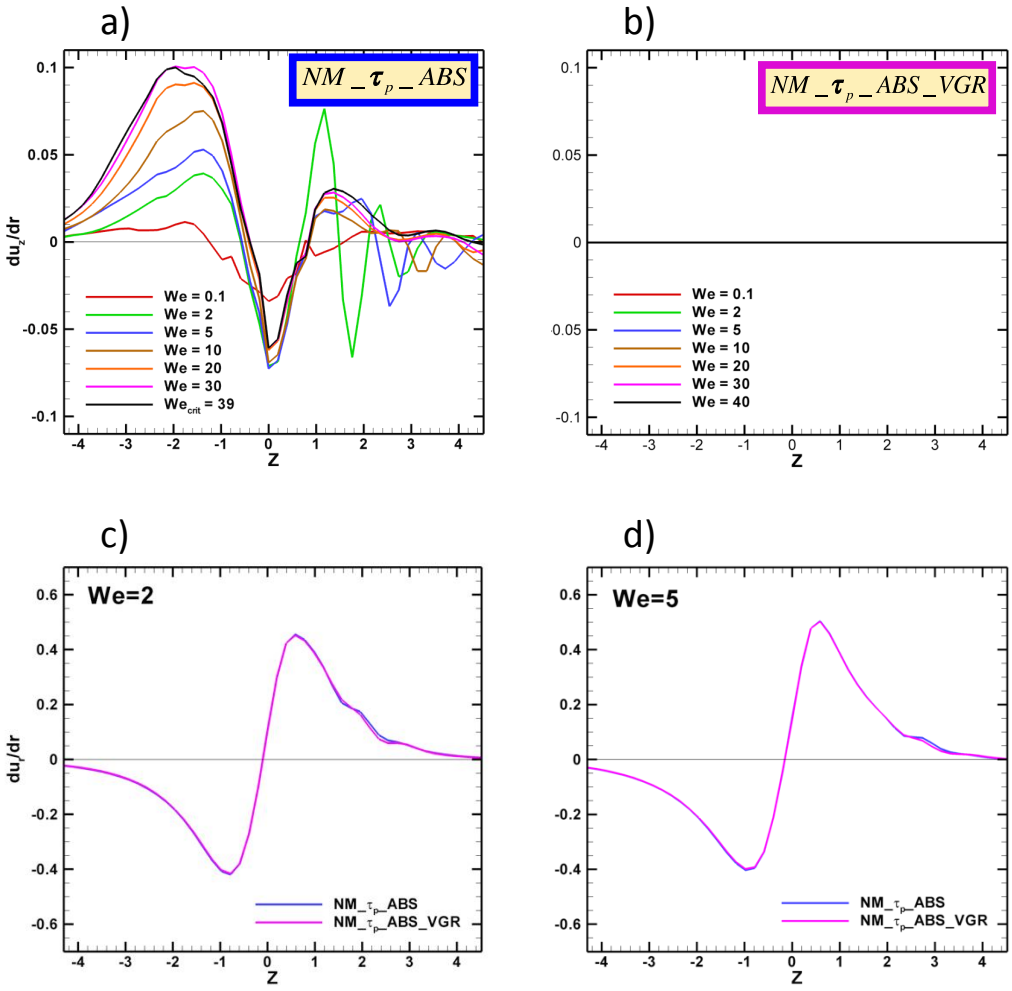

Figure 6.10. At centreline: (a) and (b) du_z/dr versus *We*; du_r/dr (c) *We*=2 and (d) *We*=5; NM_τ_p_ABS and NM_τ_p_ABS_VGR

6.6.2 Conformation-tensor solutions – Micellar NM_Π_ABS model

We_{crit} levels In addition to the ABS-correction, this second strategy to attain high-*We* solutions focuses on solving the problem when cast in primary variable conformation tensor form (see eqs.(8-10)). The critical elasticity level attainable with NM_Π_ABS is We_{crit}=175 (Table 6.3)[6], which stands at some 4.5 times that achieved with NM_τ_p_ABS. Hence, as

[6] We_{inc} – NM_Π_ABS: analogous to NM_τ_p_ABS_VGR with earlier We_{crit}=175

proposed in theory, the posing of the problem through its corresponding differential constitutive equation (with its data dependency) and its boundary conditions, does discretely have an impact on tractability of numerical solutions. Moreover, the constitutive equation solved for each case plays an important role, since the $\boldsymbol{\Pi}$-based equation is reinforced relative to the $\boldsymbol{\tau_p}$-based equation, maintaining positive definiteness via (i) f_{Π} acting as a RHS-equation scaling-factor, and (ii) the explicit absence of the rate-of-deformation tensor $\boldsymbol{D}$. Consistently, f_{Π}*-functional* values originating from NM_Π_ABS are larger compared with the remaining τ_p -versions (Table 6.1) (López-Aguilar et al 2014). In contrast to the further achievements with Π-VGR-correction, one can state that this position is not substantially altered under combination with the conformation tensor implementation (as in NM_Π_ABS_VGR). It is conspicuous that NM_τ_p_ABS_VGR capability in this regard outperforms the {NM_Π_ABS, We_{crit}=175} implementation, with the exaggerated response of {NM_τ_p_ABS_VGR , We_{crit}=370}.

Hence, though the conformation tensor approach is certainly a reasonable candidate to consider for generating high-*We* steady-state solutions, one concludes thus far and in practical terms, that the superior method of implementation is VGR-correction imposed on NM_τ_p_ABS.

6.7. General applicability – PTT(ε=0.25,β=1/9) solutions: EPTT and LPTT results

We_{crit} levels In an effort to assess more widely the generality and applicability of current findings to cover alternative constitutive models, one may appeal to the class of Phan-Thien-Tanner models, being non-thixotropic and phenomenological viscoelastic models derived from a network-basis. Table 6.3 lists counterpart high We_{crit} findings for such model solutions, under application of ABS, VGR and Π-corrections, as above. These are now impressively large, unrealised elsewhere, and offer wide scope for new application accordingly (large deformation scenarios, as in microfluidics). Conspicuously, the ABS-correction yields an order-of-magnitude increase in We_{crit}, from $O(10^2)$ under the natural-signed version (López-Aguilar et al 2014), to $O(10^3)$ under EPTT_ABS results. Specifically, We_{crit}=210 for the natural signed EPTT model (López-Aguilar et al 2014), has now been further increased to We_{crit}={4000, 4250, 1000} for {EPTT_ABS, EPTT_ABS_VGR,

EPTT_ABS_Π}[7]. Consistently to the thixotropic context above with Π-correction, which also subsumes ABS-correction, there is improvement in We_{crit} of some five-times above the natural-signed EPTT_τ_p alternative; yet, this lies some four times lower than that achieved under EPTT_ABS and EPTT_ABS_VGR counterparts. Note, the level of We_{crit}=210 for the natural-signed EPTT model (López-Aguilar et al 2014), is already elevated above that for thixotropic NM_τ_p, (see also We_{crit}=11 for natural-signed linear-version LPTT). As previously reported elsewhere (López-Aguilar et al 2014), such high-*We* solutions attainable with EPTT versions, are in part a consequence of its non-linear exponential explicit f_τ-*We* functionality (Table 6.3). In contrast, linear f_τ-*We* relationships are observed within steady-state f_τ for thixotropic NM_τ_p (Table 6.3) models or non-thixotropic LPTT version. This is reflected in complex flow via the relatively large EPTT f_τ-maxima encountered as *We* is elevated and when compared to those under NM_τ_p (or LPTT) solutions (Table 6.1).

Considerations at very high-We levels Fig. 6.11 gathers a sample of high-*We* EPTT_ABS solutions, via the stress discriminant in the expression for the eigenvalues, s_1 and s_2 (eqs.(18-19)). Here a fresh phenomenon arises, not prominent at more moderate *We*–levels. At such large *We*=O(10^3) levels, numerical noise becomes evident in the solution exit-zone (Fig 11a), which is first detected around *We*~750 cross-stream and emanating from the centreline. This feature, which grows with further rise in *We*, comes from solution anomalies arising between interior domain and boundary section solution approximation (applies similarly at inlet-station, 1000<*We*<2000). These *theoretic-discrete* inlet-outlet region considerations are not graphically evident at relatively low *We*<220; they onset earlier at exit than entry at *We*~750; strengthen at exit *We*~1000; become strong and clearly manifested around *We*~2000, at inlet and outlet; to be finally, amplified as *We* rises up to We_{crit}=4000, when inlet fluctuations are apparent and penetrating into the field up to the contraction itself. These inconsistencies are dealt with by a feedback-feedforward technique on stress/kinematics, to mimic steady fully-developed flow state, taking primary information from the interior-domain discrete solution and translating this to the domain boundary sections. This is accomplished by averaging internal stress/velocity-gradient components (velocity remains unadjusted) and substituting this refreshed information into inlet and outlet neighbour nodal points, to thus reset the stress

[7] We_{inc} – EPTT_ABS, EPTT_ABS_VGR and EPTT_ABS_Π: analogous to NM_τ_p_ABS_VGR to *We*=400, in 50 to *We*=500, in 250 to corresponding We_{crit}

components. Implementation of such a procedure, removes the source of solution discrepancy arising at inlet-outlet, to provide the counterpart and repaired solution forms of Fig. 6.11b, which have been extended to even larger *We*-levels (*We*=5000+).

6.8 Conclusions

Highly elastic thixotropic solutions have been achieved through three alternative approaches (independent, interchangeable): (i) absolute f_τ-functional correction (ABS-correction – related to positive energy dissipation (Bird et al. 1960, 1977; Aris 1962) and accurate viscosity prediction); (ii) centreline velocity gradient correction (VGR-correction – f_τ-values as with ABS-correction); (iii) $\boldsymbol{\Pi}$ conformation tensor correction ($\boldsymbol{\Pi}$-correction – change of variable). The first two alternatives have provided an increase of some ten times in We_{crit} on their preceding versions. ABS-correction adjusts {We_{crit}=4.9, NM_τ_p} to {We_{crit}=39, NM_τ_p_ABS}; whilst VGR-correction renders {NM_τ_p_ABS_VGR, We_{crit}=370} layered on top of ABS-correction. The third alternative {NM_Π_ABS, We_{crit} =175} has also increased We_{crit} by some five times with respect to NM_τ_p_ABS solutions.

The s_2-eigenvalue has been identified as a suitable marker for numerical stability retention. Localised minima first arise on the centreline, just downstream of the contraction, which are found responsible for linking-up and stimulating contraction-wall minima, that ultimately dominate overall as *We* rises. Then, localised undershoot–overshoot phenomena (reflected in N_1 and *f*-functional data) are observed on the backface of the contraction-wall, with subsequent solution penetration into the field. The ABS-correction retards the appearance of such s_2 undershoot–overshoot phenomena, although ultimately their presence does not affect the quality of solutions in primary variables. This is noted through smooth and tractable trends in { τ_{rz}, N_1, N_2}-fields and *We*-incrementation. N_2 provides insight on trends in upstream vortex-dynamics with *We* elevation (López-Aguilar et al. 2014): reflecting initial vortex-enhancement, then, vortex-suppression {NM_τ_p_ABS_VGR, 175<*We*<370}.

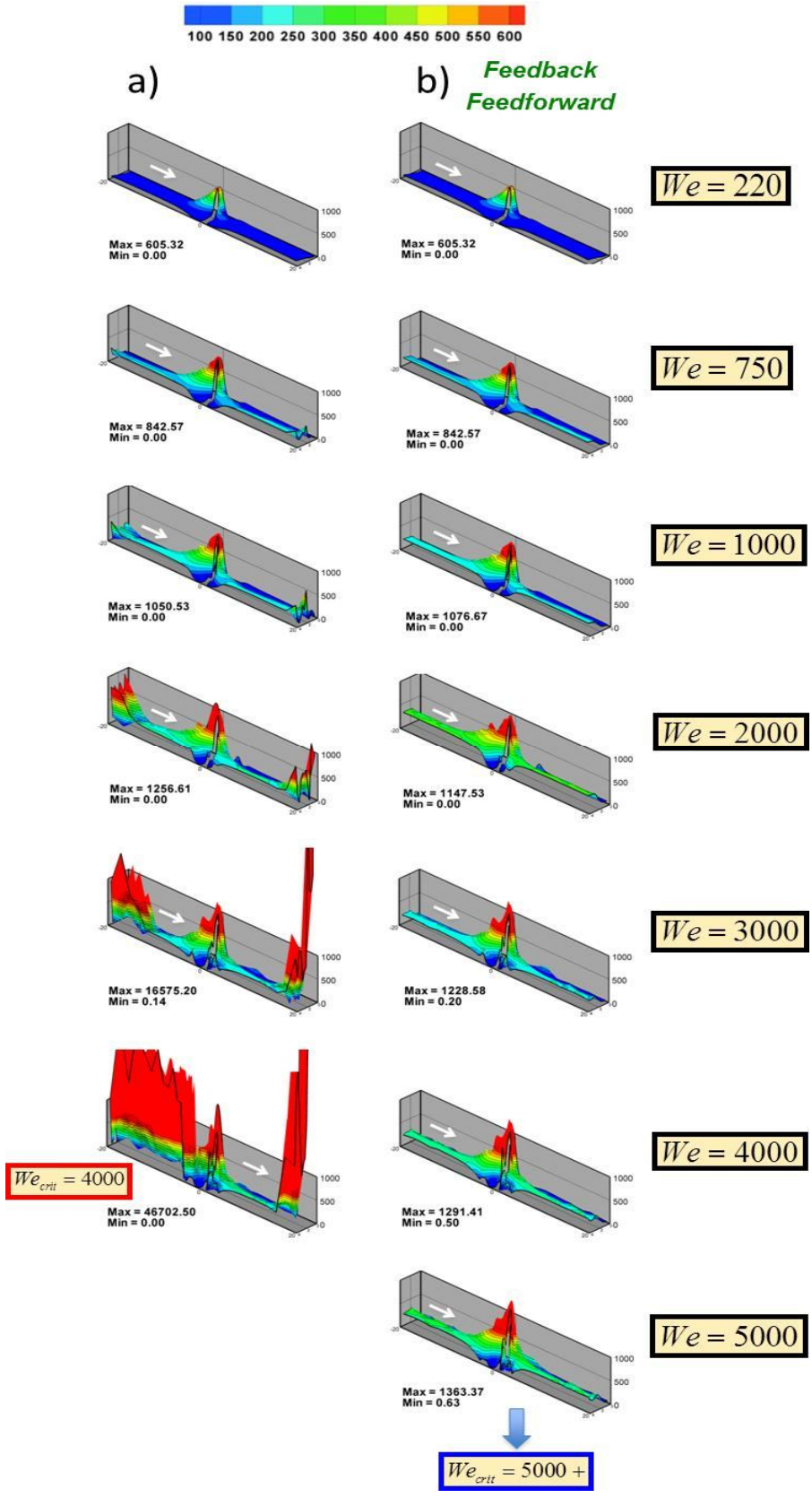

Figure 6.11. Stress discriminant fields versus *We*; EPTT and EPTT_ABS

Theoretical observations are derived on Π-component response under centreline deformation conditions. This is detailed through *We* rise via: (i) $\{s_1, s_2\}$ eigenvalue-pair dual-nature in correspondence with $\{\Pi_{zz}, \Pi_{rr}\}$; (ii) location of discontinuities in the linearised inhomogeneous Π-component estimation, interpreted against the components of its poles; and (iii) numerical $\{\Pi_{zz}, \Pi_{rr}\}$ departure from their linearised inhomogeneous estimation. In the first aspect this relies upon $\{s_1, s_2\}$ eigenvalue-pair dual-nature being dictated by the sign-switch in N_1. The third aspect dictates the degree and capture of departure from the linear viscoelastic regime.

In addition, generalisation of current findings for thixotropic theory has been explored under classical non-thixotropic models too. This has led to incrementation in We_{crit} well over an order of magnitude for network-based time-independent PTT models [ABS-correction relates to positive stored elastic energy in this case (Hulsen 1990)]; in contrast to two orders of magnitude achieved for thixotropic models. Stable solutions have been extended for the *exponential*-PTT version, from the natural-signed {EPTT, We_{crit}=230} to {EPTT_ABS, We_{crit}=4000}; and {EPTT_ABS_VGR, We_{crit}=4250}. In its conformation-tensor form, incrementation is observed with {EPTT_ABS_Π, We_{crit}=1000}. In terms of the *linear*-PTT version, the natural-signed {LPTT, We_{crit}=11} is now adjusted to {LPTT_ABS, We_{crit}=210}. The relatively larger We_{crit} under EPTT are due to its larger f_τ-values, coming from its exponential f_τ-*We* relationship, as opposed to those under the linear relationship given with LPTT and NM_τ_p models (López-Aguilar et al. 2014). At very high *We*=O(10^3) and for EPTT, it has been shown how to ensure satisfaction of fully-developed inlet-outlet region conditions (theory to practice, avoiding inlet-outlet inconsistencies), to ultimately gather smooth solutions at even larger elasticity levels (*We*=5000+).

CHAPTER 7

Numerical modeling of thixotropic and viscoelastoplastic materials in complex flows

This chapter is concerned the application of the constitutive developments in Chapters 5 and 6, in the numerical modelling of thixotropic and viscoelastoplastic material systems through two approaches: (i) the new micellar thixotropic constitutive model for worm-like micellar systems that introduces viscoelasticity into the network-structure construction/destruction kinetic equation, studied in chapters 5 and 6; and (ii) adopting a Bingham-Papanastasiou model. The appearance of plastic behaviour arises through the micellar-polymeric viscosity, by increasing the zero-shear viscosity (low solvent fractions), whilst the Bingham-Papanastasiou introduces plastic features through the solvent viscosity. The characteristics of thixotropic worm-like micellar systems are represented through the class of Bautista-Manero models. The correction incorporated in Chapter 6, based on physical arguments for fluidity, in which absolute values of the dissipation-function are adopted in complex flow, permits access low-solvent fractions and high-elasticity levels. Considering elastic and plastic influence separately, solutions are compared and contrasted for contraction-expansion flow, identifying such flow field features as vortex dynamics, stress field structure, yield front patterns, and enhanced pressure-drop. Particular attention is paid to the influence of enhanced strain-hardening that is introduced through stronger thixotropic structural features.

7.1 Introduction

This study addresses the topic of modelling complex flow of micellar-yield stress fluids in the 4:1:4 contraction-expansion benchmark flow problem. Here, two sources of plastic behaviour are considered: (i) through the *solvent viscosity*, offered by Bingham-Papanastasiou model (Papanastasiou 1989; Mitsoulis 2007; Belblidia et al. 2011; Al-Muslimawi et al. 2013); and (ii) through the *polymeric viscoelastic contribution*, introduced via Bautista-Manero models

(Bautista et al. 1999; Manero et al. 2002; Boek et al. 2005; López-Aguilar et al. 2014a and b). The class of Bautista-Manero models has been derived to represent the characteristics of thixotropic worm-like micellar systems. Herein, low-solvent fractions and high-elasticity levels are accessible. This is achieved through a correction to the constitutive equation for these polymeric Bautista-Manero models, based on physical arguments for fluidity, in which absolute values of the dissipation-function are adopted in complex flow (López-Aguilar et al. 2014b).

Yield-stress concept Although the concept of viscoplastic materials was first introduced by Bingham over nine decades ago (Bingham 1922), still this topic remains one of the most controversial in rheology today (Belblidia et al. 2011; Bingham 1922; Barnes 1999; Renardy 2010). Viscoplastic properties exhibit a so-called 'yield stress, τ_0 effect', which governs the transition from solid-like to liquid-like response. Under flow, these materials develop plastic plug-like flow zones, due to elastic resistance from the microstructure, in which any deformation essentially disappears. The controversy surrounding yield stress, is associated with its existence, representation, experimental measurement and data interpretation. Note that, in practice, most materials weakly yield, or creep in the limit of zero shear-rate.

Barnes and Walters (1985) demonstrated, through experimental data gathered from a constant stress rheometer, that in this context the yield stress concept was a pure idealisation. Thereby, given sufficiently accurate measurement, no 'actual' yield stress truly existed. Subsequently, the non-existence of yield stress, claimed by Barnes and Walters, was challenged by Hartnett and Hu (1989). These authors used a falling ball viscometer to demonstrate unambiguously that an aqueous Carbopol solution exhibited a yield stress - to an engineering approximation. To further complicate the situation, Møllera et al. (2006) related the uncertainty in interpretation of some rheometrical measurement to material time dependency; that is, to thixotropic behaviour and time-scale. Notably, no single method has been universally accepted as the standard for measuring yield stress, and it is not unusual to find large variations in results obtained from different methods with the same material (Bonn 2006).

Theoretical and numerical modelling of viscoelastoplastic material So-called Bingham fluids display a distinct finite stress level (yield stress) at vanishingly low shear rates. In areas of intense deformation, above the yield stress limit, the material is observed to flow and behave as a Newtonian fluid. The presence of these unyielded and yielded regions across the flow domain, provide a corresponding interface between them, or yield-front, as an intrinsic

discontinuity to the representation. Then, more complex shear viscous response may be included through power-law type rate-dependency (Herschel-Bulkley or Casson models). A drawback to using these models is their discontinuous stress representation. This necessitates using robust numerical techniques for discretisation, to accurately describe the yielded-unyielded regions and their corresponding interface (Belblidia et al. 2011).

To date, one successful approach proposed to deal with this discontinuous representation is the regularisation method of Papanastasiou (1989). As such, the resulting Papanastasiou viscoplastic model consists of a single unified, modified constitutive relation - applicable to both yielded and unyielded regions alike. Such an approach proffers the advantage that it eliminates the need for explicit tracking of the yield-surface. Here, an *exponential stress-growth* parameter is introduced to access numerical solutions, which in limiting terms may practically replicate ideal model results. This model has been successfully applied in a plethora of studies, to describe viscoplastic and viscoelastoplastic flows, in simple-ideal and complex flow scenarios (Mitsoulis 2007). This would include - entry-exit flows from dies; flow past objects and squeeze flows; steady Oldroyd-B 4:1:4 contraction-expansion flow (Belblidia et al. 2011); and steady die-swell flow for exponential Phan-Thien-Tanner models (EPTT, viscoelastic, shear-thinning, strain-hardening/softening; Al-Muslimawi et al. 2013). Here, the conventional yielded-unyielded regions across the flow domain were studied. Additionally, in Belblidia et al. (2011), *vortex dynamics*, *excess pressure drop versus yield-stress* and *enhancement with viscoelasticity* were all reported; whilst in Al-Muslimawi et al. (2013) *swelling-ratio* and *excess pressure loss* received attention.

Worm-like micelle solution systems are a versatile family of fluids, as already outlined in previous chapters. In this particular section of the work, the capability of generating yields-stress characteristics (Calderas et al. 2013) is evaluated in complex flow. This application is vital in industrial fields like drilling fluids for enhanced oil-reservoir recovery (EOR) (López-Aguilar et al. 2014a), and additives in household-products, paints, cosmetics, health-care products, drag reducing agents (López-Aguilar et al. 2014a; Yang 2002).

Micellar constitutive models – Apart from the well-known Bautista-Manero-Puig approach, many approaches have been pursued to model wormlike micelle flow behaviour. Particular attention is paid to De Souza (2009 and 2011) work, who has proposed an alternative thixotropic-viscoelastoplastic model, based on a structure equation defined on the second invariant of the stress tensor τ_p to drive the structure-destruction mechanics. Then,

the differential equation for their *'structure parameter'* is introduced within and to form a generalised viscoelastic differential constitutive equation. In contrast, the family of Bautista-Manero models use the dissipation function $\boldsymbol{\tau}_p : \boldsymbol{D}$ (i.e. NM_τ_p) to this same end (López-Aguilar et al. 2014a and b). The de Souza model has been used in ideal simple and complex flow situations to represent thixotropic and viscoelastoplastic characteristics; see for example, overview for models representing viscoelastoplasticity (de Souza and Thompson 2012); and flow in an expansion-contraction setting (Hermany et al. 2013).

7.2 Governing equations, constitutive modelling and problem specification

The governing equations and constitutive equations considered in this chapter have been detailed in chapter 2. The non-dimensional continuity and momentum conservation princples are expressed in eqs.(2.11)-(2.12), whilst the stress equations is given in (2.27)-(2.28). The schematic representation of the 4:1:4 axisymmetric, rounded-corner contraction/expansion flow problem, alongside its corresponding mesh data, are reported chapter 5.

7.2.1 Viscoelastoplastic Bingham-Papanastasiou model - solvent contribution form

In this Chapter 2, non-Newtonian viscoplastic properties are introduced via a regularization approach adopting the Bingham-Papanastasiou model (Papanastasiou 1989), eqs.(2.47)-(2.48). Hence, yield stress contributions are recognised as entering through the solvent viscosity functionality alone. Note, there are other alternative formulation choices to embrace plastic behaviour via Papanastasiou regularisation (Papanastasiou 1989), namely: *(a)* within polymeric viscosity functionality alone; and *(b)* via both solvent and polymeric viscosity contributions. Studies illustrating the consequences of applying these various options have already been conducted and reported upon elsewhere, with polymeric representations under Oldroyd-B (Belblidia et al. 2011) and EPTT (Al-Muslimawi et al. 2013) models.

A general differential statement of the **viscoelastic** Bingham-Papanastasiou model employed here, with only solvent yield stress contribution**,** may be expressed in dimensionless form as:

$$\boldsymbol{T} = \boldsymbol{\tau}_s + \boldsymbol{\tau}_p \tag{7.1}$$

$$\boldsymbol{\tau}_s = 2\beta\varphi\left(II_D; m_p, \tau_0\right)\boldsymbol{D} \tag{7.2}$$

$$We\overset{\nabla}{\boldsymbol{\tau}}_p = 2(1-\beta)\boldsymbol{D} - f_\tau \boldsymbol{\tau}_p, \tag{7.3}$$

The Papanastasiou regularisation specifies an exponential functional-form in its solvent viscosity contribution, based on the second invariant, $II_D = \frac{1}{2} tr\boldsymbol{D}^2$, of the rate of deformation tensor, viz:

$$\varphi\left(II_D; m_p, \tau_0\right) = \eta_0 + \frac{\tau_0\left(1-e^{-m_p|II_D|^{1/2}}\right)}{2|II_D|^{1/2}}, \tag{7.4}$$

where parameters of $\{\tau_0, m_p\}$ represent, τ_0 the base cut-off yield stress factor, and m_p the regularisation stress growth exponent (with scale of time). The τ_0-parameter expresses the stress level below which plastic behaviour is observed and is equivalent to a Bingham Number, $Bn = \tau_0 = \tau_y L_{char}/\eta_0 U_{char}$.

7.2.3 Micellar NM_τ_p_ABS Bingham-Papanastasiou model

To proceed to the micellar viscoelastoplastic representation, one needs to specify the generalised functional f_τ, in eq.(7.1)-(7.3), imbuing a thixotropic networked nature to the fluid system. Here, the new constitutive equation, based on the Bautista-Manero model-class, has proposed in chapters 5 and 6 (eqs. (2.33)-(2.36)) is employed for modelling wormlike micellar systems. This constitutes the base-level constitutive background upon which the present study is founded.

7.2.4 Material functions Under such a description, the NM_τ_p_ABS-Papanastasiou (named NM_τ_p_ABS-Pap) dimensionless material functions for viscometric flow may be extracted, as:

$$\eta_{Shear} = \beta\varphi\left(II_D; m_p, \tau_0\right) + \frac{(1-\beta)}{f_\tau} \tag{7.5}$$

$$\eta_E = 3\beta\varphi\left(II_D; m_p, \tau_0\right) + \frac{3(1-\beta)\, f_\tau}{\left(f - 2We\dot{\varepsilon}\right)\left(f + We\dot{\varepsilon}\right)} \tag{7.6}$$

$$N_1 = \frac{2(1-\beta)We\dot{\gamma}^2}{f_\tau^2} \tag{7.7}$$

These material functions in eqs.(7.5)-(7.7) provide the vital background and model reference against which to interpret anticipated complex flow response. One notes the extremely low levels of β-solvent fraction attained practically, those of β={10^{-2},10^{-3}}; chosen to enhance the viscoelastoplastic characteristics inherent to these yield-stress polymeric micellar fluids, under NM_τ_p_ABS-pap modelling. Moreover, the micellar construction and destruction parameters are ω=4.0 and ξ_{G0}={1,0.1125}. Here, at each solvent-fraction level, fluids with {ω,ξ_{G0}}={4,1} (relatively larger structure destruction parameter) display weaker strain-hardening characteristics (smaller peak in extensional viscosity) relative to those with {ω,ξ_{G0}}={4,0.1125} (relatively reduced structure destruction parameter) (see Fig. 3.3-3.5). Consideration of the solvent viscoplastic Papanastasiou features are evaluated through variation of yield stress parameter τ_0={0.01,0.1,0.5,1}, and the regularisation stress-growth exponent m_p={10,10^2,10^3,10^5,10^7}. Also, viscoelastoplastic behaviour is pursued through β-variation for NM_τ_p_ABS, with decreasing β={0.9,0.5,1/9,10^{-2},10^{-3},10^{-4},10^{-5}} (Calderas et al. 2013). The special cases for which either τ_0 or m_p attain null values, characterise absence of viscoplasticity, and thus collapse the fluid representation to that of the NM_τ_p_ABS model. In Fig. 3.3-3.5, dimensionless plots are provided of the material function against deformation rates in simple shear and uniaxial extension deformations.

7.3 Numerical results: Vortex dynamics - τ_0 and We variation

As Weissenberg number (*We*) and yield stress (τ_0) are increased, the kinematic nature of this complex flow is illustrated through the streamline patterns and graphs of vortex-intensity of {Fig. 7.1 and Table 7.1}. These data are generated under *solvent* Papanastasiou parameters of m_p=10^2 and τ_0={0,0.01,0.05,0.1}, which enforces the *solvent* plastic characteristics. In addition, the *polymeric* NM_τ_p_ABS parameters used are ω=4 and ξ=1, with solvent fraction of β=10^{-2}. Interestingly, vortex activity (size and intensity) decreases as either *We* is increased at a fixed τ_0, or τ_0 is increased at a fixed *We*.

At We=0.1 and τ_0=0 (viscoelastic NM_τ_p_ABS, no solvent yield stress), the upstream and downstream vortex structures appear relatively symmetric in structure about the contraction. Here, the upstream vortex is slightly larger and more intense (Ψ_{min}= $-\Psi^*_{min}$x10^{-4}=12) than the downstream vortex (Ψ_{min}=9.05). Larger yield stress levels under NM_τ_p_ABS-Pap representation, lead to vortex-intensity suppression. In particular, at τ_0=0.01, both upstream

(Ψ_{min}=5.88) and downstream (Ψ_{min}=4.35) vortex-intensity drops by some 50% away from the {NM_τ_p_ABS, τ_0=0} reference solution. Notably, additional incrementation of τ_0={0.05,0.1} generates even further vortex suppression of {96%,99%}.

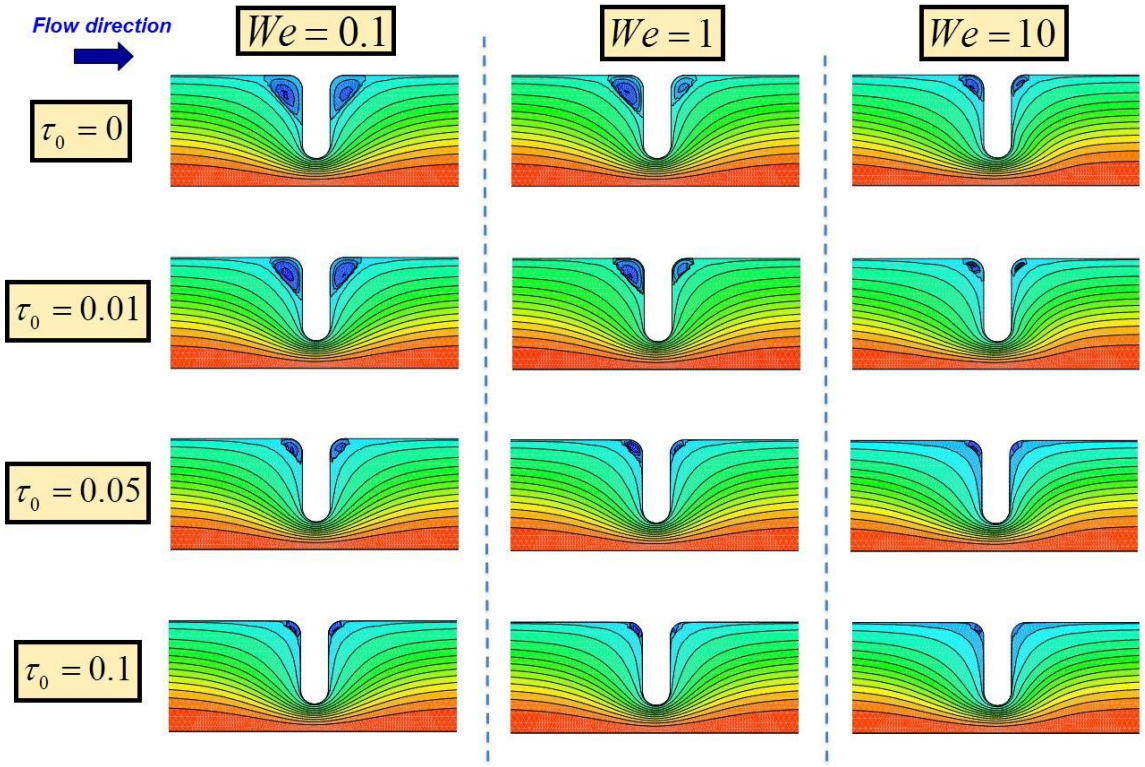

Figure 7.1 Streamlines against τ_0 and *We*; {m_p, β, ω, ξ_{G0}}={10^2,10^{-2},4,1}

Table 7.1 Vortex intensity (Ψ_{min}=-Ψ_{min}^{*} $x10^{-4}$) against τ_0 and *We*; {m_p, β, ω, ξ_{G0}}={10^2,10^{-2},4,1}

	Ψ_{min}=-Ψ_{min}^{*} $x10^{-4}$					
	We=0.1		*We*=5		*We*=10	
τ_0	Upstream	Downstream	Upstream	Downstream	Upstream	Downstream
0*	12.0	9.05	8.59	2.51	1.28	0.727
0.01	5.88	4.35	3.76	1.02	0.442	0.385
0.05	0.543	0.358	0.356	0.156	0.136	0.048
0.1	0.147	0.117	0.106	0.017	0.043	~0

*Solutions reduced to NM_τ_p_ABS (NM_τ_p_ABS-Pap τ_0=0)

As *We rises through {1,10} at* τ_0*=0.01*, this declining vortex behaviour is still further exaggerated, with percentage-drop in intensity from each corresponding NM_τ_p_ABS solution of {60%,65%}.

At *larger* τ_0*-values of {0.05,0.1} at We={1,10}*, this vortex suppression response from NM_τ_p_ABS solution, and at each fixed *We*-level, is even more marked, O(95%); with the downstream vortex almost completely disappearing at {τ_0=0.1, *We*=10}.

These trends are clearly illustrated in the graphical plots of Fig. 7.2-top (m_p=10^2), upstream-downstream vortex-intensity versus τ_0 at each fixed *We*-level (negative exponential form). The common trend across all three *We*={0.1,1,10} curves is the drop in intensity to around the same intensity level by τ_0=0.05. Since the starting intensity at τ_0=0 for each *We*-level rises with fall in *We*, this leads to ever increasing intensity drop-rates as *We* rises. The upstream (left) trend graph versus the downstream (right) graph, illustrates the more marked intensity goes with the upstream vortex activity. Such trend adjustment is nonlinear in change with *We*-level, the largest being around *We*=1.

Regularisation stress growth exponent m_p***-variation*** The upper graphs for (m_p=10^2) versus the lower graphs for (m_p=10^3) of Fig. 7.2, illustrate the influence of increased yield stress characteristics and enhancement of plastic behaviour through the *solvent* (see material functions, Fig. 2). Here, there is steeper early decline in intensity, from τ_0=0.0 to τ_0=0.01, that is apparent in all instances of *We*. Asymptotic larger τ_0-behaviour is rather more rapidly assumed under (m_p=10^3) response, this being quite evident even at the τ_0=0.01 level.

Solvent fraction β***-variation*** As above, polymeric concentration effects on vortex dynamics are illustrated in Fig. 7.3 through β={10^{-2},10^{-3}} comparison. At such low solvent fraction levels, there are no significant differences in vortex dynamics to observe; only manifesting a slight increase in the vortex intensity for τ_0<0.05, which is larger with smaller *We*-level.

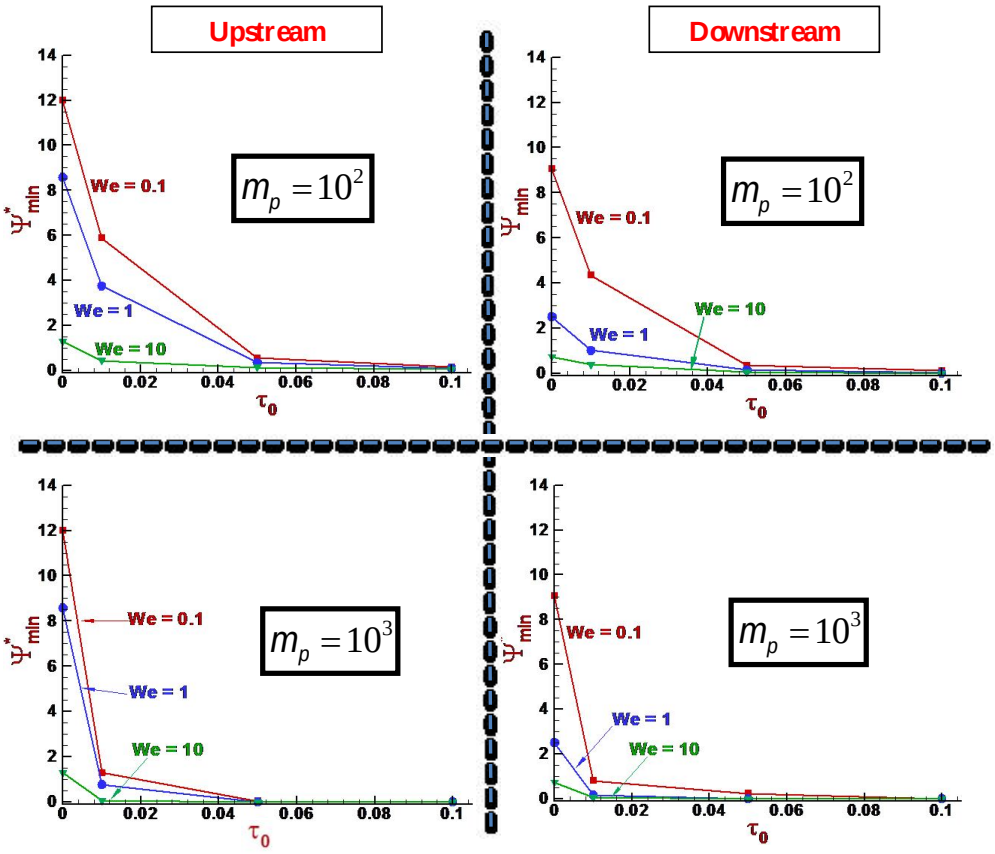

Figure 7.2 Vortex intensity (Ψ_{min}=- Ψ_{min}^{*} $x10^{-4}$) against τ_0 and *We*;
$\{\beta, \omega, \xi_{G0}\}=\{10^{-2},4,1\}$;

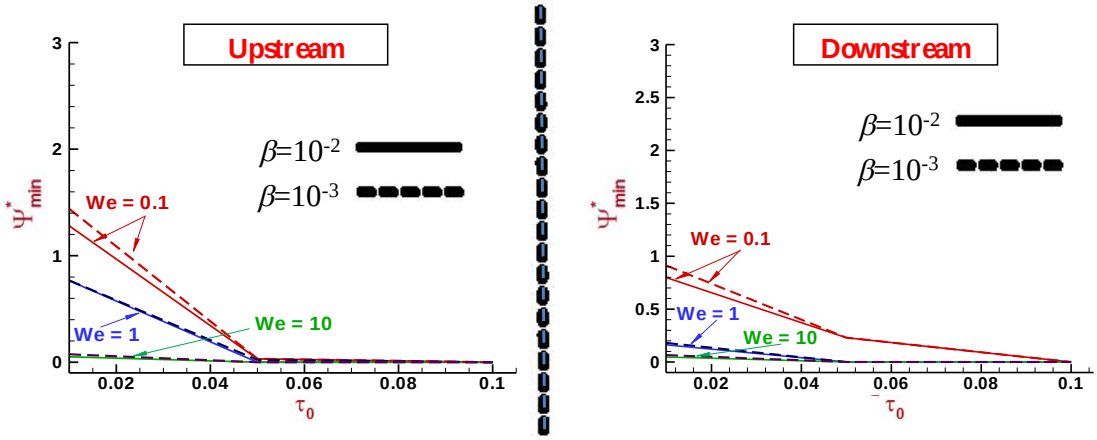

Figure 7.3 Vortex intensity (Ψ_{min}=- Ψ_{min}^{*} $x10^{-4}$) against τ_0 and *We*; { m_p, ω, ξ_{G0}}={10^3,4,1};
β=10^{-2}(continuous lines), β=10^{3}(dashed lines)

7.4 Normal stress differences - τ_0 and We variation

Adopting the parametric study approach as above and under the setting $\{\beta, m_p\}=\{10^{-2}, 10^{3}\}$, the influence of plasticity and elasticity on normal stress difference is gathered through N_1-data fields of {Fig. 7.4; Table 7.2} and $\{\tau_0, We\}$ increase. Then, τ_0-incrementation at *any fixed* $We=\{0.1,1,10\}$ level, reveals little adjustment in N_1 magnitude or distribution. In contrast, at *any fixed* $\tau_0=\{0,0.01,0.1\}$ *level*, N_1-extrema suffer a drop as *We* is elevated. This feature can be tied to the wall shear-zones, and as such is a manifestation of shear-thinning. In the extreme case of $\{\tau_0=0.1, We=1\}$, then $\{N_{1max}, N_{1min}\}=\{1.06,-0.94\}$ are 62% less intense relative to $We=0.1$ data of $\{N_{1max}, N_{1min}\}=\{2.76,-2.50\}$. At $We=10$, this trends is more abrupt, with $We=10$ data of $\{N_{1max}, N_{1min}\}=\{0.59,-0.46\}$, which represent a drop of 80% relative to the same $We=0.1$ extrema. Here, the red-positive and blue-negative regions, both upstream and downsteam of the contraction, become less intense as *We* is elevated (as a consequence of shear-thinning/strain softening, enhanced by low-β solvent-fraction levels). Nevertheless, the domain occupation of the red-positive region grows in size, whilst the blue-negative zone contracts. Moreover, as *We* rises, the blue-negative zone at the centreline (and its local maxima) is convected downstream, as observed elsewhere (López-Aguilar et al. 2014b).

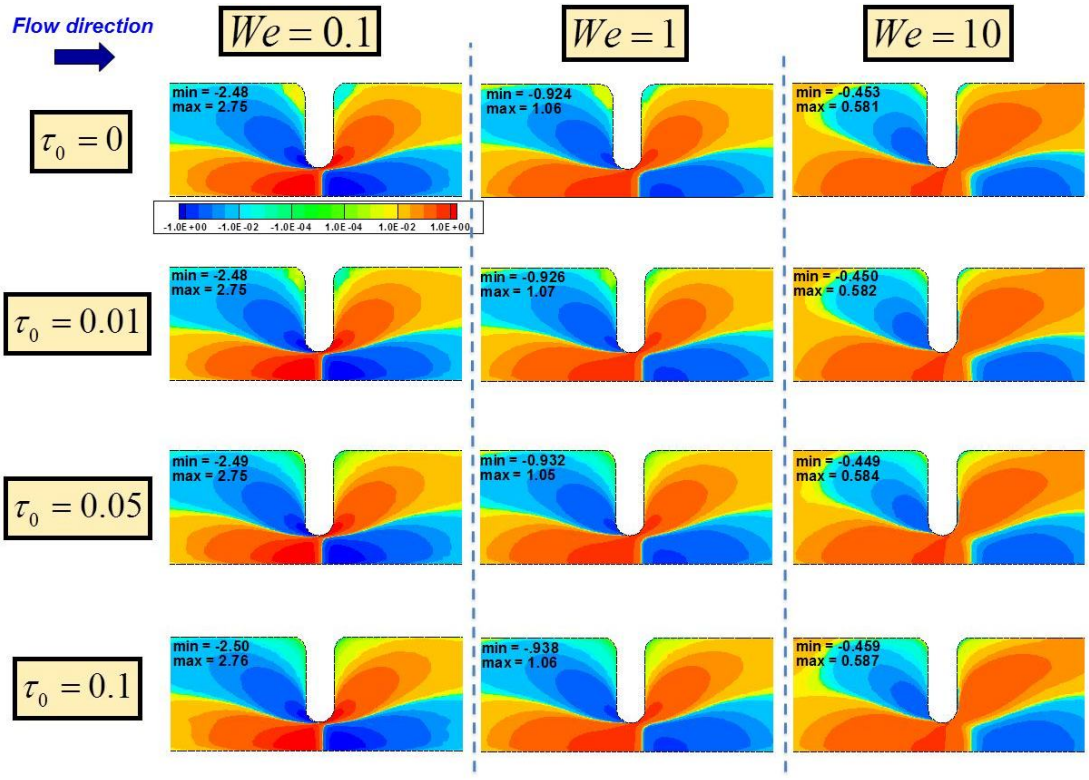

Figure 7.4 N_1 against τ_0 and *We*; $\{m_p, \beta, \omega, \xi_{G0}\}=\{10^{3},10^{-2},4,1\}$

In the upstream and downstream salient-corner zones, N_1-data fields of {Fig. 7.4; Table 7.2} provide vortex-like structures, essentially identifying N_2-contributions to N_1, that evolve in the same fashion as do the true kinematic vortex-structures (see section 4 above). Hence, these vortex-like N_2-structures shrink as τ_0 and *We* rise. One notes with look ahead, that these structures are exaggerated when extensional viscosity effects are introduced via ξ_{G0}-variation.

Table 7.2 First normal stress difference (N_1) against τ_0 and *We*; $\{m_p, \beta, \omega, \xi_{G0}\}=\{10^3,10^{-2},4,1\}$

		N_1		
τ_0		*We*=0.1	*We*=5	*We*=10
0	Max.	2.75	1.06	0.581
	Min.	-2.48	-0.924	-0.453
0.01	Max.	2.75	1.07	0.582
	Min.	-2.48	-0.926	-0.450
0.05	Max.	2.75	1.05	0.584
	Min.	-2.49	-0.932	-0.449
0.1	Max.	2.76	1.06	0.587
	Min.	-2.50	-0.938	-0.459

7.5 Yield fronts – yielded and unyielded regions, τ_0 and We variation

Fig. 7.5 conveys the solution perimeter and divide between yielded (red) and unyielded (blue) regions at $\{\beta, m_p\}=\{10^{-2},10^3\}$ for the NM_τ_p_ABS-Pap model. Once more, the effects of plasticity are analysed, via $\tau_0=\{0.01,0.05,0.1\}$, and those due to elasticity, via *We*=$\{0.1,1,5,10\}$. The cut-off criterion for these fields is based on the magnitude of stress (through its second-invariant, see Mitsoulis 2007; Belblidia et al. 2011; Al-Muslimawi et al. 2013) exceeding τ_0 in each instance. The dominant and most interesting features to report here are those given in terms of *τ_0-incrementation at fixed We-level*. For instance, at ***τ_0=0.01 and We=0.1***, red yielded regions are found near the tube-wall, where the shear rates are relatively large. Approaching the geometry centreline, blue relatively slender unyielded regions appear around and along the centreline, upstream and downstream of the contraction. In shape, this unyielded centreline-zone resembles a necking-filament, with bulbous zones either side of the contraction. This structure-pattern tapers to a sharp end that is directed towards the contraction, connected by a slender column-like thread that passes through the contraction along the centreline. In the recess zones (geometry salient-corners) concave-shaped unyielded regions are also present.

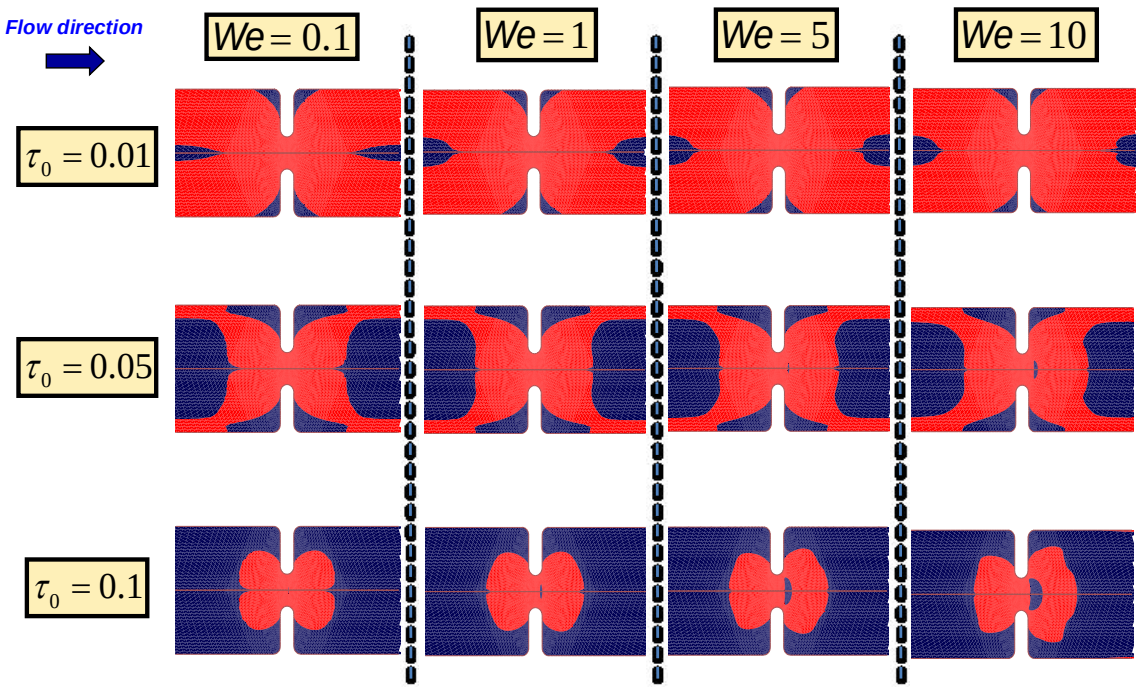

Figure 7.5 Yield fronts against τ_0 and *We*; $\{m_p, \beta, \omega, \xi_{G0}\}=\{10^3,10^{-2},4,1\}$

As yield-stress level is ***raised to*** τ_0***=0.05***, the unyielded regions in the core-flow have considerably expanded outwards, towards the tube walls; also, those in the recess zones have elongated upstream and downstream. This defines the perimeter of the yielded regions, which appear connected and are pinched by the expanding unyielded zones.

Finally, at even higher τ_0***=0.1***, the unyielded salient-corner/core-flow regions have now merged; surrounding and isolating the yielded zone, which is now restricted to a domain lying across and on either side of the contraction-plane (shamrock-shape). For $\{\tau_0=0.1, We\leq 1\}$, these regions preserve their characteristic sharp-cusp tip at the centreline; a feature that is gradually being suppressed with rise in *We* (almost non-existent at *We*=10). A significant new feature to note is the birth and growth of a halfmoon-shaped unyielded region, just downstream of the contraction, emerging about the centreline. This feature is apparent in $\{\tau_0=0.1, We\geq 1\}$ and $\{\tau_0=0.05, We\geq 5\}$ solutions; subsequent to its appearance, it expands downstream, as either τ_0 or *We* rise.

7.6 Thixotropic destruction parameter ξ_{G0}-variation – extensional viscosity effects

As illustrated in Fig. 3.3-3.5, reduction of the ξ_{G0}-destruction parameter (of polymeric NM_τ_p_ABS model; López-Aguilar et al. 2014b), leads to the consideration of additional extensional viscosity features in this viscoelastoplastic context. Here, solutions generated under ξ_{G0}=1 are contrasted against the relatively more strain-hardening configuration of ξ_{G0}=0.1125.

Vortex dynamics In {Fig. 7.6 and Table 7.3}, the streamline patterns reveal interesting results, when contrasting the two levels of strain-hardening, ξ_{G0}={1,0.1125}, and elasticity levels, *We*={0.1,5}. ***At We=0.1***, ξ_{G0}-solutions are graphically invariant on vortex structure with ξ_{G0}-change at each fixed τ_0-value. Here, under ξ_{G0}=0.1125, larger upstream and downstream minimum vortex intensity values (Table 7.3) are predicted (vortex-enhancement) relative to the solutions at ξ_{G0}=1.

In contrast, ***at We=5*** and ξ_{G0}=0.1125, notably larger upstream minimum vortex intensity values are obtained with respect to those under ξ_{G0}=1. Here, the change is strain-hardening characteristics with ξ_{G0}=0.1125 is now so dramatic that the downstream vortex structure is visually lost for $\tau_0 \geq 0.01$, and the upstream vortex takes on a convex-shape. Moreover, the minimum upstream vortex intensity values for ξ_{G0}=0.1125 solutions are remarkably larger (at least two orders of magnitude) than those under ξ_{G0}=1.

Table 7.3 Vortex intensity ($\Psi_{min}=-\Psi_{min}^{*}\ x10^{-4}$) against τ_0, ξ_{G0} and *We*; {m_p, β, ω}={10^3,10^{-2},4}

$\Psi_{min}=-\Psi_{min}^{*}\ x10^{-4}$

	We=0.1				*We*=5			
	ξ_{G0}=1		ξ_{G0}=0.1125		ξ_{G0}=1		ξ_{G0}=0.1125	
τ_0	Ups	Dns	Ups	Dns	Ups	Dns	Ups	Dns
0*	12.0	9.05	14.5	9.91	3.39	0.629	202.4	0.188
0.01	1.26	0.797	1.81	1.05	0.199	0.055	119.2	~0
0.05	0.032	0.023	0.039	0.025	0.004	~0	28.7	~0
0.1	~0	~0	~0	~0	~0	~0	2.89	~0

*Solutions reduced to NM_τ_p_ABS (NM_τ_p_ABS-Pap τ_0=0)

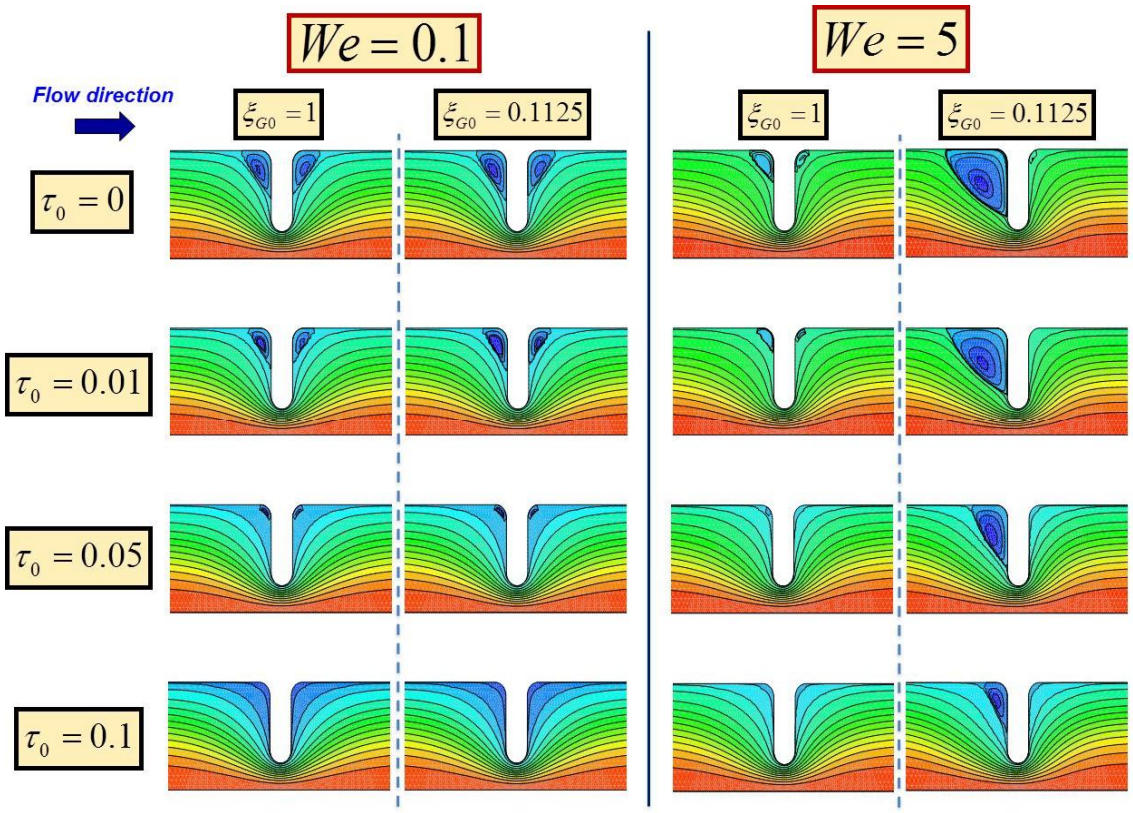

Figure 7.6 Streamlines against τ_0 and We={0.1,5}; {m_p, β, ω}={10^3,10^{-2},4}; ξ_{G0}={1,0.1125}

Upstream vortex & the normal stress differences N_1 and N_2 In Fig. 7.7, comparison of streamlines, N_1 and N_2-data fields are provided under the strain-hardening setting of ξ_{G0}=0.1125. Here, particular attention is paid to the close signature between the kinematic upstream vortex-structures and the vortex-like structures in N_2-fields (with its reflection/counterpart on N_1-data). Correspondence in shape and declining trends as the yield stress τ_0 is increased, are identified amongst these structures. This close relationship between vortex dynamics and N_2-N_1-data fields has already been commented upon elsewhere (López-Aguilar et al. 2014a;Tamaddon-Jahromi and Webster 2011).

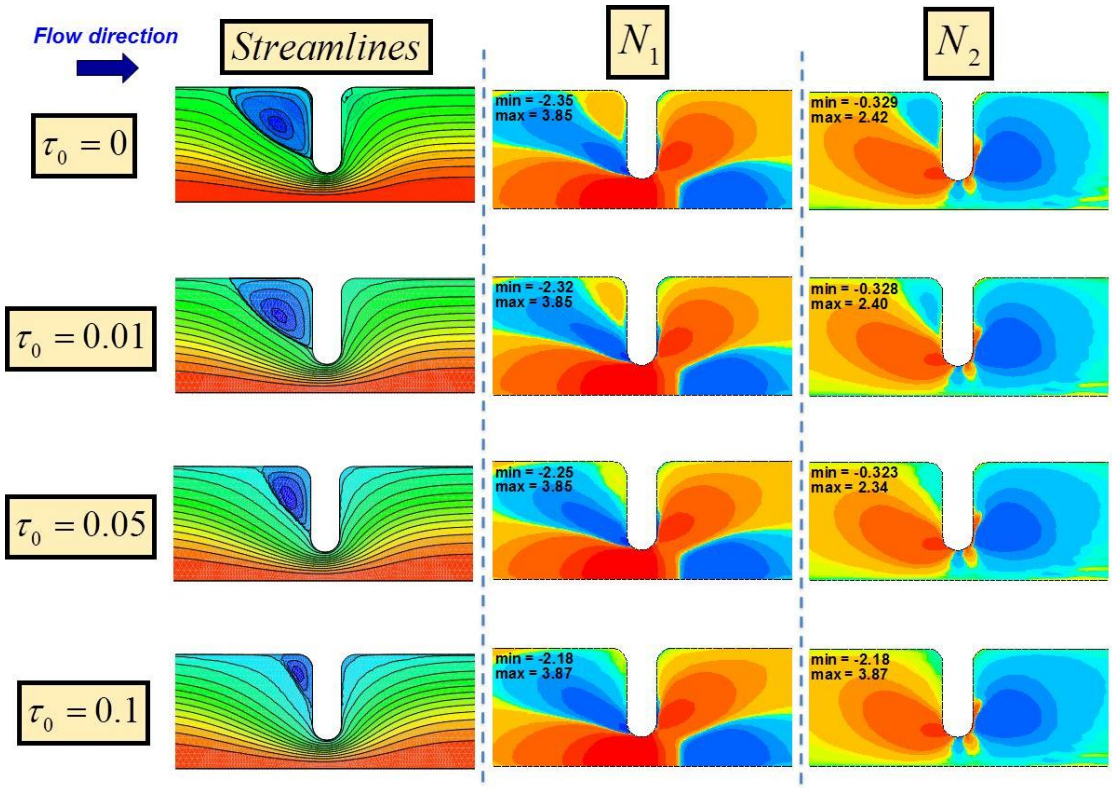

Figure 7.7 Streamlines, N_1 and N_2, against τ_0; We=5; $\{m_p, \beta, \omega, \xi_{G0}\}=\{10^3,10^{-2},4,0.1125\}$

Excess pressure drop In Fig. 7.8, the effects of m_p and ξ_{G0}-variation on *epd* are evaluated as the yield stress τ_0 is elevated and at three elasticity parameter levels, $We=\{0.1,1,5\}$. Consistently, it is evident from these data that any variation that leads to solid-like behaviour produces *epd* enhancement. Furthermore, these *epd* data-curves adopt a linear trend with change in τ_0 (Belblidia et al. 2011). One notes here, that the presence of viscoelasticity and pronounced strain-hardening characteristic do not change this trend in signature. The positive slope in the data-curves for all *We*–values reveals an increase in *epd* as τ_0 is elevated. Interestingly, the same effect is observed with m_p-variation; a growth in slope is observed when passing from $m_p=10^2$ to 10^3. From this enhancing *epd* evidence, the most prominent is that of ξ_{G0} (with its corresponding strain-hardening effects). For this parameter, going from $\xi_{G0}=1$ to the relatively more strain-hardening level of 0.1125, translates into an increase of ~0.25 units in *epd*, covering the entire range of τ_0 examined. In contrast, rise in elasticity through *We*, provides smaller *epd* values - likely caused by marked shear-thinning and strong N_1 characteristics of the viscoelastoplastic fluids analysed (see Fig. 1 and 2).

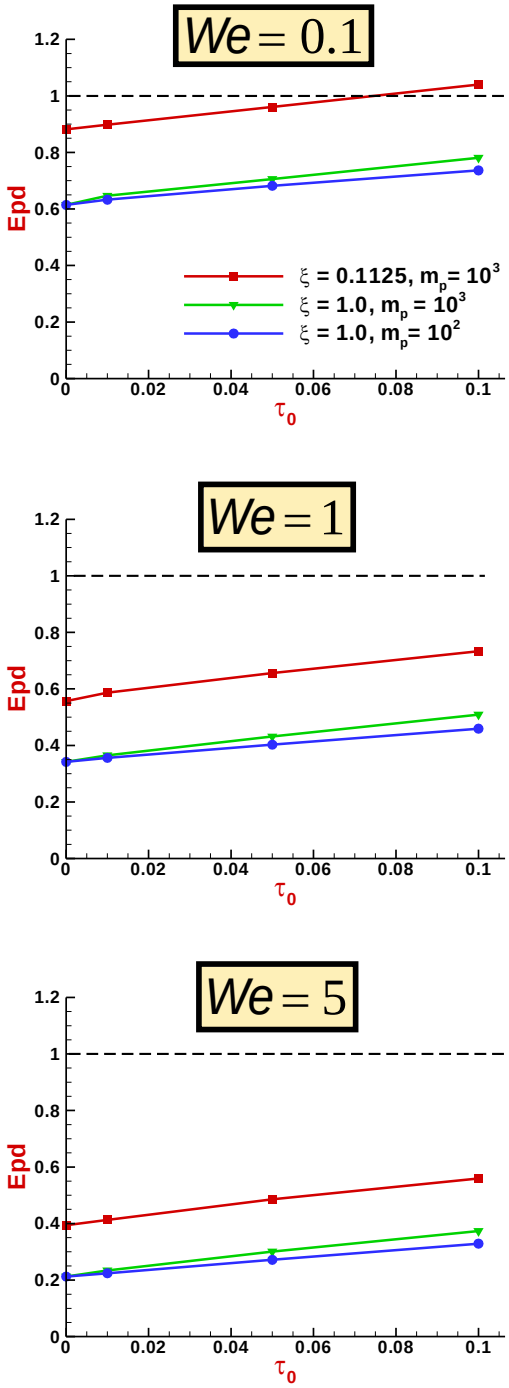

Figure 7.8 *epd* against τ_0; *We*={0.1,1,5}; {β, ω}={10^{-2},4}

Yield fronts The effects of ξ_{G0}-variation on yield fronts is provided in Fig. 7.9. This illustrates the divide between yielded (red) and unyielded (blue) regions at {β, m_p}={10^{-2}, 10^3} for NM_τ_p_ABS-Pap solutions. Here, at {τ_0=0.01, *We*=0.1} and ξ_{G0} =0.1125, the

unyielded regions at the centre of the flow field appear larger than those for ξ_{G0} =1. Such disparity is minimised with further rise in level of yield stress, $\tau_0 \geq 0.05$.

At the higher elasticity level of ***We=0.5***, stronger strain-hardening characteristics through ξ_{G0}-variation do begin to influence yield-front shape. Here, taking *We*=0.5 solutions in comparison to *We*=0.1 solutions, the unyielded {τ_0=0.01} regions at the centreline would appear wider in the radial direction, and their tip changes more abruptly. These characteristics are simply stretched out radially with further rise in τ_0. Strictly at *We*=0.5 and in comparison across ξ_{G0}={1, 0.1125} solutions, there are notable asymmetries in salient-corner vortex zones. Moreover at τ_0=0.1, the additional strain-hardening ξ_{G0}=0.1125 solution, is observed to suppress the half-moon-shaped unyielded region, present in the ξ_{G0} =1 solution.

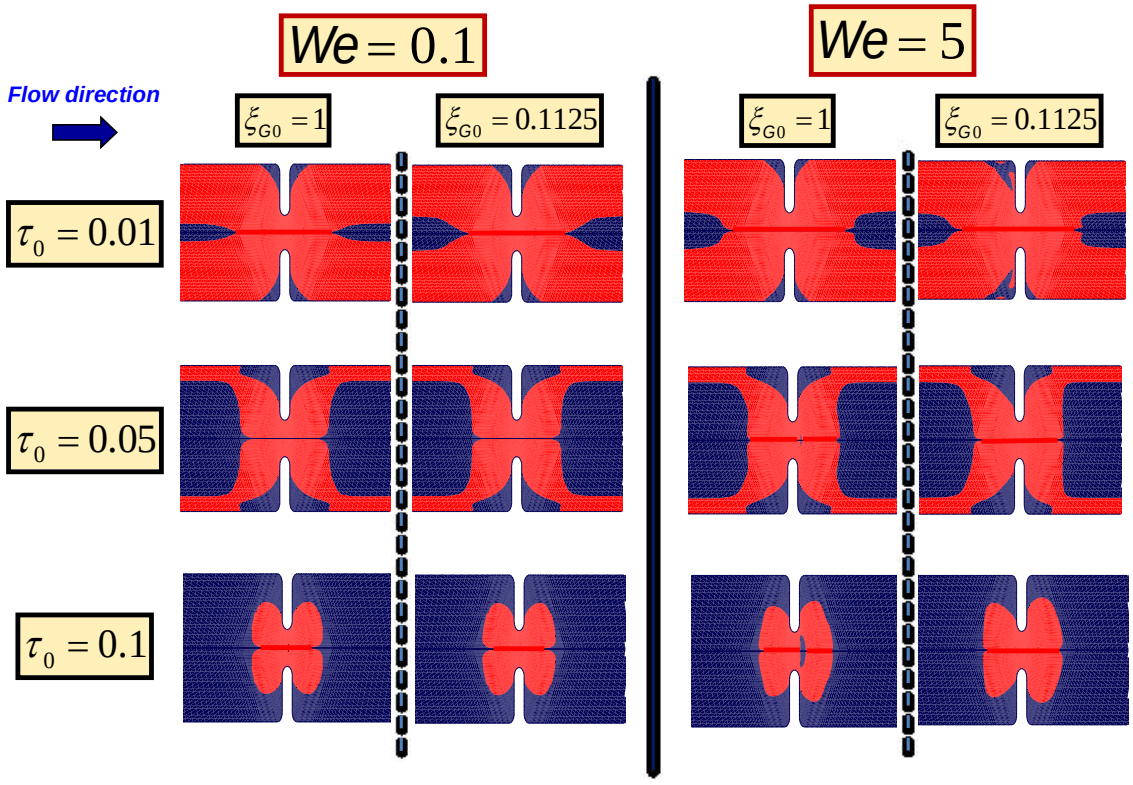

Figure 7.9 Yield fronts against τ_0 and *We*={0.1,5}; {m_p, β, ω}={10^3,10^{-2},4}; ξ_{G0}={1,0.1125}

7.7 Conclusions

Yield stress elastic thixotropic solutions have been obtained through two different constitutive routes (and models thereby): (i) in the *solvent contribution*, via Papanastasiou regularisation; and (ii) in the *polymeric contribution*, via thixotropic-micellar (NM_τ_p_ABS-

Pap) models. Numerical solutions have been reported whilst varying elastic and plastic contributions through parametric variation of - yield-stress cut-off τ_0={0.01,0.05,0.1}, regularisation stress growth exponent m_p={10^2,10^3}, polymer concentration β={10^{-2},10^{-3}} and thixotropic destruction parameter ξ_{G0}={1,0.1125}.

Numerical solutions under NM_τ_p_ABS-Pap model reveal interesting findings on vortex-dynamics, N_1 fields, yield-front patterns and excess pressure drop, according to yield-stress {τ_0, m_p}-parameter variation, strain-hardening (ξ_{G0}) and elasticity incrementation (β). *Vortex intensity and size* is observed to sharply reduce with increasing {τ_0, m_p} (yield-stress) and elasticity levels (strain softening). There is reduction in the initial negative slope of the vortex intensity curve versus τ_0 as *We* is elevated at base-level m_p=10^2. From this position, considering m_p-elevation at each fixed *We*-level, there is increased drop in vortex intensity with τ_0-rise. Clearly, enhancing solid-like features dampens the mobility of the material (vortex-dynamics).

On structure influence In contrast to these yield stress consequences above where ξ_{G0}=1, now considering each fixed τ_0-level, the exaggerated strain-hardening properties observed when decreasing the thixotropic ξ_{G0} destruction–parameter (from unity to 0.1125, characterising more mobile fluids), have a major impact on vortex activity. This is encapsulated through upstream vortex enhancement and downstream vortex suppression. The influence of change with elasticity (*We*-rise, from 0.1 to 5) appears as a counter effect to that due to strain-hardening – with upstream vortex reduction for ξ_{G0}=1, and enhancement for ξ_{G0}=0.1125. This is true $\forall\ \tau_0$–solutions, though most emphasised at τ_0=0. Appealing to corresponding viscometric properties, this observation may be attributed to the influence of strain-softening. It is particularly attractive that *We*-rise promotes asymmetry in the streamline patterns about the contraction.

Structures and trends in the *normal stress-difference* fields reflect those in re-entrant-corner vortex patterns, with elevation in yield stress, elasticity and strain-hardening. Hence, these N_2 vortex-like features in the upstream and downstream recess corner zones contract as the yield-stress τ_0 and the elasticity levels are increased. Interestingly, at the extreme setting {τ_0, *We*}={0.1,10}, downstream vortex activity practically disappears. Consistently, these trends are more exaggerated when strain-hardening is enhanced through ξ_{G0}-reduction, which

represent more structured fluid states.

On yield-front patterns These reveal significant influence with yield stress τ_0–variation. Here, symmetric unyielded regions first appear at τ_0=0.01, with upstream and downstream slender core regions at the centreline and concave unyielded regions confined in recess zones. When the cut-off yield-stress level (τ_0 value) is increased, the core region expands outwards towards the wall and approaches the recess unyielded zones, which now have elongated away from the corner. Further increase of the yield stress provokes unification, of core and recess yielded zones, to define a central single shamrock-shaped yielded-region about the contraction-gap. In contrast, elevation in elasticity provokes asymmetry in the recess unyielded-zones. There is also formation of a new halfmoon-shaped unyielded-region, about the centreline just beyond the contraction-plane, in the middle-to-high yield-stress range ($\tau_0 \geq 0.05$) and for elasticity levels ($We \geq 5$). ξ_{G0}-reduction (thixotropic-structural influence) suppresses the formation of this halfmoon-shaped unyielded region.

On excess pressure drop (*epd*) Here, findings versus increased yield stress (τ_0) follow linear functionality. The *epd*-slopes slightly rise with elevation in m_p. The *epd*-intersection point at τ_0=0 (coinciding with NM_τ_p_ABS solutions) is shifted to lower levels as elasticity is increased. One associates this *epd*-lowering for NM_τ_p_ABS thixotropic solutions with its marked shear-thinning and strong N_1 properties. Moreover, relatively more-structured fluids, characterised with smaller ξ_{G0}, display distinctly larger *epd*-values throughout the τ_0–range covered.

CHAPTER 8

Pressure-drop and kinematics of viscoelastic flow through an axisymmetric contraction-expansion geometry with various contraction-ratios[1]

In this chapter, one of the relevant benchmark problems in pressure-driven flows, that of flow through an axisymmetric expansion-contraction geometry, is addressed. Three fluids have been considered: a Newtonian, Boger and a shear-thinning polymer solution. Particular attention is given to the pressure-drop and kinematics obtained in a flow apparatus specifically designed for various contraction-ratios (2:1:2, 4:1:4, 6:1:6, 8:1:8, 10:1:10). Both viscoelastic fluids present large magnitudes of normal stress under simple shear flow. The three fluids have the same viscosity at low shear-rates. The Boger fluid (polyacrylamide in a syrup-water solution) possesses a constant viscosity over a wide range of shear-rates. The shear-thinning fluid also has a wide range of first Newtonian plateau before the onset of shear-thinning.

[1] The contribution of J.E. López-Aguilar in this part of the work has been on simulations of 4:1:4 contraction-expansion settings for Boger fluids, and the simple shear rheometric data fitting for Boger fluids. Experimental work is part of the DEng doctoral research of MIng M. Pérez-Camacho at Facultad de Química, UNAM.

Findings for the Boger fluid reflect, initially, a decreasing pressure-drop below the Newtonian reference line (excess pressure-drop lower than unity), followed by values larger than one as the contraction-ratio increases. This can be explained on the basis of the extensional viscosity behaviour in the contraction section of the geometry. The shear-thinning polymer solution (HASE-type associative polymer) shows a reduction in *epd* below the Newtonian curve for small contraction-ratios (due to shear-thinning). However, in more abrupt contractions, the extensional flow behaviour dominates the shear-thinning effects: first attaining Newtonian behaviour (producing an *epd* of one), and then, showing values larger than unity as the contraction-ratio becomes more severe.

Kinematic fields illustrated by flow visualization reveal several different sizes of the corner-vortex, which are related to the relative contributions from the first normal stress difference (N_1) and extensional stress throughout the geometry. Transitions from lip-to-corner vortex are related to the transition from shear-dominated to extension-dominated flows. Experimental data, for the Boger fluid on 4:1:4 contraction-ratio, are contrasted against numerical simulation results for a constant-shear-viscosity/extension-hardening FENE-CR model. Trends demonstrate qualitative agreement on *epd* and vortex activity, which also reveal an interesting interplay between N_1 and extensional viscosity.

8.1 Introduction

One of the original works on contraction flows of viscoelastic liquids (Alves et al. 2004) analysed vortex growth patterns through an axisymmetric contraction flows for various contraction-ratios. Much data from elastic and shear-thinning fluids show a correlation of the Weissenberg number (*We*) with the elasticity number, illustrating the relationship between vortex growth and fluid elasticity.

To gather information on the cause of vortex appearance, Boger et al. (1987, 1992) studied different contraction-ratios in the axisymmetric contraction ($4<\beta_o<16$) using two similar Boger fluids. The first was made with polyacrylamide and corn syrup, whilst the second consisted of a mixture of polybutene-polyisobutylene (PIB/PB). By increasing the shear-rate at the contraction, for a 4:1 ratio, the vortex-separation line changed in pattern from concave to convex-shaped.

In the PIB/PB solution with β_o=4, vortices were observed at low shear-rates. Upon increasing the shear-rate, the *upward displacement* of the length *Lv* of the salient-corner vortex, began to decrease, and simultaneously, a small second vortex (lip-vortex, of small growing length) appeared next to the re-entrant corner-lip. Subsequently, this secondary vortex grew considerably till its length *Lv* (distance to the separation point) overtook that of the first vortex.

In the same contraction and for both fluids, since the flow conditions at the contraction depend on the rheological properties of the particular fluid involved, differences in the growth of the extensional viscosity caused different flow patterns (Binding 1991). Hence, the growth of the second (lip-) vortex (due to extensional fluid properties) was different in both Boger fluids, although the same contraction-ratio and shear-rate were employed.

White et al. (1987) and, White and Kondo (1977) proposed that the vortex appearance reflects an underlying mechanism of stress relief in the contraction. For a polyacrylamide solution and prior to the contraction region, Cable and Boger (1978) studied the development of radial velocities in axisymmetric contractions with ratios of 2:1 and 4:1. Two flow patterns were identified, namely, the vortex growth regime and the divergent regime. This work analysed the presence of both extensional and shear flow and their influence upon flow kinematics.

It was found that vortex-growth scales with shear-rate (displaying outward streamlines); and at the contraction-entrance, the extensional viscosity retards the fluid and causes divergence towards the walls.

Binding et al. (1991, 2006) analysed the flow dynamics in the contraction, paying particular attention to the extensional and shear components of the flow, and the elasticity, represented by the first normal-stress difference. Two mechanisms were proposed: the first related to the quasi-radial flow at low shear-rates, generated by the presence of elasticity under shear flow. This flow corresponds to the region of vortex growth. The second mechanism corresponds to funnel-type flow at high shear-rates, which favours the development of uniaxial extensional flow at the contraction-centreline. This aspect corresponds to the development of the lip-vortex, which tends to inhibit the growth of the

primary (salient-) vortex. Finally, the salient-vortex is incorporated into the growth of the secondary lip-vortex. Still, some open questions remain re the contraction zone - such as, the appearance of the lip-vortex, and the dynamic change in flow patterns.

Rothstein and McKinley (1999, 2001) studied a contraction-expansion geometry with various contraction-ratios ($2<\beta_o<8$) for two Boger fluids - the first, based on polystyrene, and the second, made of a (PIB/PB) mixture. For the first Boger fluid and with a contraction-ratio of 2:1:2, the lip-vortex was present at all shear-rates. For the other ratios (4:1:4 and 8:1:8), corner vortices were observed, and associated with extensional flow contributions. Hence for the polystyrene solution, the dominant flow-type depended strongly upon the contraction-ratio. With the PIB/PB solution under the same flow conditions, such transition in kinematics was not apparent, inasmuch as the lip-vortex was always observed. An explanation was proffered, in terms of the solubility of the components of the solution, such as with a compatible/good solvent (polystyrene), different patterns may be observed. The shear to extension-dominated flow transition itself has been suggested to depend on the ratio of the first normal-stress difference to the extensional stress.

Experimental studies are still scarce on pressure-drops within axisymmetric contraction-expansion flows. Cartalos and Piau (1992) studied various viscoelastic fluids made of flexible and semi-rigid molecules (partially-hydrolised polyacrylamide dissolved in glucose-water and polyethylene oxide dissolved in a sugar-water solution, as the flexible molecules solutions; and PAA partially-hydrolised without salt, as the semi-rigid molecules solution).

Experimental data on pressure-drop versus flow rate for pseudoplastic fluids identified three regimes (linear viscoelastic regime, intermediate quadratic regime and final viscous regime). At low rates of deformation with small molecular deformation, the first regime is characterized by a linear relationship between pressure-drop and deformation-rate. In the second regime, the pressure-drop varies with the square of the flow rate, and may be attributed to the onset of extensional elastic stress. The third mechanism, associated with a

second-Newtonian region, involves high molecular deformation and increasing hydrodynamic interactions with the solvent.

In the studies of Rothstein and McKinley (1999, 2001), excess pressure-drops larger than that of the reference Newtonian fluid were found. These experimental data are not matched by the numerical calculations (Cable and Boger 1978). Results from the latter analysis indicate a reduction of pressure-drop with We below the Newtonian reference fluid, attributed to the onset of elasticity under shear flow (N_1). Once the minimum has been reached, the *epd* then shows a continuous increase. This response may be attributed to a change of flow-type through the contraction, from a shear to extension-dominated flow-regime.

Most significant theoretical developments have focused on Boger-type fluids in axisymmetric and planar contractions for low *We* numbers. In this, various constitutive equation representations have been considered, such as the Oldroyd-B model. Nevertheless, this model has been found wanting in its ability to predict the observed large excess pressure-drops at high strain-rates.

8.2 Experimental section

8.2.1 Axisymmetric contraction-expansion flow apparatus

The flow apparatus comprises four sections: feed, test, electronic control and fluid recovery sections.

1.- Feed section. Here, a tri-phasic 1/12 HP pump (G) of variable speed was instrument-ted. It possesses a special gear reduction system (H), with gear ratios of 2:1, 4:1 and 8:1, to support small flow rates (0.01 ml) and Reynolds numbers (<0.1). The piston (A) is built with an aluminum smooth surface of 3 cm inner diameter with two stabilizers to allow for a centered and continuous displacement.

2.- Test section. This section has two parts *(i), (ii)* - a first part*(i)* of a concentric-tube heat exchanger (D) of 65 cm length and 5.2 cm inner diameter and 6.27 cm external tube diameter. The thermal bath (L) ensures a constant fluid-temperature in the contraction region. The second part*(ii)* contains an acrylic tube of 55.5 cm length and 5.2 cm inner

diameter, which coincides with the dimensions of the inner tube of the heat exchanger. Here, the contraction-expansion is built with a disc made of a polymeric material. This can be inter-changed relatively easily, hence allowing for use of various contraction-ratios. Table 8.1 discloses the dimensions of the discs used.

The flow of the test fluid is regulated using a voltage controller (Baldor BC 140) of 115 volts. This is coupled to the motor and gears that displace the piston to deliver a constant flow rate. The flow rate is measured from the time elapsed, the cross-section area of the piston and the displacement length.

3.- Electronic control section. This consists of two pressure transducers (Piezotronic), of 0-10 psi range. These are placed 7 cm above and below the contraction region, outside the vortex developing region and in the fully-developed zone. The signal from the transducers is received in a data acquisition unit (Q) (Dataq, DI-158). This device transmits the data in real time to a computer for storage and manipulation. Then, for each flow-rate trial and commencing from rest or between flow-rates, constant signals identify the establishment of steady-state pressure-drop across the contraction.

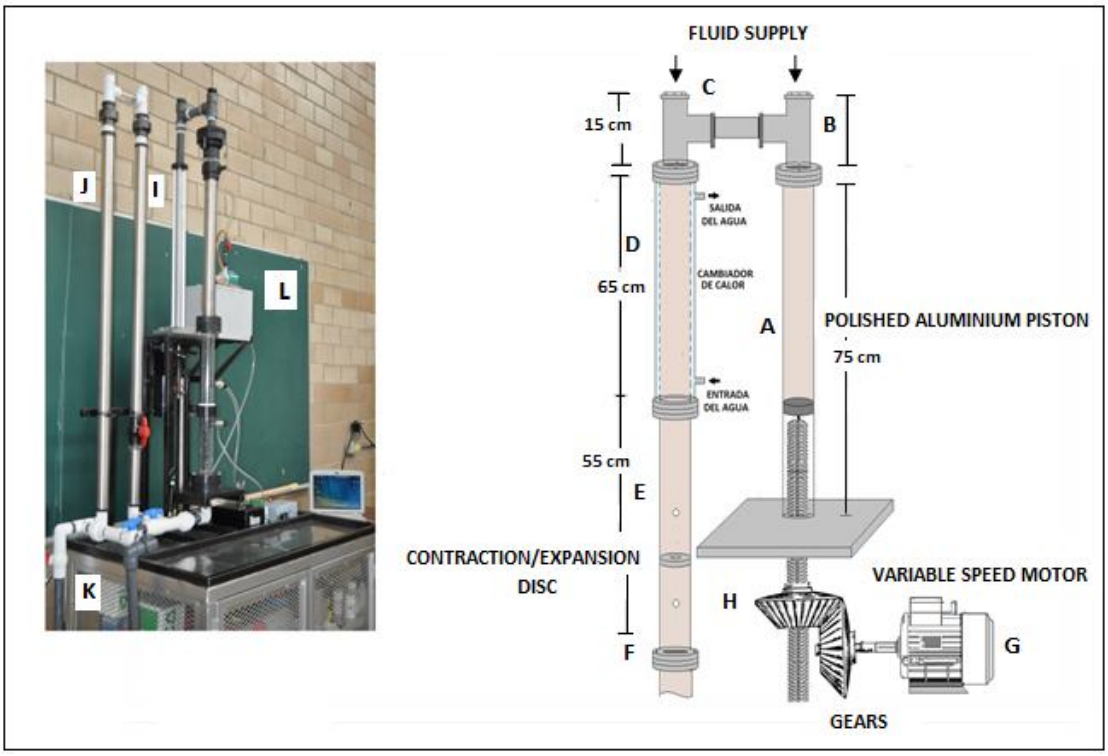

Figure 8.1 Experimental apparatus

Table 8.1 Contraction disc dimensions

CONTRACTION/EXPANSION RATIO	DISC DIAMETER D_D (cm)	DIE DIAMETER d_c (cm)	THICKNESS CONTRACTION L_c (cm)	ASPECT RATIO L_c/R_c
2:1:2	4.5	2.25	0.5	0.44
4:1:4	4.5	1.125	0.5	0.88
6:1:6	4.5	0.750	0.5	1.33
8:1:8	4.5	0.562	0.5	1.77
10:1:10	4.5	0.450	0.5	2.22

4.- Fluid-recovery section. The liquid flowing from the region below the test section cannot be discharged to atmospheric pressure, since gravity interferes with the imposed flow through the voltage regulator. A second stainless-steel tube (I) was adapted, of same dimensions as the test tube. In addition, a third tube (J) was fixed to allow for fluid recovery to a container. This tubing arrangement facilitates flow control, without the effects of gravity.

8.2.2 Flow visualisation

For vortex observation, a special chamber with a camera was built of dimensions 45x45x40 cm around the contraction section (see Fig. 8.2).

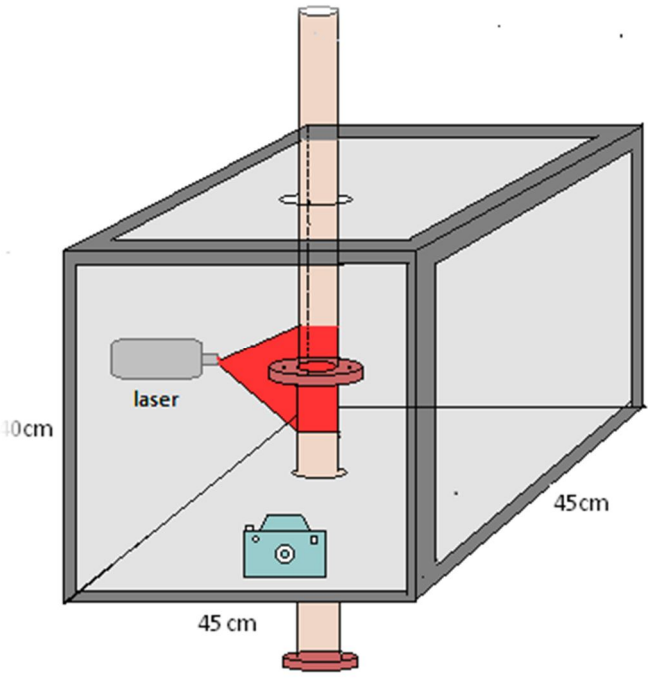

Figure 8.2 Vortex visualisation chamber

A reflex-type photo-camera (Nikon D5000) was mounted. Images were provided with an exposure time of 35 s and vortex dimensions were measured using an imaging programme (Java applications). The dimensions are measured from the number of pixels, using the tube with inner diameter of 4.5 cm as a basis to compute a ratio of 0.00195cm/pixel.

8.2.3 Pressure-drop calculations

As above, two pressure transducers of high sensitivity are placed in the fully-developed flow sections, upstream and downstream of the contraction (see Fig. 8.3). The individual pressure-drop contributions comprise those of the fully-developed flow before and after the contraction, the pressure-drop in the contraction channel and the extra pressure-drop due to non-Newtonian effects:

$$\Delta P_{Total} = \Delta P_1 + \Delta P_2 + \Delta P_C + \Delta P_{Extra}. \tag{8.1}$$

The first three contributions are considered as arising from pressure-shear flow in a tube (Hagen-Poiseuille flow). The latter, the so-called extra pressure-drop, is determined by the shape factor at the contraction region for a Newtonian fluid, according to the Sampson formula (Sampson 1891):

$$\Delta P_{Extra} = \frac{3Q\mu}{R_c^3}. \tag{8.2}$$

The total pressure-drop is then rewritten as:

$$\Delta P_{Total} = \frac{8Q\mu\left(L_1 + L_2\right)}{\pi R_1^4} + \frac{8Q\mu L_c}{\pi R_c^4} + \frac{3Q\mu}{R_c^3}. \tag{8.3}$$

Since the calculation of the extra pressure-drop in a non-Newtonian fluid is not known in advance, this is estimated experimentally from the measurements of the total pressure-drop as follows:

$$\Delta P_{Extra} = \Delta P_{Total} - \left[\frac{8Q\eta\left(L_1 + L_2\right)}{\pi R_1^4} + \frac{8Q\eta_c L_c}{\pi R_c^4}\right]. \tag{8.4}$$

In Equation (8.4), η is the fluid viscosity in the fully-developed regions, and η_C is the viscosity of the fluid in the contraction itself. Equation (8.4) is used to estimate ΔP_{Extra} acknowledging that the viscosities η and η_C may be significantly different depending on the rheological nature of fluids under analysis (recall that constant-viscosity Boger type and pseudoplastic fluids are analysed in this work).

8.3 Rheological characterisation of the test fluids

The experimental measurements consider three fluids - a Newtonian, a Boger and a shear-thinning fluid. The Boger fluid is made from a solution of polyacrylamide (0.1 wt.%) in corn syrup, and the shear-thinning fluid is an aqueous solution of an associative polymer (HASE, hydro-phobically-modified alkali-soluble emul-sion, 2.5 wt. %). The HASE polymer (Acrysol TT-935, from Rom & Haas) was prepared by dissolving the polymer in water and adjusting the pH to 9, using 0.1 M of 2 amino-2 metil-1 propanol. The Newtonian fluid is a solution in corn syrup in water.

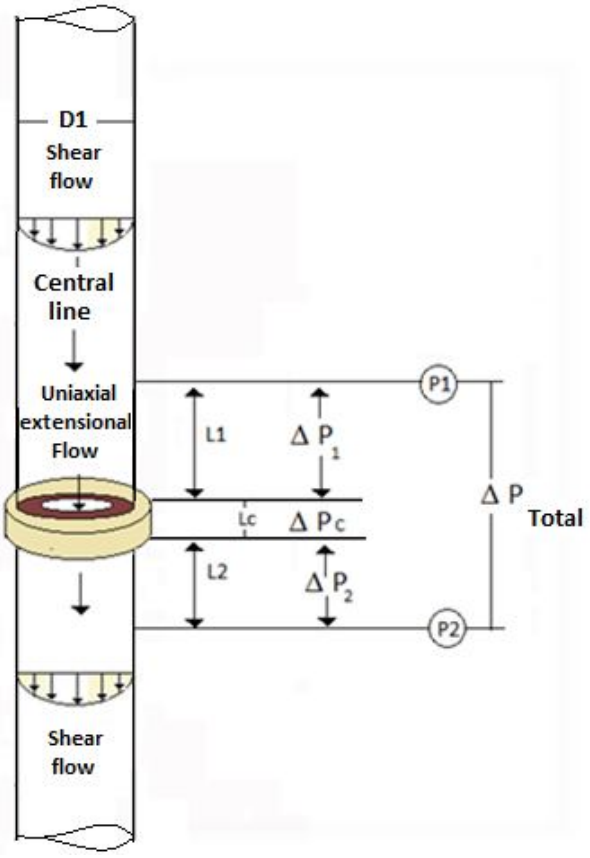

Figure 8.3 Schematic representation of contraction-expansion flow apparatus

The rheological properties of the fluids were measured in a controlled-stress rheometer TA-Instruments AR-G2, in a cone-and-plate fixture, of 40 mm diameter and 1° angle between the cone and plate.

In Fig. 8.4, the shear viscosity and first normal-stress difference are plotted against shear-rate. The Newtonian fluid viscosity amounts to 13.5 Pas and the zero shear-rate viscosities of the two viscoelastic fluids were adjusted to this value (by dilution). Note that N_1 is larger with the HASE fluid, whilst both viscoelastic fluids approach the same value at high shear-rates.

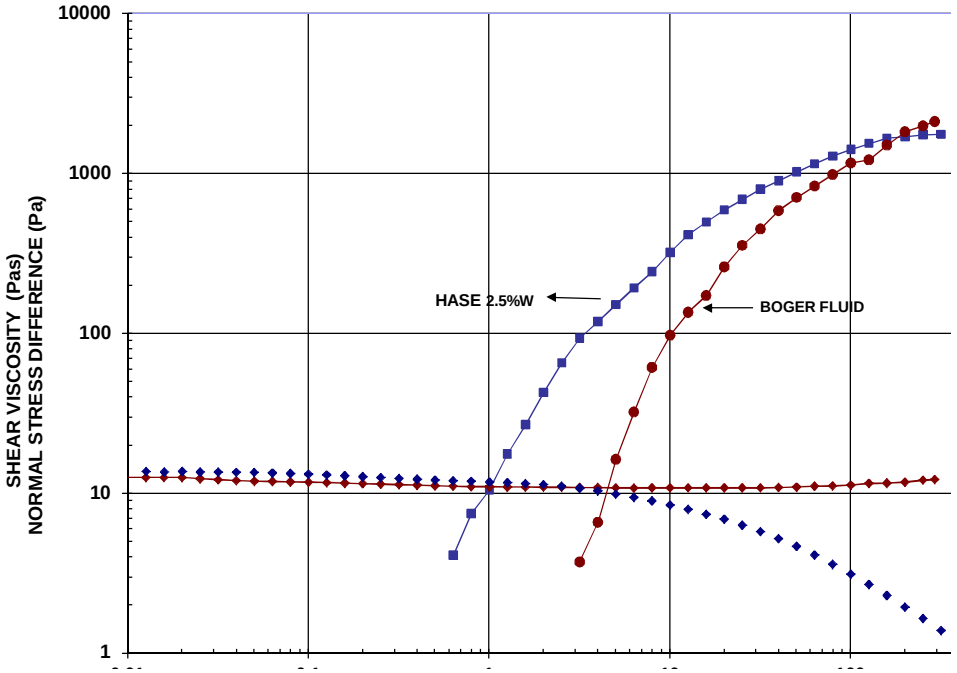

Figure 8.4 Shear viscosity and first normal-stress difference as functions of shear-rate, for Boger and HASE fluids

Predictions of viscometric functions in simple shear and uniaxial extension have been extracted using BMP (Bautista et al. 1999) (representing HASE fluid) and FENE-CR (Chilcott and Rallison 1988) (for Boger fluid) constitutive equations. The expression derived for the shear viscosity corresponding to i-modes of the BMP model is:

$$\varphi_{ss} = \sum_{i=1}^{n} \frac{1}{2} \left\{ -\left(K_i \lambda_i \dot{\gamma}^2 - \varphi_o \right) + \left[\left(K_i \lambda_i \dot{\gamma}^2 - \varphi_o \right)^2 + 4 K_i \lambda_i \dot{\gamma}^2 \varphi_\infty \right]^{1/2} \right\}, \qquad (8.5)$$

φ_{ss} is the fluidity or inverse viscosity at steady-state, K_i is a kinetic constant associated with the structure modification and λ_i is a structure relaxation time, $\dot{\gamma}$ is the shear-rate, the fluidity at vanishing shear-rates is φ_o and φ_∞ stands for the fluidity at high shear-rates. Then, the first normal-stress difference is given by:

$$N_1 = \frac{2\tau_{12}\dot{\gamma}}{G_o\varphi_{ss}}, \tag{8.6}$$

where G_0 is the elastic modulus and τ_{12} is the shear stress.

Table 8.2 Model parameters for shear viscosity BMP model

Modo	φ_o = 1/Pa s	φ_∞ = 1/Pa s	K = 1/Pa	λ = s
1	0.074	0.1	2000	0.00005
2	0.0001	1.66	0.000053	0.0687285

In Fig. 8.5, the shear viscosity of the HASE fluid is predicted by eq.(8.5), and N_1 is predicted by eq.(8.6). The model parameters are shown in Table 8.2.

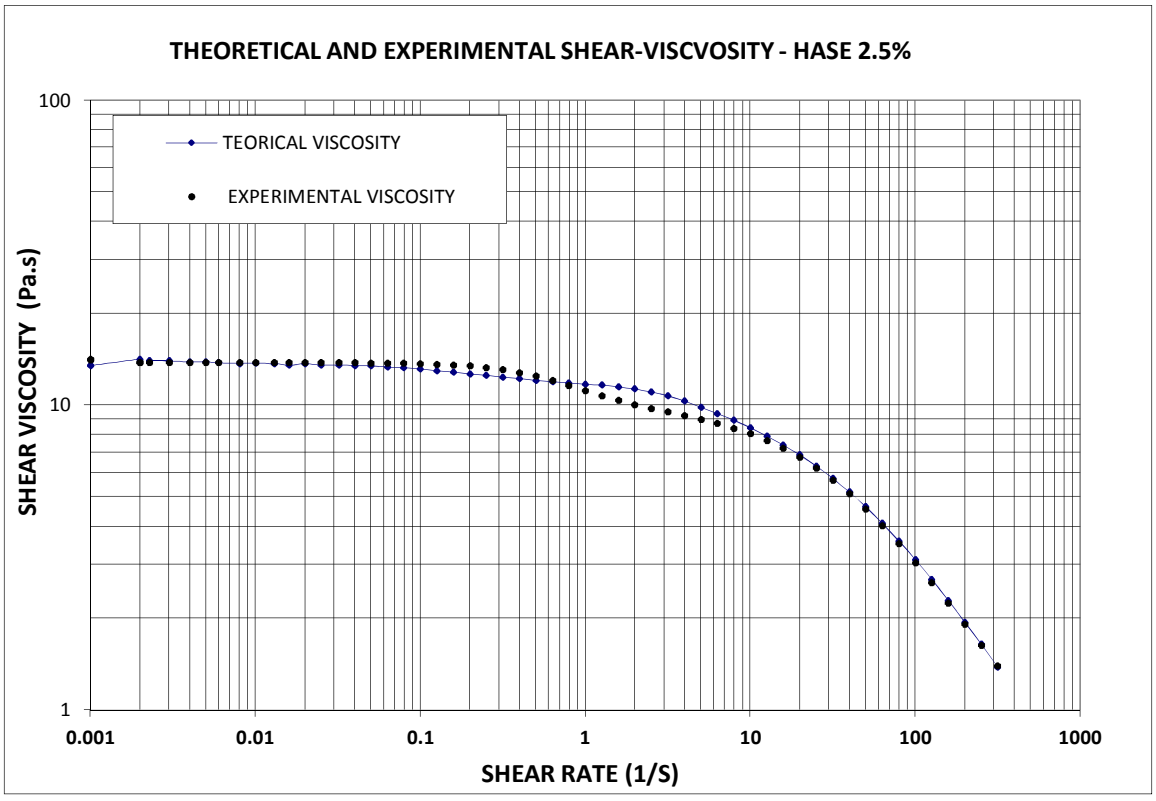

Figure 8.5 Data and predictions of shear viscosity according to eq.(8.5)

Predictions for uniaxial extensional flow consider the following expression for the extensional viscosity (Bautista et al. 1999):

$$(\varphi-\varphi_o)(G_o\varphi-2\dot{\varepsilon})(G_o\varphi+\dot{\varepsilon})=3\lambda\left(\frac{K}{\eta_\infty}\right)G_o^2\varphi\dot{\varepsilon}^2 \tag{8.7}$$

where $\dot{\varepsilon}$ is the strain-rate. The extensional stress is given by:

$$N_1=\frac{\varphi-\varphi_o}{\lambda\left(\frac{K}{\eta_\infty}\right)\dot{\varepsilon}}+3\mu_s\dot{\varepsilon}, \tag{8.8}$$

where μ_s represents the solvent viscous contribution. The extensional viscosity is then:

$$\eta_E=\frac{N_1}{\dot{\varepsilon}}. \tag{8.9}$$

Experimental data covering the uniaxial extensional viscosity for the HASE fluid is provided by Tan et al. (2000). Predictions with the BMP model for simple shear and extensional flow are given in Mendoza-Fuentes et al. (2009). In Fig. 8.6, these predictions are shown for the 2.5 wt. % solution.

For the Boger fluid, the FENE-CR model by Chilcott and Rallison (1988) is used in extensional flow. See Chapter 2, section 2.3.10; and Chapter 3, section 3.2 for further details on model representation and rheology, respectively.

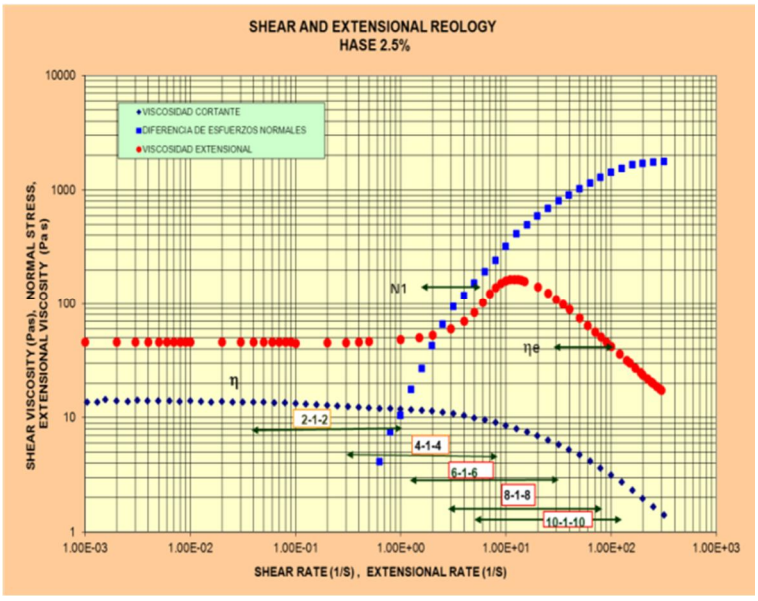

Figure 8.6 Shear and uniaxial extensional viscosity data. Lines with arrows indicate range of strain-rates corresponding to each geometry

8.4 Experimental results - Vortex growth dynamics

In Figures 8.7A-7E, corner-vortex growth is shown for the Boger and HASE fluids in the five geometries. Each photograph was taken at the shear-rate indicated, evaluated at the contraction and for the corresponding *De* number. The shear-rate is the largest attained for each geometry. In Fig. 8.7A and for the 2:1:2 contraction-expansion, the shear-rate at the contraction is around $1s^{-1}$ and a small corner-vortex appears with the HASE fluid. For the Boger fluid, in contrast, the vortex is of negligible size. At this shear-rate, the magnitude of N_1 is small in the Boger fluid case, amounting to ~10Pa with the HASE fluid.

In the 4:1:4 geometry, the representative shear-rate at the contraction has increased to $8s^{-1}$, which corresponds to N_1–values larger than 100Pa with the HASE fluid. The vortex size for the HASE fluid is quite large, whilst with the Boger fluid is still small (Fig. 8.7B).

In the 6:1:6 expansion-contraction, the shear-rate is now $28s^{-1}$ and N_1 with the HASE fluid has grown to near 1000Pa, which is reflected in the large vortex size. The Boger fluid vortex is also large, but still smaller than the HASE vortex, corresponding to lower N_1 (Fig. 8.7C).

The 8:1:8 geometry presents extremely large vortices with the HASE fluid, and also the Boger fluid, with values of N_1 for both fluids around 1000Pa. The representative shear-rate is now $66s^{-1}$ (Fig. 8.7D)

At the shear-rate of around $130s^{-1}$, in the 10:1:10 contraction-expansion (Fig. 8.7E), a most interesting result is that N_1 for both fluids approaches the same value; and this coincides with equity in vortex size generated. Here with both fluids, large corner-vortices are observed, which clearly indicates a relationship between vortex-size and first normal-stress difference.

Figures 8.8A,8.8B display the non-dimensional reattachment length (*Lv*, length-scale associated with vortex-size) plotted against Deborah number, for both Boger and HASE fluids.

In Fig. 8.8A, the Boger fluid illustrates that *Lv* is constant at low *De* numbers, but a decrease in the reattachment length is observed as the lip-vortex develops. As the extensional flow dominates, the transition to a corner-vortex is observed in the 2.5 – 5

range of *De* numbers, corresponding to the 6:1:6 and 8:1:8 geometries. The large increase in vortex size is observed in the 10:1:10 case.

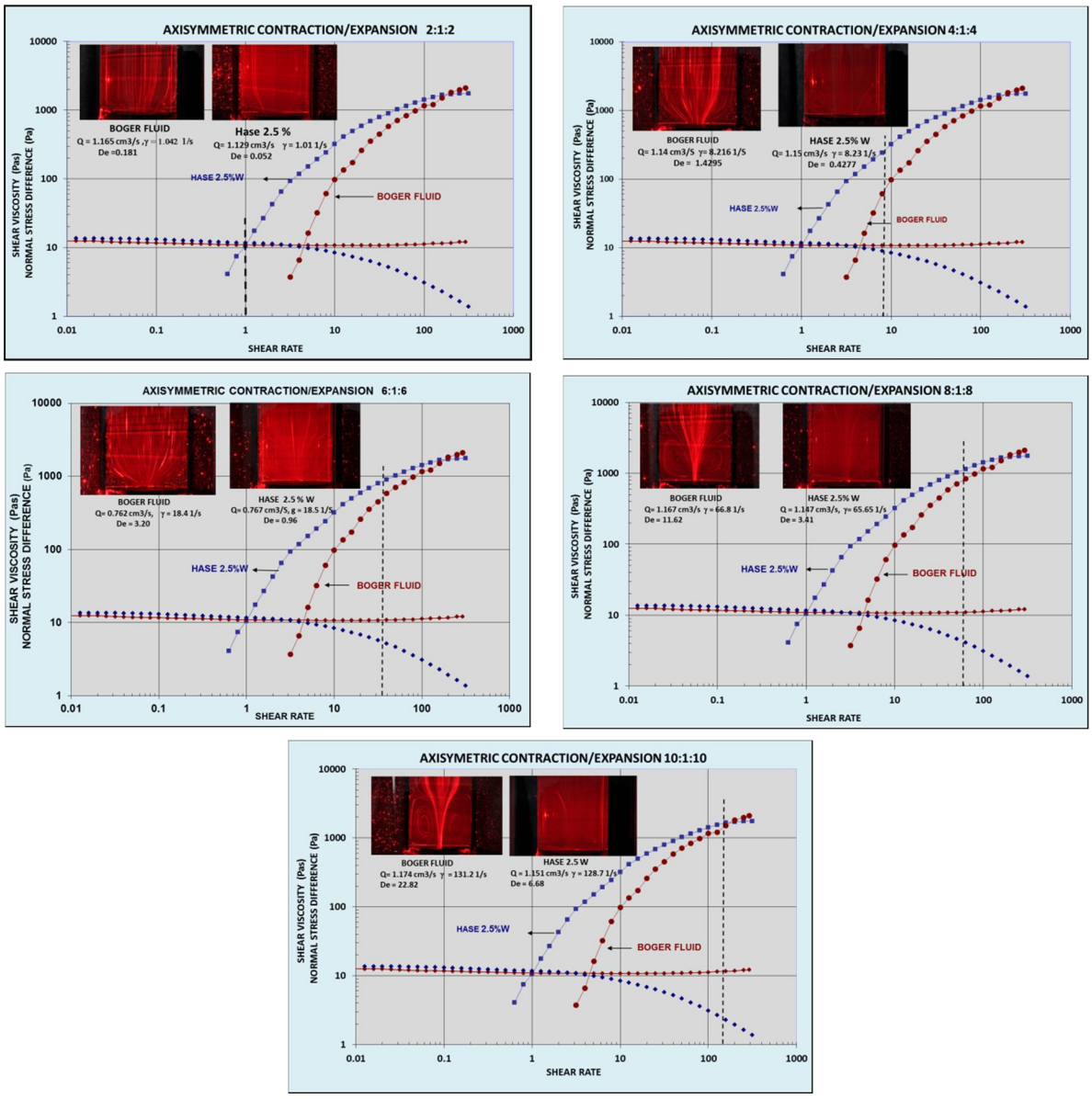

Figures 8.7 A-E Relationship of first normal-stress difference with vortex dimensions for each geometry. The vertical broken line indicates representative shear-rate at contraction region

In contrast, with the HASE fluid, the transition lip-to-corner vortex occurs at fairly low *De* numbers in the 4:1:4 geometry, as shown in Fig. 8.8B. In summary, the vortex reattachment length-scales with the strain-rate, and is a strong function of N_1 (López-Aguilar et al. 2014). With a view ahead, this relationship is observed in numerical solutions

for the Boger fluid within the 4:1:4 setting, discussed below and found applicable elsewhere (López-Aguilar et al. 2014).

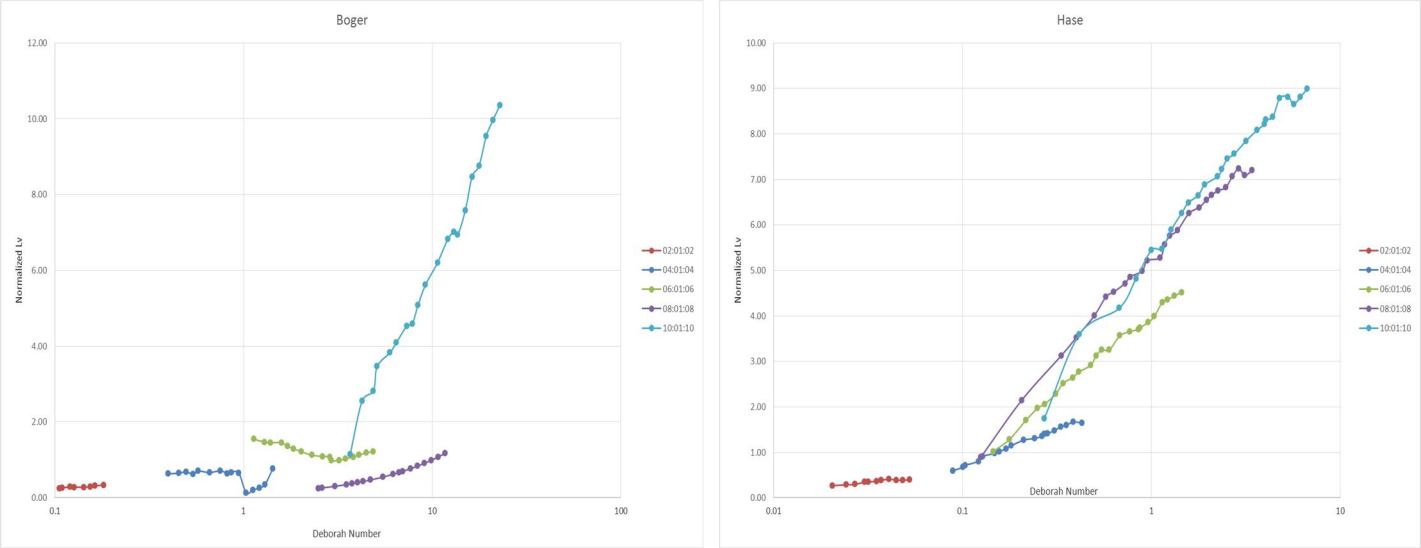

Figures 8.8A and B Vortex growth (normalized reattachment length, *Lv*) against Deborah number for Boger and HASE fluids, respectively

8.5 Pressure-drop

In Figures 9A-9E, the extra pressure-drop (*epd*) is plotted versus Deborah number for both Boger and HASE fluids. The unity Newtonian reference line is also indicated. In Fig. 8.9A, the 2:1:2 expansion-contraction data is reported. The flow rate in this case is small and corresponds to the shear-rate region where the viscosity is constant for both fluids (first Newtonian region). The Boger fluid provides a negligible N_1 in this range (see Fig. 8.7A). It is most interesting to observe the growth in Boger-*epd* data with *De*, which achieves an upper asymptote some three times that of the reference-line. This scaling with the extensional viscosity reveals that, here, the flow is completely dominated by extensional fluid properties. In contrast, the HASE fluid manifests only a small normal stress contribution. Now, since the viscosity is also constant in this range for this liquid, one concludeds that the maximum and further decline in HASE-*epd* data is due to the combined effects of extensional viscosity and N_1.

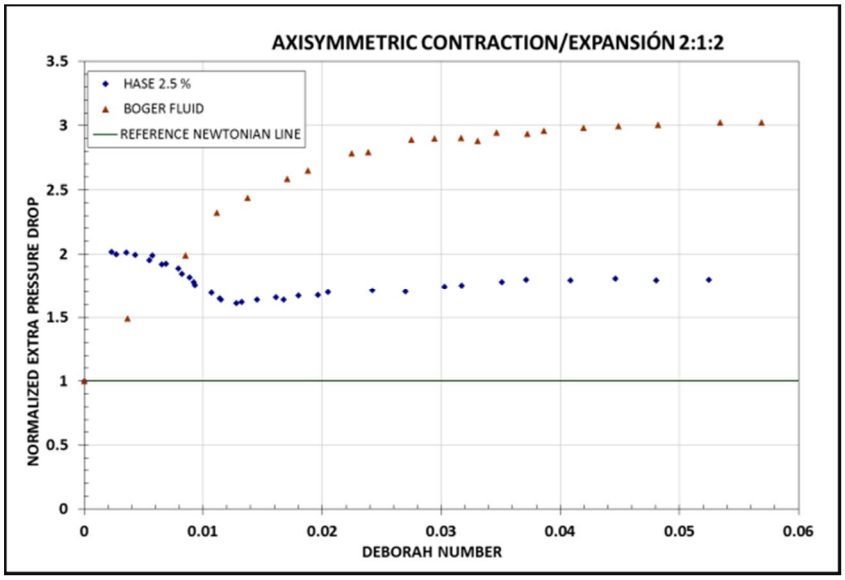

Figure 8.9A *epd* versus *De* number, 2:1:2 contraction-expansion

Results on *epd* for the 4:1:4 geometry are illustrated in Fig. 8.9B. Here, the range of shear-rates spans from 1 to 8s^{-1}, corresponding to *De*-values around 0.1 to 1.5. The Boger fluid presents a non-negligible N_1; whilst the HASE fluid becomes shear-thinning, with relative large N_1, accompanied with a growing extensional viscosity (see Fig. 8.6).

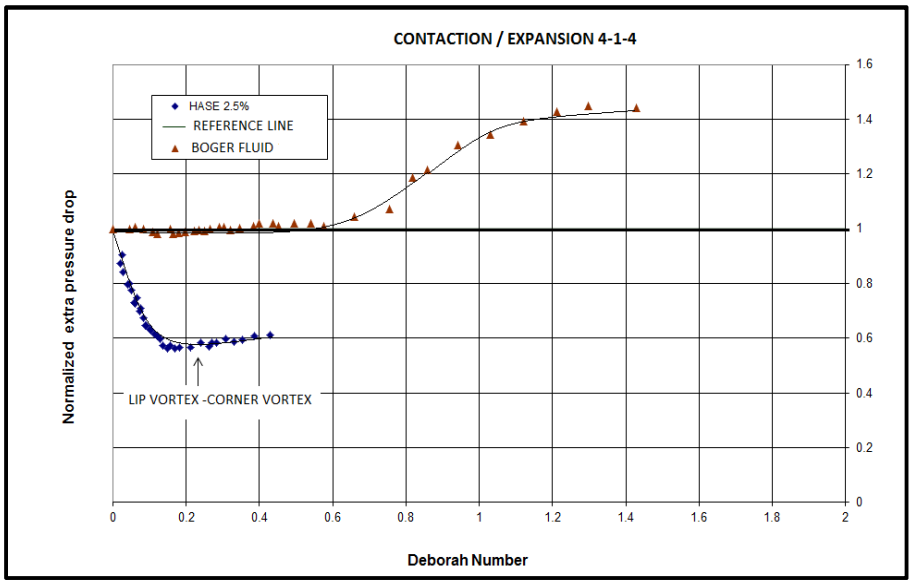

Figure 8.9B *epd* versus *De* number, 4:1:4 contraction-expansion

Here, the growth of *epd* with *De* is not as spectacular as in the 2:1:2 geometry, due to suppression from normal stress contributions. The HASE fluid presents a radical switch in behaviour. It achieves *epd*<1, reaching ~0.6 (~40% drop), attributable to the combined effects of shear-thinning and N_1. There is a slight upturn, beyond the minimum, where one observes a change in vortex activity: from a lip-vortex to a corner-vortex. Since this outcome is associated with a transition from shear-dominated to extension-dominated flow, the extensional component is held responsible for this upturn in *epd*.

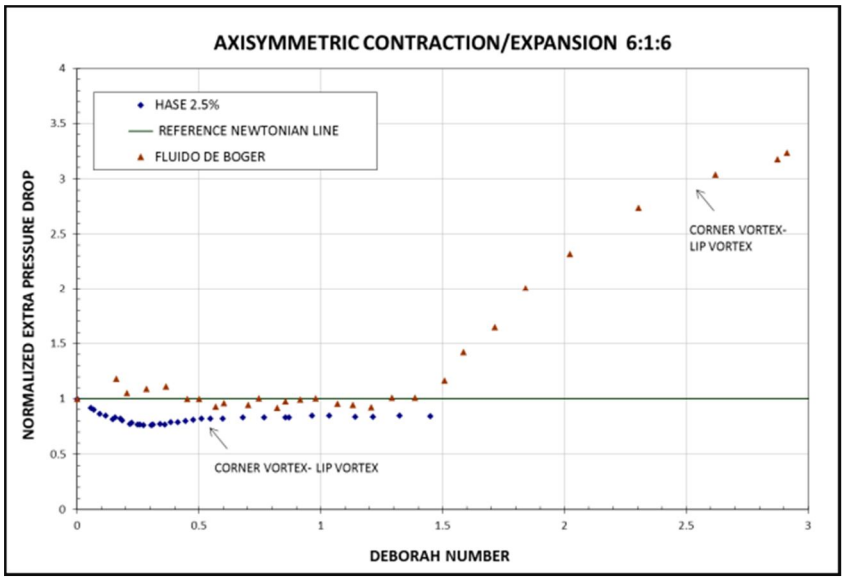

Figure 8.9C *epd* versus *De* number, 6:1:6 contraction-expansion

As the contraction-ratio increases further to 6:1:6, extensional properties begin to dominate normal stress contributions arising from shear. In Fig. 8.9C, the Boger fluid *epd* rises to values larger than 3. Note, in Figures 9B, 9C, the notorious low *De*-range Boger-*epd* behaviour is depicted - where *epd* drops slightly below the unity-Newtonian line; prior to upturn and continuous rise for larger *De* numbers, crossing the unity-Newtonian line; ultimately proceeding to a critical *De* number (De_{crit}). Here, De_{crit} is defined as the elasticity stage at which the *epd*-curve cross the Newtonian reference line (*epd*=1). These trends correspond to those observed in numerical solutions for Boger fluid representations. There, an interplay has also been observed between N_1 (dominating at low *De*) and extensional viscosity (overtaking and eventually dominating, as *De* is increased). See discussion below on numerical solutions for the 4:1:4 geometry and Boger fluids, and recall the competing

roles these two quantities exert on *epd*-estimation (Walters et al. 2009). Here, the transition from lip to corner-vortex is observed near *epd*=3, past the region where the concavity of the curve changes, and the slope decreases. Beyond the De_{crit} (or its critical shear-rate), there is an almost linear region of *epd* versus *De*, which is common in flows with 4:1:4 and 6:1:6 geometry options.

Relative to 4:1:4 geometry data and with the HASE fluid of Fig. 8.9C, extensional properties become manifest in a smaller *epd*-drop (25%) below the unity-Newtonian line. This feature is also influenced by (greater) shear-thinning effects. After the minimum, again the transition from lip-to-corner vortex signals the onset of extension-dominated flow.

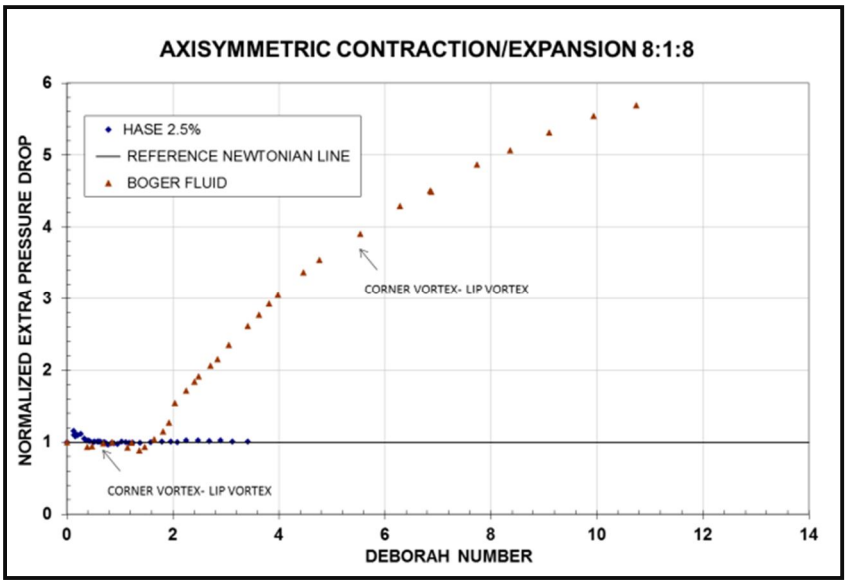

Figure 8.9D epd versus *De* number, 8:1:8 contraction-expansion

In Fig. 8.9D and here for the 8:1:8 geometry, both viscoelastic fluids have similar N_1-values. Yet, the HASE fluid presents a maximum in extensional viscosity (strain-hardening/softening transition) and a pronounced shear-thinning response (see Fig. 8.6). Fig. 8.9D displays an intriguing result with the HASE fluid: all three contributions, from extensional viscosity, shear-thinning and N_1, counter-balance to produce an equivalent-Newtonian response. The change from lip-to-corner vortex is observed to occur at low *De*, similarly to results in Fig. 8.9C.

Correspondingly, on observed *epd* with the Boger fluid, there is an initial minor *epd*-drop (*epd*<1), and thereafter, a De_{crit} is reached. Beyond this critical *De*-value, *epd* grows linearly and attains the region of extension-dominated flow. There, the transition from lip-to-corner vortex is encountered, accompanied with a change in curve-slope. Here, spectacular increases in Boger-*epd* are noted (*epd*~6) in the high *De* number range.

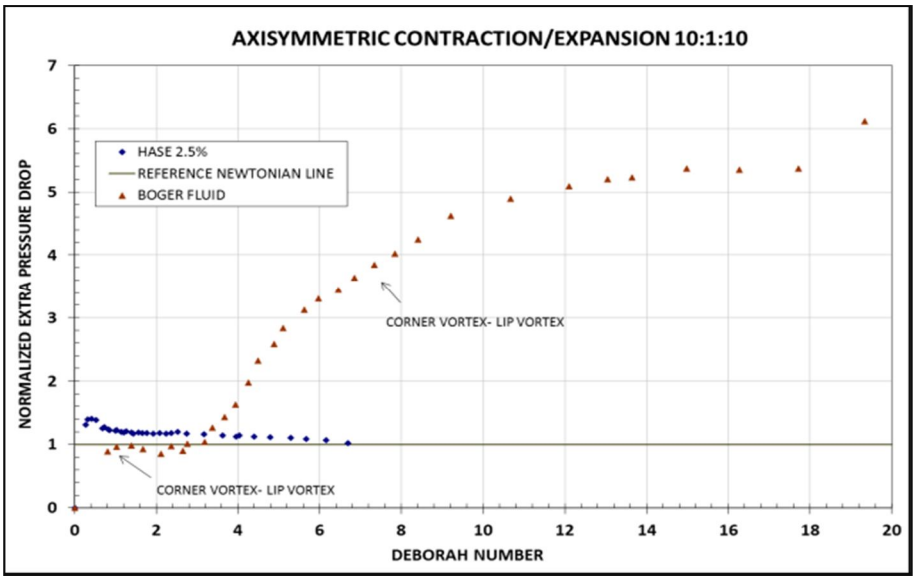

Figure 8.9E *epd* versus *De* number, 10:1:10 contraction-expansion

In the 10:1:10 geometry of Fig. 8.9E, the Boger fluid presents extremely high levels of normal stress and extensional viscosity; in fact, the largest values attained across all trial geometries. This is reflected through the increase in De_{crit} and the transition level from lip-to-corner vortex. Once again, this transition occurs beyond the *epd*-linear region, at {*epd*, *De*}=~{4,7}. At low *De*, the region of *epd*-drop is wider. The near-asymptotic values of *epd* obtained at high *De* numbers (up to *De*=18) are slightly lower than those observed in Fig. 8.9D (for 8:1:8 case). This concurs with larger N_1-contributions and delayed transition from shear-dominated to extension-dominated flow, occurring at *De*>7.

Here, the HASE fluid supports extremely high normal stress response, yet far from the limiting slope of 2; and also, is strongly shear-thinning. Data in Fig. 8.6 reveal that the flow in this geometry significantly penetrates the strain-softening regime. This triple-combined effect produces *epd*>1 throughout and up to *De*~7, with the transition from lip-to-corner

vortex occurring in the low-*De* range (*De*~0.5). This indicates an extension-dominated flow throughout most of the *De* range.

In Fig. 8.10, De_{crit} for the Boger fluid is plotted against the accumulated Hencky strain, defined as

$$\varepsilon = 2\ln(\beta_o), \tag{8.10}$$

where β_o is the contraction-ratio. This expression arises from the estimation of the total accumulated strain gathered by a fluid element, moving along the centreline from upstream to the middle of the contraction (Rothstein and McKinley 2001). It is provocative to note that the De_{crit} curve is qualitatively similar to the growth of extensional viscosity with Hencky strain. Indeed, in computational predictions of *epd* using the FENE-CR model (Tamaddon-Jahromi et al. 2010), it has been shown that De_{crit} scales with increase in extensional viscosity.

As such, for the Boger fluid and the 4:1:4 contraction-expansion, there stands a striking similarity between the predictions of Tamaddon et al. (2011) and the present experimental results. Indeed, the predictions for *epd* using FENE-CR at low *De* numbers, describe all the documented features of:- an initial region of *epd*-drop (*epd*<1); attainment of a minimum and upturn; prior to continuous rise, crossing the unity-Newtonian reference line; attaining *epd*>1 for higher *De* numbers and tending towards an ultimate asymptotic plateau. The increase in *epd* mimics the shape of the experimental curves, although the calculated magnitudes (28% increase over unity-Newtonian line) are predicted to occur at large *De* numbers. This contrasts with results presented in Fig. 8.9B, where increases of the order of 40% are observed at *De* numbers around unity.

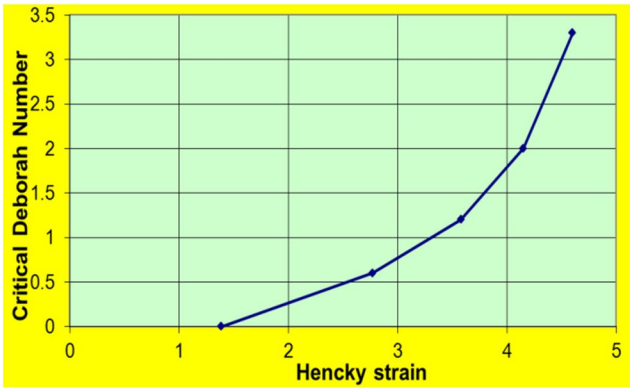

Figure 8.10 Critical Deborah number versus accumulated Hencky strain for 5 contraction-expansion geometries

Moreover, another notable feature of the predictions, which complies with the present experimental data, is the increase in calculated *epd* and De_{crit} with rising extensional viscosity. As the contraction-ratio becomes more severe (larger), the level of extensional stress, developed within the contraction, dominates that of normal stress, arising from shear. The experiments reveal large magnitudes in *epd* with increasing extensional effects for rising contraction-ratios.

The transition from lip-to-corner vortex is suggested to signal the transition from shear-dominated to extension-dominated flow (Rothstein and McKinley et al. 2001). For the shear-thinning fluid and to quantify this transition, the ratio of normal stress (on wall) to extensional stress (along centreline) is calculated, according to:

$$\Xi = \frac{N_1/\eta(\dot{\gamma})\dot{\gamma}}{\eta_E\dot{\varepsilon}/\eta_o\dot{\varepsilon}} \,. \qquad (8.11)$$

From Fig. 8.6, it is possible to estimate this stress-ratio (Ξ) as a function of the strain-rate or *De* number (noting, assumption made on comparable deformation rates). Results are shown in Fig. 8.11. What is essentially needed here is appropriate maxima in N_1 and extensional viscosity for the flow in question.

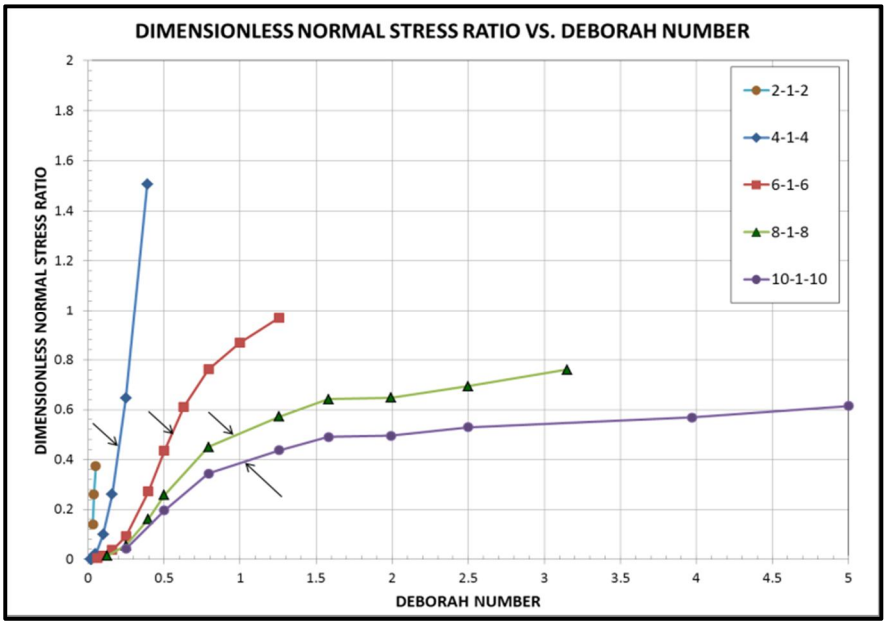

Figure 8.11 Non-dimensional stress ratio versus Deborah number for 5 geometries, indicating (arrows) transition of lip-to-corner vortex, HASE fluid

In Fig. 8.11, the Ξ=1 value corresponds to the transition of shear-dominated flow (>1) to extension dominated flow (<1). It is noteworthy that the lip-to-corner vortex transition (indicated by arrows) occurs in the 0.4-0.5 range of the stress-ratio, corresponding to *De* numbers from 0.2 to 1.0 for the five geometries. Ξ>1 only occurs in the 4:1:4 geometry, in accordance with the large *epd*-drop (*epd*<1) observed in Fig. 8.9B. In addition, this plot clearly demonstrates that the equivalent-Newtonian balanced-*epd* response, shown in the 8:1:8 contraction-expansion (Fig. 8.9D), corresponds to a near-balance state of shear and extensional flow, where the lip-to-corner vortex transition appears at the stress ratio, $\Xi = 0.5$.

8.6 Numerical results

Numerical simulations have been performed to compare against the counterpart experiments on Boger fluids, whilst selecting the 4:1:4 (rounded) contraction-expansion geometry. Note, in these simulations, lip-vortices are suppressed through the contraction-tip rounding (not so in the experiments). These steady-state predictions have been performed via a hybrid finite element/finite volume algorithm, based around an incremental pressure-correction time-stepping structure (López-Aguilar et al. 2014; Nyström et al. 2013;

Tamaddon-Jahromi et al. 2011; Walters et al. 2008, 2009). Then, numerical solutions on salient-corner vortex activity (related to *Lv* experimental data) and *epd* are reported using the FENE-CR model to represent the Boger fluid properties. Here, the solvent fraction β=0.85 and extensibility parameter L={3,6,10} have been chosen to match the experimental characterization of the Boger fluid, as in Fig. 6B. In particular, the extensibility parameter has been adjusted to capture the window of variation in simple shear N_1 experimental data.

Note the wall (maximum) shear-rate used in the experiments, $\dot{\gamma}_{wall} = \frac{4Q}{\pi R_c^3}$, is four times the characteristic rate chosen in the numerical situation, $\dot{\gamma}_{avg} = \frac{Q}{\pi R_c^3}$ (derived from the average velocity in tube flow). Taking the experimental-rate choice as the basis for comparison, rescaling of the numerical characteristic rate is given as $\dot{\gamma}_{wall} = 4\dot{\gamma}_{avg}$, and hence De=4We. Here, $We = \lambda_1 \dot{\gamma}_{avg}$ is the Weissenberg number derived in the numerical framework. One notes that experiments are performed by increasing the deformation-rate (through Q) for a single fluid (fixed λ_1); whilst, simulations are performed at fixed rate and by increasing fluid relaxation time (λ_1). Due to the nonlinear equation dependency on velocity-scale, this will affect any direct comparison attempted (Tamaddon-Jahromi et al. 2008). Nevertheless, a delay factor of 16, would appear to apply between *epd*-features, from experimental to simulation results (*i.e.* $16De^{\exp} \sim De^{\sim}$).

In the case of the 4:1:4 contraction-ratio and despite the disparity in physical configuration (sharp–experiments /rounded-numerical), agreement in trends between numerical predictions and experimental results is striking. The *epd* data-curves reveal an initial negative slope for De<{4,8,12} with respective, L={3,6,10} (Fig. 8.12A). Then, local *epd*-minima continually fall away from the reference-line, with {epd_{min},L,De}~ {0.99,3,4}, {0.97,6,8}, {0.95,10,12}, as both L and De rise. Crossing points at {De_{crit},L}={5.5,3}, {12,6}, {24,10} are influenced by the extensibility parameter L. The appearance of epd_{min} and De_{crit} is delayed as L is increased, and as N_1 strengthens (Fig. 8.6B). Beyond such De_{crit}, the *epd*-curves cross the unity reference-line, reaching percentage relative maxima (epd_{max}) to unity of {10%,28%,10%}. Here, at relatively higher elasticity levels than those

covered in experiments, two different behaviour patterns emerge: (i) under L={6,10}, monotonic rise to their limiting Deborah number De_{lim}={32,36},[2] prior to establishing an asymptote; and (ii) L=3, rises to a maxima (at De=10), asymptoting to a plateau, and declining thereafter (Fig. 8.12B). This second pattern is direct evidence of the complex interplay between N_1 and extensional viscosity. Here, *(a)* N_1 dominates at low elasticity levels, stimulating the initial *epd*-drop (*epd*<1); *(b)* when De is increased, the strain-hardening properties of the fluid balance N_1 effects, and provoke the *epd* data-curve to locate a minimum and rise thereafter; and *(c)* finally, as De is increased further (inset Fig. 8.12B), the *epd*-data curve locates a maximum (another extensional viscosity-N_1 balance state), and N_1 dominates with a declining *epd* trend. The numerical {De_{crit}^{num}=5.5,L=3}, is some 18 times larger than the experimental result of De_{crit}^{exp}=0.3.

Consistently, under *ideal theoretical flows* in Fig. 8.6B, (simple shear) N_1 and (simple uniaxial) extensional viscosity data reflect this interplay as De is elevated: *(a)* at low elasticity levels, N_1 data-curve rises with a quadratic functionality with the shear-rate, whilst the extensional viscosity remains constant; *(b)* at larger De, strain-hardening in extensional viscosity is observed, whilst N_1 weakens its quadratic rising slope; and *(c)* finally, at even higher elasticity levels, the extensional viscosity data-curves plateau, and those for N_1 rise monotonically. Due to their relatively low De_{lim}, this complex behaviour is not observed in solutions with L={6,10}.

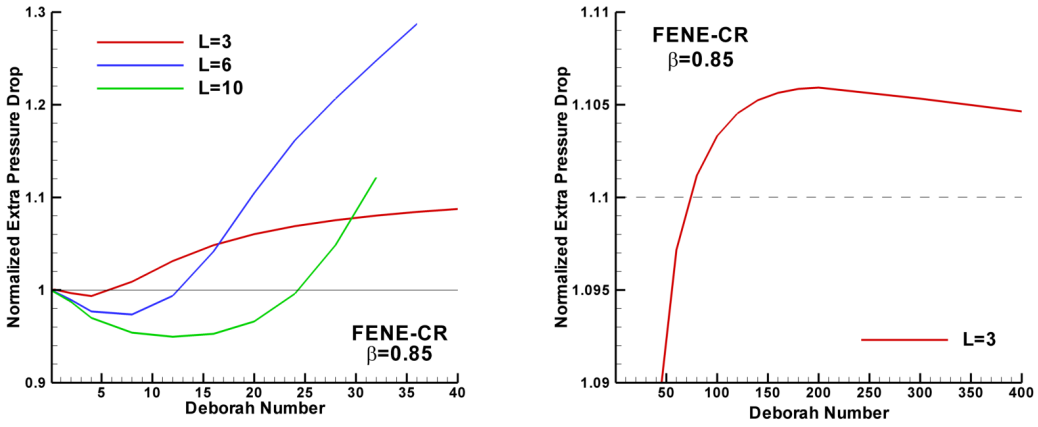

Figure 8.12A and B Numerical *epd* predictions versus De; Boger fluid; β=0.85, FENE-CR L={3,6,10}

[2] De_{lim} represents the final Deborah number with a stable solution

Analogous trends are observed to the experimental findings between vortex dynamics and *epd*-prediction in the streamline patterns of Fig. 8.13A. Here, for L=3 and 0.4<*De*<300, upstream vortex enhancement is apparent through streamline fields and upstream vortex intensity curves. Beyond *De*>300, this flow-pattern is suppressed as *De* rises. Such growth-maximum-suppression behaviour is likewise apparent in *epd*-data (Fig. 8.12B). In contrast, under *L*={6,10}, upstream vortex enhancement is exclusively observed. Corresponding reattachment vortex lengths (*Lv*) are provided in Fig. 8.13B. These data are in accord with experimental findings at low *De*, where the reattachment vortex length (*Lv*) is observed to grow as *De* rises (see Fig. 8.8).

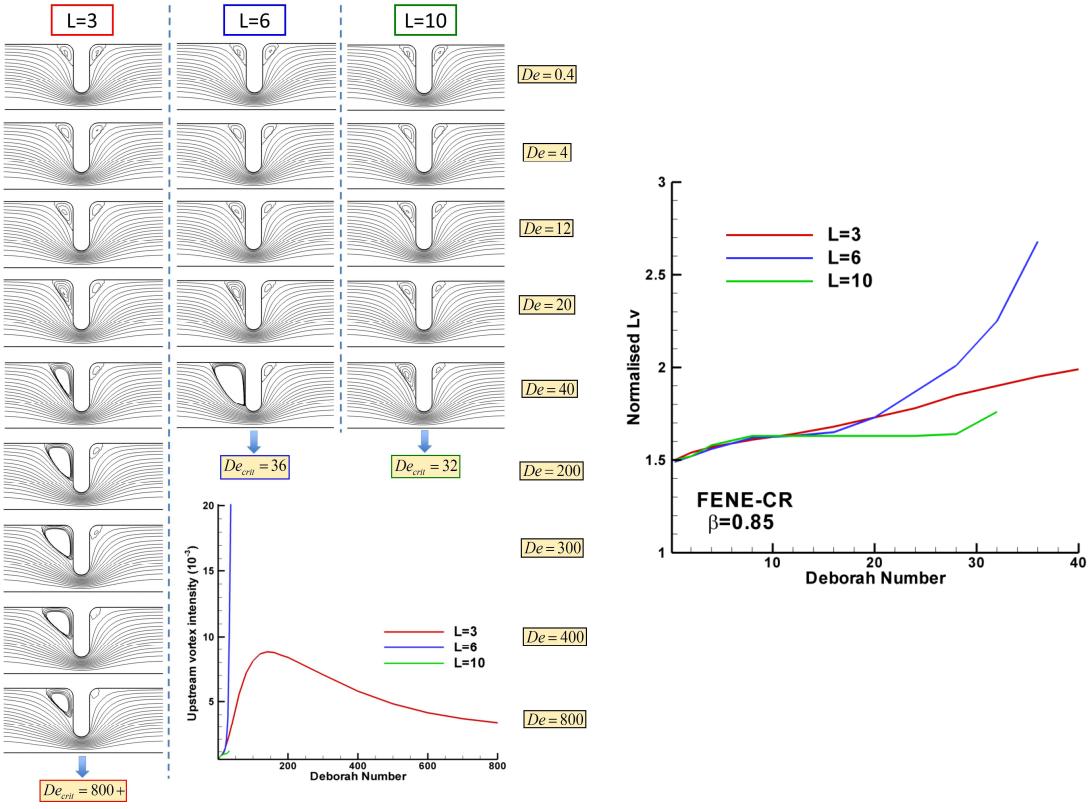

Figure 8.13A and B Numerical streamline patterns and vortex intensity and *Lv* predictions versus *De*; Boger fluid; β=0.85, FENE-CR *L*={3,6,10}

8.7 Conclusions

This work has revealed provocative results on the kinematics and pressure-drop measurements in the axisymmetric contraction-expansion geometry for Boger and shear-thinning elastic fluids.

Besides the large differences existing between Boger and shear-thinning elastic fluids, this study has exposed the binding relationship between the magnitude of the first normal stress difference and vortex growth. When the magnitude of N_1 for both fluids is similar, vortex-size is comparable, independent of the nature of the fluid.

For the Boger fluid, the 2:1:2 contraction-expansion is a unique case, in which the range of strain-rates of this *creeping flow* correspond to constant viscosity and negligible normal stress. The associated *epd* measured (*epd*=3) amounts to three times the Newtonian reference (*epd*=1). For other and increasing contraction-ratios, the resulting *epd* reflects the balance between N_1 and extensional viscosity. The transition of lip-to-corner vortex occurs in the more severe contraction ratios (β_o>6). Furthermore and relative to the unity-Newtonian reference line - the initial *epd*-drop below (*epd*<1); the subsequent crossing (*epd*=1); and continuous increase above (*epd*>1), all agree with FENE-CR numerical predictions using small extensibility-parameters. The crossing-point (De_{crit}) scales with the accumulated Hencky strain, with growth qualitatively similar to that noted in extensional viscosity with strain.

The shear-thinning HASE fluid possesses larger normal stresses at comparable strain-rates than those of the Boger fluid. Hence, N_1 substantially influences the resulting *epd*, even in the 2:1:2 geometry. Shear-thinning dominates in the 4:1:4 geometry, where *epd*-drops are measured of around 40% below the Newtonian reference line. The transition between shear to extension-dominated flows occurs at low *De* numbers, as the lip-to-corner vortex transition is observed accordingly. The equivalent-Newtonian *epd*-response, observed in the 8:1:8 contraction-expansion, derives from a balance between shear-dominated and extension-dominated flow types. The lip-to-corner vortex transition occurs at a stress-ratio near unity in this case (Ξ ~1).

CHAPTER 9

A Computational Extensional-Rheology Study of Two Biofluid Systems

The main focus of the present chapter is to determine, through computational modelling, the extensional rheological response of some model biofluids, with a view to ultimately aiding experimentally-based analyses and clinical practice. This is accomplished in the present study through model extensional flows and rheological investigation, addressing filament stretching and contraction flows, and upon which significant advances are presented. As such, two biofluid flow systems within the human body are of current interest: *(i)* respiratory disorders and sputum in the lung-airways (associated with filament stretching), where stretchiness of mucus-sputum in situ is vital; with clinical focus on chronic obstructive pulmonary disease (COPD/sputum); and *(ii)* bile-flow in the biliary system (contraction flow): with clinical focus on disorders of primary sclerosis cholangitis, and common bile duct narrowing. Both sputum and bile biofluid systems are represented through kinetic theory rheological fluid modelling, with capability to represent material structure - entanglement, branching, anisotropy. This is practically achieved by appealing to the class of pom-pom differential constitutive models, extracted from polymer-melt physics and deployed here through a Single Extended pom-pom (SXPP) approximation. This class of models is sufficiently rich to enable description of both network-structure and rheological properties, exhibiting viscoelastic response (memory), with strain-hardening/softening and shear-thinning properties.

9.1 Introduction

To advance the present work, two known ideal-benchmark flow problems are introduced to mimic the targeted biofluid systems under study, involving bile and sputum. For the bile-duct narrowing work, a *steady* 4:1 contraction flow problem is considered (Walters and Webster 2003; Owens and Phillips 2002), whilst a *dynamic* FiSER-CaBER filament-stretching flow is utilised for the respiratory study (McKinley and Sridhar 2003). The information sought from the contraction-flow bile studies, is related to *confined* complex flow field description, under varied rheological description. Hence, seeking flow field structure through vortices and stress build-up. At this early stage of the study, a key aim has been to also assess what quality of computational *free-surface* FiSER-CaBER characterisation may be extracted for such model biofluid systems through the proposed kinetic network-theory fluid modelling. This is accomplished via use of the Single Extended pom-pom (SXPP) model (Verdier 2003; Aboubacar et al. 2005; Aguayo et al. 2007), exhibiting viscoelastic response of strain-hardening fluids that also display *shear-thinning* properties. Crucially, the present work is directed towards casting direct insight into the precise role and impact that the various rheological properties have towards seeking effective biomarkers. Hence, this will pinpoint those rheological properties of key importance, and therefore gain clinical advantage through advanced predictive aids on: disease progression, modification to diagnosis and treatment procedures, and drug modification/delivery. Motivationally, improved understanding of flow systems within the human body and their functioning will facilitate appropriate intervention at pre-symptomatic, acute or chronic stages of illnesses – hence, addressing patient-specific needs and those most pressing in a modern healthcare system. To achieve this goal, the main focus here lies in developing high-quality predictive solutions, to associated complex flow model systems, representative of sputum in the respiratory system and bile in the biliary system.

Specifically, the focused challenge of the present study relates to the advanced prediction of biofluid flows within two bio-systems associated with the human body – the respiratory and biliary systems. In particular to pathologies of *(i)* the lung-airways (respiratory disorders): chronic obstructive pulmonary disease (COPD, smokers' disease, 3rd leading cause of death worldwide, 2020), and *(ii)* the biliary system: primary sclerosing cholangitis (cancerous), and common bile duct narrowing (CBD). To provide some background - disease progression left untreated may result in fatal cancerous conditions and/or organ transplant. Some of the novelty and appeal of the present study lies in the embodied advanced bio-rheology predictive technology, with the ultimate aim of developing new biomarkers, and producing improved diagnostic tools to aid in next-generation clinical practice. It is important to appreciate, that the rheological properties of bile or sputum are not only patient-specific, but also pathologically dependent, and in this analysis their rheological

response, particularly *under extension*, represents a key cornerstone to the present research approach. In particular, bile and sputum rheological description is handled computationally via filament-stretching, which finds embodiment in *CaBER-FiSER* rheometer apparatus.

Bile duct disorders and study Unfortunately, the vast majority of published work on bile duct disorders has focused on clinical aspects and procedures for diagnosis and treatment, with less regard to the actual flow dynamics or rheological implications of bile flow itself (Sugita et al. 2003). Some relevant numerical studies have considered the geometrical complexity of the biliary network, whilst neglecting the additional complexity of the rheological description of bile. Some viscous inelastic (shear-thinning) bile flow modelling has recently emerged (Ooi et al. 2004; Li et al. 2007; Holdsworth et al. 1989). However, a comprehensive rheological analysis of bile flow within the biliary system remains relatively uncharted (Holdsworth et al. 1989). Note, some issues relating to bile rheological characterisation are also encountered within sputum characterisation, as discussed below. Specifically, under contraction flow studies for *bile/biliary system disorders*, the well established *4:1 contraction benchmark problem* (Walters and Webster 2003; Owens and Phillips 2002) is appealing and representative of the confined flow settings encountered in the biliary system (mixed shear-extensional flow). Here, accurate determination of flow field variables and structures is thought to be vital for appropriate clinical response - to avert advanced constrictions/blockage in the bile system (Sugita et al. 2003) – as with gallstone blockages and cancerous conditions. Such flow field features are apparent as a direct consequence of rheological properties (Tamaddon-Jahromi and Webster 2011), and may be associated with the response of bile flow within the biliary ducts (Sugita et al. 2003).

In the present context, bile flow rheology may be modelled through a number of approaches, some of which emerge from kinetic-molecular theory (pom-pom models; Blackwell et al. 2000; Aboubacar et al. 2005; Aguayo et al. 2007; used here; as likewise for sputum) and yet others from micellar network theory (worm-like micelles, mimicking bile cellular design; López-Aguilar et al. 2014). The modelling may account for macro-to-micro length-scales (microfluidics) (Verdier 2003), transient dynamics (Tamaddon-Jahromi et al. 2011), viscoelastoplastic yielding (Verdier 2003; Al-Muslimawi et al. 2013) and, in some instances, elastic duct-wall deformation (Echendu et al. 2013). Here, pom-pom parametric variation is conducted over structural network description to explore a wide variety of (i) topologies (entanglement ε_{pom}, branching q) related to molecular architecture, (ii) rheological properties (tension-hardening or softening, shear-thinning), and (iii) relaxation mechanisms (backbone stretch, multiple time-scales). Subsequently, additional consideration may also be given to representation of additives (assumed fibre-like, specific size range, concentration), thixotropy (time dependency; López-Aguilar et al. 2014; Aguayo et al. 2007),

and alternative bile compositions (molecular weight, concentration). As a consequence, clinical treatment is envisaged through directed-variation of bile rheology, which may practically be triggered via appropriate drug administration. Adjustment in drug design, through bile rheological modification, is aimed at lowering both pressure drops and duct swelling. Industrially, examples already exist of such technology deployed in practice (enhanced oil-recovery through surfactants and rheological adjustment – smart fluids; López-Aguilar et al. 2014). In more extreme bile-duct narrowing instances (blockage), direct medical intervention may be required, where duct widening is necessary via a stent implant or a bypass. Again here, modelling may be introduced beneficially, to detect effective working of the stent-implant or bypass functionality, *in situ* and post-operative.

Respiratory disorders and study For background here, the rheology of sputum has been extensively reported in studies involving the application of steady and oscillatory shear. Sputum is generally considered as a non-Newtonian viscoelastic gel that exhibits shear-thinning and thixotropic properties (Lai et al. 2009). Sputum (and/or sputum-mucus mixtures) is a biofluid secreted by goblet cells present along the airways. Mucus is a slimy substance produced to help remove inhaled dust, bacteria, and other small particles. This biofluid contains a number of enzymes, degraded cellular material, bacteria and white blood cells that act as an immune defence system against infection and inflammation. Infected patients tend to cough up considerable sputum daily, the constitution of which is impregnated with cell residue. Damaged airways of the lung tend to make considerably more mucus than under normal conditions. An excess of sputum production may block air tracks and even exacerbate COPD symptoms. Thus, a particular therapy adopted is often designed to adjust sputum rheology (shear), through drug administration (typically – mucolytics and anticholinergics), and increases sputum production.

Challenges in experimental measurement relate to the large degree of variability in values of rheological parameters of samples from patient-subjects with the same diseased state. Commonly, samples of biofluid (sputum and bile likewise) from both healthy and unhealthy subjects are rheologically characterised in terms of viscosity, elastic modulus (G'), loss modulus (G''), and also yield stress (Lopez-Vidriero and Reid 1978; Broughton-Head et al. 2007; Serisier et al. 2009). For sputum, Lopez-Vidriero and Reid (1978) provide a summary of viscosity of samples of mucoid, purulent and mucopurulent (mixture of mucoid and purulent) sputum from a range of diseased patients, including those with Chronic Bronchitis, Bronchiectasis and Asthma. They reported viscosity values depend more on whether the sample is mucoid or purulent than diseased state; the former being generally more viscous than the latter. A major concern, when comparing values of viscosity between different data sets, is that the viscosity is often measured at an arbitrary level of shear rate and found to vary in sputum viscosity within the same subject on different days

(Broughton-Head et al. 2007; Serisier et al. 2009). Notably, measurements of sputum (shear) viscosity generally lack standardisation and have failed to provide a global biomarker for diseased states. It is the case that the variability of results is mainly due to the differences between subjects, methods of collection, and diseased state. Furthermore, this casts doubt on the appropriateness of shear rheometry in the measurement of bulk rheological properties of sputum, which is inhomogeneous and can contain cells and aggregates (Kini 2002). Homogenisation of the sputum prior to rheological measurements can be attempted by means of shearing the sample several times in a syringe (Serisier et al. 2009). Comparisons of viscoelastic measurements between homogenised and non-homogenised samples of the same sputum sample show that values of G' and dynamic viscosity can change up to a few decades of magnitude (Broughton-Head et al. 2007). This suggests that the homogenisation procedure itself strongly influences the structure of the sample, and this may mask any differences detectable and stimulated by the precise nature of the disease.

Filament stretching Under filament-stretching considerations, the filament stretching rheometer (McKinley and Sridhar 2003; Eggers 1997; Anna and McKinley 2001) has emerged as a favourable apparatus for measuring the extensional properties of highly-mobile low-medium viscosity fluids. This measuring device determines access to crucially important bulk rheological properties such as Trouton ratio, extensional viscosity and characteristic time. This is precisely the modelling procedure adopted in the present study, where trends of increasing apparent extensional viscosity in time are derived over acceptable ranges of deformation rate. Filament samples may vary in length (nano, micro, macro) and loading (length/breath). Subsequent necking leads to significant thinning and reduction in the central region of the liquid bridge, whilst end-effects result in considerable shearing within the near end-plate zone (filament-foot). Previous and relevant studies on filament stretching span numerous application areas including - micro to macro-filamentation, coatings, cavitation, printing, foaming, extrusion, gas-droplet formation, conventional and dynamically-loaded journal-bearing lubrication. A comprehensive overview of filament stretching technology is provided by McKinley and Sridhar (2003), covering the flow dynamics within filament-stretching rheometers for non-Newtonian fluids. These authors also commented (McKinley and Sridhar 2003) on the challenge to reach large strains (Hencky-strain, measure of time or strain build-up). In the present context, it is anticipated that sputum samples exhibit strain-hardening, through rapid deformation in dilute polymer solutions, allowing for various representative constitutive equations used to model such flows. For example with Boger fluids, exhibiting constant shear viscosity and pronounced strain-hardening in uniaxial extension, the overall dynamical response within elongating liquid-filaments is now well-reported in the open literature. Regarding the thinning and breakup of filaments, Eggers (1997) provided a comprehensive experimental and numerical review

on break-up for Newtonian filaments and jets. Moreover in step-strain mode, Anna and McKinley (2001) examined the transient dependence of the diameter of the filament, the time to break-up as a function of the sample molecular weight; with comparison against the theory for break-up of slender viscoelastic filaments. In the present analysis, kinetic network-theory fluid modelling (via SXPP) is called upon to pursue the detailed numerical differential equation computation and analysis.

Typically, the dynamic development of the mid-filament diameter is monitored during the process of necking and failure, from which the appropriate rheological calculations are performed (dynamic extensional viscosity, characteristic time). In step-strain mode (CaBER), the filament stretching rheometer may be employed under capillary-breakup conditions (Eggers 1997; Anna and McKinley 2001). CaBER trials impose a rapid axial step-strain of prescribed magnitude, and then allow the sample to relax and breakup under the action of capillary forces (fluid self-selecting time scale). Commonly, this implies short initial stretched samples (user-controlled), and much shorter than under FiSER-mode (continuous stretching, imposed rate/time scale). This is a practical attraction of the CaBER-mode for *in-situ* sample testing (point-of-healthcare clinical dispensation and treatment for out-patients), avoiding the need for sample transportation and possible degradation (technique of choice). Although the flows in these two types of filament-stretching rheometer differ, both devices generate, *a priori* a uniaxial extensional deformation – hence, accessing dynamic extensional viscosity. The CaBER-form also offers the capability to estimate sputum principal characteristic time (measure of elasticity, resistance to thinning, time for stress-growth), necessitating cylindrical filamentation. FiSER and CaBER trials are conducted here under pom-pom (SXPP) material modelling to analyse the influence of material-system parameters on the cylindrical filament shape (minimal radius) and therefore to the material characterisation itself.

Concerning FiSER and CaBER filament-stretching, as a suitable rheometric technique in deployment on biosystems pertinent for respiratory disorder study, comparison between numerical predicted data and theoretically derived results (transient simple uniaxial extensional flow) may be used as a directive. For example, this may elucidate which rheological extensional test, is more suitable to determine material properties, and which more practical in gathering diagnostic data. FiSER is found to produce faithful extensional viscosity values alongside corresponding experiments, with the drawback of being impractical in experimental/field-clinical usage given its size/sample requirements. That is, to within certain deformation ranges/parameter sets. Alternatively, CaBER is effective in determining the characteristic time, but considerable care must be taken over the mid-plane filament-diameter measurement window to ensure

agreement/consistency with theoretical data. One thesis proposed here, is to explore the possibility of utilising FiSER in predictive mode, to dictate effective use of CaBER for deployment clinically.

9.2 Governing equations and rheology

The governing equations considered in this chapter have been detailed in chapter 2. The non-dimensional continuity and momentum conservation principles are expressed in eqs.(2.11)-(2.12). Some relevant characteristic quantities are introduced based on a characteristic velocity scale U (average velocity) and a length scale L (radius at contraction or filament initial length L_0). A time scale ($t = L_0/U$) is derived, the inverse of which defines a characteristic deformation rate for contraction flow; in the filament setting, the initial stretch-rate is taken as the time-scale, as ($\dot{\varepsilon}_0 = U/L_0$).The dimensionless group numbers of Reynolds number ($\mathrm{Re} = \rho UL/\eta_0$ for contraction-flow, and $\mathrm{Re} = \rho\dot{\varepsilon}_0 L_0^2/\eta_0$ for filament-stretching), Deborah number (likewise, $De = \lambda U/L$ in contraction-flow and $De = \lambda\dot{\varepsilon}_0$ in filament-stretching), and capillary number ($Ca = \eta_0\dot{\varepsilon}_0 L_0/\chi$, filament-stretching alone) are introduced considering density ρ together with the zero-shear rate viscosity (η_0) as a viscosity scale. Here, χ is the interfacial surface tension coefficient, relevant for free-surface conditions. Then, the stress and pressure are non-dimensionalised with ($\eta_0 U/L$ or $\eta_0\dot{\varepsilon}_0$) scales.

From a viscoelastic modelling viewpoint, the kinetic/molecular-based pom-pom model is considered. Then, the mass-momentum governing equations should be supplemented by a constitutive equation for stress, which may be represented in general form as:

$$De\frac{\partial \boldsymbol{\tau}}{\partial t} = -De\boldsymbol{u}\cdot\nabla\boldsymbol{\tau} - f_1\boldsymbol{\tau} + 2(1-\beta)\boldsymbol{d} + De(\boldsymbol{\tau}\cdot\boldsymbol{L} + \boldsymbol{L}^{\dagger}\cdot\boldsymbol{\tau}) - De\,\xi\left(\boldsymbol{\tau}\cdot\boldsymbol{d} + \boldsymbol{d}\cdot\boldsymbol{\tau}\right) - \frac{\alpha De}{1-\beta}\boldsymbol{\tau}\cdot\boldsymbol{\tau} + \frac{1-\beta}{De}(f_2 - 1)\boldsymbol{I} \tag{2.52}$$

Here, for the Single Extended pompom (SXPP) model, one identifies the functionals (f_1, f_2) and four additional parameters (q, ε_{pom}, λ_{pom}, α_{pom}). These parameters govern the number of side-branch arms to the molecular-backbone chain-segment (q), system entanglement (ε_{pom}), the stretch of the back-bone segment (λ_{pom}), and the degree of system anisotropy (α_{pom}). Corresponding forms extracted from the physics for these functionals (f_1, f_2), in terms of the base network-description parameters (q, ε_{pom}, λ_{pom}, α_{pom}) and (β, De, $\boldsymbol{\tau}$) may be given by:

$$f_1 = f_2 = f(\lambda,\boldsymbol{\tau}) = \frac{2}{\varepsilon_{pom}}\left(1 - \frac{1}{\lambda_{pom}}\right)\mathrm{e}^{\nu\left(\lambda_{pom}-1\right)} + \frac{1}{\lambda_{pom}^2}\left(1 - \left\{\frac{De}{(1-\beta)}\right\}^2 \frac{\alpha_{pom}}{3}\mathrm{tr}\left(\boldsymbol{\tau}\cdot\boldsymbol{\tau}\right)\right), \tag{2.53}$$

where, the free parameter v is estimated by data-fitting and found to be inversely proportional to the number of side-branch arms dangling from an end of the molecular chain-segment (v = c/q, with c taken as 2), see Blackwell et al. (2000). The parameter ε_{pom} is the ratio of the backbone stretch (λ_{0s}= λ) to the orientation (λ_{0b}) relaxation times (larger values indicate more highly-mobile system states, less degree of entanglement). With the single-equation (SXPP) approximation to the pom-pom model, representation of the back-bone stretch parameter λ_{pom}, is collapsed from its generalised differential evolutionary form to an instantaneous algebraic response, given through expression:

$$\lambda_{pom} = \sqrt{1+\frac{1}{3}\frac{De}{(1-\beta)}\left|\mathrm{tr}(\boldsymbol{\tau})\right|}\,,\ \varepsilon_{pom} = \frac{\lambda_{0s}}{\lambda_{0b}}\,. \tag{2.54}$$

In this respect, the viscometric data of relevance for the current study and this SXPP model are reported in Chapter 3, section 3.3, covering extensional viscosity response for the various system-network variation parameters.

9.3 Contraction flow analysis: relevant to biliary duct and bile flow studies

The 4:1 axisymmetric rounded-corner contraction-flow problem has been used to analyse the influence of the XPP rheometrical parameter setting on the development of flow field structure, governing system-network composition under viscoelastic creeping flow conditions. Such a flow configuration is utilised as a model idealisation for bile duct narrowing within the biliary system. The length of upstream and downstream sections are 27.5L and 49L, respectively. To solve the governing system of partial differential equations for the XPP model, appeal is made to the inlet boundary-condition treatment employed by Aboubacar et al. (2005). That is, by imposing fully-developed velocity and extra-stress XPP-profiles on flow-entry. These are provided from computations based on the equivalent axisymmetric entry-channel flow problem. Fully-developed boundary conditions are established at the outflow ensuring no change with respect to velocity component U_z and vanishing component U_r. In addition, no-slip boundary conditions are imposed along contraction-geometry walls. Once flow kinematics have been established at the inlet, stress can be gathered by solving the corresponding consistent set of ODEs. Simulations are initiated from a (We=0.1)-solution state and continuation in We parameter-space is employed until a critical level of Weissenberg number is reached (We_{crit}), beyond which either oscillation or numerical divergence is encountered.

Based on various elasticity levels (We), the present study presents an analysis for the influence of the number of dangling molecular-arms q across the range {2,5,10}. The remaining XPP parameters setting are unperturbed, Re=0, ε_{pom}=0.666, α_{pom}=0.15 and β=1/9 (Fig. 9.1). The flow

field structure is traced for each setting of arms-q, through vortex patterns for a series of steady-state solutions up to critical levels of Weissenberg number. Then, at the level of We=10, corresponding solution states are provided along the downstream wall, manifested through principal stress N_1 (variation in q and α_{pom}, respectively), and stretch λ_{pom} (Fig. 9.2).

9.3.1 Vortex behaviour with q-variation As depicted from Fig. 9.1, elasticity levels attainable in the numerical simulations have been found to decline with increasing number of dangling branched-arms (q), with We_{crit} for q={2, 5, and 10} being {60, 30 and 11}, respectively. It is important to bear in mind that the flow here is not purely extensional, but of complex dynamical form. As all model-fluids in consideration exhibit practically identical shear viscosity, it is anticipated that the increase in maximum value in extensional viscosity (strain-hardening) with increasing branched-arms is a major factor in determining the reduction in We_{crit}. Notably, one generally observes significantly larger vortices with increasing levels of elasticity (We) and number of branched-arms (q). Here, salient-corner vortex cell-size shape adjustment against We, measured on the vertical wall (L) and horizontal wall (X), follow similar patterns to one another, relatively independent of q-parameter. Note that, the magnitude of X is larger than for L at any chosen $We\geq5$. This growth-trend for X and L can be associated with all the strongly strain-hardening cases considered ($q\geq5$). In addition, major increments are observed in vortex strength between We values of 5 and 10 for $q\geq5$ (Fig. 9.1), with convex curvature attached to the vortex separation-line. Moreover, for q={2, 5}, vortex strength decreases sharply from {3.01, 25.09} at We=10, to {0.46, 12.97} at We_{crit}. This is likely due to the drop in level of softening at intermediate extension-rates.

9.3.2 First normal stress and stretching with q-variation Independent of the fluid model, the components of the deformation tensor have their largest value (peak-maxima) around the corner; this stimulates corresponding response in all solution components at the same location. This increase is followed by a levelling plateau along the downstream wall, a flow characteristic commonly attributed to the 4:1 benchmark contraction-flow problem. Under XPP modelling, profiles of N_1 and λ_{pom} along the downstream wall (y=3) are displayed in Fig. 9.2 at We=5. There is a significant increase in the level of N_1 and λ_{pom} with increasing arms-q from the corner (peak) and beyond (downstream-wall plateau). The relative increase in N_1 from the reference-base of (q=2) to (q=10) is nearly three times. Equivalently, λ_{pom} almost doubles (1.7 times) its reference-base level for (q=2). Prior to the contraction zone, in the upstream channel, and independent of the number of branched-arms q, there is relatively no variation in N_1 and λ_{pom} fields (unstretched material: λ_{pom}=1). Within this zone, shear dominates over extensional deformation.

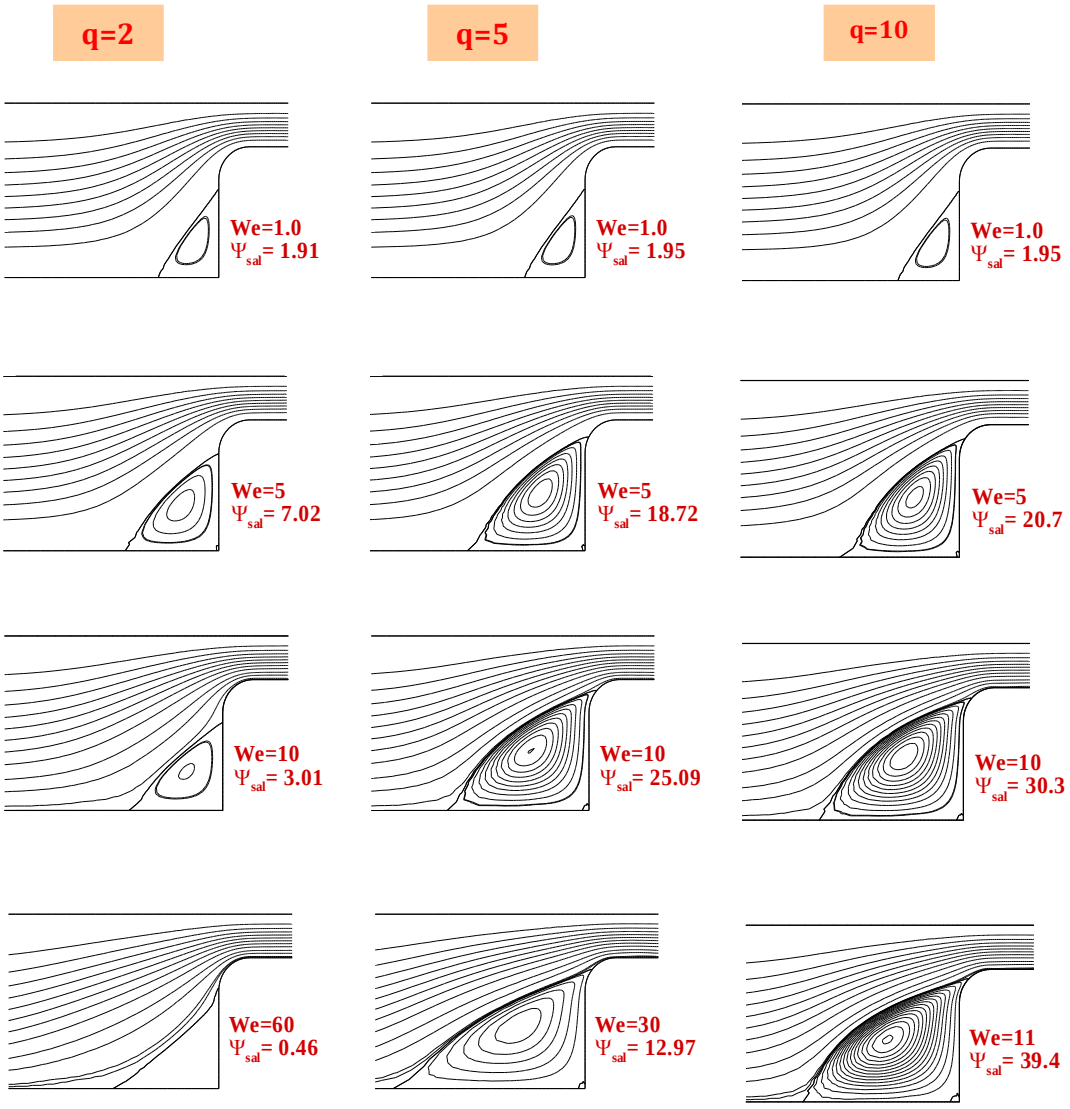

Figure 9.1 Stream function; increasing *We*; ***q*-variation** {2,5,10}; ε_{pom}=0.666, α_{pom}=0.15, β=1/9

9.3.3 Vortex behaviour with ε_{pom}-variation, low (ε_{pom}=0.999), median (ε_{pom}=0.666), and high levels of entanglement (ε_{pom}=0.333) The influence of ε_{pom}, the ratio of the relaxation time of the stretch of the backbone to that of its orientation, on the vortex structure is shown in Fig. 9.3 for q=10, α_{pom}=0.15, and β=1/9. This ε_{pom} parameter may be used to interpret the degree of entanglement of the structured-network system. High values of ε_{pom} correspond to molecular-chains with relatively short backbone lengths but long arms to slow down the dynamics. In this case the system is less entangled, and the orientation and stretch relax almost simultaneously. Alternatively, low values of ε_{pom} correspond to highly-entangled systems. The orientation relaxation time with low values of ε_{pom} is much slower than the relaxation time of the backbone stretch. In Fig. 9.3, one may observe that the combination of extensional viscosity and the degree of entanglement clearly

influence vortex activity, under vortex size and intensity. As opposed to under the same shear viscosity with increasing q, changing ε_{pom} from 0.333 to 0.666 and 0.999, generates delay in shear-thinning response. Here, one observes larger vortex intensity (Ψ_{sal}) with increasing levels of elasticity (We) at different ε_{pom}. However, at the low value of ε_{pom}=0.333, the magnitude of the salient-corner vortex cell-size of the horizontal wall (X) is larger than that obtained for ε_{pom}=0.666 and ε_{pom}=0.999. This is to be regarded as a consequence of the higher degree of entanglement for ε_{pom}=0.333 state, when interpreted against those for ε_{pom}=0.666 and ε_{pom}=0.999 states. Nevertheless, at We=10 (We_{crit}=9 for ε=0.999), there is about 54% and 61% increase in salient-corner vortex intensity from ε_{pom}=0.333 to ε_{pom}=0666 and ε_{pom}=0.999, respectively. This finding one may attribute to the difference in level of strain-hardening from ε_{pom}=0.333 to ε_{pom}=0.999. Note that, the shape of the vortex separation-line evolves from convex at We=1, to concave at high We.

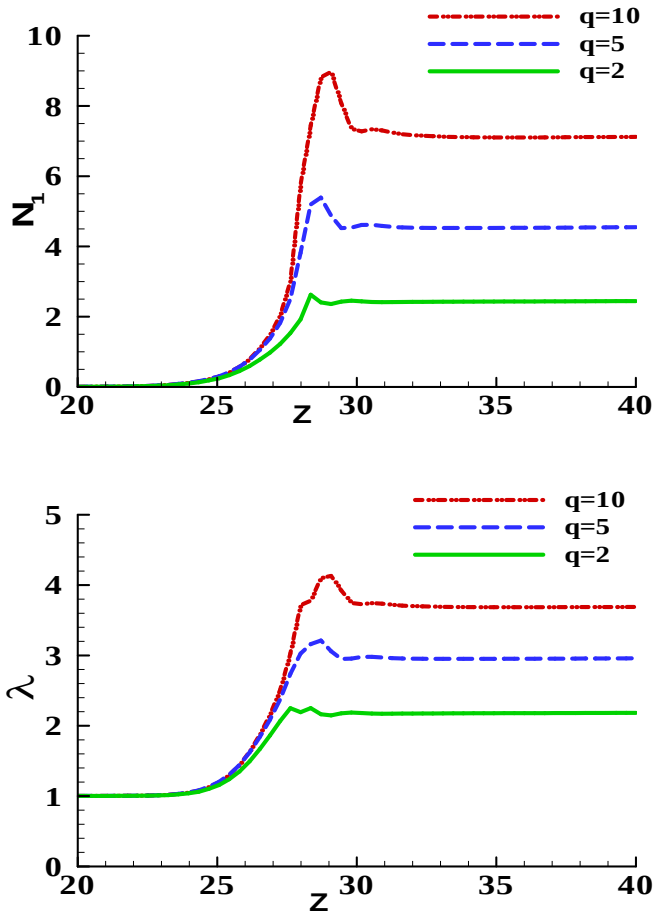

Figure 9.2 First normal stress (top) and backbone stretch (bottom) along the downstream wall, ***q*-variation** {2,5,10}; ε_{pom}=0.666, β=1/9 , We=5

9.3.4 First normal stress, stretching, and fringe pattern fields with increasing *We* In Fig. 9.4a, field plots are presented for polymeric first-normal stress (N_1) for ε_{pom}=0.666, q=10, α_{pom}=0.15, β=1/9. Note that maximum in N_1 field plot for *We*=10 is located around the corner just after the constriction, whilst for *We*=1 and 5, the maxima in N_1 are located before the contraction. From *We*=1 to *We*=10 of Fig. 9.4a, N_1-maxima increase from 2.57 to 29.34 units with a downstream shift in location of such stress-maxima. There is some noticeable cross-stream influence away from this stress-maxima towards the centreline, which is evident at *We*=1 and that increases with rise in *We*.

For molecular stretch, λ_{pom} in Fig. 9.4b, one can distinguish regions where there is relatively unstretched material. These regions correspond to inflow and recirculation zones. Such regions of unstretched material correspond to zones where shear deformation dominates over extensional deformation. In addition, there is a '*banded entry-flow*' zone of stretched material, where the influence of increasing levels of elasticity is reflected in larger extension of the polymeric molecular-chains. For *We*=1, stretch generates a value of $\lambda_{pom}\approx$2.38 at the boundary wall, whilst for *We*=5, this rises to $\lambda_{pom}\approx$4.19. At larger levels of elasticity (*We*=10), solution differences become more apparent over *We*=1 and *We*=5. The relative increase in λ_{pom} over the contraction zone, from (*We*=5) to (*We*=10), lies around 60%, as opposed to 43% increase from (*We*=1) to (*We*=5).

Fig. 9.5 demonstrates the Principle Stress Difference (*PSD*) fields for the SXPP model at *We*=5 and 10 with ε_{pom}=0.666, q=10, α_{pom}=0.15, β=1/9. *PSD* contains information covering both shear and extensional response ($PSD=\sqrt{N_1^2+4\tau_{xy}^2}$) and conveys patterns of discrete bands and levels of equal stress. Such evidence is often held as a direct measure of correspondence to stress-birefingence data extracted from counterpart experimental flow investigations (Verbeeten et al. 2004). On the symmetry line, where τ_{xy}=0, *PSD* patterns represent the first-normal stress-difference response. Moreover, fringe patterns are detected that begin to originate from the corner and expand outwards from that station. In addition, within Fig. 9.5, the banding pattern along the downstream wall (in shear deformation) is more expanded for *We*=10 than for *We*=5, and likewise, even the fringes away from the wall appear relatively more widespread. No sign of maximum shifting is observed as elasticity levels are raised. However, the relative increase in *PSD*-maxima lies around 70% from *We*=5 to *We*=10.

The study of the *biliary system* (which practically would be constituted by a set of contractions; Sugita et al. 2003) through the idealised *4:1 contraction problem* (Walters and Webster 2003; Owens and Phillips 2002), has enabled the determination of the effects of rheological properties and

complex shear/extensional flow conditions on flow field variables and structures. In this work, first normal stress difference (N_1)-fields and vortex structures have been found to be highly indicative flow features, based on the presence of duct narrowing (and by implication near-blockages). In this respect and relating to *bile/biliary system disorders*, accurate bile rheological characterisation (through complex constitutive equations), N_1 and vortex-structure dynamics are all key determination factors worthy of further investigation.

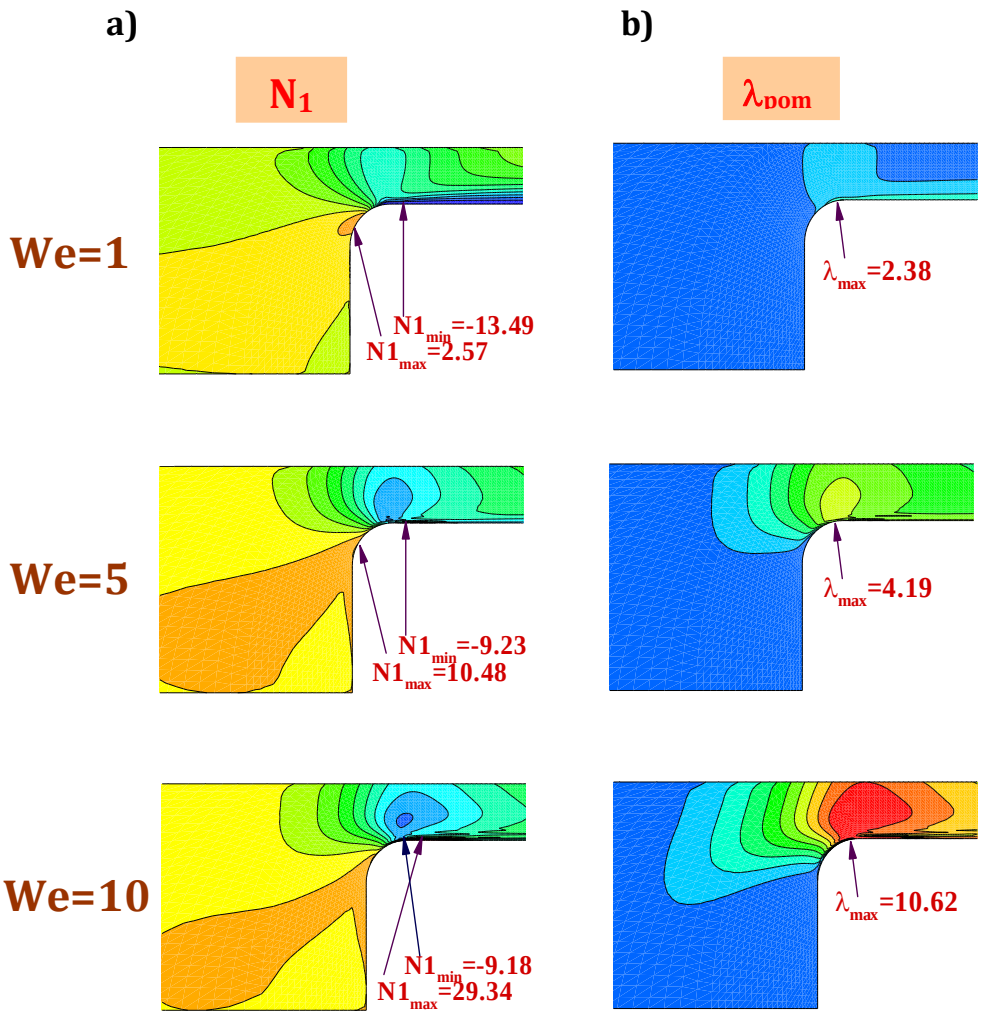

Fig. 9.4 a) First normal stress-difference (N_1), b) backbone stretch (λ_{pom}) fields: SXPP axisymmetric; increasing *We*; ε_{pom}=0.666, q=10, α_{pom}=0.15, β=1/9

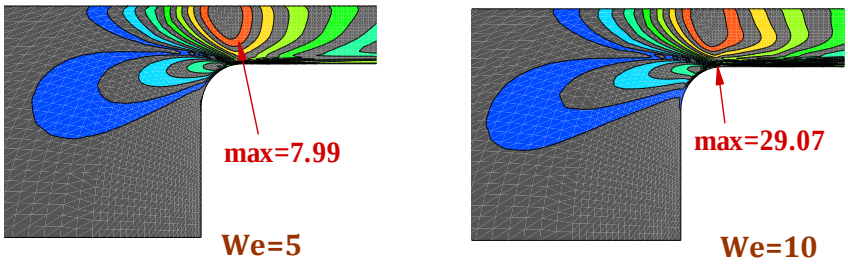

Figure 9.5 Fringe pattern (Principle Stress Difference, PSD) fields: SXPP axisymmetric, *We*={5, 10}; ε_{pom}=0.666, q=10, α_{pom}=0.15, β=1/9

9.4 Filament Stretching: towards a rheometer and biomarker for respiratory disorders

Under the filament-stretching procedures of current interest, the filament is stretched between two flat circular end-plates through a controlled synchronous motion to a specific time/length, followed by a sudden halt. This leads to both stress growth (FiSER) and relaxation (CaBER), followed by filament break-up. In the FiSER mode, the time-scale is inversely proportional to the initial constant stretch-rate that is imposed for the moving-plates. In contrast, for the CaBER mode, a self-selective, own time-scale of material sample is chosen. The problem is axisymmetric about the axial z-axis, along the filament centreline and perpendicular to the end-plates. The origin is taken at the intersection between the filament mid-plane and this axis. The moving domain has an initial aspect ratio ($\Lambda_0 = L_0 / R_{plate}$=0.54) and a final aspect-ratio ($\Lambda_f = L_f / R_{plate}$=$2L_f/D_{plate}$), where L_f and R_{plate} represent the filament final-length and plate-radius, respectively.

The filament stretching problem involves a free-surface determination, where capillary forces act upon the liquid-gas free-surface to determine its displacement. The force balance on this interface may be expressed as a function of the Cauchy stress ($\boldsymbol{\sigma}$), ambient surrounding pressure (p_a), principal radii of curvature (R_1 and R_2) (Sujatha et al. 2008) and normal vector ($\boldsymbol{n}$) to the free-surface,

$$\boldsymbol{\sigma}\cdot\boldsymbol{n} = -p_a\boldsymbol{n} - \chi\left(\frac{1}{R_1}+\frac{1}{R_2}\right)\boldsymbol{n}. \qquad (6)$$

Based on an initial imposed stretch-rate ($\dot{\varepsilon}_0$), the appropriate corresponding boundary conditions are those of no-slip on the end-plates (upper +, and lower -), under axial velocity component, $V_z = \dot{\varepsilon}_0 L(t)$, where $L(t) = \pm 0.5 L_0 \exp(\dot{\varepsilon}_0 t)$.

9.4.1 Filament behaviour with *q*-variation During CaBER (fixed plate-position in time; step-strain phase) and for a small number of arms (q=2), transient development in filament-surface profiles reveal that, the fluid progressively thins at the filament mid-plane (see Fig. 9.6), with no wave-like profile perturbations (little resistance to the necking down). This trend adjusts for fluids with medium to large number of arms, see $q\geq 4$ profiles. This symmetrical reflective wave-like motion (stimulated by fluid resistance to break-up) is observed to commence at the end-plate zones, expanding outwards and towards the mid-plane (Fig. 9.6, $q\geq 4$), prior to reflection backwards from the mid-plane towards the end-plates. Due to enhanced strain-hardening properties and through temporal trends observed in R_{mid} development, Fig. 9.7 plots confirm that as the number of branched-arms increases the resistance to break-up is increased. This is reflected in longer break-up times as q is increased. The filament breaks-up earlier for q=2 (~2 time units) compared to those corresponding to q=4 (~9.5 units), q=8 (~19 units), and q=15 (more than 20 time units).

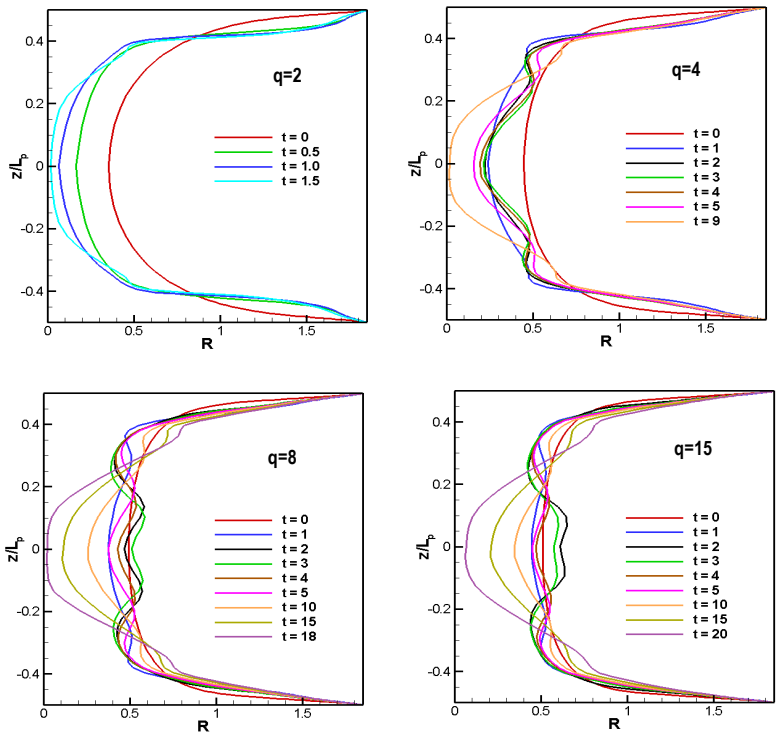

Figure 9.6 CaBER, transient development of free-surface, ***q*-variation** {2, 4, 8, 15}; *L/D*=2, (ε_{pom}=0.99, α_{pom}=0, β=0.262)

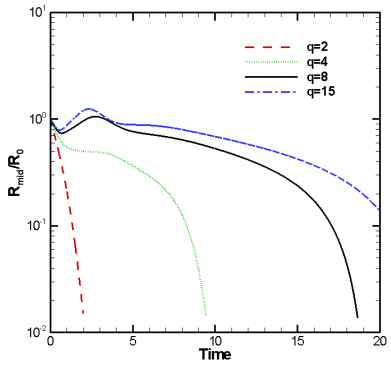

Figure 9.7 CaBER, transient development of R_{mid}, ***q*-variation** {2, 4, 8, 15}; *L/D*=2, (ε_{pom}=0.99, α_{pom}=0, β=0.262)

9.4.2 Filament behaviour with ε_{pom}-variation Recall that in theory the parameter ε_{pom}, representing the ratio of stretch to orientation relaxation times, is inversely proportional to the entanglement molecular weight of the backbone segments. Therefore, values of ε_{pom} approaching unity correspond to molecular chain-segments with relatively short backbone-lengths, yet displaying long arms to retard the dynamics. Small values of ε_{pom} (tending towards zero), correspond to highly-entangled backbone configurations.

Hence, as ε_{pom} increases, the polymeric model-system reflects less entanglement (inverse relationship), and is more mobile. This state will exhibit pronounced strain-hardening, and hence

more resistance to break-up. Under CaBER and at large level of ε_{pom} (Fig. 9.8 right), stronger presence of reflective waves throughout the filament is observed, when compared with (Fig. 9.8 left, centre). Then, for example at ε_{pom}=0.99 (Fig. 9.8 right), the reflective wave is first apparent at t=2 units, traveling from the end-plates towards the mid-plane; after ~t=4 units the wave is being suppressed and reflected backwards towards the plates. The wave-shape is considerably damped as ε_{pom} is reduced (more entangled/less mobile system), and less resistance is observed through the reduced time to break-up (see for example, Fig. 9.8 left, Fig.10). This is observed comparatively in the centreplane temporal trace of R_{mid}-profiles of Fig. 9.9, where filament break-up is earlier at ~3 time units for ε_{pom}=0.2, compared to {5, 19} units for ε_{pom}={0.33, 0.99}.

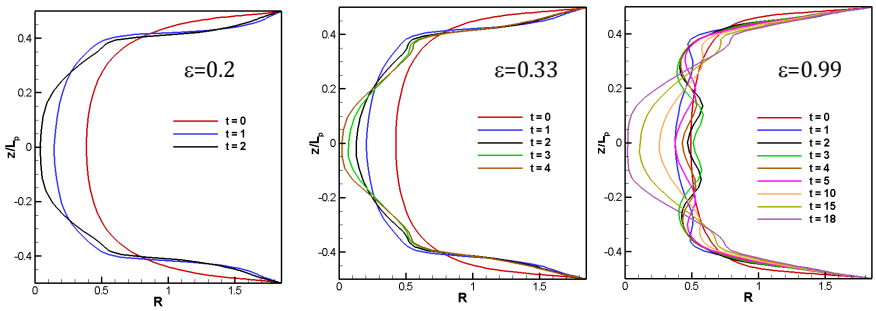

Figure 9.8 CaB*ER*, transient development of free-surface, $\boldsymbol{\varepsilon_{pom}}$ **-variation** {0.20, 0.33 & 0.99}; L/D=2,

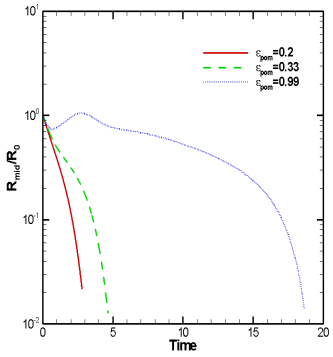

Figure 9.9 CaB*ER*, transient development of R_{mid}, $\boldsymbol{\varepsilon_{pom}}$**–variation** {0.20, 0.33 & 0.99}; L/D=2, (q=8, α_{pom}=0, β=0.262)

9.4.3 Filament behaviour with β-variation Concerning CaBER, first, one may comment on the impact of solvent-fraction β-elevation upon the early-time response as illustrated in Fig. 9.10. Under such β-change, the fluid-filament exhibits greater resistance at the lower level of β=0.262 (highly-polymeric), once more, through the manifestation of a symmetrical reflective wave; whilst this is absent at the higher level β=0.915 (solvent-dominated) state. Corresponding temporal developments in R_{mid}-profiles are depicted in Fig. 9.11. These profiles depict a clear tendency

towards enhanced strain-hardening at low β levels, as filament break-up time increases from 8 units for β=0.915 to 19 units for β=0.262.

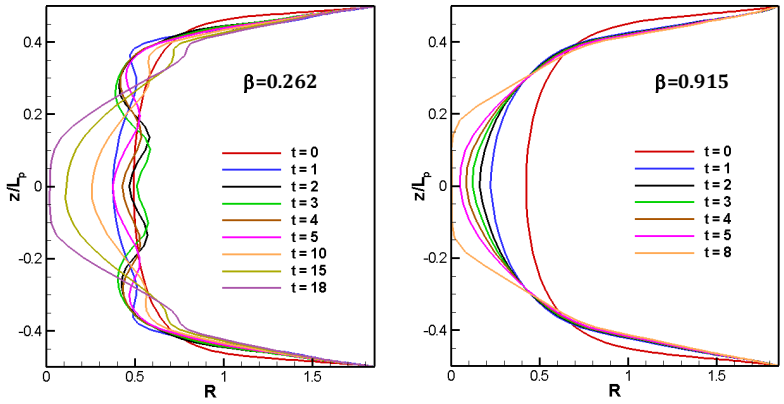

Figure 9.10 CaBER, transient development of free-surface, ***β*-variation** {0.262, 0.915}; L/D=2, (q=8, ε_{pom}=0.99, α_{pom}=0)

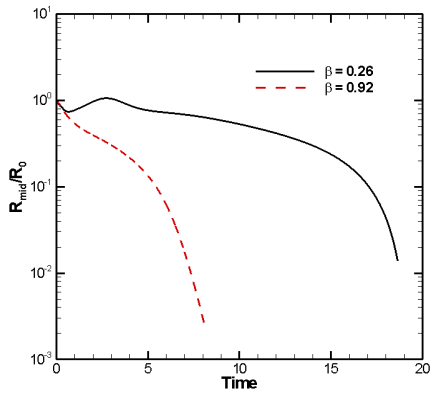

Figure 9.11 CaBER, R_{mid} transient development, ***β*-variation** {0.262, 0.915}; SXPP (ε_{pom}=0.99, α_{pom}=0, q=8)

9.4.4 Extensional viscosity estimation, *q*-variation After investigating the impact of the several SXPP parameters on the numerical predictions for CaBER and FiSER, one may assess the ability of the present numerical toolset for estimating rheometrical properties of the fluids under consideration. Specifically, in assessment of the rheometrical capability and potential for good biomarker qualities, from the data generated. Firstly, extensional viscosity estimation is considered, through the comparison of its theoretical prediction (obtained from transient uniaxial extension data – red intense solid line in Fig. 9.12), versus those extracted from numerical results (black dotted lined) and its average (light green solid line). This estimation was obtained using $\eta_{Ext}=\left(\tau_{zz}-\tau_{rr}\right)/\varepsilon\left(t\right)+3\mu_s$ and $\varepsilon\left(t\right)=-\left(2/R_{mid}\right)\left(dR_{mid}/dt\right)$ (Sujatha et al. 2008). The extensional deformation rate used for the theoretical estimation is $\dot{\varepsilon}=1$, which somewhat matches with the numerical solutions, for which $\{\varepsilon_{pom},\alpha_{pom},\beta\}$={0.99,0,0.262}. The branching of the polymeric molecular-chains, in the range of q={2, 4, 8, 15}, has proven to have the strongest influence on

material property estimation. This is illustrated in Fig. 9.12 and 14. Here, comparison across parameter variation renders q as the finest/most accurate calibration parameter, provided that q-variation lies within a relatively reasonable q={2,4,8,15} range. Parametric variation on ε_{pom} and β do not provide such clear boundaries of measurement, even though their variation range covers most of their domain. On-going through such a wide range of q-variation, coverage is provided for polymeric melt-like fluids (small q) with small Trouton ratios, up to highly-mobile (dynamic, polymeric solution-like) fluids (large q), which show relatively larger peaks in extensional viscosity (see Fig. 2.9). As observed from Fig. 9.12, it has been possible to determine a suitable measurement window (highlighted within the red dotted square) in which accurate extensional viscosity estimation can be captured. This measurement window corresponds to fluids with intermediate q-values (q=4, 8). The criterion employed for window-capture, is the matching between the transient theoretical and average numerical predictions, both in value and temporal trend. Notably, for FiSER, the theoretical and numerical curves follow similar dynamic trends. Beyond the accurate prediction windows, these curves predict more disparate viscosity values. In contrast for CaBER, numerical solutions provide a poorer quality extensional viscosity estimation as q is increased (elevated strain-hardening characteristic); yet their averages are relatively accurate with respect to the theoretical predictions within the measurement window indicated. Again, the results outside the window provide inaccurate estimations from CaBER results. Specifically, for the case of the q=2 model-fluid, the numerical solution is insufficiently adequate, in being too short in time to break-up, to be compared against the theoretical data. Alternatively for q=15, the average numerical curve lies far below the theoretical data-curve. This may be attributed to a consequence of the strong early presence of a reflective wave under these branching conditions, and the disturbance this has on temporal centreplane stressing-states (confirmed by counterpart FiSER solutions, where reflective waves are avoided).

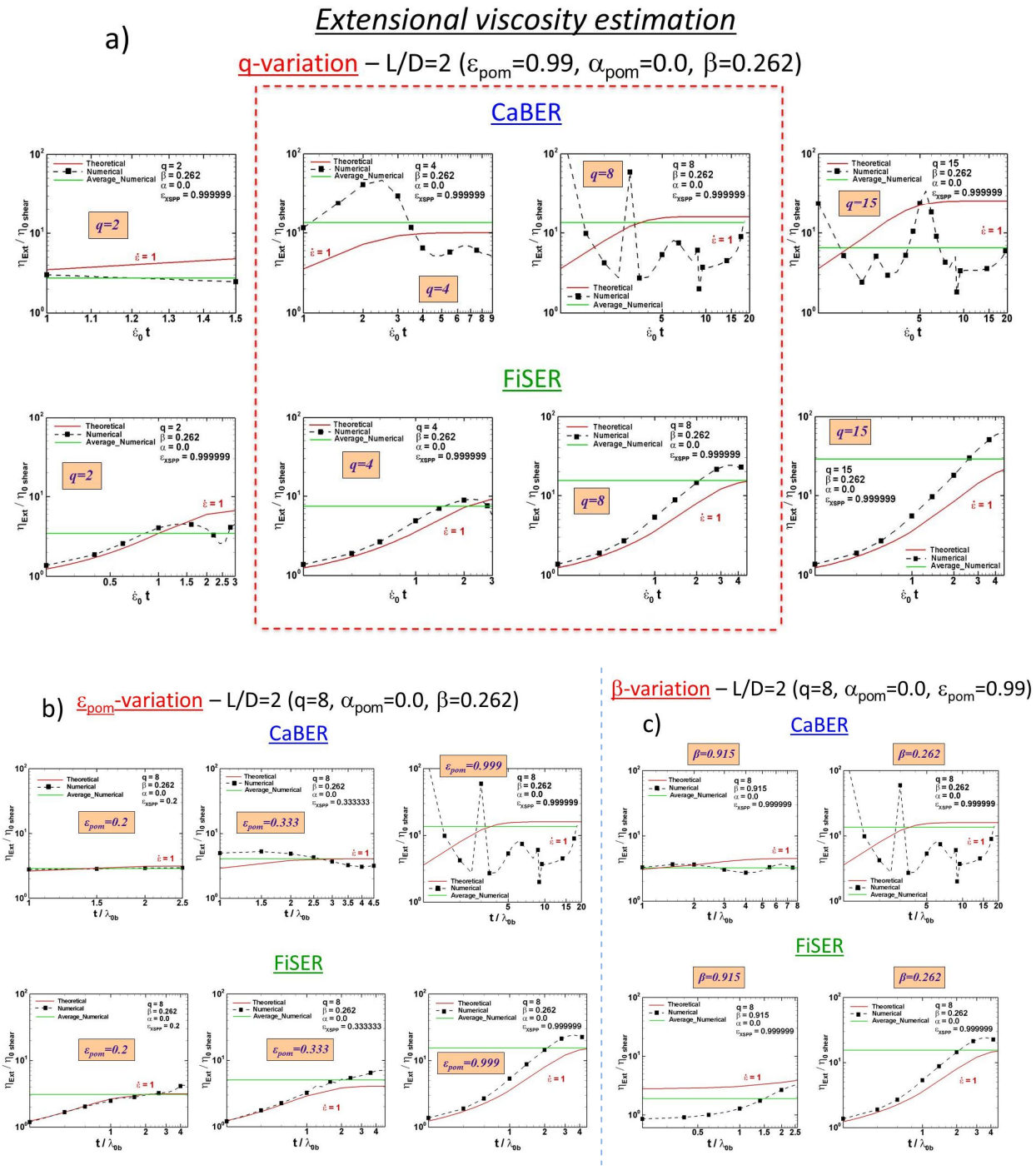

Figure 9.12 Extensional viscosity estimation transient development contrasting CaBER and FiSER; SXPP α_{pom}=0; **a) *q*-variation (center)** q={2, 4, 8, 15}, ε_{pom}=0.99, β=0.262; **b) ε_{pom}-variation (left)** ε_{pom}={0.2,0.33, 0.99}, β=0.262, q=8; **c) β-variation (right)** β={0.262, 0.915}, ε_{pom}=0.99, q=8

In terms of relative time-duration of each CaBER and FiSER trial, FiSER provides the shortest time, with times of ~O(4) units, whilst CaBER displays times as large as ~O(20) units. As pointed out above, FiSER trials can qualitatively reproduce dynamic extensional viscosity data throughout

the complete trial-cycle. There, the average numerical prediction faithfully reproduces theoretical estimation. In comparison and by nature, CaBER is temporally longer and manifests disturbance from reflective waves due to the step-strain, conditions that do not nurture accurate extensional viscosity estimation. Therefore, in conclusion, FiSER alone has proven to be suitable for wider use over filament time-evolution and in estimation of extensional viscosity for moderate polymeric-like fluids: q={4,8} and {ε_{pom},α_{pom},β}={0.99,0,0.262}. Here, and to avoid impractical experimental FiSER fluid measurement, the recommendation is to use such predictive simulation instead. In contrast, CaBER is tightly restricted to only a narrow terminating temporal-interval of effective extensional viscosity estimation capability, and is thus much less preferable.

9.4.5 Stress-growth characteristic time estimation Fig. 9.13 illustrates the ability of FiSER and CaBER to estimate the characteristic time (λ_{est}) of a model fluid. Here, converse to findings on *extensional viscosity estimation* in the preceding section, now CaBER procedures are found to provide accurate *characteristic time estimation* (original design intention of the step-strain CaBER experiment); whilst FiSER procedures prove notably less reliable in this respect. Once more, q-variation is the key parameter used in determining λ_{est}. Here, for CaBER-mode, the branching-factor variation, q={2,4,8,15}, predicts λ_{est} ranging between 1 and 5 units (boxed regions, upper row/centre Fig.14). This provides the coarser, and therefore more definitive, calibration factor for a rheometer. Moreover, the pattern of λ_{est} curves provides some practical guidance as to effective measurement-estimation windows. These curves peak abruptly at an early stage of measurement; which becomes sharper, as either q or ε_{pom} are increased, or β is decreased (parameters that also promote larger extensional viscosity, see Fig. 2.9). After such a peak, λ_{est} curves decline to a minimum. Beyond this second extrema, a relatively smooth pattern emerges to take up a second maximum. Finally, the curves decline again before locating filament break-up. This last relatively smooth period is recommended as the most suitable interval for data collection (boxed-highlight, Fig. 9.13).

In contrast, FiSER results do not show such positive and practically measureable characteristic features in λ_{est} estimation. Varying the branching (q), (ε_{pom}) and (β) factors do not change λ_{est} curves, which lie close together after the peak-value encountered earlier in the trial. These λ_{est}-peaks appear at Hencky strain ~1.5 in all cases, for which lower maxima are observed with either larger q or ε_{pom}, or smaller β. Hence overall, CaBER is the preferred technique of choice for characteristic time estimation.

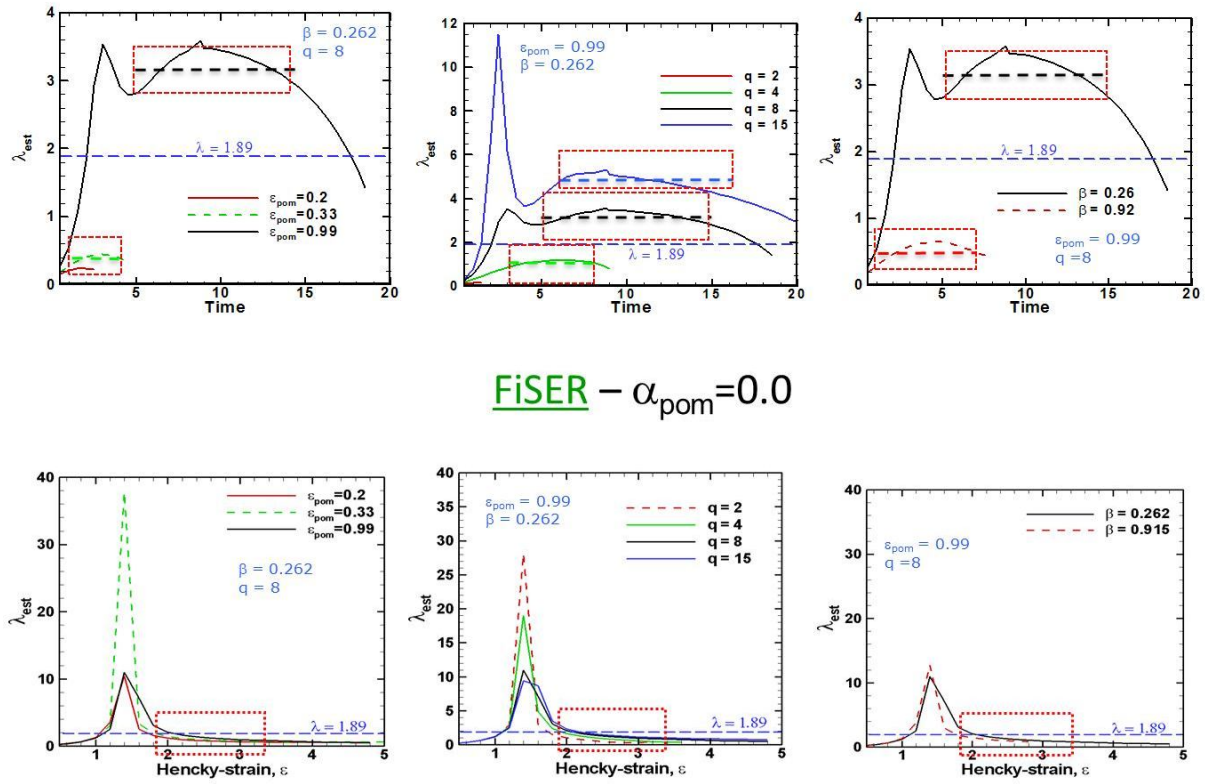

Figure 9.13 Characteristic time estimation transient development contrasting CaBER and FiSER; SXPP α_{pom}=0; ***ε*****$_{pom}$-variation (left)** ε_{pom}={0.2, 0.33, 0.99}, β=0.262, q=8; ***q*-variation (center)** q={2, 4, 8, 15}, ε_{pom}=0.99, β=0.262; ***β*-variation (right)** β={0.262, 0.915}, ε_{pom}=0.99, q=8

9.5 Conclusions

Under the 4:1 contraction problem, mimicking a bile duct narrowing, one has observed that differences in solutions, derived across variation in the number of branched-arms-q, are related principally to properties of extensional viscosity and first normal stress-difference, and barely at all to shear viscosity. The level of elasticity reached is also related to the degree of strain-hardening (Aboubacar et al. 2005; Aguayo et al. 2007). For moderate levels of increase in extensional viscosity, We_{crit} is often larger than that obtained for strongly-hardening fluids. Vortex cell-size and curvature of vortex separation-lines follow similar trends as either q (number of arms) or ε_{pom} (less degree of entanglement) are increased. Firstly, a growth-trend is observed through X and L; which can be associated with enhancement in strain-hardening, provoked by parametric change, either through q or ε_{pom} (irrespective of the background physics upon which these parameters were introduced). This proves particularly so for $q \geq 5$ and $\varepsilon_{pom} \geq 0.333$. In addition, major increments are

observed in salient-corner vortex intensity with $5 \leq We \leq 10$ for $q \geq 5$; and for $\varepsilon_{pom} \geq 0.333 \ \forall \ We$. Conspicuously, for $q=\{2, 5\}$, vortex strength decreases sharply from {3.01, 25.09} at $We=10$, to {0.46, 12.97} at We_{crit}. This is most likely due to the drop in level of softening at intermediate extension-rates. In pure shear flow, established over the exit-channel, significant increase in N_1 and λ_{pom} is observed. At any given arm-q-level chosen, and as characterised by maxima in N_1, variable levels are sustained along the downstream wall. Adjustment in solution levels for (N_1, λ_{pom}) with increase in arms-(q) may be attributed to shear response in first normal stress-coefficient, at the prevailing shear-rates developed in the exit-channel.

Corresponding findings on filament stretching, under CaBER, are related to predictions of the evolution of mid-filament radius R_{mid}, and filament shape. As q (number of -arms), ε_{pom} (less degree of entanglement; more mobile systems) and β (polymer concentration) increase, fluid strain-hardening properties are enhanced. This provokes (i) longer time-cycles for each CaBER and FiSER trial; and (ii) under CaBER, symmetrical reflective wave-like motion (stimulated by fluid resistance to break-up). Such wave-like motion is observed to commence at the end-plate zones, to expand outwards and towards the mid-plane, to be reflected back from the mid-plane, and finally to be damped away at later trial-stages.

Regarding estimation of material properties, and thus on the development of predictive rheological toolsets, here significant advances have been made. The assessment capabilities of CaBER and FiSER have been effectively analysed, with respect to extensional viscosity and characteristic-time estimation. Specifically, FiSER produces faithful *extensional viscosity estimation* within appropriate deformation ranges/parameter sets. One notes that the FiSER technique is impractical in experimental/field-clinical usage given its size requirements (*suggest to be replaced with simulation alternative*). Alternatively, CaBER is suitable for clinical use, given its reduced size, but is restricted to effective determination of fluid-sample *characteristic time* alone. Practical guidance as to measurement gathering through characteristic-time curves is proposed. These CaBER-curves peak abruptly at the onset of the test, and decline thereafter to reach a relatively smooth trend, which provides a reasonably window for effective and practical measurement of characteristic material-time. Note that, as observed through ideal theoretical uniaxial extension response, any mechanism to adjust physical characteristic response (parametrically via number of arms q, entanglements ε_{pom}, or polymer concentration β) that raises extensional viscosity levels, has a counterpart effect on complex flow solution features (as in temporal R_{mid} profiles for filament stretching; vortex growth for contraction flow; see discussion under results described with q-variation).

Overall, this work has permitted the determination of some key factors of influence for two biological flow systems and their related disease states, namely: biliary duct systems and disorders (contraction flow) and respiratory systems and COPD (filament stretching). Firstly, N_1 and vortex structures have been exposed, that in broad terms are indicative flow features with bearing on biliary system narrowing. In contrast under filament stretching, extensional viscosity/characteristic-time prediction windows (forecasts) have been successfully devised – providing the necessary guidance for experimental FiSER/CaBER trials – and leading towards specification of a reliable biorheometer and establishment of an effective biomarker. In this manner, dynamic extensional viscosity trends have been well captured *via FiSER*, and effective practical measurement of characteristic-time has been extracted *via CaBER*. Moreover, this predictive toolset has already been successfully deployed to evaluate healthy and unhealthy sputum clinical samples (to appear subsequently). These results provide illustration of the significant progress being made towards predictive guidance in clinical data-acquisition. The ambition for the future is for this work to be more strongly linked to clinical requirement, and thereby, ultimately lead to improved preventive disease diagnosis and therapy.

CHAPTER 10

Concluding remarks and future directions

This research work has dealt with the numerical modelling of complex fluids in confined and free-surface steady-state and transient complex flows. Particular attention has been paid to the flow of wormlike micellar solutions through the constitutive approach of Bautista-Manero. Moreover, viscoelastoplastic and biofluid predictive applications have been investigated, alongside comparison between experiments and numerical simulations performed on the flow of Boger and pseudoplastic-fluids in contraction-expansion situations.

The numerical modelling component of this work has been accomplished through collaboration between the rheology groups at Universidad Nacional Autónoma de México (UNAM, leaded by Dr. O.M. Brito); and at the Institute of non-Newtonian Fluid Mechanics, Swansea University, Wales UK, (INNFM, leaded by Prof. M.F. Webster, performed by J.E. López-Aguilar). The experimental results exposed in Chapter 8, were obtained at UNAM, as part of the doctoral research and corresponding thesis of M.Eng. M. Pérez-Camacho.

On wormlike micellar fluids and equations of state In this thesis, the study complex flows of wormlike micellar systems under the approach of Bautista-Manero, has leaded to corrections in this family of constitutive equations that account for (i) the inclusion of the viscoelasticity (via the characteristic time) into the structure construction-destruction mechanism; and (ii) the consideration of the absolute value of the dissipation function as the driving influence to depart from Oldroyd-B-like behaviour. The first correction, described in Chapter 5, has risen in deriving inconsistent results for MBM-EPD values at the Stokesian limit with the 4:1:4 contraction-expansion problem. At this limit, inclusion of the characteristic time (viscoelasticity) into the structure equation provided consistent *epd* results

and larger We_{crit} with respect to those for the MBM model. Here, significant trends were observed in vortex dynamics and *epd* values as the viscoelasticity level was increased. Vortex activity (in size and strength) resembled the evolution of extensional viscosity with the elevation of extension rate, and provides a close relationship between evolution in kinematic structure with that in second and first-normal stress-difference data fields. Meanwhile, a particular version of the micellar models (NM_T) was found to display rising trends in *epd* as *We* increased. In addition, the f_τ-functionality and dependency on Weissenberg number, indicates a capability to attain relatively large We_{crit}. Here, the stronger the f_τ-*We* functionality, the larger the attainable We_{crit} for convergence. Consistently, the EPTT model provides the larger We_{crit}=O(10^2), with its exponential f_τ-*We* functionality; whilst the micellar (in their steady-state form) and LPTT models attained relatively smaller We_{crit}=O(10) , with their linear f_τ-*We* functionality.

The second correction, described in Chapter 6, deals with the fact that in complex flows the natural-signed micellar models generate negative unphysical fluidity values (accommodated here within the dimensionless f_τ-functional); and hence, negative viscosities result. This has its origin in the negative dissipation function values generated in complex flow, which are not observed in positive-valued simple ideal flows (as considered in theoretical construction). With the consideration of the absolute value of the dissipation function in the structure equation, this inconsistency is resolved, and $f_\tau \geq 1$ are obtained throughout the field. Moreover, We_{crit} values are considerably increased (We_{crit}=O(40) for NM_τ_p_ABS, with respect to the results of We_{crit}=O(1) under natural-signed versions). This observation is quite general and found applicable to other models too, such as the Phan-Thien-Tanner models (for which natural-signed EPTT We_{crit}=O(10^2), in contrast to O(10^3) for EPTT_ABS). Apart for these constitutive corrections, the specification of consistent deformation-rate boundary conditions at the pure-extension flow-centreline has proved highly effective in deriving smoother solutions at impressively high elasticity levels (We_{crit}=O(10^2) for micellar models and We_{crit}=O(10^3) for EPTT models). Locally enforced boundary conditions, through the deformation-rate components at the flow-centreline, are those of vanishing-shear on the shear component, and a simple uniaxial extension relationship between the extensional gradients. Adoption of a conformation-tensor version of the micellar and PTT constitutive equations has lead to an increase in We_{crit} with respect to the stress-tensor based versions (not as effective as the ABS-correction). This has also provided the framework to evaluate solution-stability, via the conformation tensor eigenvalues. In this

sense, the second eigenvalue of the conformation tensor has been identified as a suitable indicator of numerical stability, which reflects zones of localised and growing negativity as elasticity levels are increased. Furthermore, some theoretical identities have been derived between the first normal stress differences and the change of sign in the eigenvalues at the centreline; upon this basis, departure from the linear viscoelastic regime can be evaluated in complex flows.

On viscoelastoplastic complex flow modelling The applicability of the corrections above is applied and illustrated in Chapter 7, in the sense of deriving numerical solutions at higher non-linear levels (either via the characteristic time or the solvent fraction). Simulation of viscoelastoplastic fluids in the complex 4:1:4 rounded contraction-expansion settings were performed, adopting the micellar thixotropic Bautista-Manero models for the polymer contribution, alongside the Bingham-Papanastasiou model for the solvent component. Here, relatively low solvent-fraction numerical results ($\beta \leq 10^{-2}$), are attainable whilst deriving elasto-plastic features from the viscoelastic Bautista-Manero models (Calderas et al. 2013). The combination of viscoelastic and plastic contributions from both micellar and Papanastasiou representations provides, shear-thinning and extensional viscosity effects through the polymeric contribution, and viscoplastic features through the Papanastasiou approximation. Generally, those features that promote plastic material behaviour (such as yield-stress), provoke a decline in fluid-mobility. This is reflected in vortex activity suppression and *epd* enhancement. In addition, viscoelasticity introduces asymmetry about the contraction, with vortex and yield-fronts deformed as *We* rises. Finally, extensional viscosity effects are responsible for upstream vortex enhancement. Moreover, a re-scaling with respect to the viscosity plateau at high deformation rates is suggested, to account for a low deformation-rate Bautista-Manero plastic contribution (as with Papanastasiou contributions), in contrast to the current zero-deformation rate characteristic viscosity, which provides a plateau at moderate deformation rates. This would shift the polymeric-originated plateau to the low-deformation-rate regime and then enhance plastic features of such viscoelastoplastic fluids, with polymer plus solvent-originated plastic plateaus.

On the experimental-to-numerical contraction-expansion flow comparison Simulations for the 4:1:4 contraction-expansion flow geometry have been performed and contrasted against experimental data for Boger fluids. Here, the constant shear-viscosity strain-hardening FENE-CR model was used to fit rheometric data for Boger solutions. These fluids were used to experimentally evaluate pressure drop and flow kinematics in flow-controlled

sharp contraction-expansion flow; the contraction ratio was varied as 2:1:2, 4:1:4, 6:1:6, 8:1:8, 10:1:10. Despite the differences in geometric specification (sharp-to-rounded corners) and procedure (*flow-controlled experiments*, procedure in which one test fluid is forced through contraction at *increasing flow rates*; to *characteristic-time controlled simulations*, in which the relaxation time or *We* is varied in simulations a fixed flow rate -procedure that could be interpreted *as change of test fluid*), coincidence of trends in results is most striking. In numerical solutions, the experimental rising *epd* and upstream vortex-size and intensity with elasticity elevation have all been captured. Here, the follow-on step will comprise the matching in experimental-geometry requirements (i.e. sharp corners and flow controlled simulations), and variation in contraction ratio.

On predictive tool development for biofluids In this last section, whilst moving away from Bautista-Manero modeling, numerical simulation has been considered to devise an effective extensional rheometer for biofluids. Here, the effects of variation over the model parameters for the network-structured non-thixotropic SXPP model (traditionally for polymer melt architectures) have been examined for two complex flows and sets of parameters that resemble biofluids. This has been accomplished through the simulation of 4:1 contraction flow for bile-flow in biliary ducts; and filament stretching flow (FiSER-CaBER) for sputum extensional properties in the lung airways. In this manner, an estimation window has been obtained, for extensional viscosity (via FiSER) and characteristic time (via CaBER), based on the number of arms parameter (q) of the SXPP model. This structure-based parameter has proven itself to be the most influential in adjusting such complex extensional-flow response, and hence, which has generated the better estimation windows. It is envisaged that given the highly dynamic nature of these biofluids, subsequent work will involve their characterisation through the time-dependent thixotropic and viscoelastic Bautista-Manero family of fluids.

References

[1] M. Aboubacar, J.P. Aguayo, P.M. Phillips, T.N. Phillips, H.R. Tamaddon-Jahromi, B.A. Snigerev and M.F. Webster, Modelling pom-pom type models with high-order finite volume schemes, *J. Non-Newtonian Fluid Mech.* 126 (2005) 207-220.

[2] M. Aboubacar, H. Matallah, M.F. Webster, Highly elastic solutions for Oldroyd-B and Phan-Thien/Tanner fluids with a finite volume/element method: planar contraction flows, J. Non-Newton. Fluid Mech. 103 (2002) 65-103.

[3] M. Aboubacar, H. Matallah, H.R. Tamaddon-Jahromi, M.F. Webster, Numerical prediction of extensional flows in contraction geometries: hybrid finite volume/element method, J. Non-Newton. Fluid Mech. 104 (2002) 125-164.

[4] M. Aboubacar, M.F. Webster, A cell-vertex finite volume/element method on triangles for abrupt contraction viscoelastic flows, J. Non-Newton. Fluid Mech. 98 (2001) 83-106.

[5] J.P. Aguayo, Prediction of viscoelastic fluid flow in contractions, PhD Thesis, Swansea University, 2006.

[6] J.P. Aguayo, P.M. Phillips, T.N. Phillips, H.R. Tamaddon-Jahromi, B.A. Snigerev and M.F. Webster, The numerical prediction of planar viscoelastic contraction flows using the pom-pom model and higher-order finite volume schemes, J. Comp. Physics 220 (2007) 586-611.

[7] J.P. Aguayo, H.R. Tamaddon-Jahromi, M.F. Webster, A second-order hybrid finite-element/volume method for viscoelastic flows, J. Non-Newton. Fluid Mech. 134 (2006) 105-126.

[8] J.P. Aguayo, H.R. Tamaddon-Jahromi, M.F. Webster, Excess pressure-drop estimation in contraction and expansion flows for constant shear-viscosity, extension strain-hardening fluids, J. Non-Newton. Fluid Mech. 153 (2008) 157-176.

[9] C.K. Aidun, J.R. Clausen Lattice-Boltzmann method for complex flows, Ann. Rev. Fluid

Mech. 42 (2010) 439-472.

[10] M.A. Alves, P.J. Oliveira, F.T. Pinho, On the effect of contraction ratio in viscoelastic flow through abrupt contractions, J. Non-Newton. Fluid Mech. 122 (2004) 117-130.

[11] S.L. Anna and G.H. McKinley, Elasto-capillary thinning and breakup of model elastic liquids, J. Rheol. 45 (2001) 115-138.

[12] A. Al-Muslimawi, H.R. Tamaddon-Jahromi, M.F. Webster, Simulation of viscoelastic and viscoelastoplastic die swell flows, J. Non-Newton. Fluid Mech. 191 (2013) 45-56.

[13] R. Aris, Vectors, tensors and the basic equations of fluid mechanics, Prentice Hall, New York, 1962.

[14] G. Astarita, G. Marucci, Principles of non-Newtonian Fluid Mechanics, McGraw-Hill, 1974.

[15] Baaijens F.T.P, Mixed finite element methods for viscoelastic flow analysis: a review, J. Non-Newton. Fluid Mech. 79 (1998) 361–385.

[16] H.A. Barnes, The yield stress-a review or ‘παντα ρει’-everything flows? J. Non-Newton. Fluid Mech. 81 (1999) 133-178.

[17] H.A. Barnes, J.F. Hutton, K. Walters, An introduction to rheology, Elsevier, Oxford, 1989.

[18] H.A. Barnes, K. Walters, The yield stress myth? Rheol. Acta 23 (1985) 323–326.

[19] F. Bautista, J.M. de Santos, J.E. Puig, O. Manero, Understanding thixotropic and antithixotropic behavior of viscoelastic micellar solutions and liquid crystalline dispersions. I. The model. J. Non-Newton. Fluid Mech. 80 (1999) 93-113.

[20] F. Bautista, V.V.A. Fernandez, E.R. Macias, J.H. Perez-Lopez, J.I. Escalante, J.E. Puig, O. Manero. Experimental evidence of the critical phenomenon and shear-banding flow in polymer-like micellar solution. J. Non-Newtonian Fluid Mech. 177-178 (2012) 89-96.

[21] F. Baustista, J.H. Pérez-López, J.P. García, J.E. Puig, O. Manero, Stability analysis of shear-banding flow with the BMP model J. Non-Newton. Fluid Mech. 144 (2007) 160-169.

[22] F. Bautista, J.F.A. Soltero, J.H. Pérez-López, J.E. Puig, O. Manero, On the shear-banding flow of elongated micellar solutions. J. Non-Newton. Fluid Mech. 94 (2000) 57-66.

[23] R.J. Blackwell, T.C.B. McLeish and O.G. Harlen, Molecular drag-strain coupling in branched polymer melts, J. Rheol. 44 (2000) 121-136.

[24] F. Belblidia, I.J. Keshtiban and M.F. Webster, Stabilised computations for viscoelastic flows under compressible implementations, J. Non-Newtonian Fluid Mech. 134 (2006) 56-76.

[25] F. Belblidia, H. Matallah, M.F. Webster, Alternative subcell discretisations for viscoelastic flow: Velocity-gradient approximation, J. Non-Newt. Fluid Mech. 151 (2008) 69-88.

[26] F. Belblidia, H. Matallah, B. Puangkird and M.F. Webster, Alternative subcell

discretisations for viscoelastic flow: Stress interpolation, J. Non-Newtonian Fluid Mech. 146 (2007) 59-78.

[27] F. Belblidia, H.R. Tamaddon-Jahromi, M.F. Webster, K. Walters, Computations with viscoplastic and viscoelastoplastic fluids, Rheol. Acta 50 (2011) 343–360.

[28] D.M. Binding, Further considerations of axisymmetric contraction flows, J. Non-Newton. Fluid Mech. 41 (1991) 27-42.

[29] D.M. Binding, P.M. Phillips, T.N. Phillips, Contraction/expansion flows: the pressure drop and related issues. J. Non-Newton. Fluid Mech. 137 (2006) 31-38.

[30] E.C. Bingham, Fluidity and plasticity. McGraw Hill, New York, 1922.

[31] R.B. Bird, Five decades of transport phenomena, AIChE J. 50 (2004) 273-287.

[32] R.B. Bird, W. E. Stewart, E. N. Lightfoot, Transport Phenomena, John Wiley & Sons, New York, 1960.

[33] R.B. Bird, W. E. Stewart, E. N. Lightfoot, Transport Phenomena, John Wiley & Sons, New York, 2007.

[34] R.B. Bird, R.C. Armstrong, O. Hassager, Dynamics of Polymeric Liquids, John Wiley & Sons, New York, 1977.

[35] R.J. Blackwell, T.C.B. McLeish and O.G. Harlen, Molecular drag-strain coupling in branched polymer melts, J. Rheol. 44 (2000) 121-136.

[36] E.S. Boek, J.T. Padding, V.J. Anderson, P.M.J. Tardy, J.P. Crawshaw, J.R.A. Pearson, Constitutive equations for extensional flow of wormlike micelles: stability analysis of the Bautista-Manero model. J. Non-Newton. Fluid Mech. 126 (2005) 29-46.

[37] D.V. Boger, Viscoelastic flows through contractions, Ann. Rev. Fluid Mech. 19 (1987) 157-182.

[38] D.V. Boger, M.J. Crochet, R.A. Keiller, On viscoelastic flows through abrupt contractions, J. Non-Newton. Fluid Mech. 44 (1992) 267-279.

[39] D.V. Boger, K. Walters, Rheological phenomena in focus, Elsevier, Amsterdam, 1993.

[40] D. Bonn, Yield stress fluids: to flow or not to flow, that is the question. Viscoplastic fluids: from theory to application, Cyprus, 2006.

[41] V.J. Broughton-Head, J. Shur, M.P. Carroll, J.R. Smith and J.K. Shute, Unfractionated heparin reduces the elasticity of sputum from patients with cystic fibrosis, Am. J. Physiol. Lung. Cell. Mol. Physiol. 293 (2007) L1240-1249.

[42] P.J. Cable, D.V. Boger, A comprehensive experimental investigation of tubular entry flow of viscoelastic fluids: Part I. Vortex characteristic in stable flow, AIChE J. 24 (1978) 869-879.

[43] P.J. Cable, D.V. Boger, A comprehensive experimental investigation of tubular entry flow of viscoelastic fluids: Part II. The velocity field in stable flow, AIChE J. 24 (1978) 992-999.

[44] F. Calderas, E.E. Herrera-Valencia, A. Sanchez-Solis, O. Manero, L. Medina-Torres, A. Renteria, G. Sanchez-Olivares, On the yield stress of complex materials, Korea-Aust. Rheol. J. 25 (2013) 233-242.

[45] Y. Caram, F. Baustista, J.E. Puig, O. Manero, On the rheological modelling of associative polymers. Rheol. Acta 46 (2006) 45-57.

[46] U. Cartalos and J.M. Piau, Creeping flow regimes of low concentration polymer solutions in thick solvents through an orifice die, J. of Non-Newton. Fluid Mech. 45 (1992) 231-285.

[47] M.D. Chilcott, J.M. Rallison, Creeping flow of dilute polymer solutions past cylinders and spheres, J. Non-Newton. Fluid Mech. 29 (1988) 381-432.

[48] T.J. Chung, Computational Fluid Dynamics, Cambridge University Press, Cambridge, 2002.

[49] M.J. Crochet, K. Walters, Computational rheology: a new science, Endeavour 17 (1993) 64-77.

[50] M. Cromer, L.P. Cook, G.H. McKinley, Pressure-driven flow or wormlike micellar solutions in rectilinear microchannels, J. Non-Newton. Fluid Mech. 166 (2011) 180-193.

[51] P.R. de Souza, Modeling the thixotropic behaviour of structured fluids. J. Non-Newton. Fluid Mech. 164 (2009) 66-75.

[52] P.R. de Souza, Thixotropic elasto-viscoplastic model for structured fluids, Soft Matter 7 (2011) 2471-2483.

[53] P.R. de Souza, R.L. Thompson, A critical overview of elasto-viscoplastic thixotropic behaviour modeling, J. Non-Newton. Fluid Mech. 187-188 (2012) 8-15.

[54] M.M. Denn, Issues in viscoelastic fluid mechanics, Ann. Rev. Fluid Mech. 22 (1990) 13-34.

[55] M.M. Denn, Fifty years of non-Newtonian Fluid Dynamics, AIChE J 50 (2005) 2335-2345.

[56] M.M. Denn, Simulation of polymer melt processing, AIChE J 55 (2009) 1641-1647.

[57] C.A. Dreiss, Wormlike micelles: where do we stand? Recent developments, linear rheology and scattering techniques. Soft Matter, 3 (2007) 956-970.

[58] F. Dupret, J.M. Marchal, Loss of evolution in the flow of viscoelastic fluids, J. Non-Newton. Fluid Mech. 20 (1986) 143–171.

[59] F. Dupret, J.M. Marchal, M.J. Crochet, On the consequence of discretization errors in the numerical calculation of viscoelastic flow, J. Non-Newton. Fluid Mech. 18 (1985) 173–186.

[60] S.O.S. Echendu, H.R. Tamaddon-Jahromi, M.F. Webster, Modelling reverse roll coating flow with dynamic wetting lines and inelastic shear thinning fluids, Appl. Rheol. 23 (2013)

62388.

[61] J. Eggers, Nonlinear dynamics and breakup of free-surface flows, Rev. Mod. Phys. 69 (1997) 865.

[62] S. M. Fielding, P.D. Olmsted, Flow phase diagrams concentration-coupled shear-banding. Eur. Phys. J. E 11 (2003) 65-82.

[63] P. Fischer, H. Rehage, Non-linear flow properties of viscoelastic surfactant solutions. Rheol. Acta 36 (1997) 13-27.

[64] J.P. García-Sandoval, O. Manero, F. Bautista, J.E. Puig, Inhomogeneous flows and shear-banding formation in micellar solutions: predictions of the BMP model. J. Non-Newton. Fluid Mech. 179-180 (2012) 43-54.

[65] J.L. Guermond, and L. Quartapelle, On stability and convergence of projection methods based on pressure poisson equation, Int. J. Numer. Meth. Fluids 26 (1998) 1039-1053.

[66] A.K. Gurnon, N.J. Wagner, Large amplitude oscillatory shear (LAOS) measurements to obtain constitutive equation model parameters: Giesekus model of banding and nonbanding wormlike micelles. J. Rheol. 56 (2012) 333-351.

[67] J.P. Hartnett, R.Y.Z. Hu, Technical note: the yield stress—an engineering reality. J. Rheol. 33 (1989) 671–679.

[68] D.M. Hawken, P. Townsend, M.F. Webster, A comparison of gradient recovery methods in finite element calculations, Comm. Appl. Num. Meth. 7 (1991) 195–204.

[69] M.E. Helgeson, M.D. Reichert, Y.T. Hu, N.J. Wagner, Relating shear-banding, structure, and phase behaviour in wormlike micellar solutions. Soft Matter, 5 (2009) 3858-3869.

[70] M.E. Helgeson, P.A. Vazquez, E.W. Kaler, N.J. Wagner, Rheology and spatially resolved structure of cetyltrimethylammonium bromide wormlike micelles through the shear-banding transition. J. Rheol. 53 (2009) 727-756.

[71] L. Hermany, D.D. dos Santos, S. Frey, M.F. Naccache, P.R. de Souza, Flow of yield-stress liquids through an axisymmetric abrupt expansion-contraction. J. Non-Newton. Fluid Mech. 201 (2013) 1-9.

[72] E.E. Herrera, F. Calderas, A.E. Chávez, O. Manero, Study on the pulsating flow of a worm-like micellar solution. J. Non-Newton. Fluid Mech. 165 (2010) 174-183.

[73] R.J. Holdsworth, S.A. Sadek, S. Ambikar and A. Cuschieri, Dynamics of bile flow through the human choledochal sphincter following exploration of the common bile duct, World J. Surgery 13 (1989) 300-304.

[74] M.A. Hulsen, Some properties and analytical expressions for plane flow of Leonov and

Giesekus models, J. Non-Newton. Fluid Mech. 30 (1988) 85–92.

[75] M.A. Hulsen, A sufficient condition for a positive definite configuration tensor in differential models, J. Non-Newton. Fluid Mech. 38 (1990) 93–100.

[76] R. Keunings, On the high Weissenberg number problem, J. Non-Newton. Fluid Mech. 20 (1986) 209–226.

[77] R. Keunings, Simulation of viscoelastic fluid flow. In C.L. Tucker III, editor. Fundamentals of computer mYangodelling for polymer processing, Oxford, New York, 1989.

[78] R. Keunings, Progress and challenges in computational rheology, Rheol. Acta 29 (1990) 556–570.

[79] R. Keunings, A survey of computational rheology, Proceedings of the XIII International Congress on Rheology, Cambrigde, UK, 1 (2000) 7-14.

[80] R. Keunings, Advances in the computer modeling of the flow of polymeric liquids, Comp. Fluid Dyn. J. 9 (2001) 449–458.

[81] S.R. Kini, Color Atlas of Pulmonary Cytopathology, Springer, 2002.

[82] S.K. Lai, Y.-Y. Wang, D. Wirtz and J. Hanes, Micro- and macrorheology of mucus, Adv. Drug Deliver. Rev. 61 (2009) 86-100.

[83] W.G. Li, X.Y. Luo, A.G. Johnson, N.A. Hill, N. Bird and S.B. Chin, One-Dimensional Models of the Human Biliary System, J. Biomech. Eng. 129 (2007) 164-173.

[84] M.W. Libertatore, F. Nettesheim, P.A. Vazquez, M.E. Helgeson, N.J. Wagner, E.W. Kaler, L.P. Cook, L. Porcar, Y.T. Hu, Microstructure and shear rheology of entangled wormlike micelles in solution. J. Rheol. 53 (2009) 441-458.

[85] M.B. Liu, G.R. Liu, Smoothed particle hydrodynamics (SPH): an overview and recent developments, Arch. Comput. Methods Eng. 17 (2010) 25-76.

[86] J.E. López-Aguilar, M.F. Webster, H.R. Tamaddon-Jahromi, O. Manero, A new constitutive model for worm-like micellar systems - Numerical simulation of confined contraction-expansion flows. J. Non-Newton. Fluid Mech. 204 (2014) 7-21.

[87] M.T. Lopez-Vidriero and L. Reid, Chemical markers of mucous and serum glycoproteins and their relation to viscosity in mucoid and purulent sputum from various hypersecretory diseases., Am Rev Respir Dis. 117 (1978) 465-477.

[88] C.W. Macosko, Rheology, principles, measurements and applications, Wiley, 1994.

[89] O. Manero, F. Baustista, J.F.A. Soltero, J.E. Puig, Dynamics of worm-like micelles: the Cox-Merz rule. J. Non-Newton. Fluid Mech. 106 (2002) 1-15.

[90] H. Matallah, P. Townsend, M.F. Webster, Recovery and stress-splitting schemes for

viscoelastic flows, J. Non-Newton. Fluid Mech. 75 (1998) 139-166.

[91] J.C. Maxwell, On the dynamical theory of gases, Phil. Trans. R. Soc. A. *A* 157 (1867) 49-88.

[92] G.H. McKinley and T. Sridhar, Filament-stretching rheometry of complex fluids, *Annu. Rev. Fluid Mech* 34 (2003) 375-415.

[93] A.J. Mendoza-Fuentes, O. Manero, R. Zenit, Evaluation of drag correction factor for spheres settling in associative polymers. Rheol. Acta 49 (2010) 979-984.

[94] A.J. Mendoza-Fuentes, R. Montiel, R. Zenit, O. Manero, On the flow of associative polymers past a sphere: evaluation of the negative wake criteria. Phys. Fluids 21 (2009) 45-57.

[95] E. Miller, J.P. Rothstein, Transient evolution of shear-banding wormlike micellar solutions. J. Non-Newton. Fluid Mech. 143 (2007) 22-37.

[96] E. Mitsoulis, Flows of viscoplastic materials: models and computations, Rheol. Rev. (2007) 135-178.

[97] F.A. Morrison, Undestanding rheology, Oxford, Oxford, 2001.

[98] R.G. Moss, J.P. Rothstein, Flow of wormlike micelle solutions past a confined circular cylinder. J. Non-Newton. Fluid Mech. 165 (2010) 1505-1515.

[99] P.C.F. Møllera, J. Mewisb, D. Bonn, Yield stress and thixotropy: on the difficulty of measuring yield stresses in practice. Soft Matter 2 (2006) 274–283.

[100] M. Nyström, H.R. Tamaddon-Jahromi, M. Stading, M.F. Webster, Numerical simulations of Boger fluids through different contraction configurations for the development of a measuring system for extensional viscosity, Rheol. Acta 51 (2012) 713-727.

[101] J.G. Oldroyd, On the formulation of rheological equations of state, Proc. Roy. Soc. A, 200 (1950) 523-541.

[102] P.D. Olmsted, Perspectives on shear-banding in complex fluids. Rheol. Acta 47 (2008) 283-300.

[103] P.D. Olmsted, O. Radulescu, C. Y. F. Lu, Johnson-Segalman model with a diffusion term in a cylindrical Couette flow. J. Rheol. 44 (2000) 257-275.

[104] R.C. Ooi, X.Y. Luo, S.B. Chin, A.G. Johnson and N.C. Bird, The flow of bile in the human cystic duct, J Biomech. 37 (2004) 1913-1922.

[105] R.G. Owens, T.N. Phillips, Computational rheology, Imperial College Press, London, 2002.

[106] T.C. Papanastasiou, Flow of materials with yield, J. Rheol. 31 (1987) 385-404.

[107] A. Parker, W. Fieber, Viscoelasticity of anionic wormlike micelles: effect of ionic strength and small hydrophobic molecules. Soft Matter, 9 (2013) 1203-1213.

[108] N. Phan-Thien, R.I. Tanner. A new constitutive equation derived from network theory, J.

Non-Newton. Fluid Mech. 2 (1977) 353-365.

[109] Puangkird B, Numerical simulations of complex viscoelastic flows, PhD Thesis, Swansea University, 2007.

[110] O. Radulescu, P.D. Olmsted, C. Y. F. Lu, Shear-banding in reaction-diffusion models. Rheol. Acta, 38 (1999) 606-613.

[111] S.R. Raghavan, E.W. Kaler. Highly viscoelastic wormlike micellar solutions formed by cationic surfactants with long unsaturated tails. Langmuir, 17 (2001) 300-306.

[112] H. Rehage, H. Hoffmann, Viscoelastic surfactant solutions: model systems for rheological research. Mol. Phys. 74 (1991) 933-973.

[113] M. Renardy, The mathematics of myth: yield stress behaviour as a limit of non-monotone constitutive theories. J. Non-Newton. Fluid Mech. 165 (2010) 519-526.

[114] J.P. Rothstein, G.H. McKinley, Extensional flow of a polystyrene Boger fluid through a 4:1:4 axisymmetric contraction/expansion, J. Non-Newton. Fluid Mech. 86 (1999) 61-88.

[115] J.P. Rothstein, G.H. McKinley, The axisymmetric contraction-expansion: the role of extensional rheology on vortex growth dynamics and the enhanced pressure drop, J. Non-Newton. Fluid Mech. 98 (2001) 33-63.

[116] R.A. Sampson, On Stokes's current function, Phil. Trans. R. Soc. A. 182 (1891) 449-518.

[117] D. Serisier, M. Carroll, J. Shute and S. Young, Macrorheology of cystic fibrosis, chronic obstructive pulmonary disease & normal sputum, Respir. Res. 10 (2009) 63.

[118] M.R. Stukan, E. S. Boek, J.T. Padding, W.J. Briels, J.P. Crawshaw, Flow of wormlike micelles in an expansion contraction geometry, Soft Matter, 4 (2008) 870-879.

[119] R. Sugita, E. Sugimura, M. Itoh, T. Ohisa, S. Takahashi, N. Fujita, Pseudolesion of the Bile Duct Caused by Flow Effect: A Diagnostic Pitfall of MR Cholangiopancreatography, Am. J. Roentgenol. 180 (2003) 467-471.

[120] K.S. Sujatha, H. Matallah, M.J. Banaai, M.F. Webster. Modelling step-strain filament-stretching (CaBER-type) using ALE techniques, J. Non-Newtonian Fluid Mech. 148 (2008) 109-121.

[121] H.R. Tamaddon-Jahromi, F.S. Syed, M.F. Webster, Studies on contraction flows and pressure-drops - extensional viscosity and dissipative stress effects, ICR, Monteray, USA (2008) 1-3.

[122] H.R. Tamaddon-Jahromi, M.F. Webster, Transient behaviour of branched polymer melts through planar abrupt and rounded contractions using pom-pom models, Mech. Time-Depend. Mater 15 (2011) 181-211.

[123] H.R. Tamaddon-Jahromi, M.F. Webster, J.P. Aguayo, O. Manero, Numerical investigation of transient contraction flows for wormk-like micellar systems using Bautista-Manero models, J. Non-Newton. Fluid Mech. 166 (2011) 102-117.

[124] H.R. Tamaddon-Jahromi, M.F. Webster, K. Walters, Predicting numerically the large increases in extra pressure-drop when Boger fluids flow through axisymmetric contractions, Nat. Sci. 2 (2010) 1-11.

[125] H.R. Tamaddon-Jahromi, M.F. Webster, P.R. Williams, Excess pressure-drop and drag calculations for strain-hardening fluids with mild shear-thinning: contraction and falling sphere problems, J. Non-Newton. Fluid Mech. 166 (2011) 939-950.

[126] H. Tan, K.C. Tam, V. Tirtaatmadja, R.D. Jenkins, D.R. Bassett, Extensional properties of model hydrophobically modified alkali-soluble associative (HASE) polymer solutions, J. Non-Newton. Fluid Mech. 92 (2000) 167-185.

[127] R.I. Tanner, Engineering Rheology, second ed., Oxford, Oxford, 2000.

[128] R.I. Tanner, K. Walters, Rheology: an historical perspective, Elsevier, Amsterdam, 1998.

[129] P. Thareja, I.H. Hoffmann, M.W. Libertatore, M.E. Helgeson, Y.T. Hu, M. Gradzielski, N.J. Wagner, Shear-induced phase separation (SIPS) with shear-banding in solutions of cationic surfactant and salt. J. Rheol. 55 (2011) 1375-1397.

[130] R.L. Thompson, P.R. de Souza, M.F. Naccache, A new constitutive equation and its performance in contraction flows. J. Non-Newton. Fluid Mech. 86 (1999) 375-388.

[131] J. van der Zanden, M. Hulsen, Mathematical and physical requirements for successful computations with viscoelastic fluid models, J. Non-Newton. Fluid Mech. 29 (1988) 93–117.

[132] P.A. Vazquez, G.H. McKinley, L.P. Cook, A network scission model for wormlike micellar solutions I. Model formulations and viscometric flow predictions, J. Non-Newton. Fluid Mech. 144 (2007) 122-139.

[133] W.M.H. Verbeeten, G.W.M. Peters, F.P.T. Baaijens, Numerical simulations of the planar contraction flow for a polyethylene melt using the XPP model, J. Non-Newton. Fluid Mech. 117 (2004) 73-84.

[134] C. Verdier, Rheological properties of living materials. From cells to tissues, *J. Theor. Med.* 5 (2003) 67-91.

[135] H.K. Versteeg, W. Malalasekera, An introduction to computational fluid mechanics: the finite volumen method, Longman, Essex, 1995.

[136] K. Walters, H.R. Tamaddon-Jahromi, M.F. Webster, M.F. Tomé, S. McKee, The competing roles of extensional viscosity and normal stress difference in complex flows of elastic liquids,

Korea-Aust. Rheol. J. 21 (2009) 225-233.

[137] K. Walters, R.I. Tanner, The motion of a sphere through and elastic liquid. In R. Chhabra and D. De Kee, editors. Transport processes in bubbles, drops and particles, Hemisphere Publ. Corp., United States of America, 1992.

[138] K. Walters, M.F. Webster, The distinctive CFD challenges of computational rheology, Int. J. Numer. Meth. Fluids 43 (2003) 577-596.

[139] K. Walters, M.F. Webster, H.R. Tamaddon-Jahromi, Experimental and computational aspects of some contraction flows of highly elastic liquids and their impact on the relevance of the Couette correction in extensional Rheology, Proc. 2nd Southern African Conference on Rheology (SASOR 2) (2008) 1-6.

[140] K. Walters, Webster M.F., H.R. Tamaddon-Jahromi, The numerical simulation of some contraction flows of highly elastic liquids and their impact on the relevance of the Couette correction in extensional rheology, Chem. Eng. Sci. 64 (2009) 4632-4639.

[141] P. Wapperom, M.F. Webster, A second-order hybrid finite-element/volume method for viscoelastic flows, J. Non-Newtonian Fluid Mech. 79 (1998) 405-431.

[142] P. Wapperom and M.F. Webster, Simulation for viscoelastic flow by a finite volume/element method, *Comp. Meth. Appl. Mech. Eng.* 180 (1999) 281-304.

[143] M.F. Webster, H.R. Tamaddon-Jahromi, M. Aboubacar, Transient viscoelastic flows in planar contractions, J. Non-Newtonian Fluid Mech. 118 (2004) 83-101.

[144] Webster M.F., Tamaddon-Jahromi H.R., Aboubacar M. Time-dependent algorithms for viscoelastic flow: Finite element/volume schemes, Numer. Meth. Part. Differ. Eq. 21 (2005) 272-296.

[145] S.A. White, A.D. Gotsis, D.G. Baird, Review of entry flow problem: experimental and Numerical, J. Non-Newton. Fluid Mech. 24 (1987) 121-160.

[146] J.L. White, A. Kondo, Flow patterns in polyethylene and polystyrene melts during extrusion through a die entry region: measurements and interpretation, J. Non-Newton. Fluid Mech. 3 (1977) 41-64.

[147] J. Yang, Viscoelastic wormlike micelles and their applications. Curr. Opin. Colloid Interface Sci. **7** (2002) 276-281.

[148] L. Zhou, L.P. Cook, G.H. McKinley, Probing shear-banding transitions of the VCM model for entangled wormlike micellar solutions using large amplitude oscillatory shear (LAOS) deformations, J. Non-Newton. Fluid Mech. 165 (2010) 1462-1472.

Index of tables

Index of figures

List of Publications

[1] J.E. López-Aguilar, M.F. Webster, H.R. Tamaddon-Jahromi, O. Manero, A new constitutive model for worm-like micellar systems - Numerical simulation of confined contraction-expansion flows. J. Non-Newton. Fluid Mech. 204 (2014) 7-21.

[2] J.E. López-Aguilar, M.F. Webster, H.R. Tamaddon-Jahromi, O. Manero, High-Weissenberg number predictions for micellar fluids in contraction expansion flows. J. Non-Newton. Fluid Mech. (2014) *Under review.*

[3] J.E. López-Aguilar, M.F. Webster, H.R. Tamaddon-Jahromi, O. Manero, Numerical modeling of thixotropic and viscoelastoplastic materials in complex flows. Rheol. Acta (2014) *Under review.*

[4] M. Pérez-Camacho, J. E. López-Aguilar, F. Calderas, O. Manero, M. F. Webster, Pressure-drop and kinematics of viscoelastic flow through an axisymmetric contraction-expansion geometry with various contraction-ratios. J. Non-Newton. Fluid Mech. (2014) *Under review.*

[5] J.E. López-Aguilar, M.F. Webster, A.H. Al-Muslimawi, H.R. Tamaddon-Jahromi, P.R. Williams, K. Hawkins, C. Askill, Chin Lye Ch'ng, G. Davies, P. Ebden, K. Lewis, *A* Computational Extensional-Rheology Study of Two Biofluid Systems, Rheol. Acta (2014) *Under review.*